1999

VOID STRUCTURE, COLLOID AND TRACER TRANSPORT PROPERTIES OF STRATIFIED POROUS MEDIA

MATHEWS, TOBIAS JOHN

http://hdl.handle.net/10026.1/2794

http://dx.doi.org/10.24382/3855
University of Plymouth

VOID STRUCTURE, COLLOID AND TRACER TRANSPORT PROPERTIES OF STRATIFIED POROUS MEDIA

By

TOBIAS JOHN MATHEWS

A thesis submitted to the University of Plymouth in partial fulfilment for the degree of

DOCTOR OF PHILOSOPHY

Department of Environmental Science
Faculty of Science

July 1999

ABSTRACT

VOID STRUCTURE, COLLOID AND TRACER TRANSPORT PROPERTIES OF STRATIFIED POROUS MEDIA

Tobias John Mathews

The characterisation of the properties of porous materials is of great importance in the effective management of natural and manmade systems. A sophisticated network model, 'Pore-Cor', of some of these properties has been previously developed. The present study has significantly extended the scope of the model's predictive capabilities.

Flow and transport behaviour was examined in laboratory sand columns of various depths. These experiments examined unsaturated flow of water and conservative solute tracer transport through homogeneous sand samples. Flow through these was not homogeneous or repeatable. Experimental observations found that this may have been due to subtle random variations in packing, and the network model was shown to be able to simulate these. Solute transport of bromide was studied, applied both uniformly and from a point source. Both scenarios were modelled using a convection-dispersion equation, and it was demonstrated that the lateral component of such transport was highly significant. It was shown how convection-dispersion equation predictions of uniformly applied tracer transport might be improved by the application of the network model and a method for improving predicted lateral solute transport was outlined.

It has been shown that levels of correlation in the distribution of differently sized voids within porous material may be responsible for large variations in permeability. This can make accurate modelling of permeability very difficult. A technique was developed for assessing the degree and nature of such correlations. The new method was tested on a variety of artificial and real samples and demonstrated to provide a quantitative assessment of such correlations. A method by which this could be used to improve network model simulations of materials possessing such correlation was described.

A method for the modelling of permeability damage due to the flow of suspensions through network simulations of porous media was developed. The new technique was shown to provide a reasonable estimate of permeability decline when compared with experimental results. Also, a new procedure for extrapolating the particle size distributions of the solid phase of simulations was created. This also performed well when compared with experimental results and was more sophisticated than existing methods.

Table of Contents

List of Figures and Tables

AUTHOR'S DECLARATION

At no time during the registration for the degree of Doctor of Philosophy has the author been registered for any other University award.

This study was financed with the aid of a studentship from the Engineering and Physical Sciences Research Council.

Seminars and conferences were regularly attended at which work was regularly presented. Consultation with other institutions and industrial contacts took place and several publications were prepared.

Signed..

Toby J. Mathews, July, 1999

PUBLICATIONS

Mathews,T.J., Matthews,G.P., Moss,A.K., Powell,G. (1994) Measurement and Simulation of Colloidal Flow Formation Damage in Sandstone, *Journal of the Society of Petroleum Engineers: Formation Evaluation pre-prints*

Mathews,T.J., Matthews,G.P., Ridgway,C.J., Moss,A.K. (1997) Measurement of Void Size Correlation in Inhomogeneous Porous Media, *Transport in Porous Media*, **28**, 2, pp135-158

Mathews,T.J.; Matthews,G.P.; Huggett,S. (1999, in press) Estimating Particle Size Distributions From A Network Model Of Porous Media, *Powder Technology*

Mathews,T.J.; Matthews,G.P. (1999) Water And Tracer Flow In Homogeneous Repacked Sand, *Water Resources Research*, in preparation

CONFERENCES, PRESENTATIONS AND TRAINING

Pore Size Analysis, March 1995, RSC Particle Characterisation Group Meeting and Annual General Meeting, Burlington House, London – Attended

Transport in Porous Media, March 1995, SCI Colloid and Surface Chemistry Group Meeting, Belgrave Square, London – Attended

Particle Size, Surface and Shape: Methods of Measurement, March 1996, RSC Particle Characterisation Group Meeting, University of Leeds - Attended

Third U.K. Colloid and Surface Science Student Meeting, July 1995, SCI Colloid and Surface Chemistry Group and RSC Colloid and Interface Science Group, University of Hull – Attended

Characterisation of Porous Solids IV, September 1996, University of Bath – Presented poster

CRAC 5 day Graduate School, October 1996, EPSRC – Participated

Chemistry Research for Britain, February 1997, Royal Society, London – Presented poster

Geofluids II, March 1997, Belfast – Presented poster

1 Introduction

The central aim of this research was the further characterisation of porous materials, with the specific intention of improving the predictive abilities of a network model of porous media. Experimental work was conducted at a variety of scales, from micro- to macro-scopic, examining various properties of several different porous materials. This work was used as the basis for further development of a network model, named 'Pore-Cor'. Model development has been conducted specifically with the intention of limiting the number of parameters not verifiable by experimental observation.

Porous materials and the processes in which they take part are of importance to a wide range of interests. For example, in reservoir engineering knowledge of the flow characteristics of oil or gas bearing materials is essential to maximise efficiency of extraction. Ignorance of the relationships between reservoir materials and the suspended and dissolved materials within them can result in costly damage to, or even destruction of, extraction potential. An understanding of the mechanisms governing the movement of water and soluble agrochemicals through agricultural soils is necessary to maximise productivity and avoid pollution of watercourses and aquifers. In industry increases in the efficiency of processes such as deep bed filtration and the production and use of catalytic substrates can be achieved through understanding the nature of porous materials utilised.

1.1 Network Modelling

The void space within a porous solid can be thought of as a network of voids (*pores*) connected by comparatively smaller channels (*throats*). Many workers have simulated this using network models that represent porous materials as an array of nodes connected by arcs (van Brakel, J., 1975). By positioning simulated voids of known geometry on the arcs and/or nodes of such a lattice, certain properties of the resultant network may be calculated and compared to those observed in real porous samples.

Early models of porous media represented porosity as bundles of straight, equal radius capillaries with no interconnections. Network models introduced the concept of

connectivity to the simulation of porosity. Network models vary enormously in levels of complexity. Such models may have two, three or more dimensions. They may range in nature from highly theoretical mathematical networks that cannot be represented geometrically to three-dimensional reconstructions of the actual void volume based on serial tomography of the material (Bryant, S. L. et al., 1993; Constantinides, G. N. and Payatakes, A. C., 1989; Koplik, J., 1982; Spanne, P. et al., 1994; Whittaker, 1984).

The network model developed here comprises a three-dimensional unit cell constructed around a regular 10 x 10 x 10 lattice of nodes. Nodes are positioned using Cartesian x, y and z co-ordinates, although since the unit cell is isotropic these axes are arbitrary. Up to 1000 cubic pores are centred on the nodes, and these are connected by up to 3000 cylindrical throats. Specific details of the model formulation are given in the next chapter. The remainder of this section shall be used to discuss some other examples of network models.

Blunt and King (1990; 1991) generated large (up to 80,000 features) two- and three-dimensional networks of equally sized voids, with pore co-ordination numbers (number of throats connected to a pore) between 3 and 12 (Blunt, M. and King, P., 1991). The sizes of the uncorrelated throats were uniformly distributed. Invasion percolation and unstable viscous flood were modelled, and the results interpreted in terms of non-linear Darcy equations and Buckley-Leverett theory.

Chatzis and Dullien (1985) used regular networks of 33 x 33 x 1 and 18 x 18 x 12 angular bulges connected by angular capillaries to simulate percolation. After transforming the simulation to a pore volume network and fitting to experiment, the points of inflection of the modelled sandstone mercury intrusion curves fit the experiments well, although elsewhere the theoretical curves differed by up to 8%.

Conner and Horowitz (1988b) modelled 10 x 10 x 10 networks of uniform pores and zero-volume throats. Mercury intrusion curves were calculated using the Washburn/Laplace equation (see Chapter 2 for details), and correction factors generated

2

for calculating pore size distributions from the first derivative of these curves. The unavoidable connectivity (average pore co-ordination number) of 6 was found to be extremely limiting.

Further discussion of other network models, where pertinent to the ongoing development of Pore-Cor, is carried out in the next chapter.

1.2 Flow and Transport in Porous Media

Flow of water and the transport of water-borne solutes and particulates through porous materials have been the subjects of considerable study. Due to environmental considerations these processes have become increasingly significant in both saturated and unsaturated porous media, and an enormous range of experimental and theoretical studies have been conducted at every scale from microscopic to field and reservoir. Much work conducted at the microscopic level has aimed to characterise the fundamental mechanisms, largely using molecular dynamics theory, by which movements within porous solids take place (Adler, P. M. and Brenner, H., 1984; Bernadiner, M. G., 1998; Sorbie, K. S. and Clifford, P. J., 1991; Thompson, P. A. and Troian, S. M., 1997). Laboratory and field studies have aimed to characterise how these mechanisms manifest at length scales ranging from less than one metre to the field scale (Biggar, J. W. and Nielsen, D. R., 1976; Bronswijk, J. J. B. et al., 1995; Butters, G. L. et al., 1989; Ward, A. L. et al., 1994; Yao, J. et al., 1997).

The physical basis of both saturated and unsaturated flow has been understood for the best part of this century, and mathematical expressions have been derived to describe situations of varying levels of complexity. The first and simplest of these is Darcy's Law, describing macroscopic flow in saturated porous media. An equivalent expression for unsaturated flow was subsequently developed in the form of the Buckingham-Darcy law, and the Richards equation combined this with water conservation terms to allow the calculation of water content or matric potential under transient flow conditions. A great deal of subsequent modelling has been based on these fundamental expressions.

The development of flow paths within unsaturated porous materials, particularly where *preferential flow* may occur, is of particular interest because of the importance of such phenomena in agricultural soils. Preferential flow is used to describe situations where large portions of a flow-conducting solid matrix, often including regions of immobile water, are bypassed by the mobile water fraction. Preferential flow is of particular importance in agricultural soils, where it can facilitate the rapid transport of nutrients and chemicals away from the surface to groundwaters, resulting in declining productivity in soils and pollution of water supplies.

Preferential flow implies that anomalously large flux or high velocity of flow through a sample occurs through a limited number of pathways. Preferential flow can be identified experimentally by the appearance of an anomalously high component of flow through one or two members of a large array of flow detectors. There is also an implication, as described below, that there is a structural difference between the flow paths containing the preferential flow and those containing the remaining flow through the sample. The threshold of preferential flow, in terms of relative flux or velocity, remains undefined throughout the literature. In this study, whether or not preferential flow occurs within certain experimental samples is considered. It follows that preferential flow must be identified in terms of whether the highest flow through the sample is a part of the overall distribution of flow through the sample, or whether it can be identified as part of a different distribution. For example, one might identify that the matrix flow through a sample was Normally distributed, and that preferential flow was characterised by an anomalous peak at the highest flow rates which was not part of the overall Normal distribution. It is in this manner, rather than any loose inference from the homogeneity or inhomogeneity of sample structure, that the existence of preferential flow is judged in this work.

Although there is some disparity in the nomenclature for different forms of preferential flow, at least three different mechanisms by which it may arise have been identified in the literature (Kung, K.-J. S., 1990a; Kung, K.-J. S., 1990b). In a heterogeneous substrate, such as a cracked or stony soil, *bypass flow* may develop if highly permeable macropores extend to the soil surface or the water pressure within them is

positive (Beven, K and Germann, P, 1982). An example of the first case would be a cracked soil experiencing heavy rainfall. If water ponds on the surface of such a soil, the permeable macropores will conduct water away much faster than less permeable areas, which may therefore remain relatively dry. Similarly, macropores underlying a layer of groundwater will preferentially transport water down through a porous material. Conversely, in soils with a negative water pressure buried macroporous regions can act as a barrier to the movement of water.

Buchter et al. (1995) observed considerable bypass flow in stony ($\approx$80% gravel) soil monoliths and staining of the flow fields revealed considerable structural heterogeneity. Flury et al. (1994) also demonstrated that, due to the bypassing of the majority of the soil matrix, structured soils represented a greater risk to groundwater than homogeneous soils in transporting soluble pollutants. They concluded that preferential flow should be considered the rule rather than the exception.

Fingering flow is used to describe the progress of unstable wetting fronts through a porous substrate, and it may be brought about by various mechanisms. Fingering has been shown to develop in sandy soils in less hydrophobic areas, and possibly correlated to particle size (Dekker, L. W. and Ritsema, C. J., 1994; Ritsema, C. J. and Dekker, L. W., 1994). Raats (1973) showed how fingering may develop if the velocity of a wetting front increases with depth and demonstrated, with the use of a Green and Ampt model, several scenarios in which this might take place. Subsequently Henrickx et al. (1993) used these criteria to demonstrate that fingering from a water repellent surface layer may result in 6 to 13 times as much solute transport to groundwaters, compared with transport from a wettable surface. Baker and Hillel (1990) showed that fingering might arise at the interface between two layers of homogeneous sand when the bottom layer is coarser than the top layer.

Kung (1990b; 1990a) identified a further form of preferential flow, *funnel flow*. Funnel flow takes place along inclined textural discontinuities, where a lower layer acts like the wall of a funnel to water moving from the upper layer. Water flows along this

lower layer accumulating until it reaches a critical pressure, when it then penetrates this lower layer by fingering flow.

Clearly, in natural porous media it is likely that more than one of the mechanisms described above may be present. Detailed experimental studies have shown that the development of preferential flow in structured soils may be sensitive to a complex combination of factors that may or may not be readily identifiable (Andreini, M. S. and Steenhuis, T. S., 1990; Williams, A. G. et al., 1999).

However, it has also been demonstrated that preferential flow may occur even when there is no discernible structural cause for such behaviour. In a dye tracing experiment on field plots Ghodrati and Jury (1990) observed considerable preferential flow, but were unable to identify the source other than to suggest that areas conducting greater flow were most likely to have higher permeabilities than surrounding areas. It has been suggested that some form of preferential flow may develop even in homogeneous samples. Porter (1968) postulated that water flows over random packings in rivulets, or small streams. These rivulets may randomly meet and coalesce to form larger rivulets, or alternatively large rivulets may divide. Experiments conducted on packings of uniform spheres, Raschig rings, Intalox saddles and Pall rings over a sampling grid appear to support this theory (Porter, K. E. et al., 1968), and a method for predicting the number of rivulets at a given depth was presented. This has also been interpreted to imply that increasing sample depth may be accompanied by a decrease in the total number of rivulets, and an increase in the volume of water being transmitted by individual rivulets (Dexter, A. R., 1995).

With regard to flow, the aim of this work was to investigate whether flow networks in homogeneous porous samples were themselves homogeneous, and whether the development of flow was amenable to modelling. In particular, the study aimed to investigate whether the network model Pore-Cor could provide supplemental information that might facilitate better predictions of the development of these flow networks (Chapters 3-6).

The importance of modelling transport through unsaturated porous material, particularly the leaching of solutes in soil, is well documented. This introduction will concentrate on the most significant developments in the field and the most relevant to this study. For a fuller discussion of the subject readers are directed to the literature (Addiscott, T. M. and Wagenet, R. J., 1985; Edwards, W. M. et al., 1993; Jury, W. A. and Flühler, H., 1992; Costa, J. L. et al., 1994; Ellsworth, T. R. et al., 1996; van Genuchten, M. Th. and Jury, W. A., 1987).

A large number of models of unsaturated transport have been formulated with the intention of predicting the transfer processes at work, with particular reference to the movement of agricultural chemicals through the root zone of farmed soils. Broadly such modelling can be divided into two categories: *deterministic* and *stochastic* models. Deterministic models assume that a given set of events will produce a uniquely definable outcome, whereas stochastic models assume there to be a degree of randomness in the systems they simulate and account for this.

Modelling has been dominated by deterministic models based on Fickian convective-dispersive transport, and these still represent the majority as far as popular models are concerned. Based in miscible displacement theory (Nielsen, D. R. and Biggar, J. W., 1962) convective-dispersive equations (CDE's) are also *mechanistic*, that is they incorporate fundamental mechanisms of the transport process. Practically this implies the use of equations derived from Darcy's Law to describe water flow and the representation of solute transport by mass flow and diffusion-dispersion mechanisms. In its simplest form the convection-dispersion equation may be written as,

$$R\frac{\delta c}{\delta t} = D\frac{\delta^2 c}{\delta z^2} - v\frac{\delta c}{\delta z}$$ [1]

where c is solute concentration, t is time, z is depth, v is pore water velocity (volume flow rate divided by the product of cross-sectional area and volume water content), R is a retardation factor and D is the diffusion coefficient.

In the latter half of this century a large number of analytical and numerical solutions to Equation 1, or variants of it, have been presented (Huang, K. L. et al., 1996; Ge, S. M. and Lu, N., 1996; Leij, F. J. et al., 1993; Nachabe, M. H. et al., 1995; van Genuchten, M. Th. and Alves, W. J., 1982). Analytical solutions tend to have the advantage of being general in form and flexible. However their inability to model transport taking place under non-steady state conditions, with regard solute and water, limit their usefulness largely to laboratory studies. As a consequence various numerical solutions have been proposed to deal with non-steady conditions, for example the partitioning of the water-filled porosity into mobile and immobile phases (van Genuchten, M. Th. and Wierenga, P. J., 1976).

The chief shortcoming of models based upon the convection-dispersion equation are the treatment of the flow fields across the unsaturated material as a homogeneous continuum. Practically this results in the assumption that modelling parameters, most importantly D and v, remain constant at all levels of observation. This limitation results in a degree of inflexibility in the modelling capabilities of these methods, and some workers have criticised this. However, convection-dispersion based models remain popular and traditional models are being augmented by research into the nature of variation in model parameters at the field scale. In particular, it has been suggested that the diffusion coefficient, D, varies according to a simple linear relationship with depth (Huang, K. L. et al., 1996; Khan, A. U. and Jury, W. A., 1990).

Stochastic models are based upon the assumption that field-scale properties of soil vary spatially, and thus variations in water and solute movement will also exist. Stochastic adaptations of traditional mechanistic models have been developed as well as stochastic models that make no reference to mechanism. The former type typically incorporates a distribution of random input data that produces a distribution of output values. Studies using such models have shown variability in v to be significantly more influential than equivalent changes in D, that is convective processes rather than diffusive (Bresler, E. and Dagan, G., 1981). Addiscott and Wagenet (1985) point out that a limitation of such techniques is that a knowledge of the nature of the variance at the field scale is necessary, or some assumption as to its nature must be made.

8

The use of entirely stochastic models is dominated by transfer functions, similar to those often applied to industrial processes (Jury, W. A., 1982; Liu, H. H. and Dane, J. H., 1996; Zhang, R. D., 1995). Transfer function models conceptualise the soil as bundles of twisted capillaries of different lengths through which water moves via piston flow. The probability, P_L, of a solute tracer added to the soil surface at time t arriving at a depth L as the applied water increases from I to $(I + dI)$ is summarised by a probability density function, $f_L(I)$, which produces a distribution function,

$$P_L(I) = \int_0^1 f_L(I) dI \qquad [2]$$

It is the probability function that allows the model to represent the variability of hydraulic properties over the field scale. Various workers have found that, measuring concentrations at depth L over a number of locations, the probability density function takes the form of a log-normal distribution (Biggar, J. W. and Nielsen, D. R., 1976; Jury, W. A. and Sposito, G., 1985; Butters, G. L. et al., 1989).

Other purely stochastic methods have been developed. For example, Knighton and Wagenet (1987) formulated a model based on a continuous time Markov process. This simulated solute movement by employing a birth-death population based approach. Using such a method future values of a modelled property are predicted purely on the basis of their current value, with no reference to past values. In this instance the movement of solute molecules between discrete layers of a simulated soil was modelled. The modelled porous matrix was characterised by a single value of v, the pore water velocity. Model predictions were compared against a series of experiments involving repacked soil columns, and were found to be in reasonable agreement with the experimental results. However, the soil columns were so narrow (approximately 10-cm circular diameter) as to make the experiments effectively one-dimensional, and measured variations in transport properties such as pore water velocity have typically been measured over much greater scales (Biggar, J. W. and Nielsen, D. R., 1976).

The intention of this work was to conduct solute leaching experiments on homogeneous sand samples using apparatus developed specifically for this study. Both

transport of a uniformly applied conservative solute tracer and of a tracer applied to a discrete region on the sample surface were studied (Chapters 3 and 4). Transport of a uniformly applied conservative solute tracer was studied to test whether predictions of solute transport using a simple convection-dispersion equation could be improved by use of network modelling techniques (Chapter 6). Network models can provide additional information concerning the structure of unsaturated porous materials that may, or may not, be of use in simulating the movement of dissolved species through them. Transport from a point source was studied to investigate the degree to which this transport was symmetrical about the point of application, and the extent to which such behaviour might also be predictable using a convective-dispersive model coupled with the network model (Chapter 6).

In addition to solute leaching the movement and deposition of suspended particles through disordered porous media is also of interest. In systems such as enhanced oil recovery, water purification and chromatography such movement and deposition is often described by the term deep-bed filtration (DBF). During enhanced oil recovery, formation damage by fines may be both undesirable and desirable. Suspended particulate material can cause extreme damage to reservoirs, and may require costly pre-filtration to prevent. However, in other circumstances suspended fines may be used as temporary plugging particles, sealing wellbores to prevent further reservoir damage. DBF theory has also been used to describe the industrial filtration of fine colloidal particles from liquid suspensions and processes involved in certain catalytic chemical reactions. Often it is the subsequent reduction in permeability, frequently a negative side effect of the process, caused by DBF that is of interest.

As a consequence of the wide range of applications in which deep-bed filtration may be implicated, many workers have derived models to help understand and predict such processes. Several distinct model types have emerged. Generally these can be categorised as either empirical, trajectory analysis-based, stochastic or network models. Examples of each type and a full discussion of the differences between approaches are given in the introduction to Chapter 9.

The network model being developed already features a crude model of colloidal deposition. Prior to this study this amounted to the removal from the simulations of all features smaller than a user defined minimum size. Effectively this simulated straining or size exclusion of particulate material within the porous matrix. The scenario this modelled was somewhat artificial, in that all void features that would be blocked by the modelled particles were accessible. That is, structural characteristics of the network such as connectivity played no part in the process. The development of an improved model of the transport and deposition of suspended material was undertaken in response to these obvious shortcomings. It was intended that the new model would feature, in addition to a more sophisticated model of straining type deposition, an alternative probabilistic model based in some way on the modelled conditions present in the simulated void structure and flowing suspension (Chapter 9).

1.3 Correlations in the Spatial Distribution of Voids

Many naturally occurring and manufactured porous media are inhomogeneous in terms of the spatial distribution of differently sized void spaces. Sandstones, for example, can be laminated because of sorting of the mineral grains and rock fragments during formation of the consolidated rock. Clay inclusion within sandstones may form clusters of small pores or dissolution may cause loci of larger void spaces in 'vuggy' samples. Soil can exhibit layering, clustering, vugs and the formation of 'peds' (regions often surrounded by preferential-flow channels). Manufactured porous media can also be inhomogeneous. Paper is a porous structure typically comprising a fibrous substrate filled and/or coated with china clay or calcium carbonate, which is bound to the substrate with starch or latex. Some catalyst substrates comprise a laminar carbon fibre mesh, bonded with resin that preferentially adheres to one side.

Fluid flow is often of crucial importance in these and other porous media. In sandstones, the flow of oil, gas and water determine reservoir properties, and the efficiency of extraction of the oil and gas. As indicated previously, the movement of water and potentially polluting soluble chemicals through soils are of major importance, and catalysts can only operate successfully if the transport of fluids to and from them, through the

substrate, is efficient. It has been shown previously (Matthews, G. P. et al., 1995) that the introduction of void size correlation into samples of similar porosity can change their permeability by several orders of magnitude. Such effects are important in the study of unfractured sandstone plugs, and are referred to as 'secondary porosity' by oil/gas reservoir simulators. Correlation effects are also important in the study of the migration of dissolved and colloidal species in soils, clays and siltstones, and in other porous media such as paper coatings on fibrous substrates (Kettle, J. P. and Matthews, G. P., 1993).

In fundamental studies of correlation effects by other workers, void space networks are usually generated with pore and throat size distributions and correlation levels governed by pre-set mathematical functions. Such models have the advantage that the void space parameters can be sophisticated and precise, while having the disadvantage that they are only loosely related to any particular experimental sample. Li, Laidlaw and Wardlaw (1986; 1990) demonstrated analytically how for the case of a linear throat size distribution, non-wetting phase (mercury) intrusion occurs at a lower applied pressure in a correlated network, and less non-wetting phase is entrapped after secondary imbibition of a wetting phase. Wardlaw (1990) also demonstrated this effect in multiple intrusion/extrusion scanning loops. Tsakiroglou and Payatakes (1991) generated $30 \times 30 \times 2$ and $20 \times 20 \times 20$ networks of cylindrical throats and spherical pores with shaped necks, and demonstrated that simulated mercury intrusion curves had a less pronounced point of inflexion within pore : pore and pore : throat correlated models than for uncorrelated structures. Ioannidis and Chatzis (1993a; 1993b) have represented porous media with a $50 \times 50 \times 50$ array of cubes, with different grey levels representing pore bodies of different sizes. Their representations were constructed according to pre-set pore and throat size distributions, and pre-set size auto-correlation functions. Correlation was shown to make mercury intrusion slightly more gradual with increasing pressure, to increase capillary hysteresis, and to reduce the residual mercury saturation. Day et al. (1994) point out that extreme positive and negative pore : pore size correlation may produce a bimodal distribution with size maxima so far apart that a two-step mercury intrusion curve results.

Most experimental studies of void size correlation effects have been based on image analysis of serial sections of resin or Woods metal impregnated samples. Adler and co-workers (1990; 1992), for example, studied resin-injected Fontainebleau sandstone sections, and measured correlation functions in terms of whether a void space existed or not at a measured distance from another void space. They then 'reconstructed' the porous medium using a 27 x 27 x 27 array of cubes, each cube being either solid or void. The array had the same porosity and correlation factor as the 2-D sections of sandstone. Wardlaw, Li and Forbes (1987) injected samples of Berea sandstone and Indiana limestone with Wood's metal, and etched the sample so that the Wood's metal stood in relief. Electron micrographs of the void space were then examined. The diameters of pores and throats were then measured, and graphs of size frequency, and correlation between throat diameter and the directly connected pores were plotted. The throat diameters for Indiana limestone were found to cover a much narrower size range, and to be more size-correlated to directly connected pores, than in Berea sandstone.

Wood's metal can also be partially injected into samples to give results analogous to mercury porosimetry (Dullien, F. A. L. and Dhawan, G. K., 1975). Lymberopoulos and Payatakes (1992) have measured correlation effects by serial tomography, using analyses based on 30 serial sections approximately 7.5 μm apart. Algorithms were developed to interpolate the void volumes between the serial sections and to distinguish pores from throats. Their results were also expressed as graphs of characteristics such as throat diameter versus the average contiguous-chamber diameter, and chamber diameter versus the average immediate-neighbour diameter. They found weak pore : pore correlation within a sandstone, but significant pore : throat correlation. Mercury intrusion was found to be weakly affected by pore : throat correlation. However, pore size clustering in combination with pore : throat correlation had a strong effect on intrusion, causing it to occur over a wider range of pressures.

Little, if any, work has focussed on generating network simulations with correlations in the spatial distributions of voids based on experimentally observed levels. When making studies of porous media that include their permeability, such measures may be extremely

13

beneficial with regard model accuracy. Consequently this study also investigated whether the levels of correlation in several real and constructed porous samples could be quantified. Ultimately it was intended that this might enable the network simulations with correlations in void size spatial distributions similar to those observed in real samples (Chapter 7).

1.4 Solid Phase Modelling

In porous materials composed of particles the characteristics of the particles affect packing structure, which in turn affects all structural properties of the material. During the preparation and development of porous materials, or in the study of the migration of fluids through them, it is often of interest to be able to infer the particle size distribution (PSD) of the hypothetical unconsolidated solid phase. For example, the effects of varying levels of cementation on sandstones have been investigated by analysis of thin sections taken from varying depths (Taylor, J. M., 1950) and by comparison of mercury intrusion curves (Matthews, G. P. and Ridgway, C. J., 1997). It may also be of interest to examine what effect this might have on apparent particle size distribution. Work has also been conducted on the progressive development of different network configurations during the process of sintering certain materials (Aigeltinger, E. H. and DeHoff, R. T., 1975). A method of estimating the particle size distribution of consolidated materials could be used to simulate such processes. Similarly, in reservoir engineering it might be possible to examine whether mineral deposition in a reservoir material had the effect of increasing the apparent size of the original particles, or if the extra mineral material merely occluded within the pores of the substrate causing a reduction in connectivity. Another example might be studying the individual sizes of the carbon granules that, upon consolidation, form a filter or a catalyst substrate.

Exact solutions have long been available which allow the calculation of the particle size distribution of regularly packed mono-sized spheres, derived from the pressure/saturation characteristics of a wetting fluid such as water or benzene (Haines, W. B., 1927), or of a non-wetting fluid such as mercury (Mayer, R. P. and Stowe, R. A., 1965), the latter calculation being currently available in the control software for mercury

porosimeters (Micromeritics, 1996). However, the mathematics for the deduction of the size distribution of poly-disperse and/or randomly packed particles is intractable.

Pore-Cor allows the inference of an approximate, but nevertheless useful, void structure for random porous media, based on the mercury intrusion curve. The present study aimed to investigate whether the network model could be used to infer the particle size distribution of the assumed-spherical particles of the solid. To the author's knowledge this was the first study of this type. The method was tested using porous samples made up from unconsolidated grains, to judge its likely success on consolidated samples (Chapter 8).

2 Pore-Cor

2.1 Introduction

The aim of this study was the further characterisation of porous media in such a way as to allow continued development of the network model Pore-Cor. It was intended that experimental observations coupled with model development would facilitate increased understanding of certain porous systems, and enable more accurate predictions of their behaviour. Model development to date has been based on the principle that the number of arbitrary fitting parameters that cannot be verified experimentally should be kept to a minimum. This work described here aimed to continue in this vein. Consequently, in addition to model development experimental studies were conducted over a range of scales to compliment theoretical work.

What follows here is a brief description of the processes and capabilities of Pore-Cor at the commencement of this work.

2.2 Void Structure Modeling

The field of network modelling of meso- and macro-porous media is well developed (Matthews, G. P. et al., 1995; Tsakiroglou, C. D. and Payatakes, A. C., 1991; Lowry, M. I. and Miller, C. T., 1995; Deepak, P. D. and Bhatia, S. K., 1994). The void space model that this project aimed to develop further is named 'Pore-Cor' (pore-level properties correlator), and can simulate a wide range of properties of meso- and macro-porous media (Matthews, G. P. et al., 1995). It conceptualises the porosity of a material as a network of voids connected by smaller channels. It has been successfully employed in the modelling of a range of materials, such as sandstones, paper coatings and tablets, and a variety of their properties, for example porosity, permeability, colloid flow and tortuosity (Mathews, T. J. et al., 1997; Matthews, G. P. et al., 1996; Gane, P. A. C. et al., 1996; Ridgway, C. J. et al., 1997).

The model described here has the particular characteristics that it has an explicit geometry upon which all properties are calculated from first principles, and that the fitting

parameters used to converge on experimental data are characteristics such as connectivity which can be checked experimentally as being within a realistic range. The absence of arbitrary fitting coefficients allows it to be used on any porous medium.

2.3 Geometry

Pore-Cor is a network model of porous media that represents the void space of samples as an array of cubic *pores* connected by cylindrical *throats*, the constricted connections between pores (Figure 2.1). The pores are centred on a regularly spaced 10 x 10 x 10 lattice of nodes, positioned using Cartesian co-ordinates *x*, *y* and *z*, the distance between which is termed the *pore row spacing*. The pore row spacing is used to adjust the porosity of the simulated porous media. Each array of up to 1000 pores and their connecting throats is described as a *unit cell* (Figure 2.1) and for modelling purposes the unit cell repeats infinitely in all directions. Other parameters include the *connectivity*, which is the average *pore co-ordination number* (number of connected throats per pore) and *pore* and *throat skews*, the skew of the pore and throat size distributions respectively.
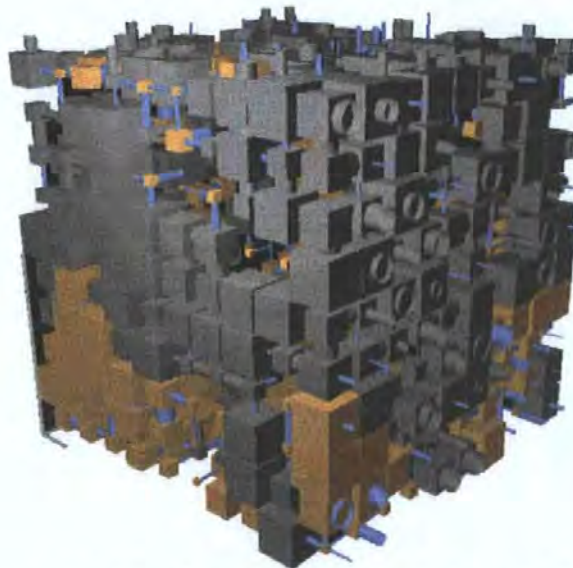
Figure 2.1 A unit cell generated by Pore-Cor showing the simulation of Redhill 65 sand. Mercury, shown in grey, has intruded corresponding to an applied pressure sufficient to fill pore diameters up to 100 microns. The large scale bar corresponds to 2.40-mm, the short one to 0.48-mm.

For calculation a *primary position* is defined as the position of a pore centre displaced by half the pore-row spacing in the *x*, *y* and *z* directions. Each primary position is at the centre of a cube defined by the centres of eight adjacent pores.

2.4 Mercury Porosimetry

The Washburn (or Laplace) equation is used to calculate throat diameter, d, from applied mercury pressure, P,

$$d = -\frac{4\gamma\cos\theta}{P}$$ [1]

where γ is the interfacial tension between the mercury and air and θ is the mercury contact angle. Limitations in the accuracy of Equation 1 arising from uncertainties in the values of γ and θ have been documented (van Brakel, J. et al., 1981b). Surface roughness may cause the contact angle to be as high as $180°$. For the purposes of this work modelling unconsolidated packed sand (Chapters 6, 8 and 9) the commonly accepted value for sandstone of $140°$ was used throughout. The interfacial tension is taken to be 0.0485 Newtons m^{-1}, which reduces Equation 1 to,

$$d = \frac{1470}{P}$$ [2]

where d is measured in microns and P is given in kilopascals. Mercury intrusion curves plot volume of intruded mercury, V, against P. V is often converted to a percentage of the total void volume and P to throat diameter using Equation 1. Typically this produces a sigmoidal mercury intrusion curve, an example of which is given in Figure 2.2. Traditionally the void size distribution has been obtained by taking the first derivative of this curve, producing a distribution with a peak at the point on the intrusion curve where the gradient is greatest. However, this interpretation of the data is only valid for a porous material comprising a bundle of tortuous, unconnected capillaries, each with a different but uniform diameter.
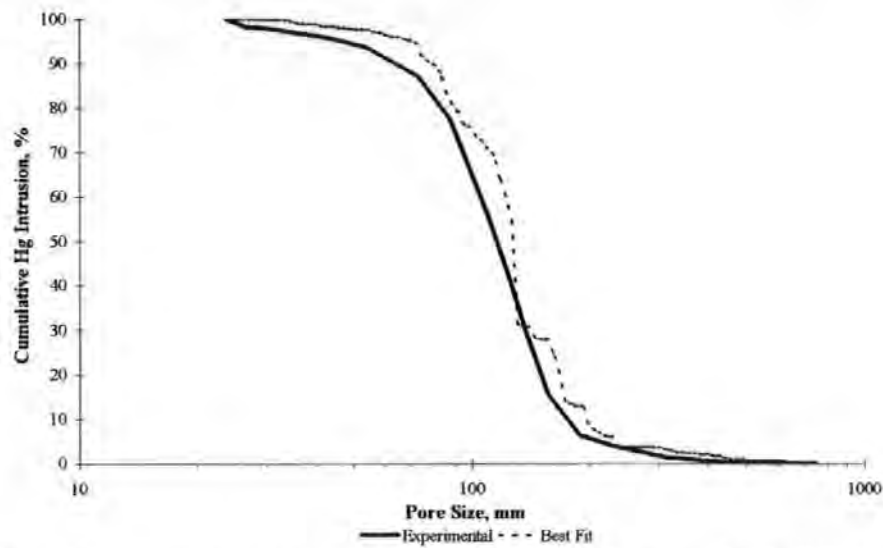
Figure 2.2 Example mercury intrusion curve and modelled Pore-Cor curve for Redhill 65 sand.

Pore-Cor uses a percolation algorithm to model mercury porosimetry. The two main limitations to using such a method based on Washburn/Laplace have been identified as i) throats are considered to be cylindrical and ii) the mapping of the effective network based on the mercury porosimetry is not necessarily the same as the real network (Garboczi, E. J., 1991). Various studies into the effects of void shape have been carried out including using arrays of packed spheres (Mason, G. and Mellor, D. W., 1991), rod- and plate-like structures (Conner, W. C. et al., 1988a), intersecting ellipsoids (Yanuka, M. et al., 1986) and ellipsoid cylinders (Garboczi, E. J., 1991). The fact that close fits to experimental results can be achieved using simple void geometries indicates that it is not necessarily valid for workers to attribute discrepancies between simple models and experiment as arising from subtle information such as pore and throat shape and formation damage. Pore-Cor's networks are based upon actual samples and are therefore closer to actual representations of the void network than to mathematical networks, unlike most other models in the literature.

2.4.1 Hysteresis

At sufficiently high pressures a sample will become saturated with mercury. However, upon decreasing the pressure more mercury remains in the sample than the amount intruded at corresponding pressures, and this is known as *hysteresis*. Even at the lowest possible pressure quantities of mercury remain in the samples, and this is termed

residual saturation. This effect is similar to the recovery efficiency of oil from a reservoir following displacement by a water flood, which is dependant on pore size distribution, connectivity and pore:throat size correlation (Wardlaw, N. C. and Cassan, J. P., 1979). Hysteresis may result from a number of causes.

2.4.1.1 Structural Hysteresis

During intrusion throat radius controls the pressure at which throats are intruded. However, secondary imbibition, emptying of mercury from pores, is controlled by pore size. Figure 2.3 shows two cylindrical throats and a pore in series.
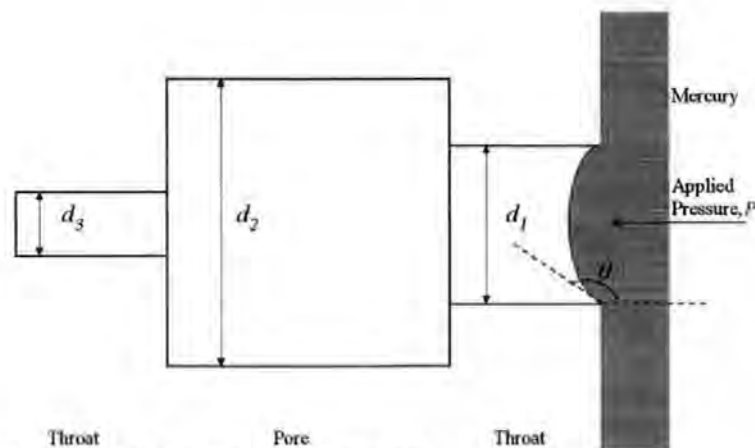
Figure 2.3 A one-dimensional pore and throat network.

Considering, for the sake of simplicity, Equation 2 it can be seen that the throat of diameter d_1 will fill with mercury when the applied pressure, P, exceeds $1470/d_1$. At this pressure the pore, d_2, also fills with mercury. When P is raised above $1470/d_3$ the final throat will also become filled with mercury. As P is subsequently decreased the final throat will empty first as the pressure falls below $1470/d_3$, extruding an equivalent volume of mercury at the sample surface. The pore will empty next, but whereas it filled as P was raised above $1470/d_1$ it will empty as P falls below $1470/d_2$, hence hysteresis occurs.

2.4.1.2 Snap-off

It has been shown that if d_2 is much greater than d_1 then the mercury has difficulty readjusting its shape to extrude through the narrower pore (Wardlaw, N. C. and McKellar, M., 1981; Chatzis, I. and Dullien, F. A. L., 1981). The ratio of d_2 to d_1, R, has been measured for a range of sandstones and limestones ranging in value from 3 to 148.7

(Wardlaw, N. C. and Cassan, J. P., 1979). A potential explanation is that as the mercury-air interface moves through irregularly shaped channels the meniscus has to adopt non-equilibrium shapes (Dawe, R. A. and Egbogah, E. O., 1978). It is always trying, however, to assume its minimum energy configuration. This can be achieved by a sudden change in shape, and consequently the interface may progress in a series of jumps, known as Haines jumps. For specific values of R this may result in *snap-off* of the mercury column. Trapped wetting phase (air) may re-expand, acting as a seed for snap-off.

Snap-off may also result from the network structure. A continuous line of unbroken mercury to the sample surface is required for emptying to take place. If a large pore is shielded from the surface by smaller voids, which drain before the pressure required for drainage of the large pore is achieved, all continuous mercury-filled routes to the surface may be broken resulting in trapping.

2.4.1.3 Correlations in Void Size Distributions

From preceding sections it can be seen that correlations between the sizes of adjacent pores and throats may affect intrusion and hysteresis. It has been shown that pore:throat size correlation has a weak effect on intrusion, while pore:throat correlation combined with pore:pore correlation has a strong effect (Constantinides, G. N. and Payatakes, A. C., 1989). It has also been observed that correlation can decrease shielding effects described in the previous section (Li, Y. et al., 1986; Li, Y. and Wardlaw, N. C., 1990; Wardlaw, N. C., 1990). Figure 2.4 shows the effects of the pore:throat size ratio on hysteresis.
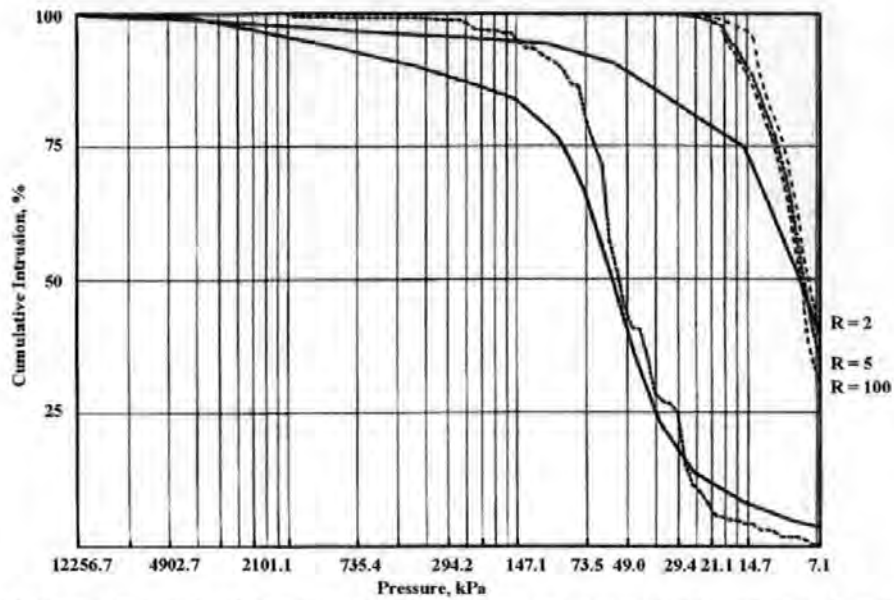
Figure 2.4 Effect on hysteresis of changing the pore:throat size ratio, R. Experimental results are shown by the solid lines, modelled results by the dashed lines.

The networks used in Pore-Cor are correlated by setting the size of each pore equal to the diameter of the largest throat entering it. Other types of correlation have also been simulated (Mathews, T. J. et al., 1997; Matthews, G. P. et al., 1995), and the work conducted here extends previous studies into the effects of correlations in the distributions of different sized pores in real porous materials (Chapter 7).

2.4.1.4 Dead-end Pores

Dead-end, or 'ink bottle', pores, that is pores connected to just one throat, also cause structural hysteresis. A mercury-filled dead end pore can only empty by surface flow of wetting phase along the walls and non-wetting phase withdrawal along the middle of the throat. This happens rarely and consequently dead-end pores, the number of which increases as co-ordination number decreases, cause trapping of mercury.

2.4.1.5 Contact Angle Hysteresis

In mercury porosimetry analysis a constant contact angle is commonly assumed, typically 140°. However, evidence exists to suggest that contact angle hysteresis, a difference between intruding and extruding mercury contact angles, takes place (Kloubek, J., 1981; Bell, W. K. et al., 1981). Obviously a difference between intrusion and extrusion will have significant effect on the Washburn/Laplace equation and it has been shown that, in principle, irreversible mercury penetration may result from contact angle hysteresis (van

22

Brakel, J. et al., 1981a). One suggestion is that mercury injected behind an advancing mercury meniscus has the effect of cleaning the meniscus, but that during extrusion impurities may collect on the meniscus (Wardlaw, N. C. and Taylor, R. P., 1976). Impurities in the meniscus have been shown to be a source of hysteresis (Shaw, D. J., 1986). Many different estimates of contact angle magnitude for different materials have been made (Good, R. J. and Mikhail, R. Sh., 1981). Modelled effects of changing connectivity are shown in Figure 2.5.
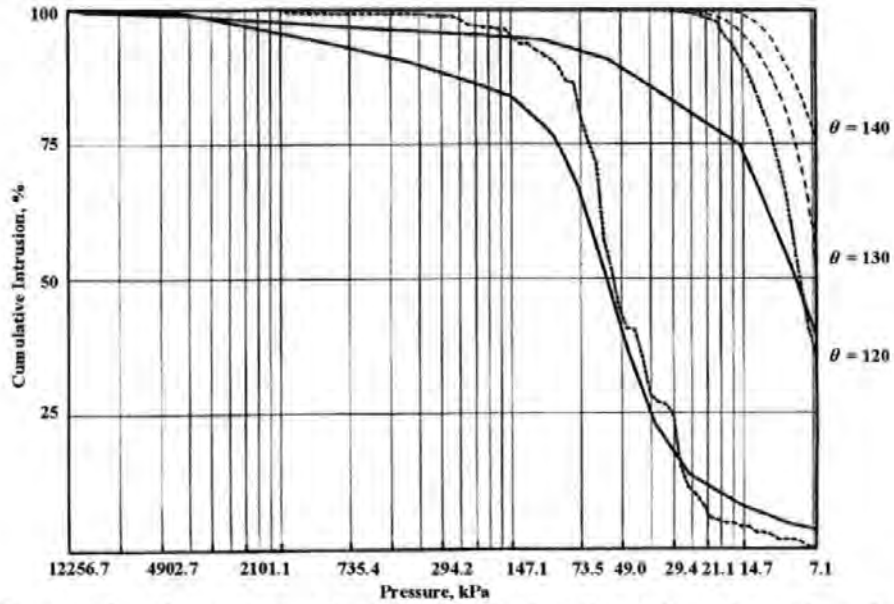
Figure 2.5 Effect of changing contact angle on hysteresis where R = 5. Experimental results are shown by the solid lines, modelled results by the dashed lines.

2.5 Void Space Modelling

A percolation algorithm, which assumes intrusion is controlled by the Washburn/Laplace throat diameters, is used to model mercury intrusion. Throat lengths are equal to the distance between pore edges, determined by pore size and pore row spacing. Pore row spacing is adjusted, after the pores and throats have been positioned, to model the experimental porosity. Throat length has little effect on simulated intrusion, and therefore the porosity can be modelled independently of mercury intrusion. Throat size distribution is log/linear, that is equally spaced over a logarithmic scale (Figure 2.6).
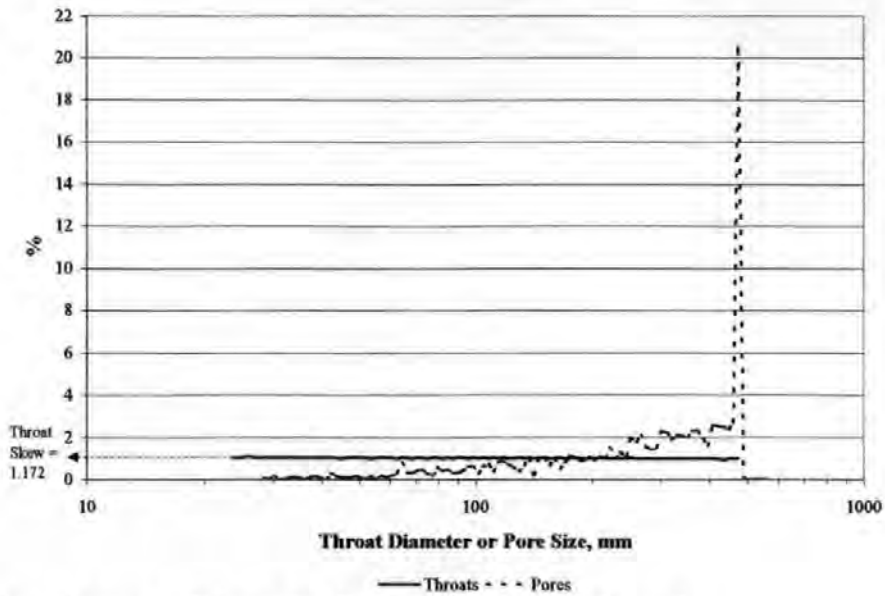
Figure 2.6 Example pore and throat size distribution for Redhill 65 sand.

The adjustable parameters are throat diameter range, skew of throat size distribution, pore:throat correlation and pore row spacing. Throat diameter range is calculated from the mercury intrusion pressure range limits and there are 100 throat diameters in each distribution. The pore size distribution, generated from the throat size distribution, may be checked against electron micrographs of the sample. Throat skew is defined as the percentage of the smallest size throats in the log/linear distribution. Figure 2.6 shows a skew of approximately 1% which, due to the 99 other sizes, results in an almost uniform distribution. The throats are randomly positioned within the unit cell, following which pores are assigned to the nodes. The random positioning of the throats introduces a degree of randomness to the pore size distribution, which can be seen in the jagged distribution Figure 2.6. The pore size distribution shown also features a *pore skew*. The pore size distribution is multiplied up by this factor and then any pore whose size is larger then the original maximum of the range is truncated to this maximum pore size. This results in a frequency peak at the maximum of the pore size distribution, but enables larger porosities to be simulated.

Simulated mercury injection takes place normal to the xy plane of the unit cell at $z = l_{cell}$ in the $-z$ direction, where l_{cell} is the length of the unit cell. An invasion percolation

method is used to calculate the fraction of the pore volume occupied at each static pressure (Spearing, M. C. and Matthews, G. P., 1991).

The gradient of the intrusion curve at the point of inflection is governed by connectivity. For simplicity the high curvature regions of the curve above and below the point of inflection shall be described the upper and lower shoulders respectively. Increasing connectivity shifts the curve to higher throat diameters and makes the upper shoulder too high as a result of increasing the gradient at the point of inflection, Figure 2.7. Breakthrough occurs at larger throat diameters, or lower pressures, because of the increase in routes through the network. This can be countered by increasing the throat skew, but resulting intrusion curves will still possess an exaggeratedly steep upper shoulder.
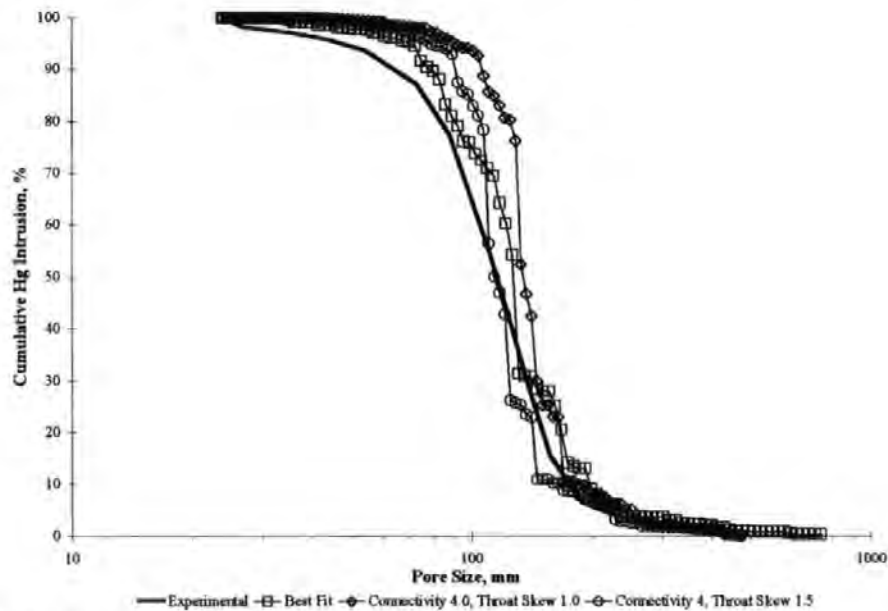
Figure 2.7 Changing connectivity and throat skew, Redhill 65.

2.5.1 Automatic Convergence of Model onto Experimental Data

Automatic methods of optimising connectivity and throat skew to produce the best fit of modelled to experimental mercury intrusion data have been developed. The curves may be fitted at the point of inflection by changing skew or by changing both connectivity and skew to improve fit, expressed on a least squares minimisation basis.

25

2.5.1.1 Fitting the Point of Inflection (The '50% Method')

The simplest method involves varying the throat skew to achieve the best fit of modelled point of inflection to experimental. The only criterion for fit is that the deviation, Δ_{50}, between experiment and simulation must be within 3% of total logarithmic range of the graph at the point corresponding to 50% of the total intruded mercury. Initially the skew is set to 1.0, then either 0.5% or 1.5% depending on which is expected to give the better fit. A third skew is then calculated using a linear interpolation/extrapolation algorithm. Further iterations are possible but previous work has shown that, generally, three are all that is necessary (Matthews, G. P. et al., 1995).

2.5.1.2 Regular Spacing Algorithm

An improved fit over that provided above is achieved by comparing the horizontal separation between modelled and experimental intrusion curves at intervals along the pore volume axis. The easiest way to achieve uniform relative weightings of deviations over portions of the curve would be to consider points evenly spaced along the vertical axis. However, the measurements obtained from mercury porosimeters are not usually evenly spaced in this way. Interpolation could produce such a series of points, but would also introduce inaccuracies because the functional form of the experimental curve is unknown. The compromise used by Pore-Cor is to use experimental points wherever possible but to remove or linearly interpolate points if the pore volume spacing is outside set limits. These limits are arbitrarily set at half and twice the spacing along the pore volume axis compared to the spacing required for the experimental points to be evenly spaced. The same set of comparison points is used for each simulation of a sample. The difference in experimental and modelled Washburn throat diameter, d, is calculated at each appropriate pore volume. Two measures of deviation are used, the linear deviation, Δ_{lin}, and the log deviation, Δ_{log}.

$$\Delta_{lin} = \frac{\sum_{i=1}^{n} \left(d_{\exp(V_i)} - d_{sim(V_i)} \right)^2}{n}$$

$$\Delta_{log} = \frac{\sum_{i=1}^{n} \left(\log d_{\exp(V_i)} - \log d_{sim(V_i)} \right)^2}{n}$$

[3]

where n is the number of comparison points, V_i is the intruded volume at a given point and the subscripts *exp* and *sim* refer to experimental and simulated values respectively.

26

Minimisation of the linear deviation (the 'linear' method) tends to give greater weighting to fitting the curve at larger throat diameters while the 'log' method gives the best fit over the whole of the curve.

Both of the above methods use the 50% method to find a mid-point for optimising throat skew. The test range for skew is then taken to be ± 0.70 at intervals of 0.10, while connectivity is tested over the range 2.6 to 5.0 at intervals of 0.1. Every combination of connectivity and throat skew is computed to find the best-fit curve and also to plot a three-dimensional surface which demonstrates the goodness of fit and uniqueness of the result.

2.6 Tortuosity

For a particle moving through a porous material, for example an ion passing through a membrane, tortuosity is defined as the ratio of the path length taken by a particle to the length of the porous sample. Frequently tortuosity has been assumed to be responsible for discrepancies between predictions and observed behaviour in various porous systems, and as such tends to have been employed largely as a fitting parameter.

Pore-Cor allows the calculation of the tortuosity of simulated porous media. This is achieved by simulating 50 weighted random walks, from top to bottom, through the unit cell. A simulated particle is assumed to enter the unit cell at a random location on the top surface. At each pore a random throat is selected, with the choice being weighted by a factor of r^2/l, where r is throat radius and l is throat length. Pore-Cor returns the median value of all the random walks as well as the inter-quartile range.

2.7 Permeability

A long-standing problem in the study of porous media has been the question of how to calculate the permeability of a solid from a knowledge of the geometry of the void space within it. The absolute permeability k of a porous solid is traditionally defined in terms of Darcy's law. With reference to a cell of the solid of unit volume, this may be written:

$$\left(\frac{dV}{dt}\right)_{cell} = -\frac{kA_{cell}\delta P_{cell}}{\mu l_{cell}} \qquad\qquad [4]$$

where μ is the viscosity of the fluid, $(dV/dt)_{cell}$ is the volumetric flow rate across the cell, $\delta P_{cell}/l_{cell}$ is the pressure gradient across the length l_{cell} of the cell, and A_{cell} is the cross-sectional area. Many attempts have been made to calculate k from primary parameters such as the diameters, lengths and positions of the pores and throats. Other workers have described equations based on characteristic parameters such as porosity, the total externally-accessible surface area per unit volume of the solid, the characteristic throat diameter d_c (often loosely referred to as the characteristic pore diameter), the tortuosity, t, and the formation factor F (Matthews, G. P. et al., 1993). The most successful to date has been that of Thompson, Katz and Raschke (Thompson, A. H. et al., 1987):

$$k = \frac{1}{226}\frac{d_c^{\,2}}{F} \qquad\qquad [5]$$

The equation predicts permeabilities correct to a factor of 7, for a range of sandstone and limestone samples covering several orders of magnitude of experimental permeability.

An incompressible fluid flowing through a tube takes up a parabolic velocity profile, with maximum flow rate down the centre of the tube. If the flow at the walls is assumed to be zero, integration over the velocity profile yields the Poiseuille equation:

$$\left(\frac{dV}{dt}\right)_{tube} = -\frac{\pi\, r_{tube}^{\,4}.\delta P_{tube}}{8\mu l_{tube}} \qquad\qquad [6]$$

$(dV/dt)_{tube}$ is the volume flow rate, r_{tube} the radius of the tube and $\delta P_{tube}/l_{tube}$ is the pressure gradient along the tube. Poiseuillian flow has been shown to occur for oil displacement in capillaries down to 4-μm in diameter (Templeton, C., 1954).

If Poiseuillian flow is assumed to occur across the whole cell in the -z direction, i.e. from the top to the bottom face of the unit cell. Then

$$\left(\frac{dV}{dt}\right)_{cell;-z} = -\frac{\pi}{8\mu}\Omega(r_{tube;z}{}^4)_{cell}\frac{\delta P_{cell}}{l_{cell}} \qquad [7]$$

Ω is an averaging operator over the whole unit cell operating on the fourth power of the individual radii $r_{tube;z}$ of all tubes lying parallel to the z axis. It is calculated by means of the 'Dinic' network analysis algorithm (Ahuja, R. K. et al., 1997). Ω is defined such that Equation 4 is satisfied, and generates a term which is related to the effective Poiseuillian capacity of the cell for flow in the $-z$ direction. Since at this stage of the calculation, all the tube lengths $l_{tube;z}$ are identical and $l_{tube;z} = l_{cell}/\beta$, where β is the number of tubes in the z direction in the unit cell (in this case 10), we can include these lengths in the averaging function, so that

$$\left(\frac{dV}{dt}\right)_{cell;-z} = -\frac{\pi}{8\mu}\Omega\left(\frac{r_{tubes;z}{}^4}{\beta l_{tube;z}}\right)_{cell}\delta P$$

$$= \frac{\pi}{8\mu}\Omega\left(\frac{r_{tube;z}{}^4}{l_{tube;z}}\right)_{cell}\frac{\delta P}{\beta} \qquad [8]$$

By considering tubes in the $\pm x$ and $\pm y$ directions as well, and comparing with the Darcy equation, Equation 1, it follows that

$$k = \frac{\pi}{8\beta}\Omega\left(\frac{r_{tube}{}^4}{l_{tube}}\right)_{cell}\frac{l_{cell}}{A_{cell}} \qquad [9]$$

Once this equation is corrected for the square cross-section of the pore a liquid permeability may be calculated (Schlicting, H., 1979).

2.8 Conclusions

A network model capable of predicting certain experimental properties of porous media has been described. Through experimental observation and model development this study aimed to enhance understanding of porous materials by improvement of the network model and by its appropriate application to situations which might benefit from this.

3 Transport Apparatus: Construction and Testing

3.1 Introduction

The chief objectives of the work described in this chapter were the design and construction of laboratory apparatus for the study of flow and transport behaviour. Unconsolidated sand samples were chosen for this, for reasons discussed in the next chapter. In particular, the apparatus was required to allow the investigation of lateral variations in these processes. Consequently the provision of highly spatially uniform water and solute application was essential, as was the ability to identify spatial variations in sample outflow. With this in mind, the three essential areas of concern regarding the design of the apparatus were determined to be; porous material containment; sample collection; uniform water/solute application.

3.1.1 Porous Sample Containment

Sample containment was fairly simple, due to the choice of unconsolidated sand as the sample material. The use of sand allowed samples to be introduced directly into the sample container in the laboratory. Samples were prepared in a cuboid, open-ended Perspex container. Perspex was chosen for cost and ease of machining, and also the fact that degradation due to long term exposure to water was relatively limited. Further details are given in Section 3.2.

3.1.2 Effluent Sampling

Many other workers have described apparatus for the laboratory study of transport through porous materials. Buchter et al. (1995) stood a soil monolith upon 19 porous ceramic plates to examine heterogeneous flow and solute transport. Other workers have used a metal grid with an array of funnels machined into it (Bowman, B. T. et al., 1994; Phillips, R. E. et al., 1995), plastic or metal grids more like open trays (Dexter, A. R., 1995; Andreini, M. S. and Steenhuis, T. S., 1990) and plastic sheets with triangular cross-section corrugations cut into them (Porter, K. E. et al., 1968; Porter, K. E., 1989) to retrieve spatial information from sample outflows.

This study employed a grid lysimeter similar to that described by Phillips et al. (1995) and Bowman et al. (1994), which allowed the study of spatial variations in outputs. This was designed to minimise impedance to drainage from the flat undersides of consolidated samples by presenting as close to zero flat surface as possible. As unconsolidated sand was chosen the samples were actually continued into the funnels, and this problem was avoided entirely. Apart from these considerations the grid lysimeter (described in Section 3.3) was chosen for its level of sophistication in allowing the study of the spatial variability of flow and transport behaviour.

3.1.3 Water and Solute Application

Water application in laboratory transport experiments is generally carried out using a *rainfall simulator*, the term being used to describe a range of equipment used for the delivery of water and tracer solutions. The most commonly used are of two types, those based on spray nozzles and those based on a grid of needles or needle-like drippers. Other systems, such as grids of capillary tubes (Dexter, A. R., 1995) and even a single catheter traversing the entire sample surface via a motorised assembly (Andreini, M. S. and Steenhuis, T. S., 1990) have also been used.

In laboratory experiments the needle-type apparatus tends to be the more commonly used. This is partly due to that fact nozzles tend to produce a non-uniform distribution of rainfall intensities (Chow, Ven Te and Harbaugh, T. E., 1965), producing a greater intensity of 'rain' directly under the nozzle that decreases with horizontal distance from the nozzle. Grids of needles are favoured for their uniformity of application (Romkens, M. J. M. et al., 1975; Bowman, B. T. et al., 1994; Phillips, R. E. et al., 1995; Hignett, C. T. et al., 1995). During this work a grid of dripping hypodermic needles was selected as the most likely to fulfil the requirement for uniform water and solute application. Although the eventual design was similar to others in the literature it featured a novel mechanism for homogenising spatial application, details of which are given in Section 3.4.

3.2 Sample Containment

The apparatus was constructed within a square cross-section, tubular steel frame approximately 2.7m high (Figure 3.1). The sample was contained 1.24 m above the floor in an open-ended cuboid Perspex case of approximately half metre side (cross-sectional area 506 x 506 mm^2) which was mounted on the grid lysimeter (Section 3.3). The container was constructed from four individual sheets joined at the corners by square brackets bolted through the plastic. The bolts used had screw heads on the inside of the container and these were finished below the surface of the plastic then sealed with silicone sealant. The edges of the plastic sides were also sealed at the corners with silicone sealant. During experimentation it was necessary to completely saturate samples, and thus the sample container had to be completely watertight. To this end it was sealed to the grid lysimeter using high bulk modulus silicon sealant.
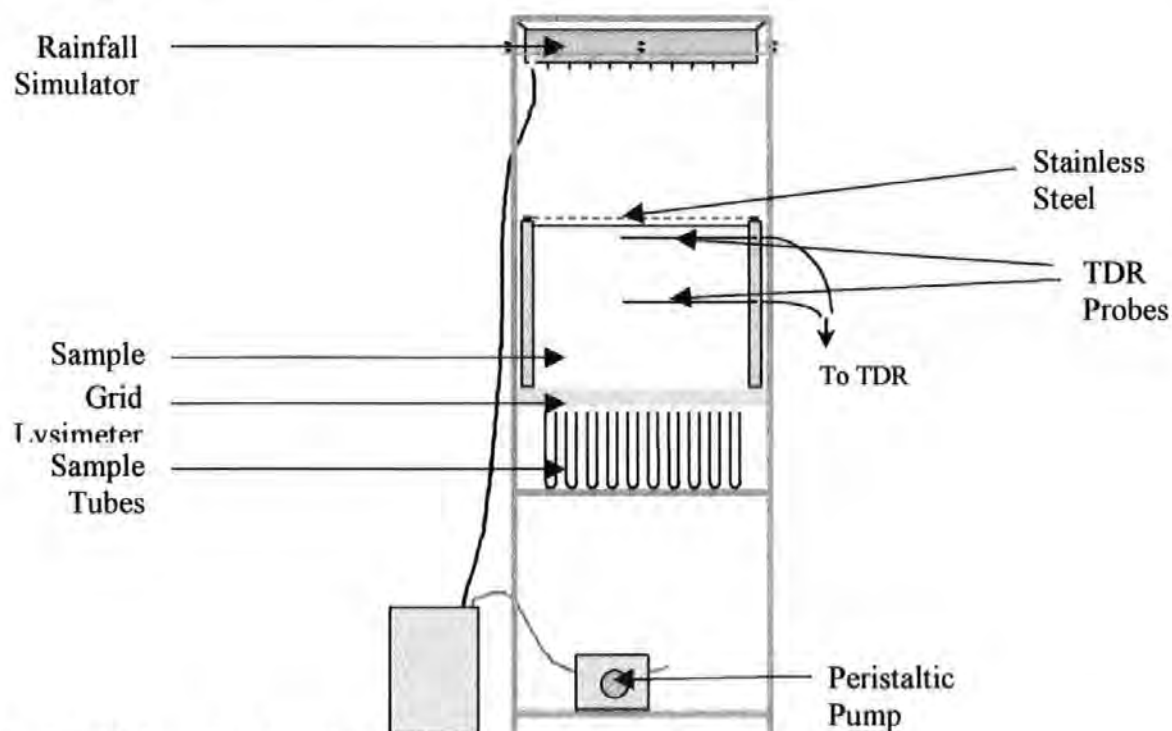
Figure 3.1 Schematic of experimental flow/transport apparatus.

3.3 Grid Lysimeter

A grid lysimeter was constructed for the study of spatial variations in flow and transport similar to the designs of Phillips et al. (1995) and Bowman et al. (1994). The lysimeter was constructed of an anodised aluminium plate with a ten by ten array of square funnels of side 38 mm machined into it (Figure 3.2). Around this array larger, sloping edge

channels of width 63 mm were also machined to allow collection of edge flow from the container walls. It was also important to prevent any resistance to flow into the sampling array, or sample saturation discontinuities at the sampling horizon (Phillips, R. E. et al., 1995; Bowman, B. T. et al., 1994). In the present study, the sand sample was continued into the sample collection funnels, thus minimising such effects.
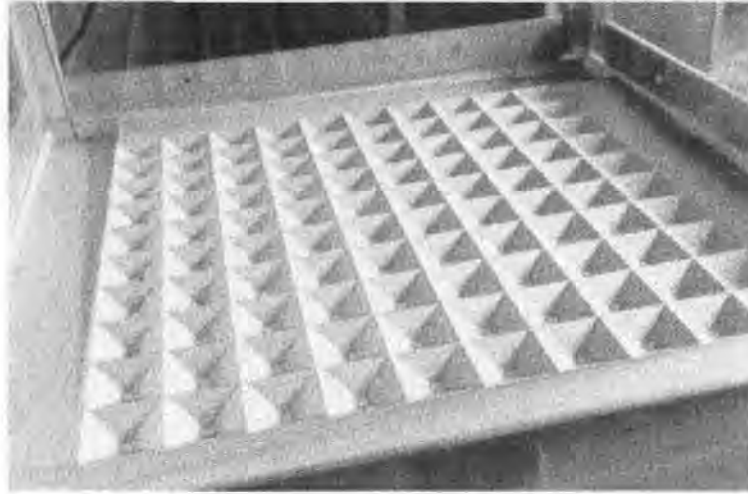
Figure 3.2 The grid lysimeter.

Stainless steel tubes cemented to the outlets from the square lysimeter funnels conducted flow to specially constructed removable racks of sample tubes for sample collection. The stainless steel tubes had small quantities of glass wool inserted prior to the commencement of each experiment to filter out large particulate material. This required great care. It was necessary to use just enough glass wool to prevent the sample from escaping, while allowing water to drain freely. To achieve this each funnel was tested in turn before sand samples were introduced.

3.4 Rainfall Simulator

The basic design consisted of a cuboid reservoir constructed from PVC with dimensions 451 x 451 x 114 mm (Figure 3.3). The reservoir featured a variable height overflow that allowed the head of water in the reservoir to be controlled. The design used here was an 'open' system, in that by the head of water over the needles controlled rainfall intensity. Other similar systems are 'closed' and regulation of the water supply is used to control intensity (Chow, Ven Te and Harbaugh, T. E., 1965; Romkens, M. J. M. et al.,

1975). The overflow took the form of a rigid plastic tube inserted vertically through the floor of the reservoir, sealed with a rubber grommet and attached at its bottom end to a hose re-circulating water to a supply reservoir. Water ('Milli-RO') was supplied from this tank via a peristaltic pump (H R Flow Inducer, Watson Marlow Ltd., U.K.) and silicon tube fed through the top of the reservoir, terminating below the level of water in the reservoir. This was done to minimise splashing in the reservoir and therefore limit the formation of air bubbles that tended to block the needles.
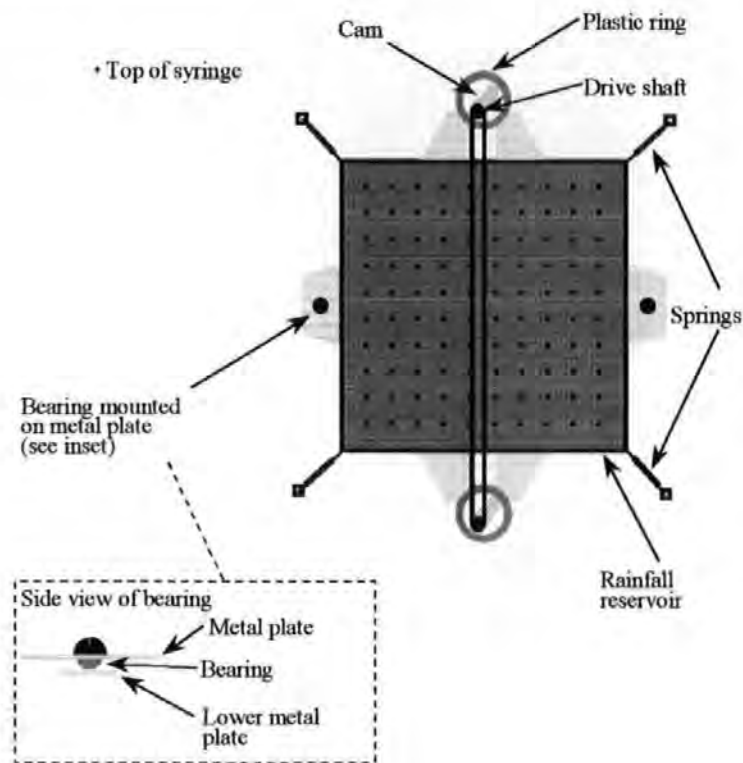
Figure 3.3 Plan view of the rainfall simulator.

Protruding from the underside of the reservoir was an array of syringe needles cemented in place with high bulk-modulus silicon sealant. After some initial tests the size of the needle array was increased in comparison to that of Bowman et al. (1994). Array size was enlarged from to a twelve by twelve array (excepting two diagonally opposite needles that could not be included due to the overflow outlet and a screw). Although the original configuration matched that of the funnels in the grid lysimeter it somewhat neglected the areas over the side channels of the lysimeter. This may have led to dryer regions at the sample edges that would have influenced the saturation of the sample over the sampling region. Although the enhancements made here improved the uniformity of water

34

application (Section 3.5.2) ideally the array of syringe needles in the rainfall simulator would cover an area larger than the surface are of the entire sample. However, this would require extra facilities for the collection and containment of the excess water which were unavailable during the work described here.

A simple mechanism was also developed for providing a degree of x-y translation to the rainfall simulator as it applied water or solute. This took the form of an electric motor that turned a vertical brass rod, upon which a cam was mounted. The cam turned within a PVC ring attached to an edge of the rainfall reservoir, which was supported on bearings running on horizontal metal plates (detail, Figure 3.3).

Testing this arrangement revealed the degree of movement of the reservoir to be greater on the side of the motor/cam. To rectify this a second brass rod was placed, running freely, in a bearing on the opposite side, synchronised to the first. Initially these were joined by means of a rubber belt drive, similar to a car's fan belt, although ultimately this was replaced with a more robust chain drive.

At the suggestion of Alex Vickers (Silsoe College, Cranfield Institute of Technology, Bedfordshire, U.K.) a stainless steel mesh (circular holes, 2 mm diameter) was interposed between the underside of the rainfall simulator and the sample surface to further homogenise application.

3.5 Rainfall Simulator Trials

3.5.1 Testing Application Rates

Various combinations of needle gauge and head height were tested (Table 3.1). Unless stated otherwise, all tests were carried out with a head height in the rainfall simulator reservoir of approximately 34 mm. Originally 25G needles, internal diameter (I.D.) 0.241 mm, were installed, but were impossible to maintain flow through. Although similar numbers of needles appear blocked from one hour to the next, this does not indicate

that the same needles were remaining blocked. After each count of blocked needles, water was pumped through any that had stopped flowing until they started to drip again. Although filtered water was used throughout the tests and experimental period, it was thought that perhaps atmospheric particulate material was entering the system and causing the apparent needle clogging. To guard against this an inline filter unit (Part Number 1119, Gelman Sciences Inc., U.S.A.) fitted with 30-μm filter paper (Grade 113, Whatman International Ltd., U.K.) was installed after the pump. However, this had no effect on needle blocking. Instead the problem may have arisen from capillary forces due to narrowness of the internal diameter, perhaps coupled with the presence of tiny air bubbles. The continuous dripping of most needles suggested that slight inconsistencies in the manufacturing process may have affected reliability.

21G (0.495mm I.D., not shown in Table 3.1) were found to drip too quickly, equivalent to more than 20mm rainfall hour^{-1}. Finally 23G (0.318mm I.D.) needles were installed. These delivered an acceptable rate of application of around 1659.7 ml hour^{-1} (6.48 mm hour^{-1}), with all needles flowing continuously.

Throughout the testing process it was often necessary to remove individual needles that consistently became blocked and replace them. Thus in Table 3.1 there are two columns for 23 gauge needles, the second representing the initial set after replacement of those that continually failed to flow. This implied inconsistencies in manufacture.

Needle Gauge	25G	23G	23G
Head Height, mm	76	34	34
Time, min.		Needles Blocked	
60	17	3	0
120	16	4	0
180	14	5	0
240	17	3	0
300	17	3	0
360	11	0	0
420	-	1	0
480	-	1	0

Table 3.1 Testing needles for the rainfall simulator.

This problem of maintaining flow was not anticipated from the literature review. Many authors refer to similar droplet-forming systems of water and solution delivery (Bowman, B. T. et al., 1994; Chow, Ven Te and Harbaugh, T. E., 1965; Andreini, M. S. and Steenhuis, T. S., 1990; Romkens, M. J. M. et al., 1975). Some suggest the use of needle gauges a small as 0.203mm I.D. (Bowman, B. T. et al., 1994), yet none refer to the problems described above. Often needles with much greater bore are used than tried here. However, this in turn gives rise to the problem of exceptionally high rates of application/ 'rainfall'.

3.5.2 Testing Uniformity of Application

It was essential that spatial heterogeneities were not introduced via water/solute application. Throughout the development of the rainfall simulator, homogeneity of application was studied by running the rainfall simulator directly over the grid lysimeter and monitoring the volumes of water delivered to the funnels. Experiments were normally carried out over the course of 7-8 hours, taking volume measurements hourly. Table 3.2 and Figure 3.4 give details of the various simulator configurations and their results.

Simulator Conditions			Applied Rainfall, ml minute^{-1}			
Needle Array	x-y translation	Mesh	Min	Max	Mean	Standard Deviation
10 x 10	✘	✘	0.163	0.340	0.280	11.97
10 x 10	Single cam	✘	0.013	0.450	0.206	47.38
10 x 10	Single cam	✓	0.044	0.239	0.141	21.76
10 x 10	Double cam	✓	0.080	0.229	0.173	20.34
12 x 12	Double cam	✓	0.148	0.287	0.230	8.80

Table 3.2 Testing the rainfall simulator.

37
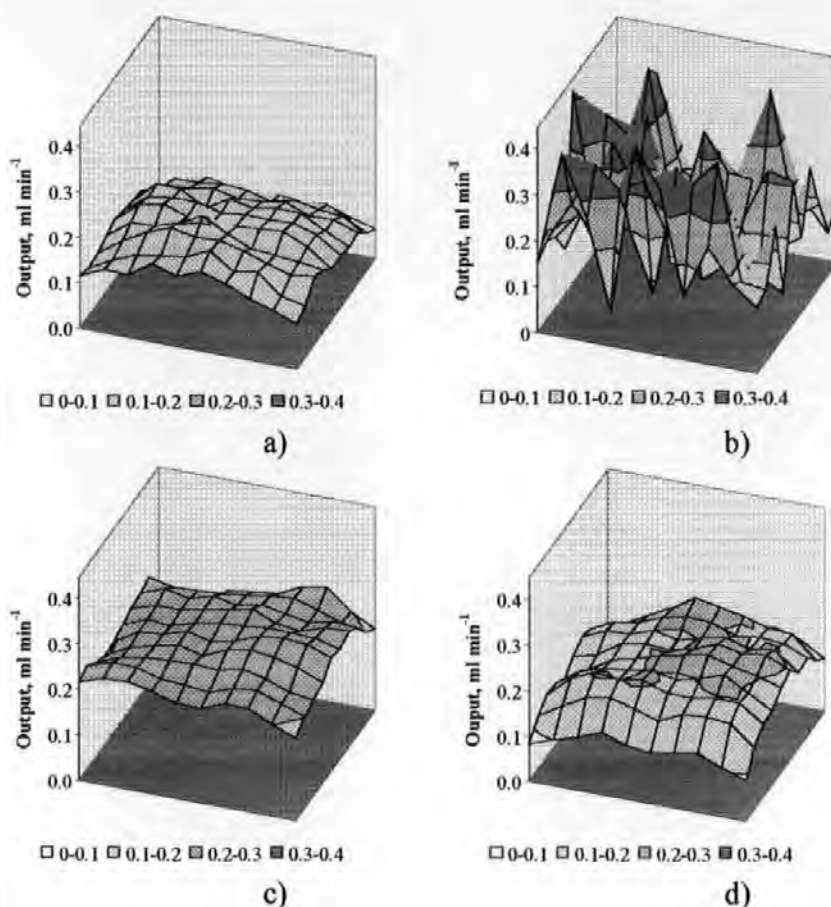
Figure 3.4 Surface plots of output rates under various rainfall simulator conditions, these being a) x-y movement alone, b) movement plus the stainless steel mesh, c) x-y movement, enhanced with the addition of the belt drive, plus the mesh and d) enhanced movement, the mesh and increased needle grid size.

It can be seen that some improvements were achieved adding the stainless steel mesh and the belt/chain drive. By far the most substantial improvements to uniformity were brought about by the extension of the needle array beyond the spacing of the grid lysimeter. Comparing relative standard deviations and coefficients of variation (Christiansen, J. E., 1942) to literature figures (Table 3.3) it can be seen that the apparatus developed here compared extremely favourably with those of other workers. Many studies fail to address the issue of spatial uniformity of rainfall application altogether. Those shown in Table 3.3 that do all employ considerably more complex designs than the apparatus described here, typically using two, or even three, electric motors and systems of gears, worm drives and so on. The design described here not only achieved acceptable levels of application uniformity, but did so with comparatively cheap and simple apparatus.

		Homogeneity of Water Application	
Workers	RSD, %	Uniformity Coefficient, %
This study	8.8	93.04
Bowman et al. (1994)	n/a	>98.00[1]
Dexter (1995)	≈19.0	n/a
Phillips et al. (1995)	11.6–22.4	n/a
Romkens et al. (1975)	8.5[2]	n/a
Andreini & Steenhuis (1990)	n/a	94.08[3]

Table 3.3 Homogeneity of application of various rainfall simulators.

The syringe themselves were also tested (Table 3.2). It can be seen that the various mechanisms employed here diminished the inherent variability in the syringe needles.

3.6 Measurement of Water Content

The sample container also provided access for measurement of volumetric water content of the samples. Water content was measured by time domain reflectometry (Topp, G. C. et al., 1980), a widely used method for field and laboratory estimation of water content. TDR is extremely flexible, and it has been demonstrated that calibrating the technique to individual samples yields little improvement in accuracy (Topp, G. C. et al., 1980). However, other authors have demonstrated some dependence on bulk density and temperature (Ledieu, J. et al., 1986). Good agreement between this method and more traditional gravimetric methods has been shown (Topp, G. C. and Davis, J. L., 1985).

The method involves measuring the lag between an incident and reflected high frequency electromagnetic pulse sent down parallel metal rods inserted in the water-containing medium. This is then used to calculate the dielectric constant of the material between the rods. Having obtained the dielectric constant, K, the water content of the material, θ, is then given by the equation (Topp, G. C. et al., 1980),

$$\theta = -0.0530 + 0.0292K - 0.00055K^2 + 0.0000043K^3 \qquad [1]$$

Pairs of TDR probes, in the form of 3-mm diameter stainless steel welding rods (Rightons, Plymouth, Devon, U.K.) spaced 20-mm apart and connected to a Tektronix 1502C cable tester, were inserted through holes drilled in the sample container at various depths throughout samples. At each depth two pairs of probes of two different lengths were

---

[1] No details given except that this figure is for rainfall rates in the approximate range 5-25 mm hour[-1].
[2] Average of five figures carried out at five different rainfall rates.
[3] Average of four figures each of which is an average of the 'before' and 'after' values for an experiment.

inserted, one pair of length 100-mm the other of 450-mm. TDR allows calculation of the average water content along the length of probes. For this reason two different lengths of probe were included so that water content could be monitored across the width of the sample and across the region closest to the edge of the container. This was to ensure that measurements across the sampling region were not greatly influenced by water contents near the walls. This was subsequently found not to be the case, although there did tend to be greater variability measured by the shorter probes, reflecting the greater averaging effect of the longer probes.

3.7 Sampling

An automated sampling system was devised for collecting effluent samples during the bulk solute transport experiments described in the next chapter. A square tray was constructed, dimensions 432 x 432 x 41-mm, that was suspended at a steep incline underneath the array of funnels. One corner of the tray fed a plastic funnel, which in turn was connected to a short length of PVC tubing. The tubing was connected at its other end to a three-way electronic timer valve, one output of which went to a waste container the other output feeding to an automatic fraction collector (2112 Redirac Fraction Collector, LKB). For most of the time the valve directed the output from the samples to the waste container. However once every 15 minutes the valve switched flow to the automated sample collector for a 15 second period, allowing a small sample to be taken.

It was found when designing the system described above performed best when relatively large bore tubing was used. Initially the system was tested with comparatively narrow (3-mm I.D.) tubing. However, this tended to cause entrapment of small effluent volumes in the tubing between the valve and the fraction collector, causing cross-contamination between samples. It was found that by using larger (6-mm I.D.) tubing the flow of effluent from the funnel was small enough that it trickled down the walls of the tube, rather than completely filling it. Consequently, even after the valve switched the flow back to the waste container the last drops of sample continued to drain freely.

3.8 Discussion

This chapter has described the construction of apparatus for studying various flow and transport behaviour of porous samples, particularly lateral variations in such behaviour. Although the apparatus was designed with the intention of studying unconsolidated sand samples, it is suitable for the study of flow through any porous material that can be supported by the grid lysimeter; such as soil blocks. The equipment designed here matches the specifications of the majority of the most sophisticated designs described in the relevant literature.

The equipment was thoroughly tested to ensure that the apparatus itself did not contribute to horizontal heterogeneities in flow and transport processes. In particular the rainfall simulator was designed to provide a constant rate, uniformly applied to samples over extended periods of study. The grid lysimeter was also designed to allow the study of lateral variations in flow and transport. This was made possible by the presence of the edge region around the volume above the 10 x 10 funnel array, which was intended to minimise the influence of edge effects and to maintain rectilinear flow above the sampling grid.

4 Transport Experimental

4.1 Introduction

The experiments and analyses described in this chapter were carried out as a means of investigating the 'base line' variability of the flow and transport characteristics of homogeneous samples, and to provide data for the modelling in the next chapter.

To characterise the approach, it is necessary tightly to define the definition of *homogeneous* and *homogeneity* when applied to porous samples. In this context, a *homogeneous sample* is defined as one in which there are nothing more than small random differences in any *pore structure related property* when integrated over scales of the order of 1-mm to 1-m. Pore structure related properties include the mode of distribution of grains of various sizes, the packing angles and geometric arrangement of these grains, and the porosity of the void space between them. Size distribution, packing angles and geometric arrangement variations are sufficiently subtle that the perturbations caused by many methods - such as resin intrusion - would invalidate the measurement. In practice, therefore, the protocol with homogeneous samples is to prepare them by careful packing initially, and verify the homogeneity in terms of lack of variation of visually observable structure throughout the sample chamber. The random porosity variation across the sample can be inferred from separate porosimetry measurements. In all subsequent discussions, 'homogeneous' will be defined in the way just described.

As discussed in Chapter 1, much work has been conducted examining flow and transport through saturated and unsaturated porous materials. Several authors have shown that preferential flow, the bypassing of significant volumes of porous media by the flowing fluid, may develop by a variety of mechanisms (Beven, K and Germann, P, 1982; Buchter, B. et al., 1995; Dekker, L. W. and Ritsema, C. J., 1994; Kung, K.-J. S., 1990b). Despite observations of unaccountable preferential flow (Ghodrati, M. and Jury, W. A., 1990), the suggestion that preferential flow may develop randomly (Porter, K. E., 1968) or that the extent of preferential flow in homogeneous samples will increase with depth (Dexter, A. R., 1995), by and large these mechanisms are all assumed to arise as a result of structural

variations in the porous matrix. Consequently, the first hypothesis under consideration is that flow through homogeneous and structure-less samples, as prepared here, is homogeneous, and any variations in flow are statistically random.

To study homogeneity of flow it is necessary to establish whether or not flow patterns arise as a result of sample structure, either inherent or introduced in the preparation process. Hence, in addition to monitoring the distribution of flow over each sample tested during the conservative tracer transport work, a further study, to investigate the influence of wetting and packing, was carried out. One sample was tested in detail to ascertain whether the flow distributions observed in the prepared samples were statistically random, or structured.

In addition to the chief hypothesis described above, other studies of the flow distributions through homogeneous samples were carried out. The first of these secondary hypotheses was that the distribution of flow fluxes and velocities through homogeneous samples would be made more or less random by changes in sample thickness. Secondly, work was conducted to test the hypothesis that the distribution of flow was dependent on sample grain size or permeability. Finally, samples were constructed to examine whether or not the development of flow distributions was affected by the layering of samples of different grain sizes/permeabilities.

Although transport of solute tracers applied uniformly to a sample surface has been studied extensively, little work has concentrated on the movement of a solute applied to a discrete region. The simplest such scenario would be the movement of a conservative solute tracer applied at a point on the surface of a homogeneous porous material. Such transport may be of interest for a variety of reasons. For example, in pollution incidents involving soluble pollutants, potential transport in the horizontal plane may be of equal concern to vertical movement. 'Chemirrigation' is the application of agrochemicals via irrigation systems (Keng, J. C. W. et al., 1998). Irrigation emitters are employed in the application of fertilisers and pesticides, and each one may be considered a point source. In such a case the likely fate of applied chemicals needs to be known to achieve the most

efficient placement and spacing emitters, with regards the optimal delivery of chemicals and minimal risk of contamination to groundwaters. Only a small number of experimental studies of such scenarios have been made (Khan, A. A. et al., 1996; Clothier, B. E. and Sauer, T. J., 1988; Ellsworth, T. R. and Jury, W. A., 1991) and even less theoretical study. Indeed, Ward et al. (1995) comment that this is largely due to the lack of experimental data. Hence, the second main hypothesis under investigation in the chapter is that a conservative solute applied at a point on the surface of a homogeneous sample will move symmetrically, about the point of application, through a homogeneous sample.

In addition to the areas of study central to the work in this chapter further measurements were taken to provide input data for the subsequent modelling (Chapter 6). Temporally detailed breakthrough curves were collected for the simpler transport scenario of a uniformly applied conservative solute tracer. This data was required for later model calibration and testing, and for establishing the general transport properties of the samples.

A summary of the aims and methods contained in this chapter is given in Table 4.1.

| | Area of Study | | | |
| | Homogeneous and Random Flow Distribution | | Symmetrical Solute Transport Distribution | |
Mode of Study	Qualitative	Quantitative	Qualitative	Quantitative
Samples				
Redhill 30, 120-mm Depth	Contour Plots (Section 4.3.2.1)	Number of Funnels Conducting No Flow/Majority of Flow (Section 4.3.2.2) χ^2-test of Distribution of Flow Velocities (Section 4.3.2.3) Mann-Whitney Test of Flow Velocities (Section 4.3.2.4) Pearson Product Moment Correlation Coefficient (Section 4.3.2.5) Variograms (Section 4.3.2.6)		
Redhill 30, Redhill 65 and Stratified Samples, All Depths	Contour Plots (Section 4.3.2.1)	Number of Funnels Conducting No Flow/Majority of Flow (Section 4.3.2.2) χ^2-test of Distribution of Flow Velocities (Section 4.3.2.3)	Visual Inspection of Breakthrough Curves (Section 4.3.4.1)	Pearson Product Moment Correlation Coefficient (Section 4.3.4.2)

Table 4.1 Summary of aims and methods for Chapter 4.

4.2 Methods

4.2.1 Samples and Preparation

Unconsolidated sand was chosen as the sample material with the intention of striking a balance between the disordered, highly heterogeneous nature of a more 'natural' medium

such as soil and the extremely artificial homogeneity of a material such as manufactured glass beads. Even in a material such as the glass beads used in Chapter 8, where the size of the solid phase is almost completely uniform, heterogeneities can easily be introduced to the void phase by the packing process.

Two sands were used throughout this investigation, coarse grained Redhill 30 and finer Redhill 65 (Hepworth Minerals and Chemicals, Sandbach, Cheshire, U.K.), both singly and layered (two layers of equal depth, Redhill 65 on top). A summary of their properties is given below in Table 4.2 and further sample details are given in Appendix A. Permeabilities were measured by constant head permeametry, and porosities were obtained by mercury porosimetry. Permeabilities and porosities for the single sands are averages of 10 measurements.

Sand	Porosity, %	Permeability, Darcies
Redhill 30	40.68	8.45
Redhill 65	44.46	2.84
Stratified	-	2.20

Table 4.2 Summary of sand porosity and permeability.

From Table 4.2 it can be seen that the effect of combining two sands of different permeabilities was to create a composite material with significantly lower permeability than either of its constituents. Although this effect could not be investigated in detail, it was presumed that this occurred due to increased efficiency in the packing of the two grain size distributions at the interface, creating a much less permeable region.

In initial tests it was observed that if the sand was simply poured into the sample container heterogeneities, visible as stripes in the sample, could be created. Consequently great care was taken in loading the sample into the container. The sand was taken from bags in a way that avoided sorting effects incurred during travel, loaded into the container via a spinner wheel, and finally agitated again to repack. This minimised any sorting.

The application of simulated rainfall to a completely dry sample resulted in the bulk of the material remaining dry, due to the hydrophobicity of the sand. To avoid this samples

were pre-saturated from the bottom up. The grid lysimeter funnels were stopped with silicone bungs bar one, which was connected to a peristaltic pump. Water was then pumped extremely slowly into the sample until ponding was seen at the surface. This typically took at least 30 hours. Time domain reflectometry (TDR) readings were taken and compared with measured porosities as a check on the level of saturation achieved.

Towards the end of the saturation the rainfall simulator was started, initially with a tray between it and the sample to prevent water being applied to the sample. The simulator was then run for several hours to establish that it was functioning correctly. Following this the tray was removed, allowing water to fall briefly on the ponded sample surface. Next the bungs were removed from the grid lysimeter allowing the sample to drain freely. For ease of removal they were strung together on lengths of thread allowing them to be removed more or less simultaneously.

Once the sample had been saturated and drained water content and rate of drainage were monitored regularly. Experiments lasted in excess of two weeks, and care was taken throughout to ensure that conditions remained stable. Experiments were abandoned if the system became less stable, for example if several needles in the rainfall simulator become irretrievably blocked. Ideally climatic conditions would also have been under the control of the operator, but unfortunately in this study that degree of sophistication was not possible.

4.2.2 Flow Distribution

The spatial distribution of flow fluxes was monitored, via the outputs of the grid lysimeter, in all of the samples tested. Ideally, both the fluxes and velocities of the flow emerging from the sample would be measured. However, this would require separation of the individual flow paths, and hence a collection grid with a resolution of similar size to the particles grains, say at intervals of 500-µm. In practice, the use of a larger scale collector array causes an integration of the fluxes and velocities, typically at intervals of a few centimetres or more, and only an integrated flux is measurable. Fluxes at length scales up to an order of magnitude smaller than the grid can be inferred by careful interpolation of the fluxes from the grid. With a sample containing grains of median size 500-µm, and a

collection grid of say 5-cm or 50000-μm, interpolation will give resolution around one order of magnitude larger than ideally required, which is sufficiently precise to provide a very useful level of information. In this work *Darcy velocity* was employed as the measure of flow through the funnels, and is given by (Kirkham, D. and Powers, W. L., 1995),

$$v_d = Q/A \qquad\qquad [1]$$

where Q is the volumetric flow rate and A the sample cross-sectional area. For the modelling of solute transport in the next chapter Darcy velocity was converted to *pore water velocity* by dividing by the average water content of the samples.

For the study of flow velocities a 120-mm deep sample of Redhill 30 sand was loaded and saturated as described previously. The subsequent investigation took place over three phases, each interspersed by a week of drying. In phases 1 and 2, the sample was pre-saturated as described previously, and then the flow through the 100 funnels was measured approximately hourly for around 8 hours a day for a week. The third phase was carried out similarly, but without pre-saturation.

The possibility of further investigating the void structure of a sample via some form of visual inspection, either through resin impregnation and image analysis or by staining, excavation and image analysis, was also considered. It was initially thought that it might be possible to see whether any variations in flow that might be observed had arisen as a result of structural differences in the packing. Unfortunately this could not be carried out for practical reasons. Any variation in the flow properties of the sand would be likely to have arisen from subtle changes in the packing. For such an unconsolidated sample it would be impossible to ensure that either impregnation or excavation did not alter the structure.

4.2.3 Bulk Solute Transport

Using the automated sampling system described in the previous chapter it was possible to obtain temporally detailed information about transport of uniformly applied conservative solute tracers. This information, as well as providing supplemental information about the transport properties of the materials being investigated, was necessary for the modelling carried out in Chapter 5.

A bromide solute tracer was chosen for its conservative nature. Preliminary work showed that a potassium bromide solution made up to a concentration of 1 g l^{-1} bromide produced exit concentrations suited to the range of the detection method (Section 4.2.5). The tracer was applied to the sample using the rainfall simulator to ensure uniformity of application. The rainfall was briefly stopped by placing a large tray on top of the sample container over the sample. Then the rainfall simulator was rapidly drained and refilled with the potassium bromide solution. Having restarted the rainfall simulator the tracer solution was then applied for a period of one minute, then replaced once more with pure water.

During bromide application it was important that any disturbance to the flow regime was kept to a minimum. This was complicated by the requirement that the individual needles needed to be 'primed', pumping water through to remove trapped air, before re-starting the rainfall simulator. The period during which water/solution application ceased was further extended due to efforts to limit cross-contamination. It was necessary, once the rainfall simulator had drained, to thoroughly rinse it before reintroducing solute/water. Nonetheless it was possible to keep this 'dead' period to within 10-15 minutes.

After bromide application sampling of the output was initiated, using the automated collection system. Samples were analysed by flow injection analysis (Section 4.2.5). Outflow was sampled every 15 minutes, producing detailed breakthrough curves (BTC's).

4.2.4 Solute Transport Distribution

An experiment to observe lateral transport was also developed, with modifications to the solution application and sampling procedures. A procedure was designed for applying the solution to a small area in the centre of the sample surface then monitoring the lateral transport of bromide via the grid lysimeter.

Solute application was localised by means of a specially constructed plastic 'mask', placed between sample and rainfall simulator. This prevented application to all but a square area of the sample surface corresponding to the area of the four central funnels of the grid lysimeter.

49

It would have been desirable to monitor bromide concentrations exiting the sample at all 100 lysimeter funnels. Due to the slow speed of bromide determination, approximately two minutes per sample, the number of samples that would have been produced (3000-5000 per experiment) could not have been assayed with the time/resources available. An alternative approach was developed to obtain as much information as possible using the experimental conditions described. Locations chosen to yield as much information regarding the hypothesis stated in Section 4.1 were monitored. An example of a typical sampling configuration is shown in Figure 4.1.

Figure 4.1 Sampling configuration for lateral solute transport experiment.

Due to the requirement to limit the number of samples, sampling was less frequent than for the study of bulk transport. It was nonetheless possible to collect enough data to produce good breakthrough curves and enable comparison with that resulting from the bulk transport experiments. The specific sampling patterns varied from Figure 4.1 for individual samples, the choice of funnels sampled from depending on which funnels were flowing.

4.2.5 Bromide Determination

Bromide concentrations were determined by flow injection analysis (FIA). Other methods were considered, including titration, inductively coupled plasma atomic adsorption spectroscopy and electrical conductivity. FIA was chosen for ease and rapidity (cf. titration) of operation, sensitivity (cf. ICP-AES) and equipment availability. The method was based on that of Freeman et al (1993). Bromide concentrations were

determined using the colourimetric chloramine-T – phenol red method of Goldman and Byles (1959). Bromide reacts with the reagents to form bromophenol blue, which can be measured photometrically at a wavelength of 583-nm.

4.2.5.1 Reagents

All reagents were of analytical grade (AnalaR, BDH, U.K.). Deionized, filtered water (Milli Q) was used throughout. Chloramine-T was prepared by dissolving 200-mg of chloramine-T in 1 litre of water. Phenol red was prepared by dissolving 6.8-g sodium acetate in approximately 500-ml of water, adding 1.5-ml concentrated acetic acid, dissolving 20-mg phenol red indicator and making up to 1 litre with water.

4.2.5.2 Manifold

The manifold used in the determination of bromide is shown in Figure 4.2. PTFE tubing (0.75-mm I.D.) was used throughout and two Ismatec FIXO pumps were employed, a reagent pump operating at 20 rpm and a sample injection pump at 60 rpm. Mixing coils pre-mixed the reagent streams prior to injection of the sample and subsequently mixed the sample with the reagents. Detection was carried out using an LKB spectrophotometer fitted with a flow cell. A manually operated Rheodyne Type 50 4-way/sample injection valve was used for sample injection.
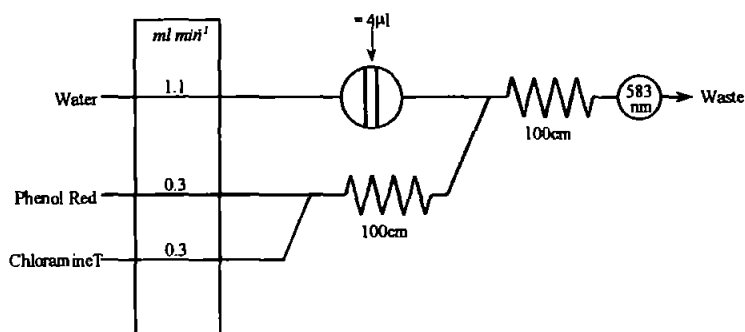
Figure 4.2 Flow injection analysis manifold used for the determination of bromide concentration.

4.2.5.3 Modifications

The method of Freeman et al. (1993) was modified slightly. The original method was highly sensitive, with a detection limit of 4 μg l^{-1} and a narrow linear range of around 0-2 mg l^{-1} bromide. In this study sensitivity was not of paramount importance, however, an extended linear range would appreciably speed up the many sample determinations by

precluding the need for time consuming dilutions. The flow rate of the carrier stream was increased from 0.75 ml minute^{-1} to 1.1 ml minute^{-1} and the lengths of the mixing coils from 600-mm and 430-mm to 1000-mm. Following these changes the acetic acid concentration was re-optimised to 1.5 ml l^{-1}. Sample volume was also decreased, in response to over-sensitivity, using the dead volume of the sample valve, approximately 4 μl. Although less sensitive, the linear range was extended to 0-12 mg l^{-1}.

4.2.5.4 Sample FIA Calibration

Details of an example calibration, carried out on the manifold described in this section, are given in Table 4.3 and Figure 4.3.

[Br$^-$], mg l^{-1}	Absorbence					Average
0.00	0.000	0.001	0.001	0.000	0.001	0.001
2.00	0.062	0.063	0.064	0.062	0.061	0.062
4.00	0.118	0.118	0.117	0.117	0.117	0.117
6.00	0.178	0.177	0.174	0.173	0.174	0.175
8.00	0.234	0.234	0.233	0.233	0.230	0.232
10.00	0.284	0.281	0.283	0.284	0.280	0.283
12.00	0.325	0.320	0.322	0.321	0.321	0.322

Table 4.3 FIA calibration data.
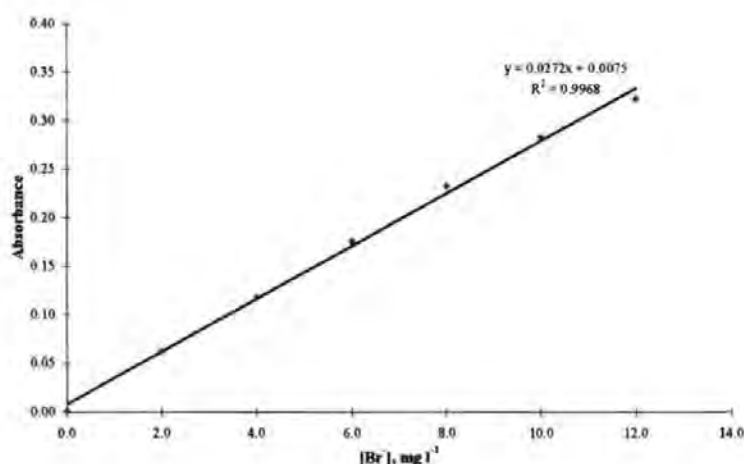
Figure 4.3 FIA calibration curve.

4.2.5.5 Discussion

Although FIA proved a useful method for tracer determination it did suffer some drawbacks from the point of view of this study, chiefly speed of determination (approximately two minutes per sample) and lack of automation. Speed was limited by reaction kinetics, which prevented further rate-enhancing improvements.

4.3 Results and Discussion

4.3.1 Samples and Preparation

Saturation was carefully monitored with the TDR probes. It can be seen on the left-hand axis of Figure 4.4 that the saturation values dropped sharply over the first few minutes of the experiment, and then stabilised. The probe measuring the average saturation of the whole of the sample at the middle depth of 60-mm then remained stable within the saturation range 33.14% to 34.23% over all three phases of the experiment (□), with a mean value of 33.70%. As might be expected, the surface probes (X , o) were much more sensitive to drying, and the middle edge probe (◊) somewhat sensitive to drying. The mean level of saturation of the bulk of the sample (33.70%) is 6.6 standard deviations below the mean porosity of the sand as measured by mercury porosimetry (40.68%). This discrepancy cannot be explained by sorting or packing effects, and must be due to unsaturation. The mean relative saturation of the sample, based on the mean values of porosity and saturation, was 82.8% throughout all three phases of the experiment.
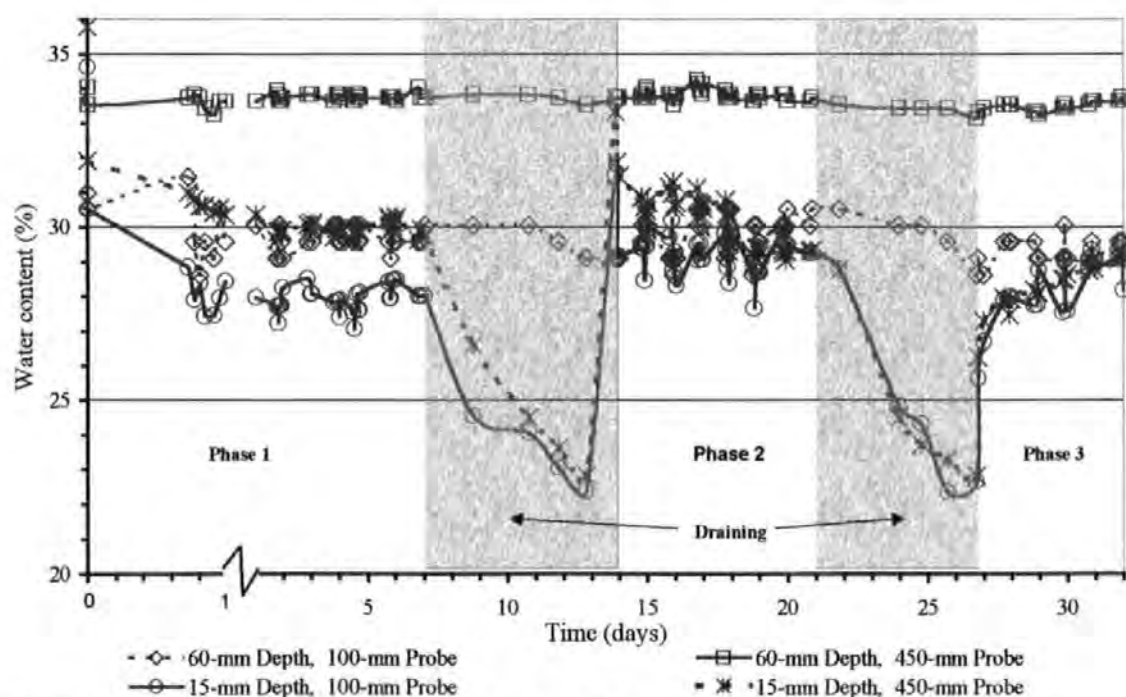
Figure 4.4 Saturation over the three phases of the flow velocity study.

It was observed that the probes installed at the surfaces of some samples gave much lower readings than those installed at greater depths, suggesting regions of decreased saturation. Subsequent gravimetric testing, however, revealed the water content to be similar to that measured at other depths. During later experiments it was deduced that this

effect was due to the TDR probes being located too close to the sample surface. As the surface of the samples became progressively more pitted with continuing water application the probes were effectively measuring the water content of not just the sand, but also the air-filled 'craters' on the surface. Hence, in Figure 4.4 the readings of the upper probes, 15-mm below the surface, are corrected by 0.3% per day during rainfall to compensate for cumulative pitting of the surface. Probe placement was carried out with reference to other work which has suggested that probes may be placed as close to the surface as 10-mm (Petersen, L. W. et al., 1995; Baker, J. M. and Lascano, R. J., 1989).

4.3.2 Flow Distribution
4.3.2.1 Contour Plots

A convenient method for examining the distribution of flow across samples was required. In lysimeter studies of structured soils Quisenberry et al. (1995; 1994) used three-dimensional histogram-type plots to show spatial variations in flow and exit concentrations of a uniformly applied tracer. Here two-dimensional surface plots are used to display flux-derived velocities, measured exiting the bottom of the samples. The 120-mm deep sample of Redhill 30 used to investigate velocity distributions will be considered first. For each of the three phases described in Section 4.2.2 the flow through each of the 100 funnels of the grid lysimeter was measured regularly. Figure 4.5 shows surface plots of the Darcy velocities (mm minute^{-1}) exiting through each of the funnels over the first day of the first phase.

In plotting the surface plots results from each collection point were interpolated using a Simpson quadratic interpolation. For an equally spaced grid,

$$v(x_i,y_j) = C_{n-3} \cdot v(x_{i-3},y_{j-3}) + C_{n-1} \cdot v(x_{i-1},y_{j-1}) \\ + C_{n+1} \cdot v(x_{i+1},y_{j+1}) + C_{n+3} \cdot v(x_{i+3},y_{j+3})$$ [2]

where v is the interpolated parameter at position x_i, y_j, and readings are taken at positions (x_{i-1},y_{j-1}), (x_{i-3},y_{j-3}) .... on the grid. C_n are the Simpson quadratic coefficients, in this case 0.625 and -0.125 for $n = \pm 1$ and ± 3 respectively. A second order interpolation was also carried out, based on observed and interpolated points, giving a final parameter spacing of

one quarter of the original observation grid. A surface fitting algorithm, part of the Visual Groundwater (Waterloo Hydrologic, Canada) modelling package, was then used further to increase the visual resolution, down to about 0.1 of the original observation grid spacing, i.e. ~ 4mm. It will be seen that this is one order of magnitude greater than the median sample grain size.

It can be seen that the flow patterns are almost identical from one measurement to the next, apart from a slight increase in the areas conducting minimal flow as the sample drains from saturation. This consistency was present throughout each of the three phases of this study. Figure 4.6 shows surface plots of the average Darcy velocities for each day of the second of the three phases.

After the first two days the pattern of flow through the sample remained almost constant, with only a slight increase in areas of low flow. This consistency was mirrored in the first and final phases.

Figure 4.7 shows the average surface plot of the last four days (ignoring the initial period as the sample drained down) of each of the three phases described in Section 4.2.2.

1042 minutes   1103 minutes

1162 minutes   1213 minutes

1305 minutes   1365 minutes

1425 minutes   1485 minutes
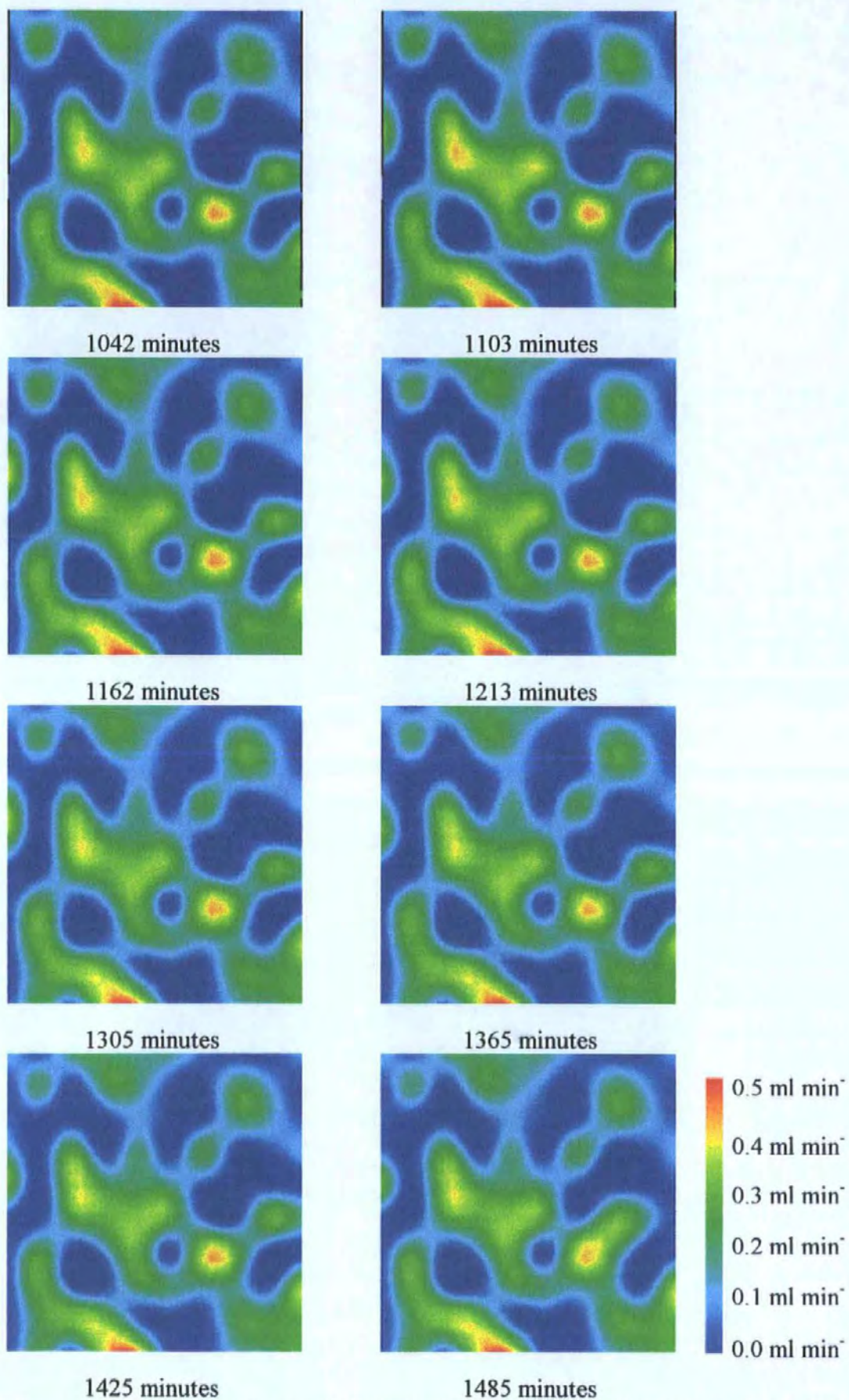
Figure 4.5 Surface plots of Darcy velocity (mm minute^{-1}) through Redhill 30 sand measured at approximately hourly intervals over eight hours on the first day of the first phase.

Day 1

Day 2

Day 3

Day 4

Day 5

Day 6

Day 7
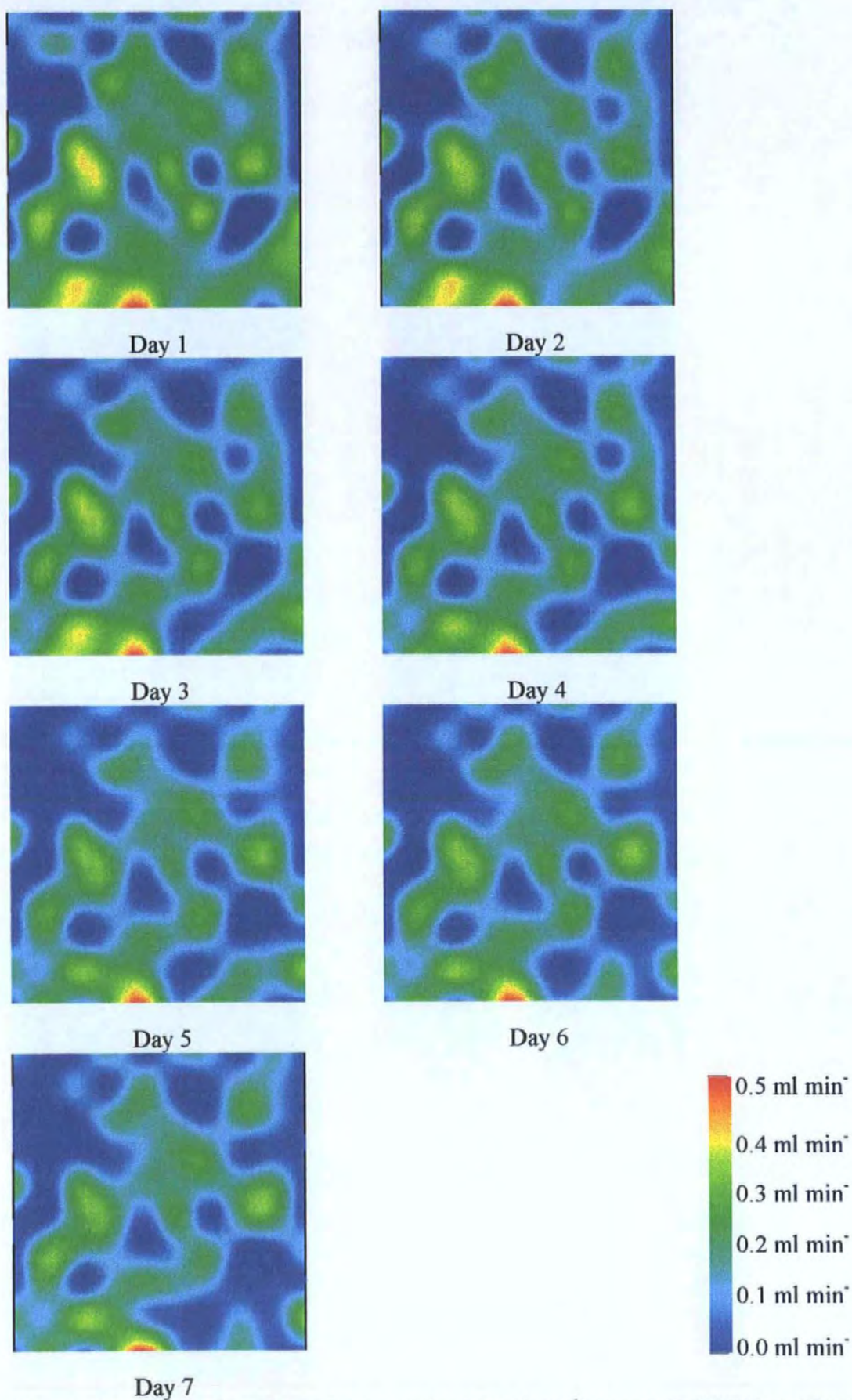
Figure 4.6 Average surface plots of Darcy velocity (mm minute^{-1}) through Redhill 30 sand for each day of the second phase.

a)

b)

0.5 ml min⁻

0.4 ml min⁻

0.3 ml min⁻

0.2 ml min⁻

0.1 ml min⁻

0.0 ml min⁻

c)
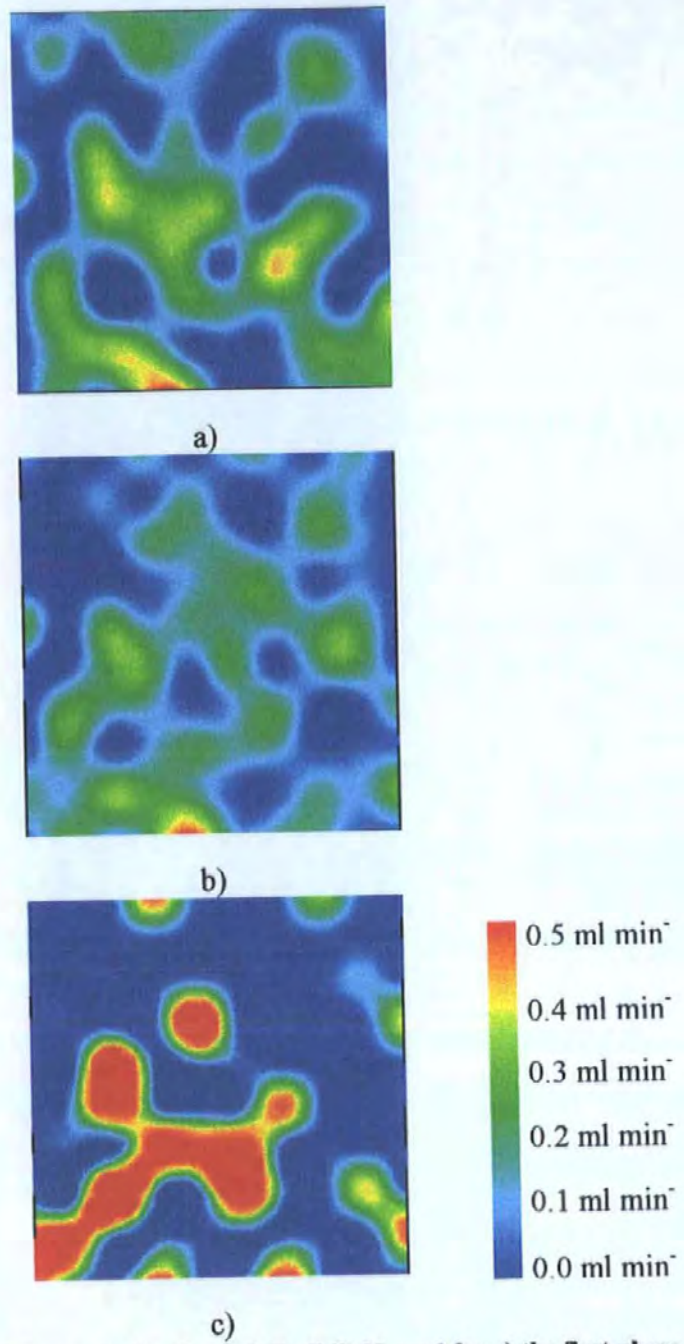
Figure 4.7 Surface plots of average Darcy velocity through Redhill 30 sand for a) the first phase, b) the second phase and c) the third phase.

There is little visual similarity in patterns of flow between the three phases. The level of variation for phases 1 and 2 appear similar, but that of phase 3 is very different. Indeed in phase 3 only 18 of the 100 funnels conducted any flow at all over the four day period. Figure 4.8 shows average surface plots for each of the six samples prepared for the solute transport experiments described in Sections 4.2.3 and 4.2.4.
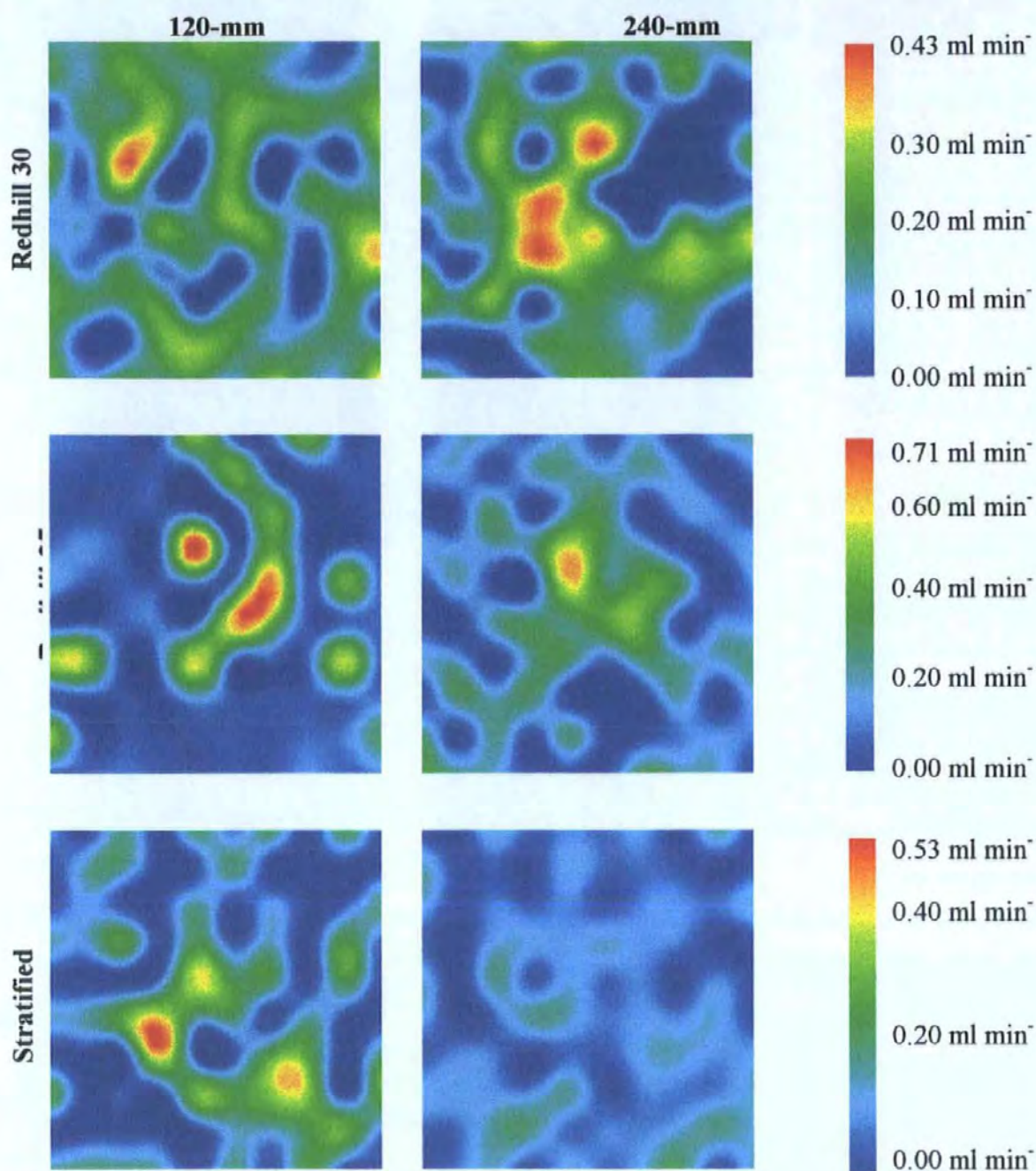
Figure 4.8 Average surface plots of Darcy velocity (mm minute⁻¹).

Visual inspection of the single layer samples reveals that the shallow Redhill 65 sample displayed by far the most extreme differences between fast and slow flowing regions. There is no visual evidence of bypass flow in the shallowest stratified sample, while the 240-mm sample displays comparatively low flow. These visual judgements are tested in the following sections.

4.3.2.2 Number of Funnels Conducting No Flow/Majority of Flow

The cumulative numbers of funnels contributing to the total flow for each of the samples are summarised in Figure 4.9. The curves were obtained by ordering the average flows through the 100 funnels from largest to smallest. The curves plot the cumulative proportion of total flow against the cumulative number of contributing funnels. For the sake of clarity the points where the curves contact the line corresponding to 100% cumulative flow are indicated with vertical dashed lines.
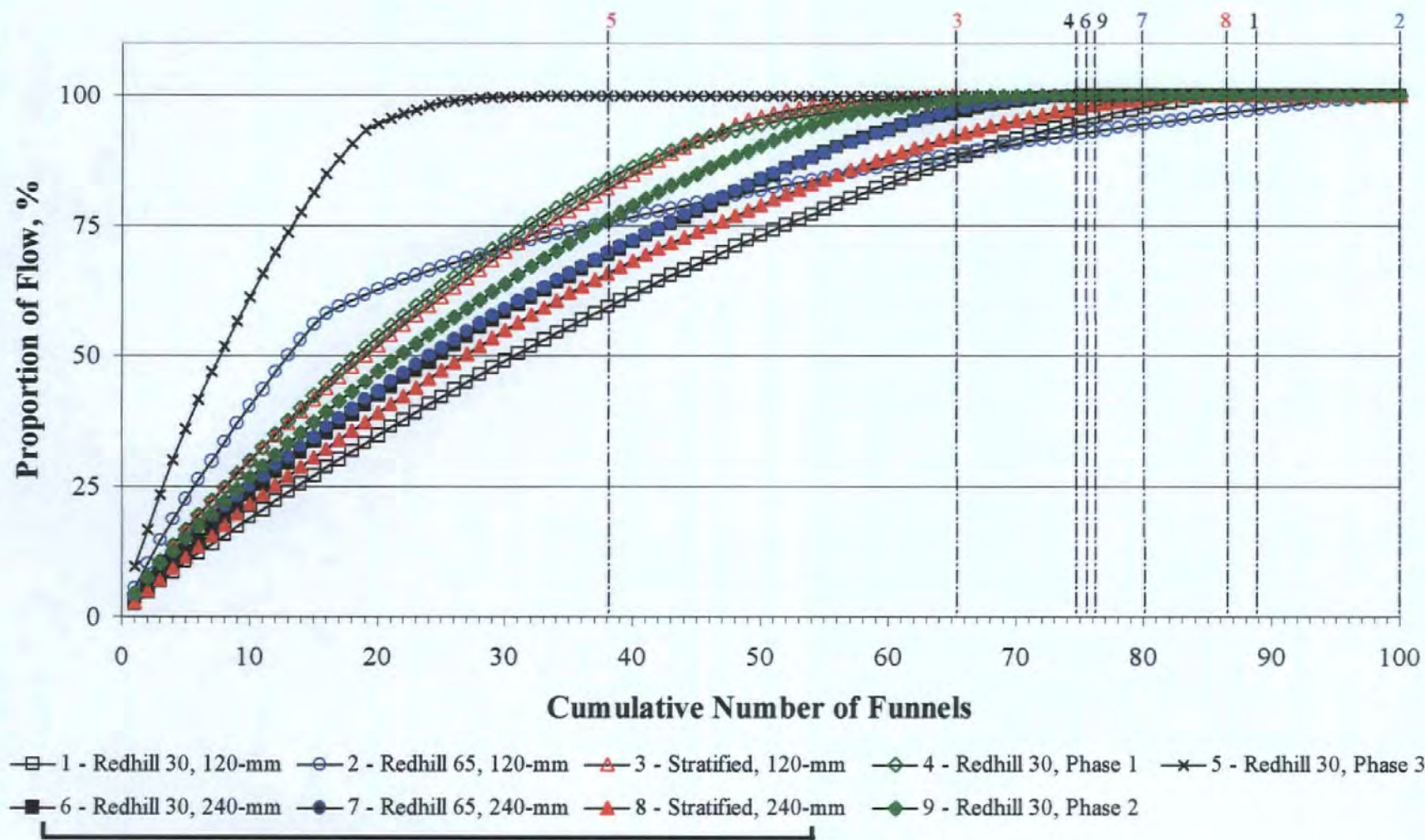
Figure 4.9 Cumulative numbers of funnels contributing to total output for all samples.

Legend:
—□— 1 - Redhill 30, 120-mm   —○— 2 - Redhill 65, 120-mm   —△— 3 - Stratified, 120-mm   —◇— 4 - Redhill 30, Phase 1   —✕— 5 - Redhill 30, Phase 3

—■— 6 - Redhill 30, 240-mm   —●— 7 - Redhill 65, 240-mm   —▲— 8 - Stratified, 240-mm   —◆— 9 - Redhill 30, Phase 2

Transport Samples

On initial inspection of Figure 4.9 it can be seen that most of the curves are similar. The proportion of flow increases gradually with number of funnels, to an asymptotal region as it nears 100%. The curves possess plateaus of varying lengths at 100% of total flow, depending on the number of funnels conducting zero flow.

The curve of the 120-mm Redhill 65 sample appears to be anomalous, especially when its surface plot (Figure 4.8) is also taken into consideration. The curve clearly illustrates that a relatively small volume of the sample conducted an unusually high (compared with the other samples) proportion of the total flow. Even more extreme is the curve corresponding to the final phase (phase 3) of the flow study. Clearly flow through both of these samples is preferential compared to the flow through all other samples.

Considering the Redhill 30 samples, bar the 120-mm transport sample, and the stratified samples it can be seen that increasing sample depth had the effect of making the initial gradients less steep. That is, increasing depth appeared to bring about a decrease in the number of funnels conducting larger volumes of water. Effectively this suggests that increasing sample depth caused flow to become more uniformly distributed across the fractions of the samples conducting flow. However, the fact that this was not the case for the Redhill 30 transport sample, and that one of the Redhill 65 samples appears anomalous, makes it impossible to be certain that this was a genuine trend.

The number of funnels conducting zero flow through each sample was highly variable, occurring as it did in the asymptotal regions of the curves. No trend was visible in the number of funnels conducting no flow, either between samples of the same materials at different depths or between same depth samples with different permeabilities and porosities. Contrary to the findings of Dexter (1995), increasing sample depth did not appear to increase the non-flowing fraction of the samples. Interestingly, although the 120-mm Redhill 65 sample displayed the greatest degree of bypass flow it had, on average, no non-flowing funnels. Although a great majority of the flow was transported through a small minority of the available volume, the rest of the sample also conducted flow, albeit in much smaller quantities.

4.3.2.3 χ^2-tests of Distribution of Flow Velocities

Using the χ^2-test average velocity distributions were compared against each other (for the three phases of the flow investigation) and against normal distributions with the same means and standard deviations. The results of the tests of phases 1 to 3 of the flow study are given below. Each distribution of 100 average velocities was initially divided up into 10 equally spaced categories. Categories containing less than 6 velocities were combined with adjacent categories.

Phases	χ^2 Statistic	Degrees of Freedom	Confidence Level, %
1 versus 2	48.47	5	<0.01
1 versus 3	103.79	3	<<0.01
2 versus 3	62.65	2	<<0.01

Table 4.4 Summary of χ^2-test of phases 1-3.

From Table 4.4 it can be seen that none of velocity distributions from any of the phases are at all similar. The comparisons of the experimental velocities with Normal distributions are summarised below.

Sand	Depth, mm	χ^2 Statistic	Degrees of Freedom	Confidence Level, %
Redhill 30	120	10.19	6	15.0
		31.22[1]	6	< 0.1
		16.82[2]	6	1
	240	23.53	5	< 0.1
Redhill 65	120	248.54	3	<< 0.1
	240	19.13	5	0.1-0.5
Stratified	120	22.24	6	0.1
	240	16.75	6	1.0

Table 4.5 Summary of χ^2-tests of velocity distributions for all transport experiment samples and [1] phase 1 and [2] phase 2 of the investigation of flow patterns.

From these results it can be seen that none of the measured distributions of Darcy velocity were Normally distributed. Figure 4.10 shows the frequency distributions compared for the first 120-mm Redhill 30 sample, the distribution most similar to a Normal distribution as tested here, prior to combining of categories containing less than 6 observations.

was employed. The Mann-Whitney test involved ranking all of the average velocities from two phases. The aim was to see whether results from the two phases occurred more or less randomly throughout the ranking, or if results from one phase tended to be bunched at one end. As such it tested the null hypothesis that velocity values from one phase came from the same population as those from another. The results are summarised below.

Phases	P, %	Result
1 versus 2	~30	Strongly accept H_0
1 versus 3	~0.02	Strongly reject H_0
2 versus 3	<0.02	Strongly reject H_0

Table 4.6 Summary of Mann-Whitney test of phases 1-3.

The threshold for acceptance of the null hypothesis is a P value of 5% or more. It can be seen that the test gave a clear indication that the velocities of water flowing through the funnels of the grid lysimeter in the first two phases came from the same population, but that the velocities from any other combination of the three phases did not.

4.3.2.5 Pearson Product Moment Correlation Coefficient

Inspection of Figure 4.5 reveals that the grid location of the maximum flow paths varied from one saturation phase to the next. This observation can be tested statistically by use of the Pearson product moment correlation coefficient. This is equivalent to plotting two sets of values against each other on a graph - in this case Darcy velocities measured at the same funnel between two phases. Strongly correlated data sets produce a straight line, upon which linear regression may be conducted to deduce the relationship between the data sets. Pearson coefficients range from -1 (perfectly negatively correlated) through 0 (uncorrelated) to +1 (perfectly positively correlated). The coefficients for the three combinations of phases are shown in Table 4.7. Thus phase 1 and 2 are weakly correlated, whereas no other correlations were discernible.

	Pearson Product Moment Correlation Coefficient		
Phases	1 vs 2	1 vs 3	2 vs 3
	0.480	0.063	0.092

Table 4.7 Pearson product moment correlation coefficients for phases 1 to 3.

there are fewer observations, this conclusion must be made with caution. The over-riding conclusion is that there is a gross difference between phase 3 and all the other experiments.

4.3.2.7 Summary of Flow Distribution Results

Distributions of flow velocities in homogeneous sand samples were found to be non-repeatable - i.e. regions of high or low flow did not tend to occur repeatedly in the same place, confirming the homogeneity of the sample in the terms defined above. The exception to this was the shallowest Redhill 65 sample, discussed below. None of the flow distributions was Normal. When the saturation protocol for the sample was the same, as in phases 1 and 2, the flow distributions were differing members of the same statistical family of distributions, as judged by the Mann-Whitney test. These distributions were non-Normal, with an anomalous high peak at low or zero flow. Re-allocation or removal of this peak left a distribution, which remained non-Normal. If preferential flow had occurred, an expected distribution might have been a Normal distribution of matric flow with an anomalously high fastest-flow peak. Extreme preferential flow may dominate matric flow to such an extent that an anomalously high low- or zero-flow peak appears. The observed distributions were thus a converse of the non-extreme preferential flow type - i.e. a mid-range flow distribution coupled with an anomalously high low- or zero-velocity peak.

The phase 1 and phase 2 flow distributions are difficult to categorise in terms of the flow models discussed in the Introduction. The distributions are non-Normal and therefore do not arise simply because of a random distribution of flow paths amongst a random arrangement of randomly sized grains. Preferential flow, as defined earlier, does not occur. There is also no evidence for any sort of rivulet flow, since this would give an anomalously large peak at higher flow rates. An explanation is that there is an array of non-conducting pathways that do not attract flow, and give the anomalous low-flow peak. These non-conducting pathways could arise from dry, hydrophobic regions of the porous matrix, or from regions in which the water has become trapped due to capillary or geometric effects. If the sample is allowed partially to drain by gravity, and then is once again very slowly re-saturated to completion, all non-conducting pathways are wetted, as evidenced by the TDR probes. When rainfall begins again, a new set of non-conducting pathways appear, but the

probes. When rainfall begins again a new set of non-conducting pathways appear, but the distribution, by Mann-Whitney, remains the same as previously. If the sample is not re-saturated, as between phase 2 and phase 3, a completely different type of non-conducting pathway distribution results. Some non-conducting pathways stay non-conducting (Figure 4.7), but others can develop into fast flow channels. The tendency for areas of the porous matrix to act in a hydrophobic manner has not been suppressed by slow total saturation, and is evident to such an extent that the flow is preferential compared to all the other flow distributions (Figure 4.9).

As mentioned previously, the results of the shallowest Redhill 65 sample appeared to be anomalous, and an outlier when compared with the results of all other samples considered. Whether this anomaly was a result of structural heterogeneity within the sample could not be investigated due to the sensitivity of these unconsolidated samples to perturbation.

The results of the investigation into flow distribution, as related to Table 4.1, are summarised in the following table.

| Mode of Study | Homogeneous and Random Flow Distribution | |
	Qualitative	Quantitative
Samples Redhill 30, 120-mm Depth	Visual inspection revealed no preferential flow in samples that were saturated prior to studying flow. When saturation was not carried out preferential flow was observed (Section 4.3.2.1).	Inspection of the cumulative number of funnels conducting flow revealed no correlation between runs conducted on the same sample (Section 4.3.2.2). The χ^2 test of average velocity distributions did not reveal any of them to be similar or to be normally distributed (Section 4.3.2.3) The velocities through samples prepared in the same way were drawn from the same distributions. If sample preparation changed this was not the case (Section 4.3.2.4). By the Pearson correlation coefficient there was no correlation in the spatial distribution of flow between runs conducted on the same sample (Section 4.3.2.5). Variograms did not indicate that there was any correlation in the spatial distribution of flow within samples (Section 4.3.2.6).
Redhill 30, Redhill 65 and Stratified Samples, All Depths	Visual inspection did not reveal preferential flow in any of the samples, bar one that was anomalous. Visually the development of flow did not appear to be dependent on sample type/depth (Section 4.3.2.1).	Inspection of the cumulative number of funnels conducting flow revealed no correlation between flow and sample depth, porosity or permeability (Section 4.3.2.2). The χ^2 test of average velocity distributions did not reveal any of them to be Normally distributed (Section 4.3.2.3)

Table 4.8 Summary of flow distribution results.

4.3.3 Bulk Solute Transport

For each of the sand samples studied bulk solute transport experiments were carried out as detailed in Section 4.2.3. Breakthrough curves are shown below (Figure 4.12).

Time = 135 m   Time = 390 m
[Br⁻] = 9.31 mg l⁻¹
[Br⁻] = 8.53 mg l⁻¹

a)

Time = 210 m   Time = 510 m
[Br⁻] = 8.72 mg l⁻¹
[Br⁻] = 7.62 mg l⁻¹
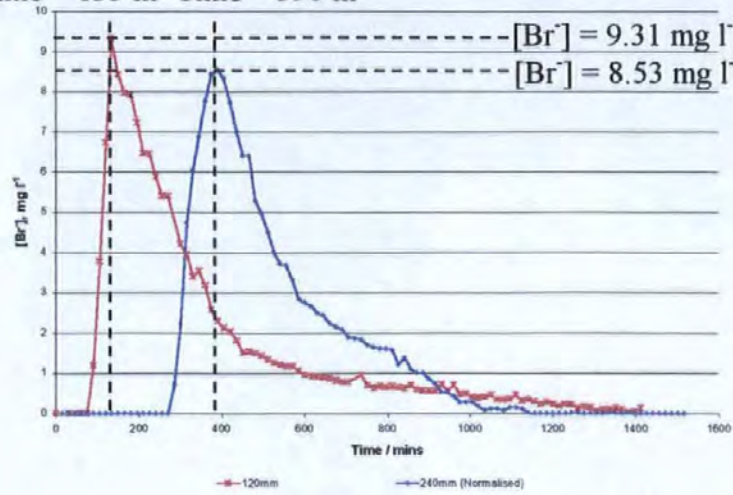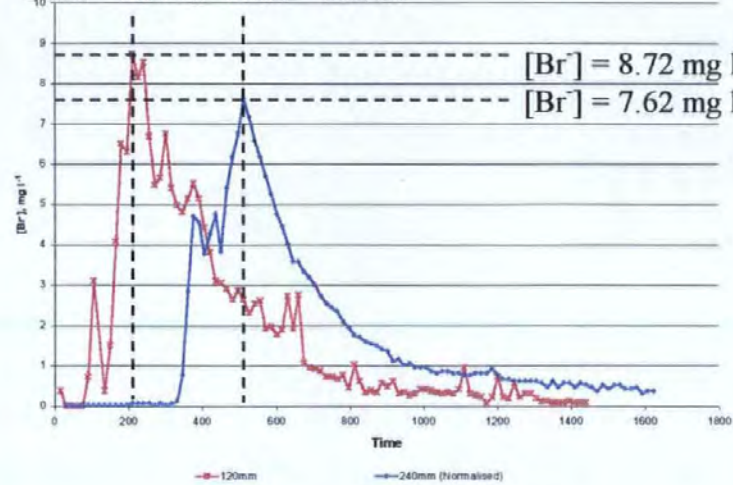
b)

Time = 255 m   Time = 465 m
[Br⁻] = 13.05 mg l⁻
[Br⁻] = 8.73 mg l⁻¹
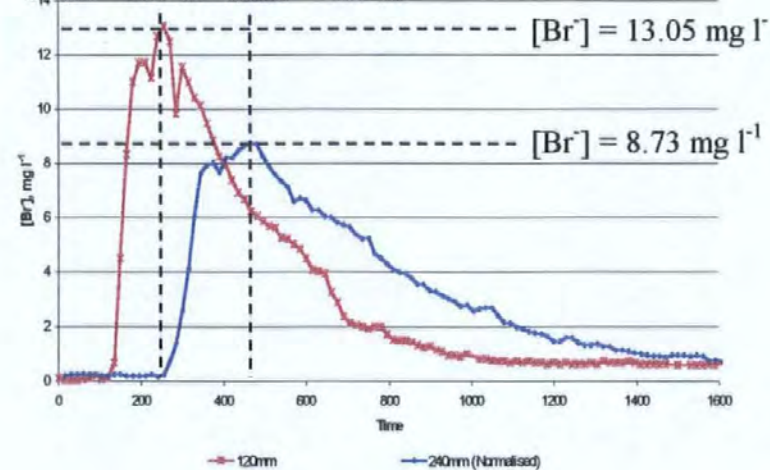
c)

Figure 4.12 Breakthrough curves for a) Redhill 30, b) Redhill 65 and c) stratified sand samples.

As is customary the areas under the breakthrough curves of the 240-mm deep samples were normalised to those of the 120-mm samples. This was necessary to compensate for solute losses through the edge channels, which were not studied. Table 4.9 gives details of the times corresponding to approximate areas under breakthrough curves.

| Sand | Depth | Time Corresponding to Area, minutes | |
		50 %	75 %
Redhill 30	120	255	435
	240	457	600
Redhill 65	120	338	510
	240	585	795
Stratified	120	375	577
	240	630	885

Table 4.9 Times corresponding to 50% and 75% (approximately) of the area under breakthrough curves for each sample tested.

It can be seen from Figure 4.12 a) and b) and Table 4.9 that transport of bromide through homogeneous sand samples was strongly dependent on sample permeability. The breakthrough curves through the finer, less permeable Redhill 65 were slightly retarded compared with those of the Redhill 30 samples. The breakthrough curves for the Redhill 65 were also diminished in terms of maximum peak height compared with those of the higher permeability Redhill 30. Barring the time of arrival of the bromide peak through the 240-mm Redhill 65 sample, transport through the least permeable stratified samples was slowest of all.

Maximum bromide concentrations were greatest for the stratified sand samples, indicating that less bromide was lost to the side channels of the grid lysimeter. Given that the interface between the two sands might be expected to represent a permeability barrier, perhaps encouraging lateral movement, this is somewhat surprising. Evidently in this instance it provided no significant impediment to bromide transport.

The results in this section were obtained primarily to provide data for the modelling carried out in Chapter 5. However, the results presented here indicate that the transport properties of the prepared samples were correlated with other sample properties, chiefly sample depth and permeability. The appearance of the maximum bromide concentration,

50% and 75% of total measured bromide all became more retarded with decreasing sample permeability. Bromide breakthrough curves also became more retarded and dispersed as sample depth is increased.

4.3.4 Solute Transport Distribution
4.3.4.1 Experimental Breakthrough Curves

The breakthrough curves produced during the solute transport experiments described in Section 4.2.4 are shown in Figure 4.13. Figure 4.14 shows the times at which the maximum concentrations occurred. Figure 4.15 shows the times corresponding to approximately 75% of the areas under the breakthrough curves (due to one funnel ceasing to flow midway through the experiment only 9 funnels are shown in the 240-mm sample of Redhill 30 sand).
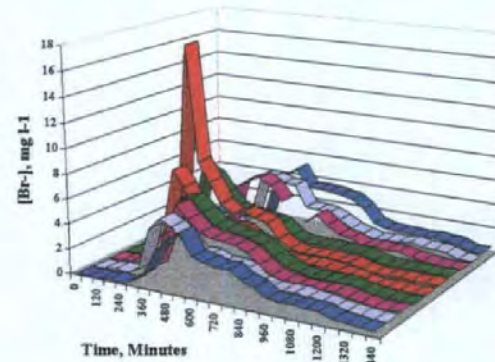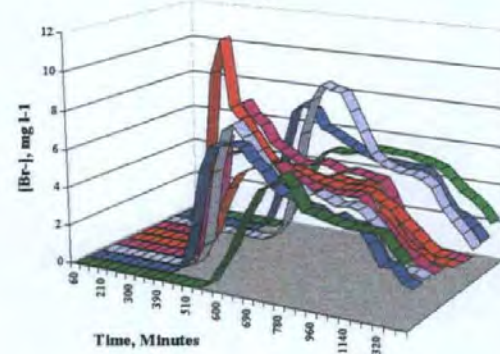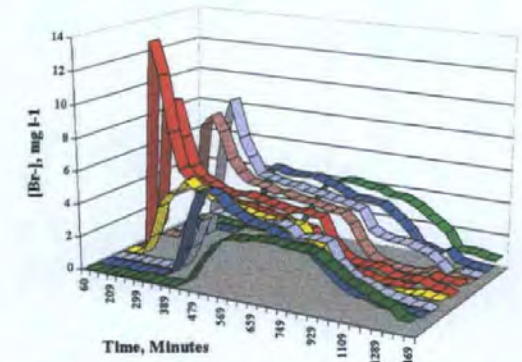
Figure 4.13 Lateral transport breakthrough curves for a-b) Redhill 30, c-d) Redhill 65 and e-f) stratified sand samples, at depths of 120-mm and 240-mm respectively in each case. Breakthrough curves are from funnels 1-10 from left to right, and those measured at funnels equidistant from the point of solute application are shown in the same colour.

From visual inspection of the breakthrough curves it can be seen that, for the most part, there is a correlation between distance from the point of application and breakthrough curve. Generally the breakthrough curves from funnels in or near the centres of samples have peaks of greater height that occur earlier than those measured in funnels further from the point of application.

Referring to the times of appearance of maximum bromide concentration (Figure 4.14) it can be seen that, the bromide moved more rapidly through the more permeable Redhill 30 than either of the less permeable Redhill 65 or stratified sand samples. Further evidence for this is provided by Figure 4.15, the plots of the times corresponding to approximately 75% of the areas under the individual BTC's. Again it can be seen that increasing sample depth tended to make these inter-sand differences more pronounced.

As suggested previously, the variability in times of arrival of maximum bromide concentration and majority of transported bromide was generally less for the more permeable Redhill 30 samples than for the Redhill 65 and stratified samples. This confirms that the range of travel times from a point source to locations at varying distances from that source is strongly influenced by the permeability of the porous media.

Again the maximum concentrations exiting through the stratified samples were generally significantly greater than those exiting the single layers. This suggests that bromide losses through the side channels of the lysimeter were less for the stratified samples than either of the other two sample types. A possible explanation for this is that the presence of the more permeable Redhill 30 underneath the Redhill 65 had the effect of accelerating flow across the sample interface, and this actually diminished lateral movement.
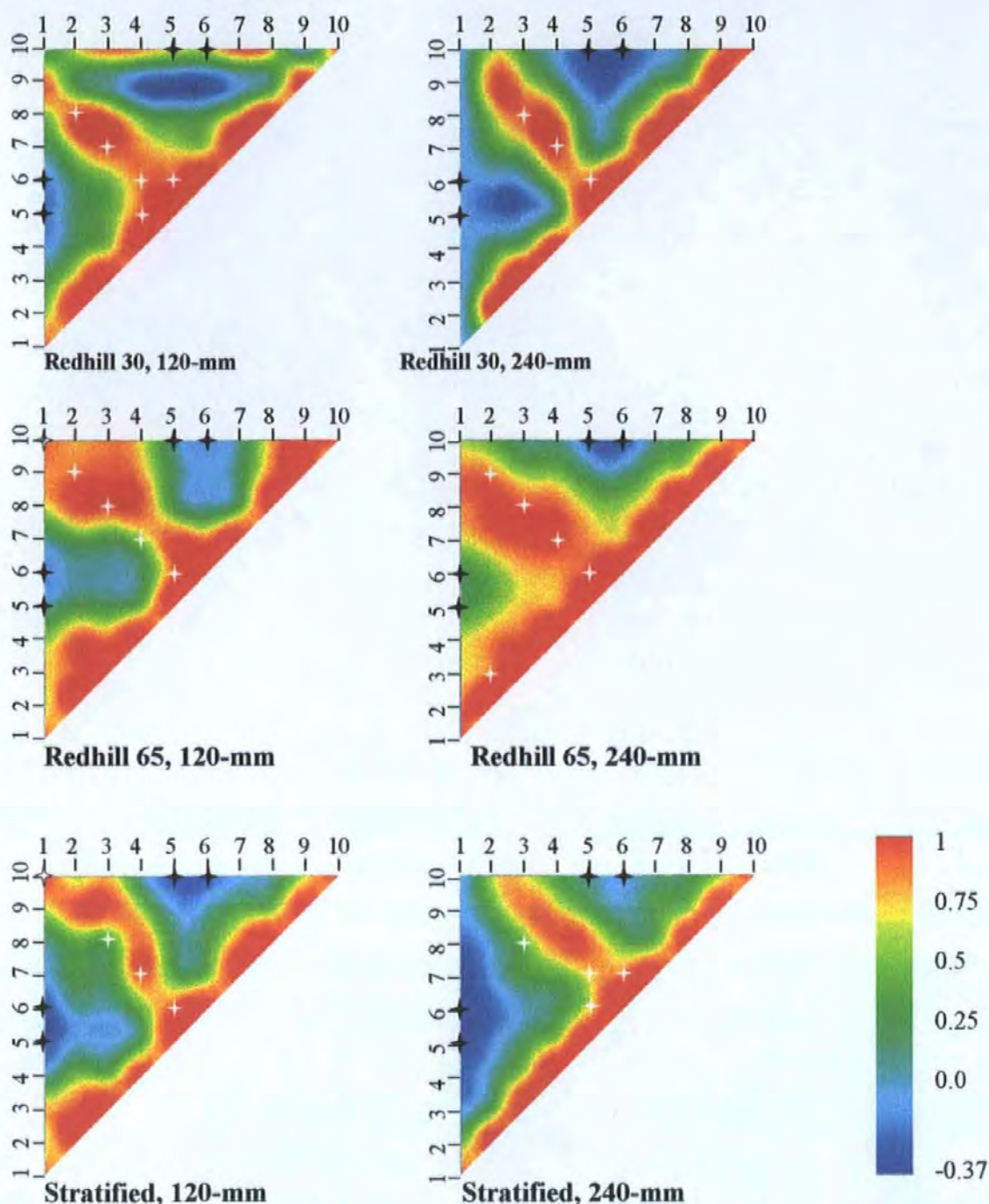
Figure 4.17 Surface plots of Pearson correlation coefficients for all funnels in lateral solute transport experiments.

Visually the surface plots of Pearson coefficients are very similar. The breakthrough curves through most of the funnels equidistant from the point of solute application are highly correlated. It can also be seen that the BTC's through pairs of funnels at greatly different distances from the point of application are not correlated. In between these two extremes the surfaces exhibit clear trends from high to low correlation, with only small fluctuations and there are no marked differences between sample types or depths.

4.3.4.3 Summary of Solute Transport Distribution Results

The apparent similarity between the breakthrough curves measured at different funnels equidistant from the point of application showed that the solute plume moved through the samples in a manner that was reasonably symmetrical about the point of application. The degree of sideways movement of the bromide tracer was significant, even within relatively shallow samples. Indeed comparing the depth of the shallowest samples, 120-mm, with the greatest diagonal distance from point of solute application to sampling location, approximately 350 mm, the extent of lateral solute movement was observed to be almost three times the vertical height of the sample.

The results of the investigation of the distribution of solute transport paths are summarised in the following table.

| Mode of Study | Symmetrical Solute Transport Distribution | |
	Qualitative	Quantitative
Samples Redhill 30, Redhill 65 and Stratified Samples, All Depths	Visual inspection revealed that bromide transport was dependent on sample permeability and distance of sampling location from the point of solute application. Decreases in permeability and increases in depth both retarded solute transport (Section 4.3.4.1).	Breakthrough curves measured at funnels similar distances from the point of solute application were more correlated than funnels at different distances from the point of solute application (Section 4.3.4.2).

Table 4.10 Summary of solute transport distribution results.

4.4 Conclusions

Results have been presented here for the flow of water and the transport of a bromide tracer through homogeneous sand samples of known grain size distribution, porosity and permeability. The flow distributions have been shown to be almost the converse of what might be expected from preferential flow, and have been explained in terms of the existence of non-conducting pathways.

With regard to tracer flow, the flow from a point source displayed a high degree of symmetry about the point of application, and lateral flow was high compared to vertical.

The findings are compatible with the homogeneity of the sample, and the lack of preferential flow that would cause greater non-symmetry. Both the water flow and tracer flow experiments show that these non-conducting pathways are randomly distributed within the porous matrix. This work is continued in the next two chapters.

5 Analysis of Tracer Migration

5.1 Introduction

For the purposes of the study documented here a simple solution of the convection-dispersion equation was chosen to model the experimental data gathered. Convection-dispersion equations are well suited to laboratory studies in that these are assumed not to suffer from the same degree of variation in hydraulic properties observed in field studies. Also, the choice of bromide as the solute tracer makes the work well suited to modelling with a simple analytical solution of the convection-dispersion equation (Equation 1, Chapter 1). The aim of the current work was to examine the accuracy of convection-dispersion equation predictions and investigate how such modelling might be improved by the application of network modelling.

The initial and boundary conditions of the experiment determined the choice of analytical solution. A general initial condition is,

$$c(x,0) = f(x) \qquad [1]$$

where $c(x,0)$ represents the solute concentration at depth x at time $t = 0$. $f(x)$ can be constant with distance, changing exponentially or a steady-state distribution for production or decay. At the sample surface, $x = 0$, there may be a first- or concentration-type boundary condition,

$$c(0,t) = g(t) \qquad [2]$$

or a third- or flux-type boundary condition,

$$-D\frac{\delta c}{\delta x} + vc = vg(t) \qquad [3]$$

$g(t)$ may also take several forms, for example constant with time, a pulse or exponentially changing with time.

At the lower boundary of the sample the following condition can be applied,

$$\frac{\delta c}{\delta x}(\infty, t) = 0 \qquad [4]$$

This condition assumes the presence of a semi-infinite soil column. An alternative to this is to assume zero concentration gradient at the bottom of the column.

Considering the experiments described in the previous chapter it can be seen that the initial condition is constant with depth, that is the sample contains no bromide throughout (verified prior to each experimental run). The boundary condition at the sample surface was a third-/flux-type, taking the form of a pulse of applied potassium bromide. The boundary condition at the bottom of the sample was taken to be semi-infinite; it has been noted elsewhere that little evidence exists to support the theory that the zero concentration gradient condition is a better description of processes at the lower boundary (van Genuchten, M. Th. and Alves, W. J., 1982). With these factors in mind the analytical solution of Equation 1 most appropriate is,

$$c(x,t) = C_i + (C_0 - C_i)A(x,t) \qquad [5]$$

during solute application $(0 < t > t_0)$, and

$$c(x,t) = C_i + (C_0 - C_i)A(x,t) - C_0 A(x,t-t_0) \qquad [6]$$

for the remainder of the experiment. In Equations 5 and 6 C_0 and C_i refer to the applied and initial concentrations respectively and therefore in this instance the equations simplify to,

$$c(x,t) = C_0 A(x,t) \qquad [7]$$

and,

$$c(x,t) = C_0 A(x,t) - C_0 A(x,t-t_0) \qquad [8]$$

Finally, in Equations [7-8],

$$A(x,t) = \frac{1}{2} erfc\left[\frac{Rx-vt}{2\sqrt{(DRt)}}\right] + \sqrt{\left(\frac{v^2 t}{\pi DR}\right)} \exp\left[\frac{(Rx-vt)^2}{4DRt}\right]$$
$$-\frac{1}{2}\left(1+\frac{vx}{D}+\frac{v^2 t}{DR}\right)\exp\left(\frac{vx}{D}\right)erfc\left[\frac{Rx-vt}{2\sqrt{(DRt)}}\right] \qquad [9]$$

81

Model parameters were adjusted to minimise the sum of the squared differences over approximately the first 75% of the area under each curve (ignoring some of the tail region). To enable comparison this sum was divided by the number of points used in its calculation and then the area, or total solute output, corresponding to the fitted region. A curve fitting routine was written in Visual Basic for Applications to automate this process. Figure 5.2 gives experimental and modelled bulk solute transport BTC's for all samples.

figure. However, the fit of the model in the peak region was more limited by the range of possible curves, given the combinations of model parameters and experimental data. Using a simplex method of non-linear optimisation and ignoring all other fit criteria, bar the condition that all other points on the curve were at lower concentrations than the peak value, it was still impossible to fit peak values of bromide concentration for any of the curves.

The optimised values of R for each sample type were approximately one, as expected for a solute chosen specifically for its conservative nature. The optimised values of D correlated qualitatively to sample permeability, which is in agreement with D being proportional to pore water velocity (Kirkham, D. and Powers, W. L., 1972).

5.2.2 Lateral Solute Transport

Using the values obtained in the previous section as starting points, Equation 7 was then used to model the breakthrough curves produced for the individual funnels in the lateral solute transport experiments. Modelling the transport from a point source to a variety of locations at varying horizontal displacements could not be achieved satisfactorily using only the vertical height of the sample, x. Using a single value of x produced a single modelled BTC, rather than an array of different curves as observed experimentally. Instead values of x_i, where i denoted the funnel number, were calculated for each funnel. x_i was calculated to be the diagonal distance from the centre of the sample surface to the centre of the sampling funnel. The areas under the modelled curves were normalised to those of the experimental curves.

Utilising values of R obtained in the previous section, each experimental curve was modelled three times as follows:

1. The breakthrough curves were modelled using the optimised parameters from the bulk solute transport experiments (Section 5.2.1).

2. The improvement in fit possible by optimising a single value of D over all funnels was investigated.

Figure 5.3 Experimental and modelled breakthrough curves for individual funnels under Redhill 30 sand at 120-mm. Crosses show experimental data points, black lines are modelled using one value of D for all curves and grey lines are modelled using a different value of *D* for each curve.

Figure 5.4 Experimental and modelled breakthrough curves for individual funnels under Redhill 30 sand at 240-mm. Crosses show experimental data points, black lines are modelled using one value of D for all curves and grey lines are modelled using a different value of *D* for each curve.
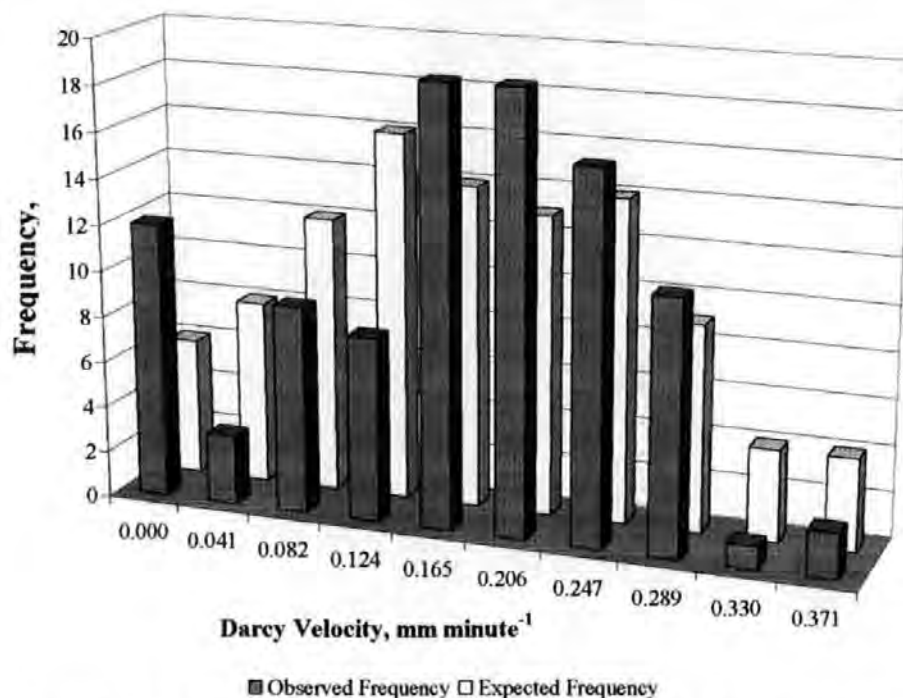
Figure 4.10 Comparison of the velocity distribution of a 120-mm Redhill 30 sample with a normal distribution.

Although the experimental distribution appears quite similar to a normal distribution, there is a prominent bar in the category corresponding to the lowest velocities. A low velocity peak was present in all of the experimental distributions, and had the effect of making the mean experimental velocities considerably lower than the peaks of the Normal distributions. Consequently none of the experimental distributions were statistically similar to the comparable normal distributions. Each experimental velocity distribution was also re-tested twice, after removing all of the zero velocities and after removing the entire low velocity peak. In both cases the normal test distributions were recalculated with the new experimental means and standard deviations. Even with both of these modifications none of the experimental velocities were normally distributed. Additionally the distributions were tested to see if they were logarithmically normal, as found in field studies by Biggar and Nielsen (1976), however this was not the case either.

4.3.2.4 Mann-Whitney Test of Velocity Distributions

Having demonstrated in the previous section that none of the experimental velocity distributions were normally distributed a non-parametric test was required to examine whether the any of the average velocity distributions from the flow pattern study were similar. For this purpose a simple Mann-Whitney test (Miller, J C. and Miller, J N., 1993)

4.3.2.6 Variograms

It is also possible to measure spatial correlations between the areas of high and low flow observed in the surface plots using semi-variograms (see Chapter 6 for a full discussion of variograms). Various directionally dependant variograms were measured, but these were found to give the same information as directionally averaged (360° search window) variograms, as might be expected from experiments which were horizontally directionally isotropic. Directional variograms are shown in Appendix B.
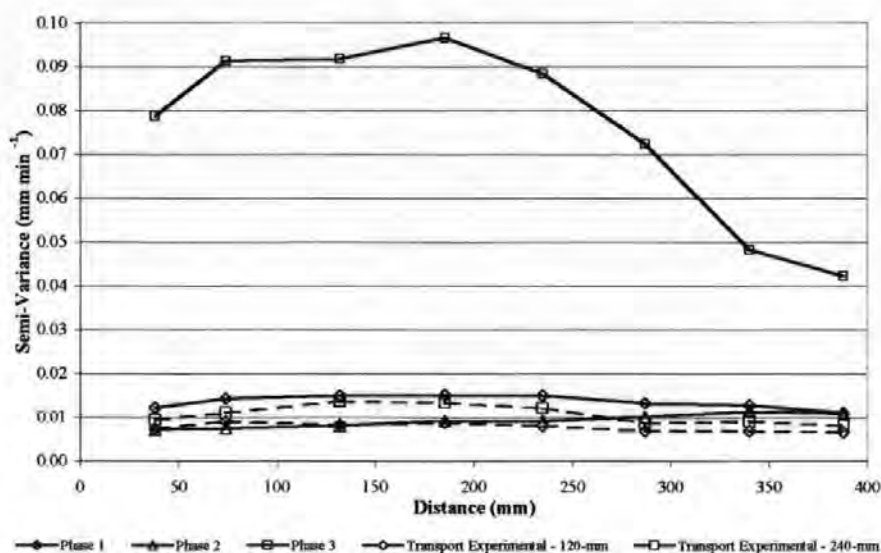
Figure 4.11 Variograms of average Darcy velocity for phases 1 to 3 and also the two transport experiments described in Section 4.2.3 and Section 4.2.4.

It can be seen that the semi-variance of phase 3 was very much greater than those of phases 1 and 2. This correlates with Figure 4.7, which showed that the Darcy velocities in phase 3 were dominated by extremes of either rapid or zero flow, relative to the velocity distributions of phases 1 and 2. All distributions other than phase 3 can be seen to have relatively low and flat variograms - i.e. there is a low level of semi-variance between sampling points, and the semi-variance does not change with distance - it occurs in an unstructured way across the sample grid. There is no discernible difference between the tracer transport experiments at different sample depths. The semi-variance of phase 3, by contrast, is most extreme at distances up to half the overall grid size. Inspection of Figure 4.7 (c) confirms that the main variance between flows is on this scale. At larger scales, between half and the whole grid size, pairs of observations tend to be increasingly limited to the edges, as central points do not have a comparison point more than 250-mm away. It can be seen that the edges are rather more correlated, tending mostly to low flow, but as
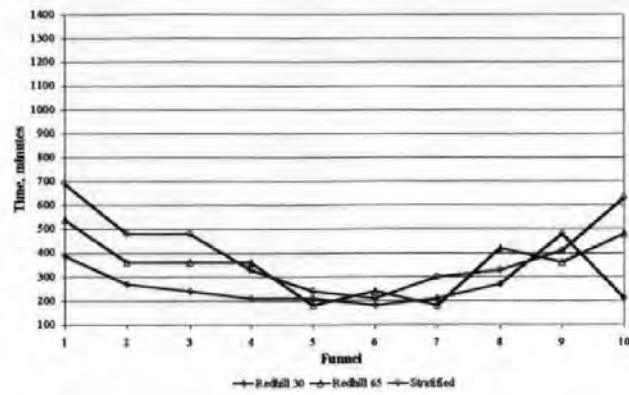
a)
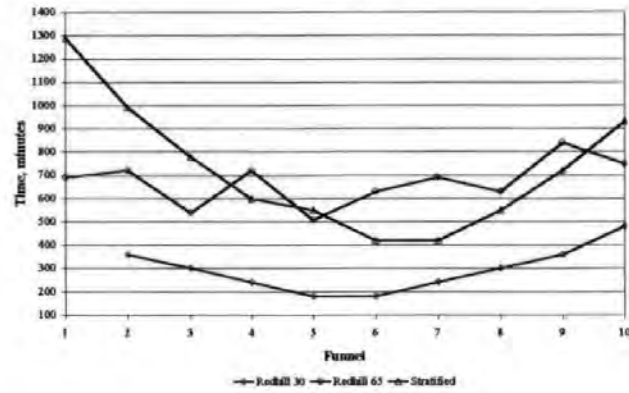
b)

Figure 4.14 Times corresponding to maximum bromide concentrations for a) 120-mm sand samples and b) 240-mm sand samples.
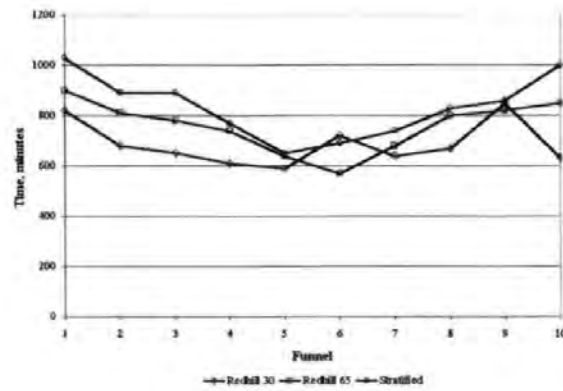
a)
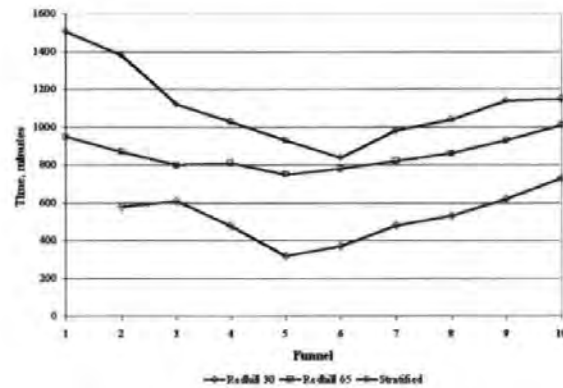
b)

Figure 4.15 Times corresponding to 75% of the area under the bromide breakthrough curves for a) 120-mm sand samples and b) 240-mm sand samples.

4.3.4.2 Pearson Product Moment Correlation Coefficient

The simple Pearson test already employed in Section 4.3.2.5 was used to examine whether the breakthrough curves of funnels equidistant from the point of application were correlated. Assuming the overall shapes of the breakthrough curves to be similar, the Pearson coefficient tends to measure correlations in times of bromide arrival more than correlations in bromide concentration. Figure 4.16 shows three fictitious breakthrough curves as might be compared using the Pearson coefficient.
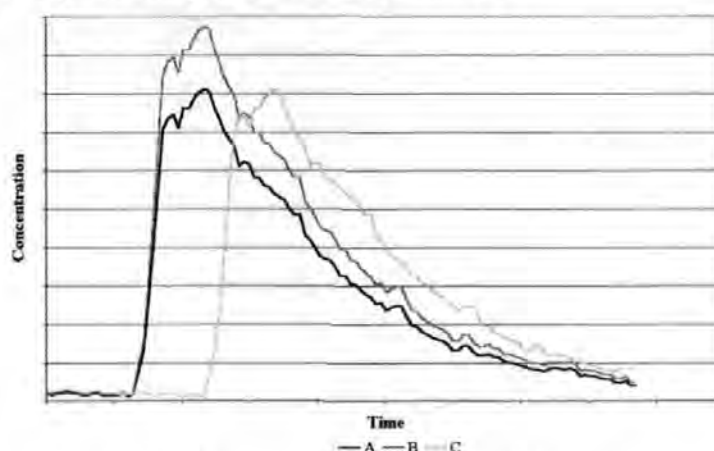
Figure 4.16 Comparison of breakthrough curves using Pearson coefficient.

Although curves A and C are identical, but shifted in time, the Pearson coefficient comparing these two is only 0.34, whereas the coefficient for A and B is almost 1. Clearly the Pearson coefficient will measure mainly correlations in arrival time, rather than curve shape. However, for the purposes of this study that is an acceptable limitation.

Figure 4.17 shows surface plots of the Pearson product moment correlation coefficients. Each point on the scatter plots represents the Pearson correlation coefficient for the breakthrough curves of one pair of funnels. To aid comparison white stars indicate pairs of funnels equidistant from the point of solute application, and black stars indicate funnels closest to the point of application paired with funnels furthest from the point of application.

Figure 5.1 shows example breakthrough curves produced by the convection-dispersion equation described above and the effects of changing the diffusion coefficient and the retardation factor.

a)

b)
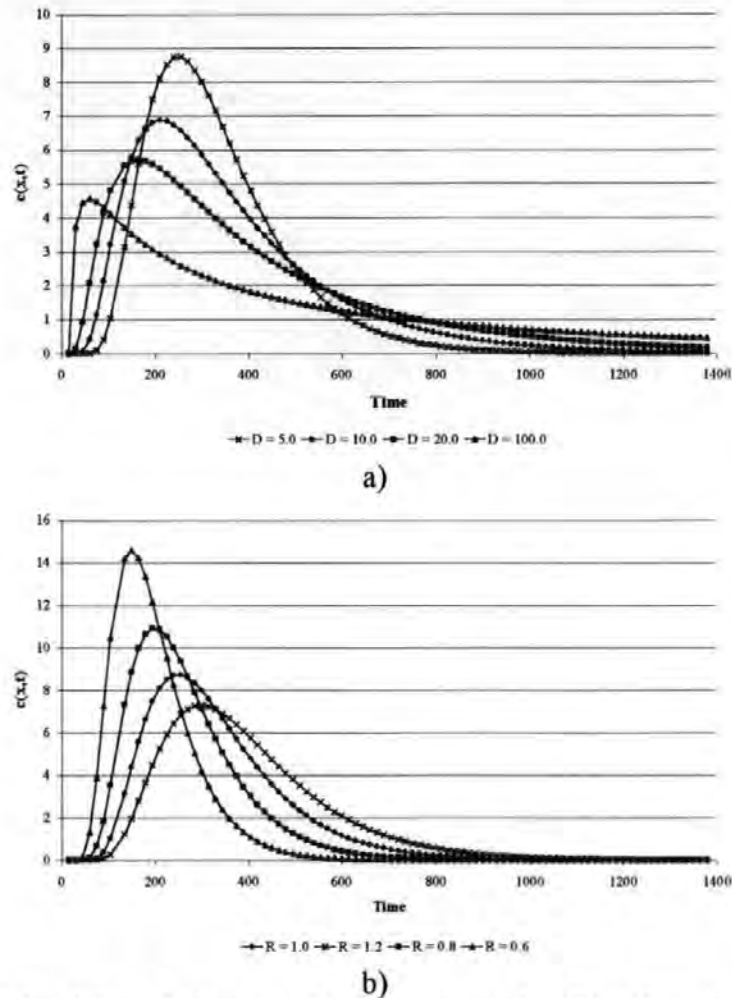
Figure 5.1 Example breakthrough curves produced by a convection-dispersion equation showing the effects of a) varying *D* and b) varying *R*.

Increasing D causes the breakthrough curve to become more spread out as greater diffusion of the solute take place within the flowing water. Increasing R causes the arrival of the solute peak to become delayed, which also allows greater diffusion to take place.

5.2 Fitting Convection-Dispersion Equations

5.2.1 Bulk Solute Transport

The convection-dispersion equation described above was fitted to the experimental breakthrough curves measured in the previous chapter. Curve fitting was achieved with reference to the squared vertical difference between experimental and modelled BTC's.

a)

b)

c)
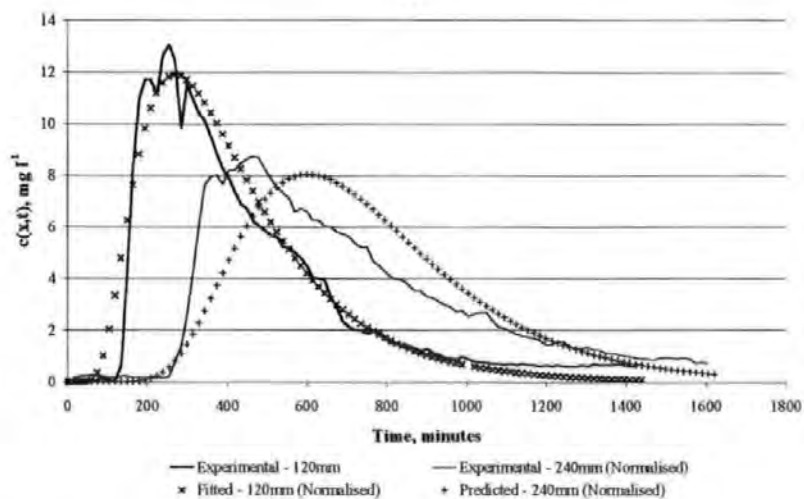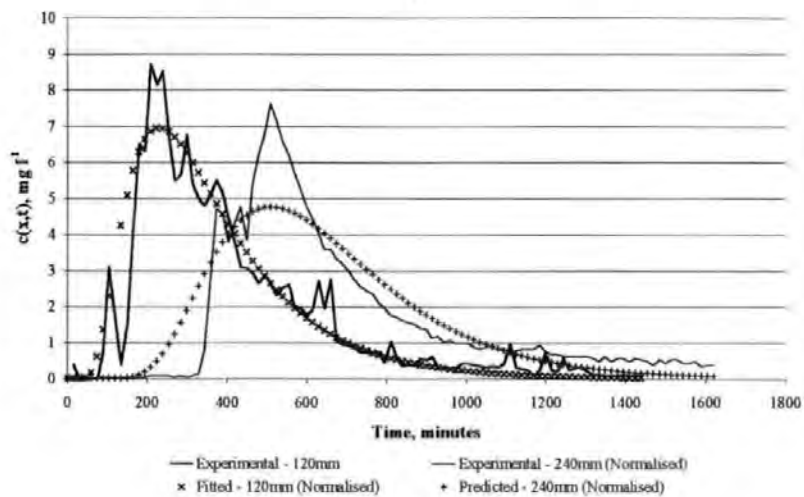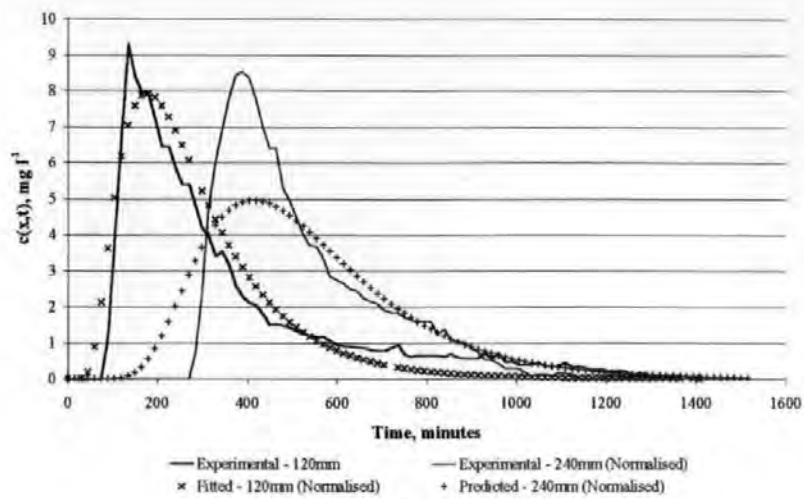
Figure 5.2 Experimental bromide breakthrough curves and fitted and predicted convection-dispersion equations for a) Redhill 30, b) Redhill 65 and c) stratified sand samples.

The values of D and R obtained from fitting the 120-mm depth samples were used to predict the BTC's for the deeper samples. The areas under the modelled curves and under the 240-mm depth experimental curve were normalised to the area under 120-mm depth curve to account for unmeasured losses of bromide through the edge channels of the grid lysimeter.

Table 5.1 shows the optimised model parameters and goodness of fit figures used in the convection-dispersion equation.

Sand	Depth, mm	Pore Water Vel., mm min^{-1}	Diffusion Coefficient, D	Retardation Factor, R	Goodness of Fit
Redhill 30	120	0.475	10.33	0.95	0.5e^{-3}
	240	0.466			1.5e^{-3}
Redhill 65	120	0.378	8.04	0.98	0.5e^{-3}
	240	0.396			0.6e^{-3}
Stratified Sand	120	0.352	6.99	1.06	0.5e^{-3}
	240	0.364			1.0e^{-3}

Table 5.1 Modelled parameters for convection-dispersion equation modelling of experimental breakthrough curves.

Visual inspection reveals that reasonable fits of model to experiment were achieved for all of the 120-mm deep samples. The best fit, both visually and with reference to the goodness of fit figures, was achieved for the 120-mm stratified sample. In the cases of the single layer samples subsequent predictions of transport through the 240-mm samples predicted the times of arrival of the solute peaks accurately, but underestimated the size of the peaks. For the stratified sample the model prediction for the 240-mm sample was rather retarded compared to the experimental BTC, but predicted the size of the peak more accurately. It can also be seen that generally the model did not accurately predict the rapidity of the decline in concentration following the solute peak, or the more gradual decline in the tail regions of the curves.

It was thought that the poor fit of the model in the region of the solute peak may have been an artefact of the measurement of fit. All points in the region over which fit was measured were treated equally. The appearance of the bromide maximum took place rather quickly, and the initial points contributed relatively little to the overall goodness of fit

3. The effect of optimising D for each of the funnels in a run was examined.

Table 5.2 shows the values of D and goodness of fit figures obtained by the three methods described above (indicated by the superscript figures). The subsequent figures show the BTC's (for the sake of clarity only the curves produced by the latter two optimisations are shown).

Sand	Depth, mm	D	Value	GOF % Improvement
Redhill 30	120	**10.33**[1]	**0.0326**	-
		10.80[2]	0.0326	0.09
		multiple[3]	0.0287	11.8
	240	**10.33**[1]	**0.0233**	-
		32.80[2]	0.0186	20.4
		multiple[3]	0.0183	21.8
Redhill 65	120	**8.04**[1]	**0.0137**	-
		9.25[2]	0.0134	2.2
		multiple[3]	0.0124	9.3
	240	**8.04**[1]	**0.0125**	-
		7.58[2]	0.0124	0.34
		multiple[3]	0.0102	18.6
Stratified	120	**6.99**[1]	**0.0219**	-
		9.01[2]	0.0204	6.9
		multiple[3]	0.0169	22.9
	240	**6.99**[1]	**0.0449**	-
		7.6[2]	0.0447	0.4
		multiple[3]	0.0333	25.7

Table 5.2 Optimised values of D for all funnels. Goodness of fit (GOF) figures are the average over all contributing funnels. Bold figures show GOF using original values of D and R from Section 5.2.1.
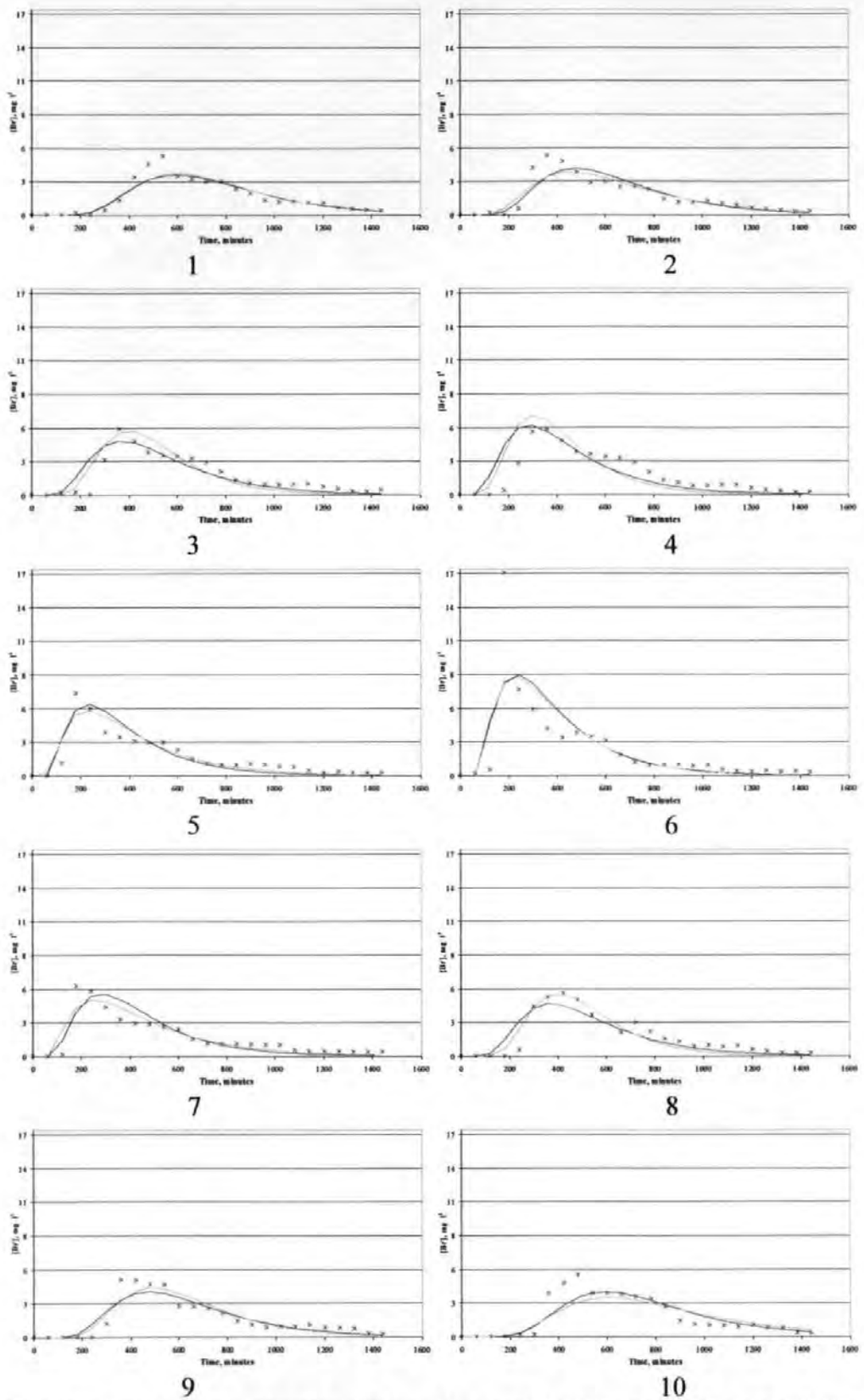
Figure 5.5 Experimental and modelled breakthrough curves for individual funnels under Redhill 65 sand at 120-mm. Crosses show experimental data points, black lines are modelled using one value of D for all curves and grey lines are modelled using a different value of *D* for each curve.
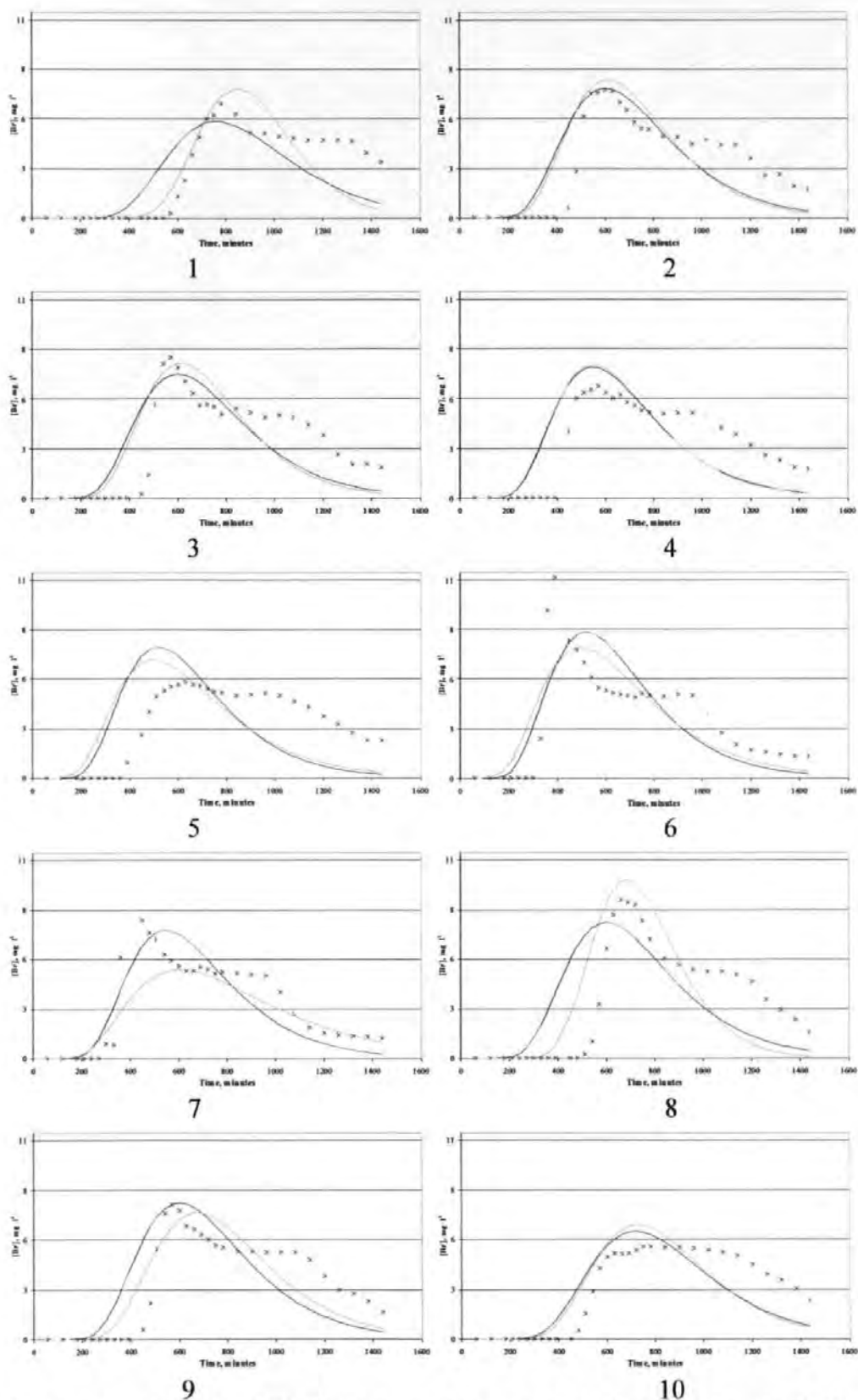
Figure 5.6 Experimental and modelled breakthrough curves for individual funnels under Redhill 65 sand at 240-mm. Crosses show experimental data points, black lines are modelled using one value of D for all curves and grey lines are modelled using a different value of *D* for each curve.
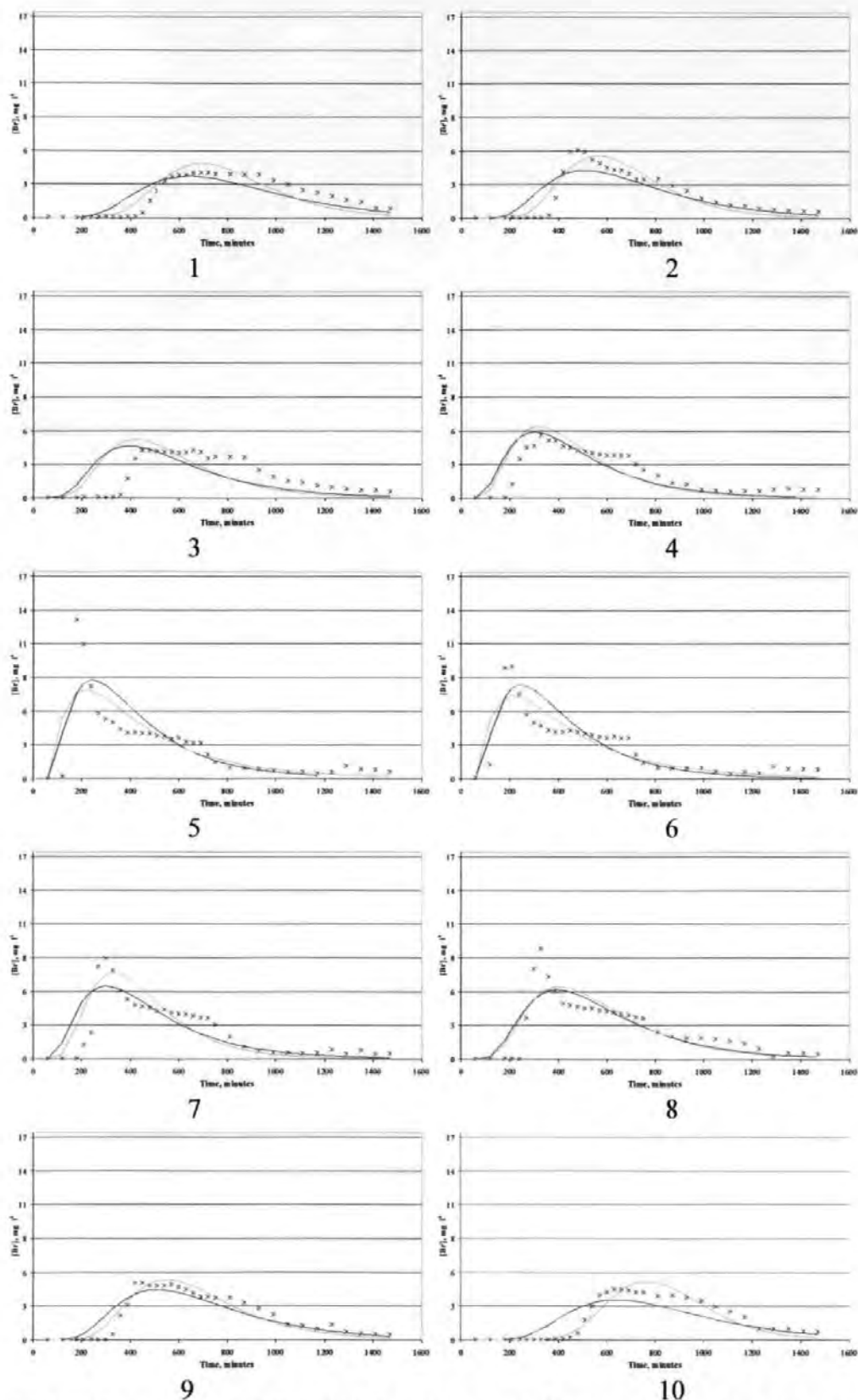
Figure 5.7 Experimental and modelled breakthrough curves for individual funnels under stratified sand at 120-mm. Crosses show experimental data points, black lines are modelled using one value of D for all curves and grey lines are modelled using a different value of D for each curve.
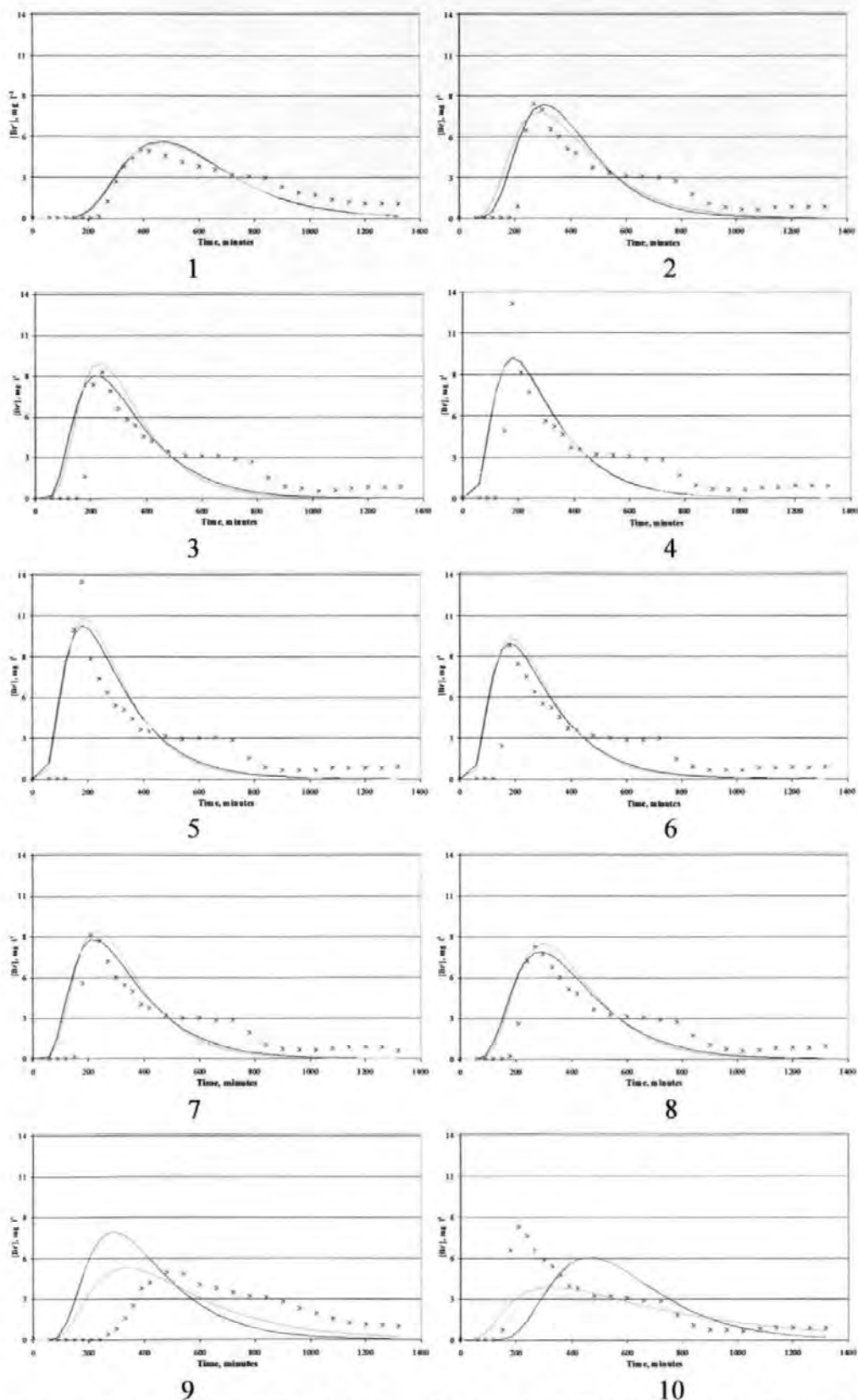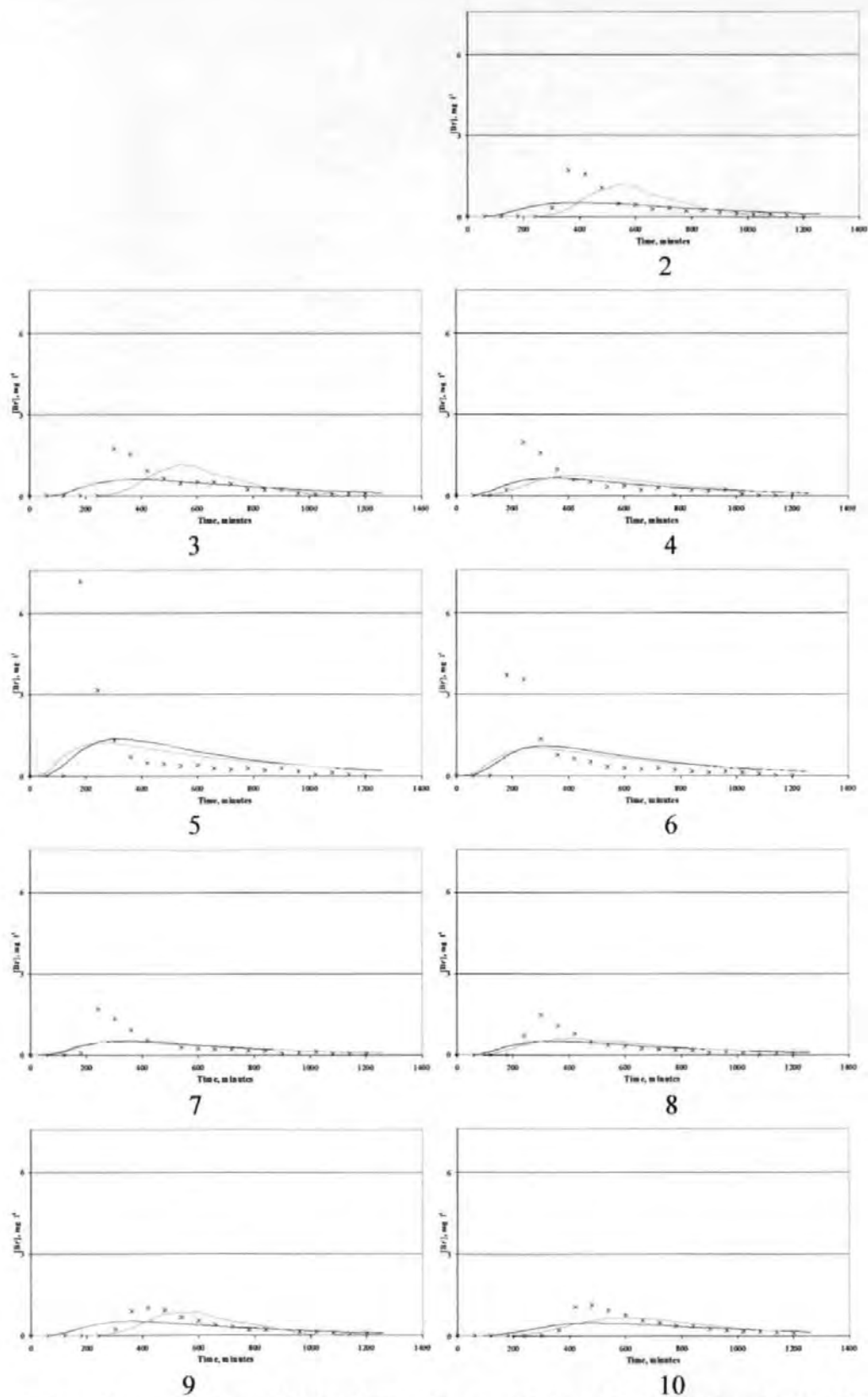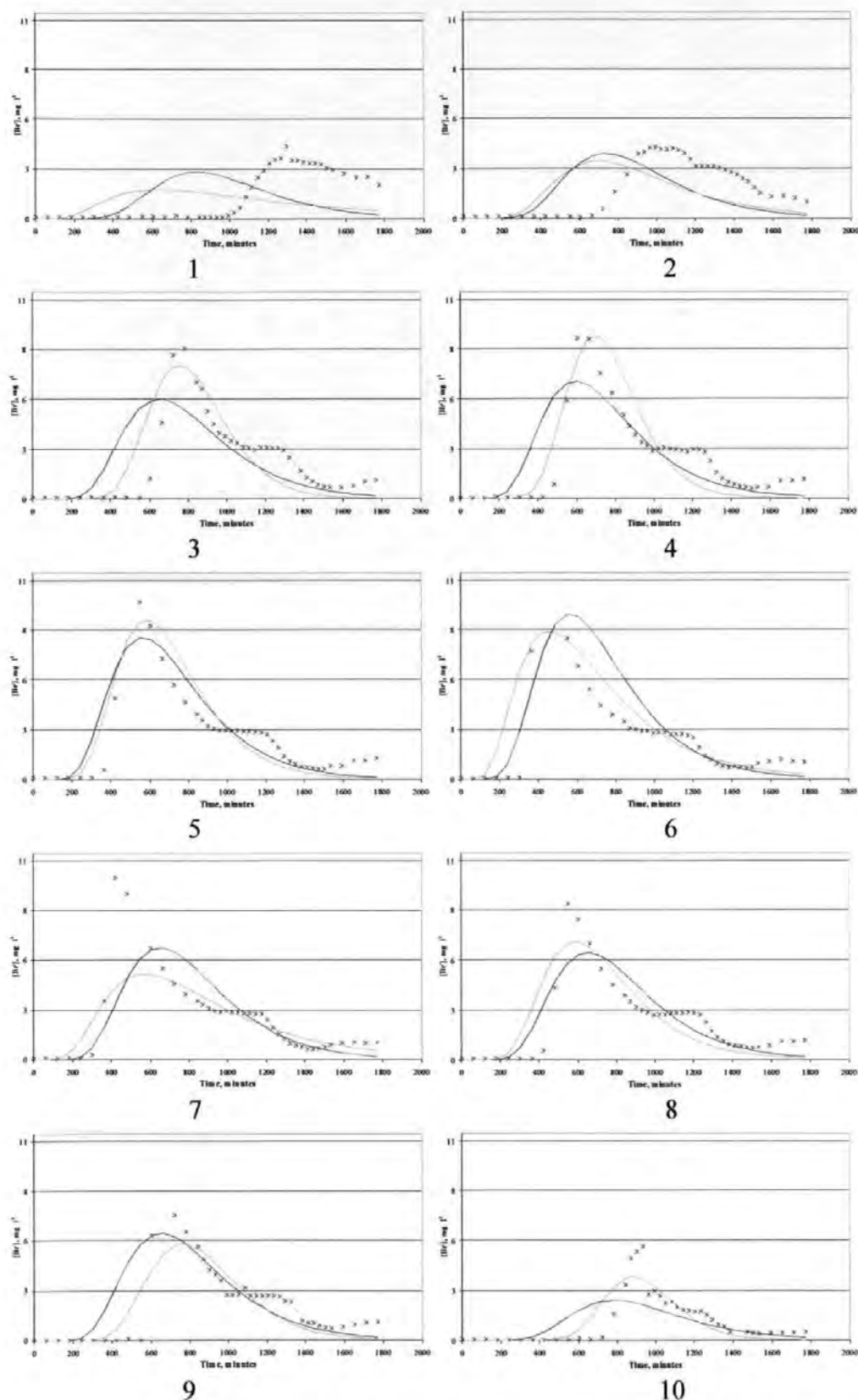
Figure 5.8 Experimental and modelled breakthrough curves for individual funnels under stratified sand at 240-mm. Crosses show experimental data points while the solid blue lines are modelled using one value of *D* for all curves and the red lines are modelled using a different value of *D* for each curve.

93

Table 5.3 shows the values of D optimised for individual funnels (grey lines in the preceding graphs), with funnels numbers corresponding to those in Figure 5.3-Figure 5.8.

Sand	Depth, mm	Funnel									
		1	2	3	4	5	6	7	8	9	10
Redhill 30	120	11.32	8.41	8.38	10.31	9.28	9.44	8.79	9.03	17.44	42.03
	240	-	5.3	18.84	26.96	51.97	43.97	28.30	21.00	5.4	12.89
Redhill 65	120	8.54	11.55	5.83	6.33	10.43	9.84	12.78	5.68	7.47	10.36
	240	2.08	2.55	3.07	3.55	5.62	4.23	2.23	8.54	1.33	1.20
Stratified	120	4.76	4.62	6.48	7.17	12.99	13.77	5.65	7.91	5.65	3.14
	240	27.94	10.50	3.31	3.05	5.73	10.51	15.59	7.16	4.90	2.5

Table 5.3 Optimised values of D for individual funnels.

Visual inspection of the predicted BTC's for the 120-mm samples reveals that the model predicted bromide transport moderately successfully. It was less successful predicting transport through the 240-mm samples, particularly the Redhill 30 sample.

For most of the samples re-optimising a single value of D produced only a small improvement in model predictions, compared with retaining the value obtained from the bulk solute transport work. Re-optimising D for individual funnels produced more substantial improvements in the fit. However, this improvement generally arose as a consequence of only one or two funnels that were inadequately modelled by a single value of D. Examining these values of D, it can be seen that there is no obvious trend to the changes in value. Visually the variation appears random and unrelated to position. This is discussed further in Section 5.3.

It is worth noting that in some instances re-modelling D for each funnels produced an improvement in fit, but visual inspection of the curves called into question how much the fit actually improved. In Figure 5.6g, for example, although the grey line represents an improved fit, as defined here, the black line more accurately predicts the time of arrival and magnitude of the bromide peak.

The modelling of the lateral transport breakthrough curves was hampered throughout by the 'step' effect observed in the tails of the experimental breakthrough curves. In each case, after the maximum concentration had exited the sample the concentration declined to

a value of around 3-mg l^{-1}. The bromide concentration of the exiting solution then remained constant for around 200 minutes, after which it dropped rapidly to almost zero. This feature of the experimental breakthrough curves made the fitting of the convection-dispersion equation particularly difficult and is discussed further in Section 5.3.

5.2.3 Sensitivity Analysis

An analysis of model sensitivity was carried out to investigate whether differences in optimised values of the model parameters appeared to be sample dependent. Using the goodness of fit figures from modelled bulk solute transport (Section 5.2.1) the effects of changing model parameters were examined. D and R were adjusted to give decreases in the goodness of fit figures of 5% and 10%.

		R Giving Reduction in GOF of				D Giving Reduction in GOF of			
	Original	5%		10%		Original	5%		10%	
R'hill 30	0.95	0.92 *3%*	0.99 *4%*	0.91 *4%*	1.00 *5%*	10.33	9.30 *10%*	11.53 *12%*	8.91 *14%*	12.07 *17%*
R'hill 65	0.98	0.95 *3%*	1.02 *4%*	0.93 *5%*	1.04 *6%*	8.61	7.13 *17%*	9.10 *6%*	6.80 *21%*	9.60 *11%*
Stratified	1.06	1.03 *3%*	1.09 *3%*	1.02 *4%*	1.10 *4%*	7.02	6.42 *9%*	7.62 *9%*	6.21 *12%*	7.90 *13%*

Table 5.4 Sensitivity analysis of modelling parameters. For each percentage level an upper and lower bound, above and below the optimised values shown in Table 5.1, is given. Figures in Italics show percentage change in model parameter from the optimised value.

The model was more sensitive to changes in R than D. Given that the expected value of R for these samples was 1, it is unclear whether the different optimised values of R represent genuine sample dependency or merely random 'noise'. The latter conclusion seems most likely given the nature of the solute tested.

The model was less sensitive to changes in the value of D, which appeared to be related to sample permeability. Similarly to R, there was significant overlap in the tested ranges, even at the 5% level. Again this makes it difficult to judge the extent to which values of D were sample dependent.

The other main source of variability within the model was the experimentally determined pore water velocity, v. Being the convective component of modelled transport, large changes in the value of v will have a significant effect on predictions. This parameter is based on measured values of the volume flow rate of exiting water and the water-filled porosities of the samples. Of these the chief uncertainty arises from the measurement of the volumetric water content by time-domain reflectometry (TDR). Values for the water content of the samples were obtained from long TDR probes, spanning the width of the sample volumes under test. Effectively these measured average water contents across the length of the probe. However, later work on the sample sands (Chapter 6) revealed that there might have been significant local variation in sample porosity, and therefore water-filled porosity.

To investigate the potential effects of uncertainty in the calculated values of v arising from measured values of volumetric water content, a further sensitivity analysis was conducted. The best fit possible at various other values of v, corresponding to specific differences in the volumetric water content, were measured by re-calibrating the model to the 120-mm experimental BTC's. These are summarised below (percentage changes in water content refer to absolute changes i.e. a measured water content of 34.2% was re-tested at 33.2%, 35.2%, 32.2%, 36.2% and so on).

Sample	Improvement in Fit Possible (%) After Changing Water Content By:					
	1%		2%		5%	
Redhill 30	-0.001	-0.007	-0.009	-0.002	0.000	0.000
Redhill 65	0.006	0.002	0.003	-0.001	0.005	-0.001
Stratified	-0.002	0.002	0.001	-0.010	-0.001	-0.012

Table 5.5 Sensitivity analysis of pore water velocity/volumetric water content.

From Table 5.5 it can be seen that the fit of model to experiment was extremely insensitive to changes in volumetric water content, even when these changes were relatively large. At each different volumetric water content re-optimising the model parameters D and R achieved, at best, negligible improvements in fit.

5.3 Discussion

The success of the simple CDE tested here in modelling the bulk solute transport curves was limited. Despite the choice of a relatively unreactive solute tracer, calibrations of model to experiment were somewhat unsatisfactory, and subsequent predictions reflected this. However, the model was similarly successful in predicting solute transport from a point source. Re-optimising D, rather than using the value obtained from the bulk solute transport work, only marginally improved model predictions. Re-optimising D for each funnel produced more significant improvements, although this was often due to improving the fits of only one or two funnels.

As mentioned previously, re-optimising the diffusion coefficient of each individual breakthrough curve yielded a very broad range of values of D. Re-optimised values of D were plotted against distance from the point of solute application to examine whether a linear relationship between D and depth can be observed (Huang, K. L. et al., 1996).
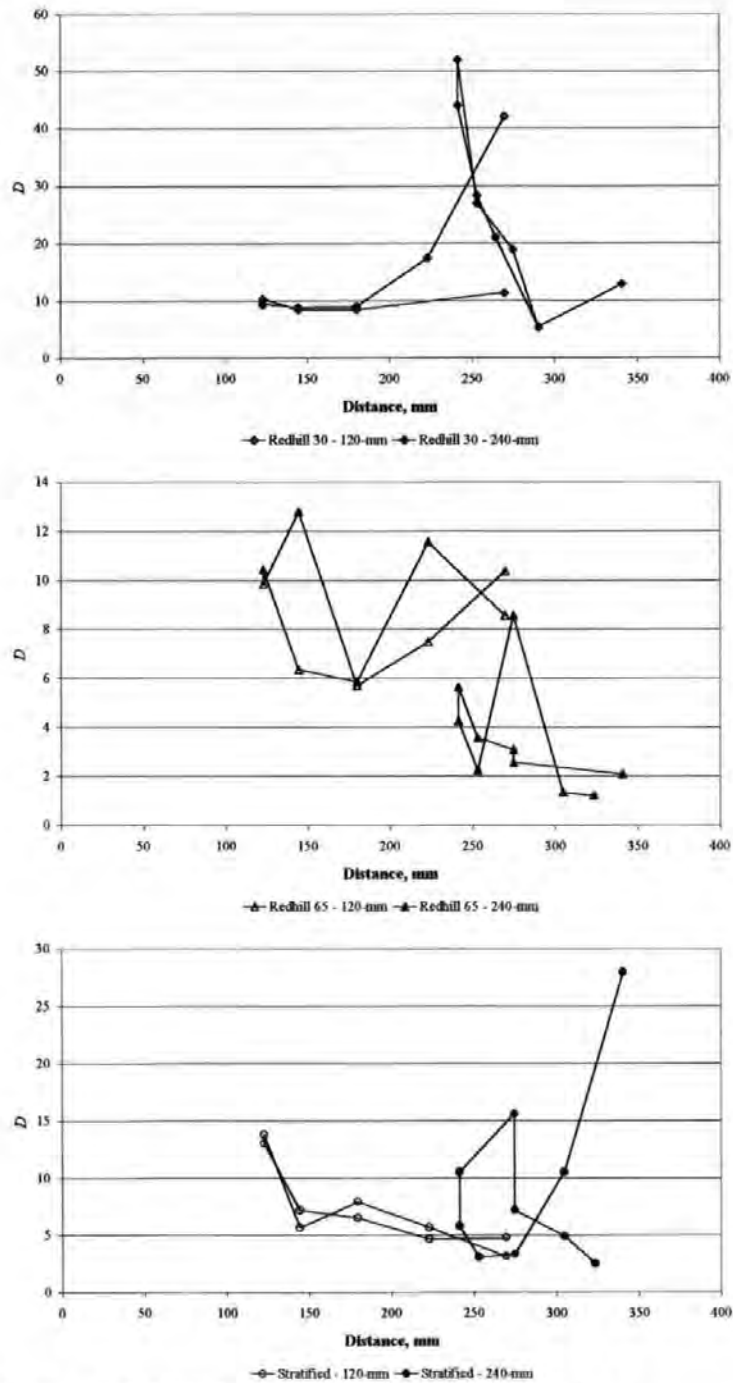
Figure 5.9 Plots of D against distance from the point of solute application.

Clearly there is no discernible relationship between D and distance using the values of D obtained here.

As mentioned in the previous section, almost all the breakthrough curves for the individual funnels showed a concentration plateau of around 3 mg l^{-1} following the output of the maximum concentration. These plateaus tended to last approximately 200 minutes before declining rapidly. The fact that this effect occurred uniformly throughout the

samples studied indicates that, rather than some experimental anomaly, this was a product of the process being examined.

One explanation of this behaviour is that, as the original pulse of bromide moved through the sample, reservoirs of relatively high bromide concentrations were created in regions of immobile water. It has been noted in systems such as this that there may be two distinct regions to the water-filled porosity (Bai, M. et al., 1995; Brusseau, M. L. et al., 1994; Hu, Q. H. and Brusseau, M. L., 1995). Low permeability microporous regions, filled here during the saturation process, may contain an immobile water fraction, or 'old' water. Regions of larger water-filled mesopores contain the mobile fraction responsible for the majority of transport, which may be referred to as 'new' water. As the original tracer pulse moved through the sample bromide may have diffused into regions of immobile water. As the pulse passed and bromide concentration in the mobile water phase declined, bromide may then have re-diffused back out of the immobile water fraction. If this was the case it would appear that the effect was 'averaged' out in the combining of all outputs in the bulk solute transport work.

5.4 Conclusions

The simple convection-dispersion equation employed here managed to reproduce gross features of the experimental solute transport, such as time of arrival of the solute peak and approximate shape of the breakthrough curve. The convection-dispersion equation was not significantly less successful in modelling solute transport from a point source than it was in modelling bulk transport.

The model employed only two parameters that could not be directly measured experimentally, the retardation coefficient, R, and the diffusion coefficient, D. These behaved in ways that appeared to be related to observable properties of samples. The modelled retardation coefficients took values of around 1 for all of the samples studied, which was appropriate given the nature of the solute studied. D appeared to be dependent on sample permeability (measured in Section 6.2). Sensitivity analyses of both of these parameters showed that the

model was not as sensitive to changes in their values as might be expected, given differences between the experimental samples studied.

Although there was a degree of uncertainty in the accuracy of the measured volumetric water content, and therefore the pore water velocity, it was demonstrated that the model was extremely insensitive to changes in this value.

To conclude, although the simple model employed here managed to reproduce some features of the experimental breakthrough curves, the experimental processes were ultimately too complex to be accurately predicted. Clearly the solution of the convection-dispersion equation employed here did not adequately represent the experimental conditions present, even in these comparatively uncomplicated samples. The most likely source of the discrepancy between experiment and model was the implicit treatment of the simulated material as a homogeneous continuum. In the following chapter this assumption is investigated, and the possibility of enhancing the model used here via network modelling is studied.

6 Network Modelling of Flow and Transport

6.1 Introduction

Work described in Chapter 4 examined the flow and transport behaviour of homogeneous sand columns. It has been demonstrated that flow through homogeneous samples was not randomly distributed. It has also been shown that flow paths through the same sample, prepared identically, were not reproducible and did not appear to be related to measurable changes in sample structure. Work prior to this has suggested that heterogeneities in flow arise as a result of observable variations in sample structure, such as barriers to permeability or structural discontinuities (Miyazaki, T., 1993a).

It has also been suggested that flow heterogeneities may develop in random packings as a function of sample depth. Porter (1968) presented a 'rivulet' model of flow for predicting flow at given depths. Subsequent work (Porter, K. E. et al., 1968) showed flow to be Normally distributed, and this has been shown not to be the case for these samples. Dexter (1995) presented a simplified version of this theory, whereby rivulets could coalesce but never split, and concluded that preferential flow in random packings should become more pronounced with depth. Again this relationship has been shown not to hold for the depths considered here.

Work described in Chapter 5 demonstrated that, although capable of reproducing gross aspects of solute transport, the simple convection-dispersion equation (CDE) was limited in its predictive abilities. Typically the response to this limitation has been more complex solutions of the CDE, using a greater number of model parameters to cope with the disparity between model and experiment. Although in many cases this has resulted in more accurate simulations, these solutions tend to be of limited usefulness beyond the scope of the studies in which they were developed, and it has been concluded that such models are seldom employed beyond the initial study (Addiscott, T. M. and Wagenet, R. J., 1985).

Implicit in the derivation of the basic CDE is the assumption that the experimental transport volume may be considered a one-dimensional homogeneous continuum. Although a few workers have developed solutions that somehow extend the CDE beyond a single dimension, for example by employing a logarithmically normal distribution, based on experimental observations (Biggar, J. W. and Nielsen, D. R., 1976), of inputs to generate a spatial array of breakthrough curves (Amoozegar-Fard, A. et al., 1982)

The experimental results obtained thus far appear to indicate that the homogeneous random packings of sand tested here have not behaved as homogeneous continua in terms of the properties upon which flow depend. In this chapter more subtle information regarding homogeneity, or otherwise, of the packings is extracted. This is done to investigate whether the variability experienced experimentally may be simulated using a network model, and whether this model might be able to provide supplemental information to enable more accurate models of the porous materials studied.

6.2 Characterisation of Redhill Sands

The two grades of sand used in Chapters 4 and 5 were characterised experimentally and then modelled using the network model Pore-Cor. Certain details regarding the chemical compositions and particle size distributions of the two sands were provided by the suppliers (Hepworth Minerals and Chemicals, Sandbach, Cheshire, U.K.) and are given in Appendix A. In addition to these details porosity and permeability were also examined.

6.2.1 Porosity

Sample porosity was obtained via mercury intrusion. Mercury intrusion curves were also required as the chief input for the network modelling. For each of the sands ten runs were carried out on a Micromeritics Autopore III (Micromeritics, Atlanta, Georgia, U.S.A.) to examine the effects of different random packings on the apparent void size distribution and porosity. Mercury intrusion curves are shown in Figure 6.1 below, and the corresponding porosities are given in Table 6.1.

a)

b)
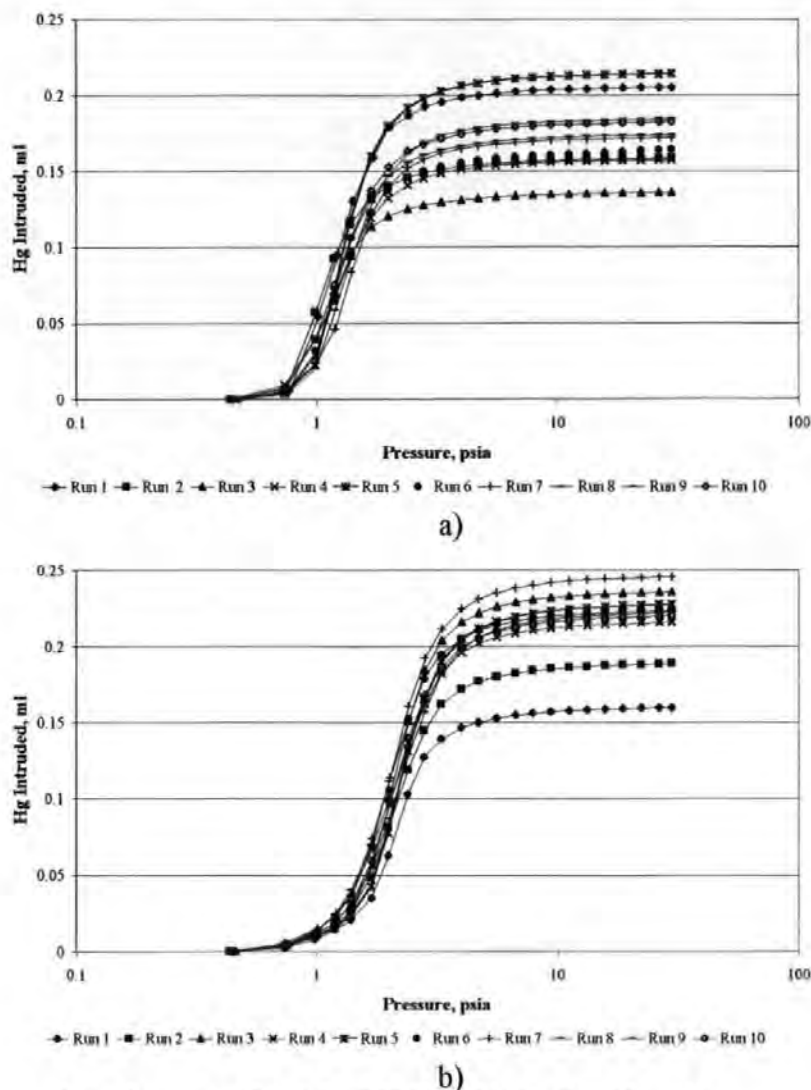
Figure 6.1 Mercury intrusion curves for a) Redhill 30 and b) Redhill 65 sands.

	Porosity, %	
	Redhill 30	**Redhill 65**
	34.9885[4]	39.6508
	38.8200	43.8329
	39.8622	44.4028
	39.9417	44.6231
	40.2365	44.9501
	40.6789	45.2838
	41.2894	45.3392
	41.6162	45.389
	41.6824	45.4483
	41.9841	45.6633
Average	40.68	44.46
Standard Deviation	1.05	1.78

Table 6.1 Porosities of Redhill sands obtained by mercury intrusion.

It can be seen from both the intrusion curves and range of porosities that, at the scales observed here, void volume and void size distribution appear highly sensitive to

---

[4] Assumed to be anomalous and ignored.

packing. From these results it can be inferred that there may have been significant local variation in porosity within the transport samples studied in the previous two chapters.

6.2.2 Permeability

The permeabilities of the two sands were obtained by constant head permeametry. Ten measurements were taken for each sand, each measurement being the average of five readings. These are presented below.

	Permeability, Darcies	
	Redhill 30	Redhill 65
	7.99	3.78
	7.12	2.87
	9.48	3.38
	10.46	2.07
	9.32	3.26
	6.27	1.86
	6.99	2.79
	7.80	2.20
	9.46	2.94
	9.58	3.46
Average	8.45	2.84
Standard Deviation	1.39	0.65

Table 6.2 Constant head permeabilities of Redhill sands.

There was considerable variation in the measured permeability. Considering the standard deviations it can be seen that permeability varied considerably more than porosity. Clearly permeability is even more sensitive to packing than porosity.

6.2.3 Unsaturated Permeability

The permeabilities measured in the previous section represent the *saturated* liquid permeabilities, or specifically the saturated hydraulic conductivities. However, the samples tested and modelled in the previous two samples were *unsaturated*. Unsaturated permeability is typically only a fraction of the saturated value, and is a non-linear function of water content (Jury, W. A. et al., 1991). The saturated permeabilities of different porous materials display a wide range of sensitivities to changes in volumetric water content (Miyazaki, T., 1993a). However, experimental measures of unsaturated permeability are significantly more difficult to obtain than those of saturated permeability. Generally

unsaturated permeability is estimated using methods that employ the water characteristic curve as the chief experimental input. Traditionally this has been achieved using a simple, Poiseuille-based capillary tube model of the porous media, where the number and size of capillaries is selected to reproduce the experimental characteristic curve (Jury, W. A. et al., 1991). More recently a large number of alternative methods of calculating the unsaturated permeability based on the water characteristic curve have been presented (Brooks, R. H. and Corey, A. T., 1964; Peat, D. M. W. et al., 1998; Kosugi, K., 1994; Mualem, Y., 1976).

The unsaturated permeability may also be estimated using the Buckingham-Darcy flux law.

$$v_D = -K(h)\frac{\delta H}{\delta z} \qquad [1]$$

Here v_d is the Darcy velocity, $K(h)$ is the unsaturated permeability, H is the hydraulic head and z is depth.

In this study it was not possible to obtain the water characteristic curve for the samples studied. Due to the relatively high permeability of the two sands used drainage would have been too rapid to measure with the apparatus available. Neither was the hydraulic head, necessary to use Equation 1, in the unsaturated samples known. This meant it was not possible to estimate the unsaturated permeability of the sands used in the transport studies. However, other workers have conducted studies of the relationship between volumetric water content and unsaturated permeability, and the results of some of these are shown below (Miyazaki, T., 1993b).
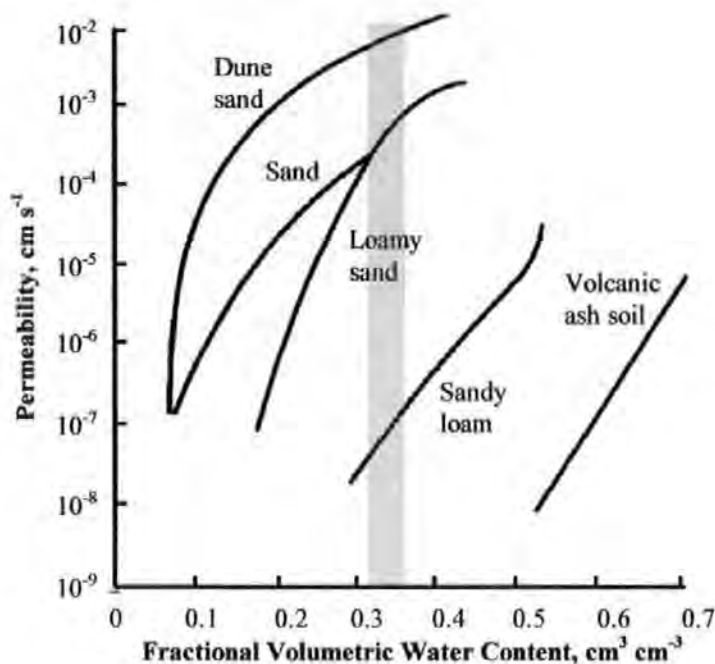
Figure 6.2 Unsaturated permeability versus volumetric water content (Miyazaki, T., 1993b). Volumetric water content corresponding to transport experiments in Chapter 4 shown in grey.

Figure 6.2 suggests that for the range of fractional volume water contents experienced here, 0.32-0.36 cm^3 cm^{-3}, a decrease in water content of 0.1 cm^3 cm^{-3} may be accompanied by a decline in permeability of just under one order of magnitude. Given the broad range of permeabilities measured in the previous section, it seems reasonable to assume that unsaturated permeability will display, at the very least, a similar variability. During the experiments described and modelled in the previous two chapters, the range of porosities measured in Section 6.2.1 would be likely to give rise to an even broader range of water contents. Given that microporous regions in the samples are likely to remain almost saturated, while areas of larger pores may drain almost completely, local saturation may be extremely variable. In turn this may produce a range of unsaturated permeabilities significantly greater than the range of saturated permeabilities measured in Section 6.2.2.

6.3 Modelling of Redhill Sands

Previous work using the network model 'Pore-Cor' has not attempted to reflect the experimental variability demonstrated in Sections 6.2.1 and 6.2.2. In mercury porosimetry it is customarily assumed that intrusion curves for homogeneous materials such as sand display minimal variability from one run to the next. Consequently, network simulations

106

tend to have been based on a single experimental intrusion curve. However, the results presented above indicate that, for the two sands considered here, the assumption of reproducibility between sub-samples of these bulk materials is invalid. An alternative modelling approach is required to account for this experimental variability.

It must be assumed that the variability observed in measured values of porosity and permeability arose from variations in packing. That is, different random arrangements of the loose particulate materials appear to be responsible for local variations in the characteristics of the bulk materials. As discussed in Chapter 2, Pore-Cor simulations are based around the initial random positioning of throats within the 10 x 10 x 10 lattice of nodes comprising the unit cell. As such different *stochastic generations*, that is different initial random arrangements of throats, of the unit cell for a given material can be thought of as equivalent to different packings of the experimental material.

A new modelling strategy was therefore devised in an attempt to model the variability experienced experimentally. Mercury intrusion curves corresponding to the most and least porous examples of the two sands were used as inputs to the network model. For each of these four simulations, twenty different stochastic generations were created. Modelling details are summarised below and unit cells corresponding to ten stochastic generations of the least porous Redhill 30 sample are given in the following figure.

Stochastic Generation	Throat Skew	Connectivity	Pore Skew	Permeability, Darcies
1	0.07	3.3	-	9.46
2	0.08	3.2	-	7.68
3	-0.05	3.0	-	4.32
4	0.09	3.1	-	10.81
5	0.45	3.9	-	14.24
6	0.09	3.3	-	6.62
7	0.30	3.6	-	6.28
8	-0.03	3.2	-	8.37
9	-0.03	3.0	-	10.56
10	0.04	3.1	-	10.51
11	0.15	3.3	-	6.68
12	0.33	3.5	-	19.01
13	0.01	3.1	-	7.01
14	0.15	3.4	-	10.37
15	-0.11	3.0	-	8.38
16	-0.03	3.0	-	6.17
17	0.20	3.4	-	11.13
18	-0.06	3.1	-	9.48
19	0.38	3.7	-	10.85
20	0.14	3.3	-	8.05
			Average	9.30

Table 6.3 Modelling details for Redhill 30 sand, porosity = 38.82%.

Stochastic Generation	Throat Skew	Connectivity	Pore Skew	Permeability, Darcies
1	0.17	3.3	-	7.25
2	0.08	3.2	-	7.99
3	0.52	3.8	-	15.97
4	-0.02	3.1	-	13.67
5	0.55	3.9	-	11.56
6	0.09	3.3	-	7.22
7	0.39	3.7	-	5.60
8	0.07	3.2	-	6.86
9	-0.03	3.0	--	11.892
10	0.04	3.1	-	11.94
11	0.05	3.1	-	11.45
12	0.32	3.5	-	22.59
13	-0.20	2.9	-	7.43
14	0.55	3.9	-	7.07
15	-0.12	3.0	-	9.02
16	0.06	3.2	-	13.02
17	0.19	3.3	-	9.42
18	0.33	3.5	-	20.80
19	0.38	3.7	-	11.94
20	0.50	3.8	-	17.32
			Average	11.50

Table 6.4 Modelling details for Redhill 30 sand, porosity = 41.98%.

Stochastic Generation	Throat Skew	Connectivity	Pore Skew	Permeability, Darcies
1	0.64	3.3	1.2	1.15
2	0.49	3.2	1.2	1.90
3	0.95	3.8	1.2	4.07
4	0.72	3.2	1.2	2.18
5	0.53	3.2	1.2	2.05
6	0.60	3.2	1.2	1.22
7	0.96	3.8	1.2	1.58
8	0.29	3.1	1.1	1.40
9	0.58	3.3	1.1	2.01
10	0.66	3.2	1.2	1.72
11	0.44	3.0	1.2	3.27
12	0.64	3.3	1.2	2.44
13	0.42	2.9	1.2	1.11
14	0.73	3.6	1.1	3.30
15	0.42	3.0	1.1	1.93
16	0.62	3.2	1.2	2.01
17	0.72	3.3	1.2	2.24
18	0.72	3.3	1.2	2.19
19	0.85	3.7	1.2	2.46
20	0.62	3.3	1.2	1.39
			Average	2.08

Table 6.5 Modelling details for Redhill 65 sand, porosity = 39.65%.

Stochastic Generation	Throat Skew	Connectivity	Pore Skew	Permeability, Darcies
1	0.59	3.3	1.3	1.77
2	0.53	3.2	1.3	2.10
3	0.50	3.0	1.3	1.63
4	0.67	3.2	1.3	3.40
5	0.98	3.9	1.4	2.92
6	0.64	3.4	1.3	2.09
7	0.90	3.8	1.3	2.70
8	0.53	3.2	1.3	1.68
9	0.52	3.3	1.2	3.35
10	0.60	3.1	1.3	2.72
11	0.58	3.1	1.3	2.31
12	0.59	3.3	1.3	3.56
13	0.37	2.9	1.3	1.70
14	0.67	3.4	1.3	2.48
15	0.36	3.0	1.2	3.03
16	0.57	3.2	1.3	4.00
17	0.67	3.3	1.3	4.11
18	0.68	3.3	1.3	3.71
19	0.89	3.7	1.3	2.86
20	0.57	3.3	1.3	2.06
			Average	2.71

Table 6.6 Modelling details for Redhill 65 sand, porosity = 45.66%.
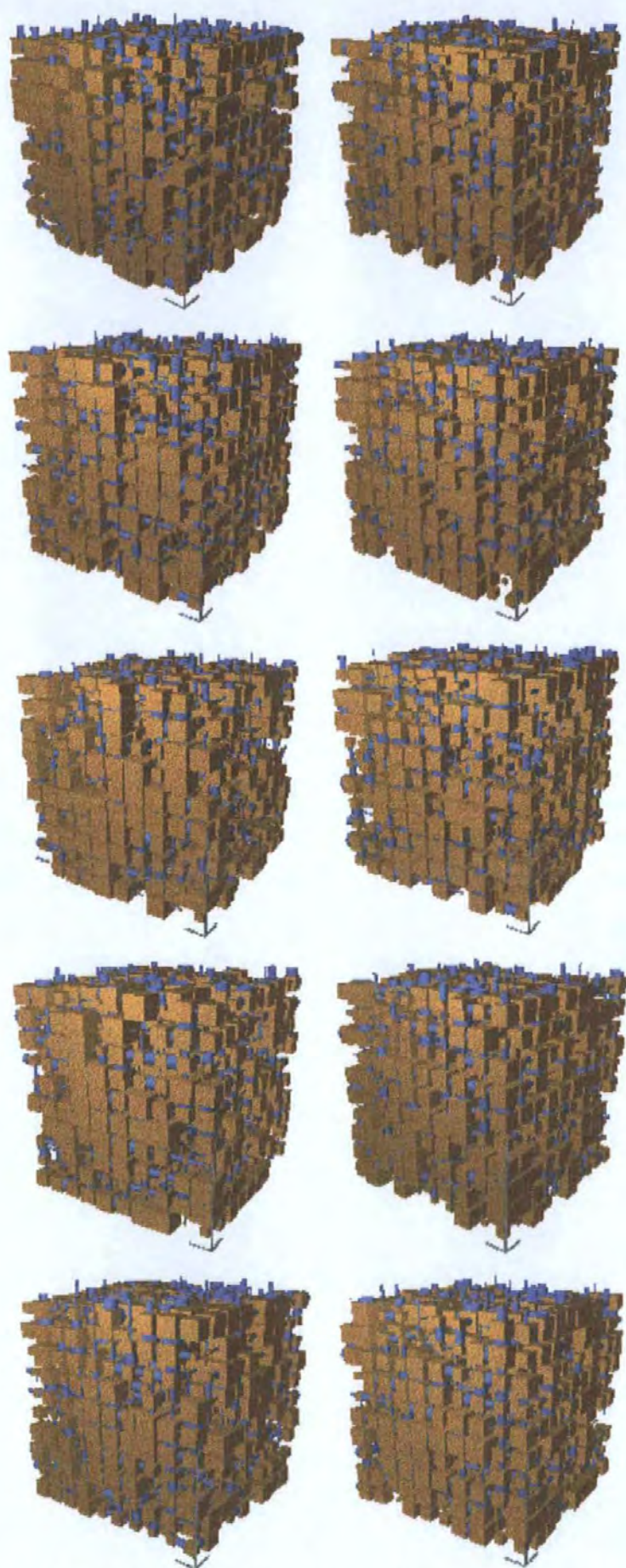
Figure 6.3 Unit cells of ten stochastic generations of the least porous Redhill 30 simulation.

6.3.1 Porosity

Porosity is one of the constraints employed in the modelling process. As such modelled porosities reflect experimental porosities extremely accurately.

6.3.2 Permeability

The stochastic modelling process generated a range of permeabilities. Figure 6.4 compares average experimental permeabilities to average modelled permeabilities. Error bars show ± one standard deviation.

◆ Redhill 30 - Experimental   ◇ Redhill 65 - Experimental
▲ Redhill 30 - Modelled (Minimum Porosity)   □ Redhill 65 - Modelled (Minimum Porosity)
■ Redhill 30 - Modelled (Maximum Porosity)   △ Redhill 65 - Modelled (Maximum Porosity)
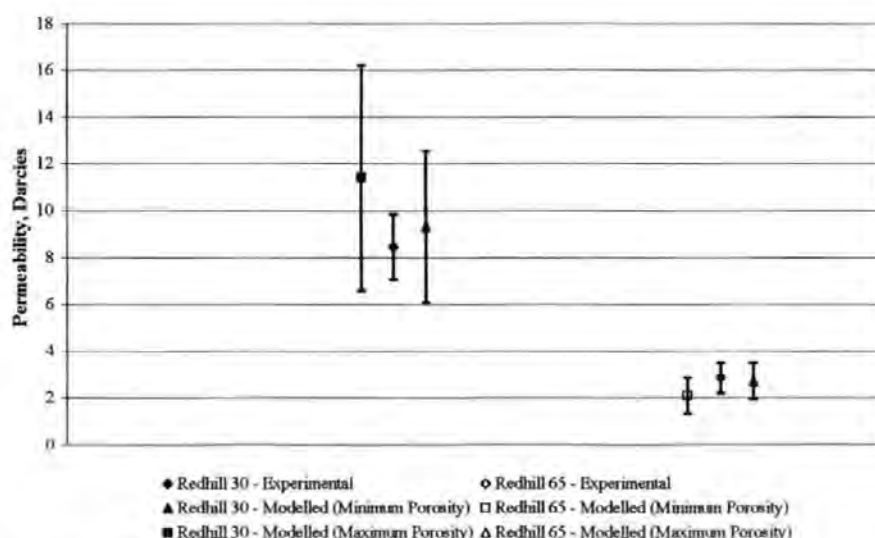
Figure 6.4 Experimental and modelled permeabilities for Redhill sands.

From Figure 6.4 it can be seen that the modelled permeability ranges generally represent the experimental values extremely well, especially considering the accepted difficulties in modelling permeability experienced by other network models (Chapter 2). In particular, the simulations of the less permeable Redhill 65 are very close to the measured values, both in terms of average permeability and range. It should be noted again that there are no calibration factors in these calculations whatsoever.

Ideally some statistical comparison should be made between the experimental and modelled permeability distributions. This was not possible in this study as it was not possible to take enough experimental measures of permeability that a statistical test would be reliable.

6.3.3 Unsaturated Permeability

The measurements in the previous section represent the saturated permeabilities of the modelled sands, being based on the entire available void network. However, unsaturated permeabilities are more relevant to the studies carried out here. Although direct estimation of the unsaturated permeabilities of the samples studied was not possible, some idea of expected experimental permeability decline with decreasing water content can be gained from previous studies (Figure 6.2).

The network model around which this work is based features no facility for the direct estimation of unsaturated permeability. However, it does include an analogous simulation, adapted here to estimate unsaturated permeability. An air intrusion algorithm exists, for modelling the effects of invasion of a simulated sample through one surface by air. In terms of the experiments conducted here, the saturated samples were allowed to drain while air intruded via the top surface, so this model is highly appropriate. The simulation of unsaturated permeability was achieved as follows.

Air was considered to be entering the unit cell through the top layer of the unit cell. Features larger than a user-specified minimum size became filled with air and blocked. Modelled air was able to move through the unit cell until it encountered a feature smaller than the minimum size. Large features near the top surface of the unit cell remain saturated if features smaller than the minimum size shield them. It was possible to incrementally decrease the size of the minimum feature until the new porosity of the unit cell was similar to the water-filled porosity of the experimental sample. Having achieved a new modelled porosity similar to the experimental volumetric water contents (unsaturated) permeability could be re-calculated.

| a) | b) |
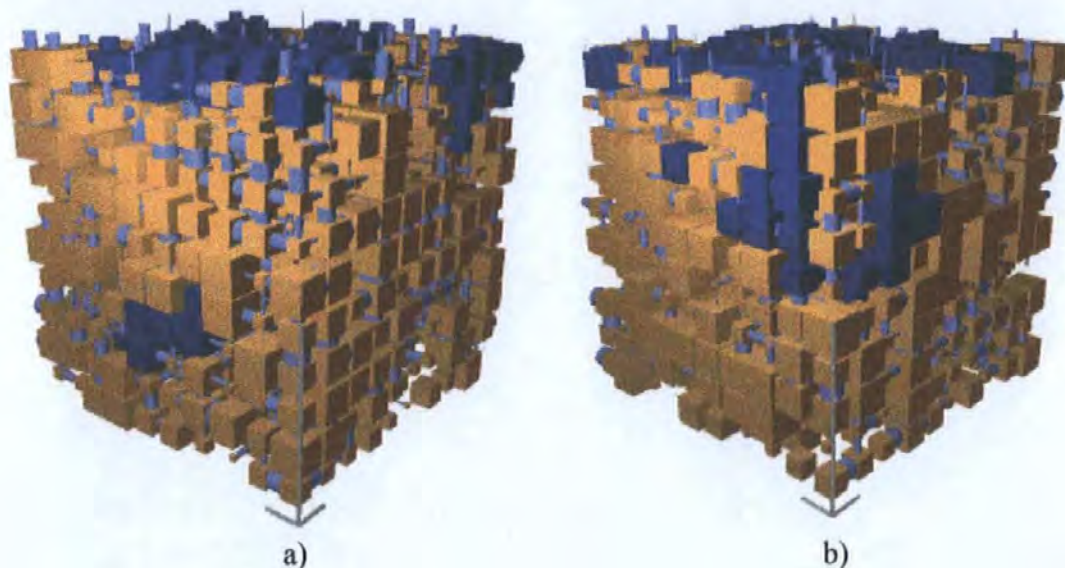
Figure 6.5 The unit cells of two stochastic generations of the least porous Redhill 30 sample. Features that have been intruded by air are shown as dark blue. The scale bars represent a) long - 2.46-mm, short - 0.49-mm and b) long - 2.40-mm, short - 0.48-mm.

Although the volumetric water contents of the experimental samples were known, further uncertainty arose from the range of porosities measured for each of the sands (Section 6.2.1). Thus, it was necessary to model a range of effective water-filled porosities reflecting the full range of water-filled porosities possible for the sand samples. Table 6.7 summarises measured volumetric water contents and ranges of experimental porosities for the 120-mm samples.

| | Volumetric Water Content, % | Porosity, % | |
		Minimum	Maximum
Redhill 30	30.96	38.82	41.98
Redhill 65	34.63	39.65	45.66

Table 6.7 Porosity ranges and water-filled porosities of the Redhill sands.

Clearly the water-filled porosities could account for quite different proportions of the total porosity, depending on the packing of the sands. Consequently a range of simulations were carried out using Pore-Cor, to represent the full range of experimental conditions.

Using the modelled parameters obtained previously (Section 6.3) the first ten stochastic generations of each of the samples were re-modelled to simulate air intrusion resulting in (approximately) the water-filled porosities given in Table 6.7. The experimental samples re-modelled corresponded to the mercury intrusion curves exhibiting the minimum and maximum porosity. The average modelled water-filled porosities and

saturated and unsaturated hydraulic conductivities are given in Table 6.8 and the following

figure shows all of the modelled results.

| Sample | Porosity, % | Water-Filled Porosity, % | | Permeability, Darcies | | |
		Experimental	Modelled	Initial	Final	Decrease, %
Redhill 30	38.82	33.70	33.38	8.89	2.40	73.0
	41.98		33.48	9.99	1.83	81.7
Redhill 65	39.65	35.10	35.03	1.93	0.55	71.5
	45.66		35.93	2.44	0.21	91.4

Table 6.8 Experimental and modelled water-filled porosities and permeabilities before and after simulation of air intrusion.

a)

b)
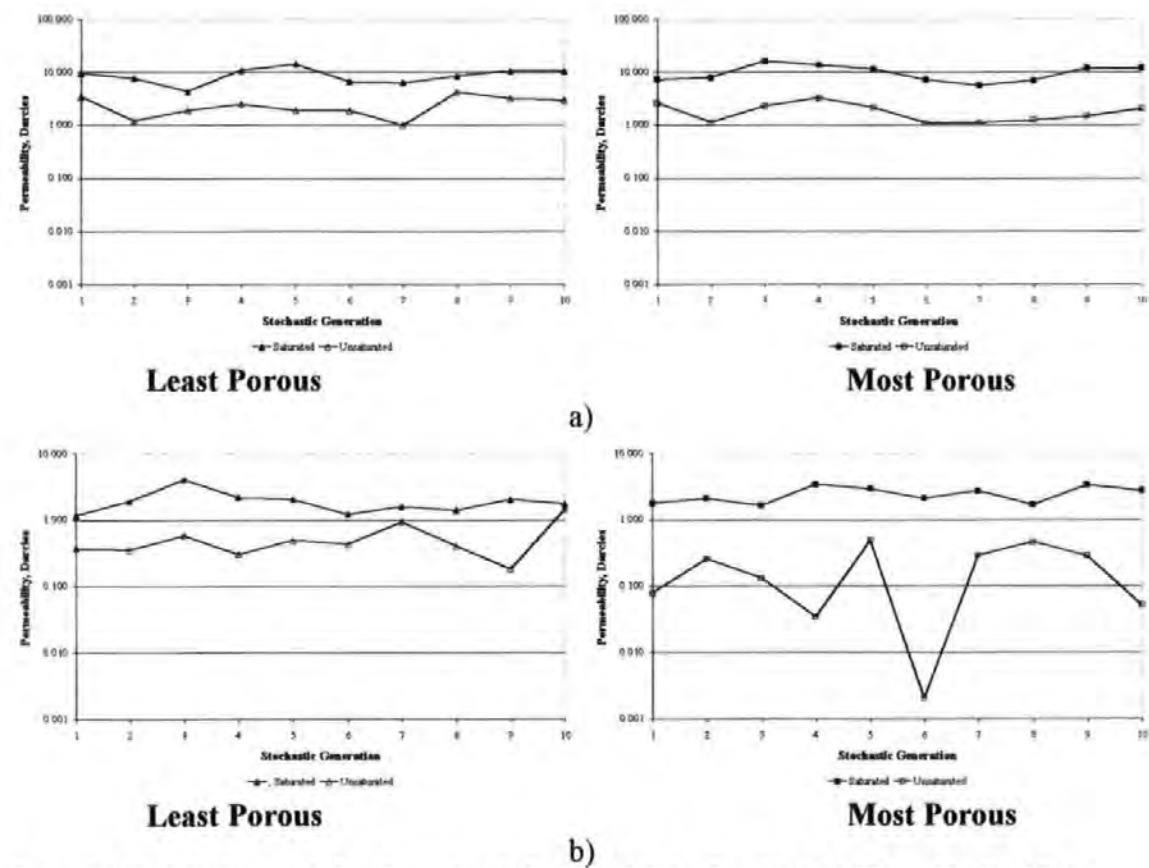
Figure 6.6 Modelled saturated and unsaturated permeabilities for a) Redhill 30 and b) Redhill 65 sands.

From Table 6.8 it can be seen that modelled unsaturated permeability was in the range 9-29% of the saturated values, with the greatest decreases seen in the higher porosity samples. It can also be seen that, on the logarithmic scales usually used to compare permeabilities, unsaturated permeability tends to track with saturated permeability. The exception to this is the most porous Redhill 65, although only one point on the unsaturated permeability line appears to deviate from this trend. The differences between saturated and unsaturated volumetric water contents were between 5-8%. The permeability results agreed with the predictions, based on previous studies of a permeability decline, of around one order of magnitude decrease in permeability for a 10% drop in water content (Figure 6.2).

6.4 Discussion

Significant insight has been gained into the nature of local random variability within homogeneous sand columns. It was demonstrated that the network model Pore-Cor, given adequate input data, is capable of realistically modelling the extensive local variability observed experimentally within apparently homogeneous sand samples. The usefulness of these insights in enhancing the modelling of porous materials is considered here.

6.4.1 Flow

The flow patterns through random packings of sands observed in Chapter 4 were neither random nor reproducible. They appeared to develop as a result of immeasurable microscopic changes in structure and/or saturation and were unaffected by differences in sample depth or permeability. It is likely that the variability observed in the permeability and porosity of different random packings of the same material was, at the very least, partly responsible for the development of flow within experimental samples.

Similar variability was observed in the modelled values of permeability to that observed in the experimental measurements. This suggests that the network model may be capable of generating estimations of flow distributions similar to those observed in Chapter 4. Given the small size of the unit cell, this is not directly possible at present. However, a possible method by which this might be achieved would be the construction of composite simulations, based upon unit cells from a number of different stochastic generations of a

modelled material. Additionally, different stochastic generations of these composite simulations could also be generated. Were this possible, the composite simulations would possess randomly positioned regions with different porosity and permeability characteristics. It would then be possible to model the development of flow through simulated samples, and to compare these with experimental samples.

6.4.2 Bulk Solute Transport

The variability of porosity and permeability demonstrated here must be, at least partially, responsible for the limited success of the convection-dispersion equation tested in the previous chapter. Solute transport will be greatly influenced by variability in unsaturated permeabilities within the experimental samples. Here this variability is assumed to be similar to that observed in measured saturated permeabilities. The network model has been shown to be capable of modelling ranges of unsaturated permeability that, as far as they could be tested here, are realistic.

One method of testing whether the ranges of modelled unsaturated permeabilities could enhance the predictions of the convection-dispersion equation would be to use them to generate a range of inputs to the model, then to analyse whether this enhanced model calibrations and/or predictions. The model parameter most closely related to sample permeability is, v, the pore water velocity. It is not possible to directly calculate values of v from modelled unsaturated permeability, however, it is possible to generate a range of values of v that are in some way similar to those of the modelled unsaturated permeabilities.

This was tested by generating a random set of (20) values of v, with an average similar to that of the experimentally measured value and relative standard deviation (ratio of sample standard deviation to sample mean) similar to that of the modelled unsaturated permeability values. This set of random values of was then used to generate a suite of modelled breakthrough curves, which in turn were averaged to produce one curve. The remaining model parameters, D and R, were then used to recalibrate this single curve to the experimental breakthrough curve of the 120-mm Redhill 30 sample and to predict transport

in the 240-mm sample. This was carried out using the modelled unsaturated permeabilities based on the least and most porous Redhill 30 sands. The results are summarised below.

Distribution	Average	Standard Deviation	Relative Standard Deviation, %
Modelled Unsaturated Permeability	1.83-2.40	0.74-1.02	40.3-42.5
Pore Water Velocity	0.462	0.198	42.8

Table 6.9 Details of modelled distributions.
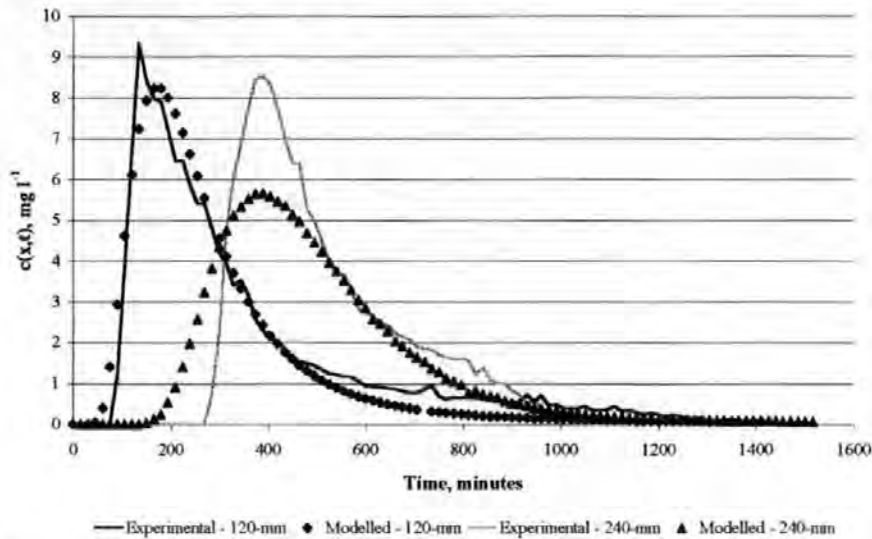
Figure 6.7 Experimental and re-modelled breakthrough curves for Redhill 30 sand.

	Goodness of Fit Figure		
Depth, mm	Original	New	Improvement, %
120	0.59×10^{-3}	0.30×10^{-3}	49.2
240	1.51×10^{-3}	1.16×10^{-3}	23.2

Table 6.10 Table of goodness of fit figures before and after re-modelling.

Comparing the new modelled breakthrough curves with those in Chapter 5, it can be seen that the fit of the calibration to the 120-mm sample was very much better than previously. The predicted transport to 240-mm was also considerably more accurate, although by a smaller margin of improvement than the calibration. It was also found that, by altering the goodness of fit criteria to give special weighting to the points of the solute peak, the appearance of the maximum concentration could also be modelled more accurately.

6.4.3 Lateral Solute Transport

The above approach represents the spatial averaging of a finite number of one-dimensional models of solute transport. As such there is no lateral component to transport,

and it could not be directly applied to the study of lateral transport from a point source, Chapter 4. The lateral solute transport observed experimentally must be represented in two or three dimensions, because there is movement in all directions on the plane perpendicular to vertical in addition to the vertical transport. The modelling of such a phenomenon would correspondingly require the extension of the conceptual basis of the model into two, if not three, dimensions.

The method described previously used stochastic generations of a network model to estimate a range of pore water velocities with which to model solute transport. Essentially the network model was used to provide the convection-dispersion equation with supplementary information about the convective component of the experimental solute transport. Were lateral solute transport to be modelled, information regarding the horizontal component to solute movement would be required. An element of this, at least, must be dependent on diffusive processes and this might be where network modelling could provide supplementary information. The following figure summarises the increase in complexity engendered in moving from one- to three-dimensional transport, and a possible method by which the more complicated situation could be investigated.

One-Dimensional Solute Transport

1 Stochastic 'dimension'

$+$ ↓ **1 Experimental Dimension**

Three-Dimensional Solute Transport

1 Stochastic 'dimension'

· · · · · ·

OR

1 Stochastic 'dimension'

$+$ **3 'Quasi' Experimental Dimensions**

· · · · · ·
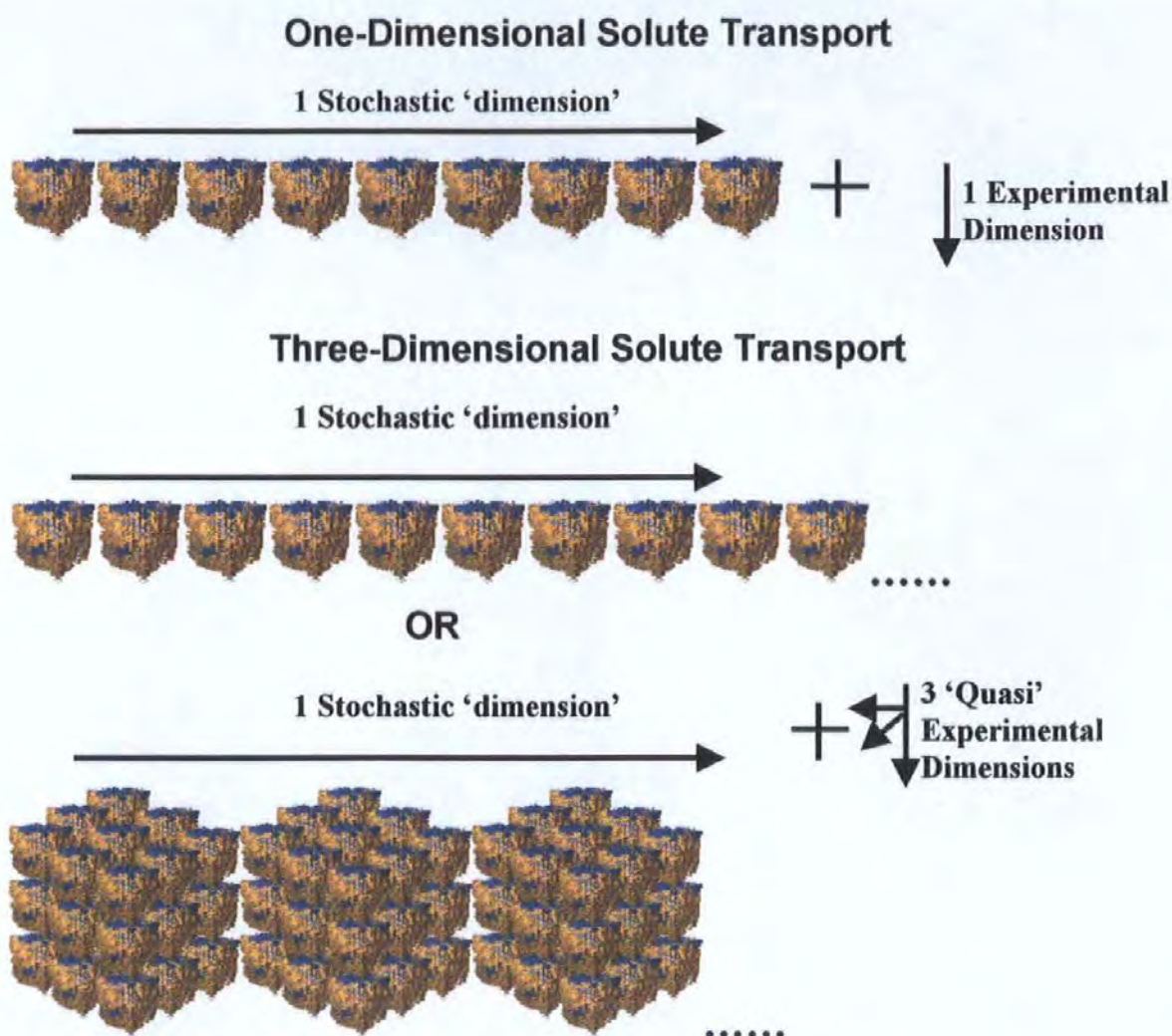
Figure 6.8 Modelling of one- and 'quasi' three-dimensional solute transport.

The network model employed here has previously been used to simulate diffusion in sandstones (Matthews, G. P. and Spearing, M. C., 1992) using a random walk based method. This could potentially be adapted to predict the diffusive properties of unreactive solutes moving through partially saturated porous materials, such as those modelled here. As implied by the above figure, this could be attempted in one of two ways. Diffusion of solute molecules entering through the centre of the top surface of a unit cell could initially be modelled over a number of stochastic generations to identify the small-scale spread to the whole range of base exit throats of the same unit cell. However, it might be envisaged that the usefulness of predictions based on such a limited length scale would be limited. Alternatively a repeating 'clone' unit cell configuration could be employed, where the progress of solute applied to the top of a central unit cell could be monitored over more extensive distances. Again, this latter approach might benefit from the construction of composite simulations, based on different stochastic generations of the modelled material.

Ultimately both approaches would need to be tested and compared against experimental results and their usefulness evaluated.

6.5 Conclusions

The work presented in this and previous chapters has gone some way towards identifying how network models can enhance the understanding and simulation of flow and transport behaviour of homogeneous porous media. Experimental work carried out to characterise the flow behaviour of two sands has demonstrated that flow does not develop in a way that is readily predictable. This unpredictability may result from random variations in packing that give rise to large differences in certain important properties of these materials. It has been demonstrated that similar variability can be reproduced in network simulations of the experimental materials. Although the network model employed cannot predict the development of flow paths in its present form, it clearly possesses the potential to do so, and a possible method of achieving this has been suggested.

The convection-dispersion equation used to model the experimental results obtained in Chapter 4 was only able to reproduce gross features of the experimental tracer transport. However, the work carried out here has gone some way towards identifying possible sources of inconsistency between the simple solute transport model and experimental results. In this chapter it has been shown that a stochastic-deterministic approach may be applied to this problem, utilising network simulations of the porous materials studied experimentally. These simulations allow the prediction of certain sample characteristics that may be used to enhance the predictions of transport behaviour. A speculative method for predicting solute transport from a point source has also been proposed.

7 Void Size Correlation in Inhomogeneous Porous Media

7.1 Introduction

As discussed in Chapter 1, correlations in the spatial distributions of differently sized voids within porous materials can have a marked effect on permeability. In the previous chapter it was demonstrated that random differences in packing of the solid phase, and therefore the spatial arrangement of the void phase, at this scale may greatly affect porosity and permeability. Correlation of these physical arrangements may, in turn, have a pronounced effect on the bulk characteristics of porous materials. Models of porous media that aim to predict the transport properties of such materials may be improved, in terms of accuracy, if some measure of correlation is available. In this chapter the development of such a method, based on variogram surfaces derived from image analysis of sections, is described, and the means by which it might be employed to enhance the simulations of a network model discussed. Although the method described below was developed to quantify levels of correlation in the spatial distribution of differently sized voids at the microscopic level, it could easily be adapted to any length scale.

The primary requirement of any method developed to examine levels of correlation in void size distribution is some way of accurately determining the sizes and positions of voids within real porous samples. Ideally these spatial distributions would be determined in three dimensions. Other workers have used sophisticated microtomographic methods to generate reconstructions of the entire void phase of certain porous media (Spanne, P. et al., 1994; Anderson, P. et al., 1994), although these do retain certain limits in terms of resolution. However, the equipment required for such determinations is expensive and not widely available. A more readily available technique for acquiring such information is the image analysis of two-dimensional representations of the void phase. Methods exist for interpolating between serial sections, thus allowing a three-dimensional reconstruction of the void phase (Lymberopoulos, D. P. and Payatakes, A. C., 1992; Yanuka, M. et al., 1984). However, the resolution of such methods is limited by the minimum distance between sections, about 7-μm., which limits their usefulness at the scales of interest here. In this study details of the distributions of voids within porous samples were obtained by

image analysis of sections taken through various samples. The primary requirement of such a method was to obtain images of the porous materials in which the solid phase and void spaces were unambiguously identified, and in which their precise sizes and positions were revealed. Other issues concerning this process are discussed in the following sections.

7.1.1 Image Analysis of Sections

In image analysis, once the void space has been identified as a two-dimensional array of irregularly shaped features, various geometrical analyses may be carried out. A standard procedure, used in this work, is to assume that the position of each feature is its centroid (i.e. the centre of gravity of a uniformly thin sheet of the same shape). The image analyser also measures *ferets*, a feret being the spacing between parallel tangents to a void feature in a given direction, Figure 7.1. The length of the void is the maximum feret, and was used as a measure of pore diameter by Ruzyla (1986), and Dullien and Dhawan (1975). The breadth of a void is either defined as the shortest feret or the feret perpendicular to the longest feret. Lymberopoulos and Payatakes (1992) defined the pore section diameter as the diameter of a circle of area equal to that of the cross section of the pore, and used this measure for the plots such as pore diameter versus neighbouring throat diameter mentioned earlier. Best et al. (1985), showed that void sizes in graphite, measured as area ÷ perimeter, overestimated the void size distribution compared to mercury porosimetry. This may be explained by the fact that mercury is a non-wetting fluid, and the extent of its intrusion when applied to a porous sample is therefore predominantly determined by the smallest width of the void feature normal to the direction of injection. Bouabid et al. (1992) used a multidirectional minimum chord method for the study of the void spaces within soils, and recommended that the smallest chord length of a feature be used as a measure of its effective capillary diameter with respect to water uptake in soils.
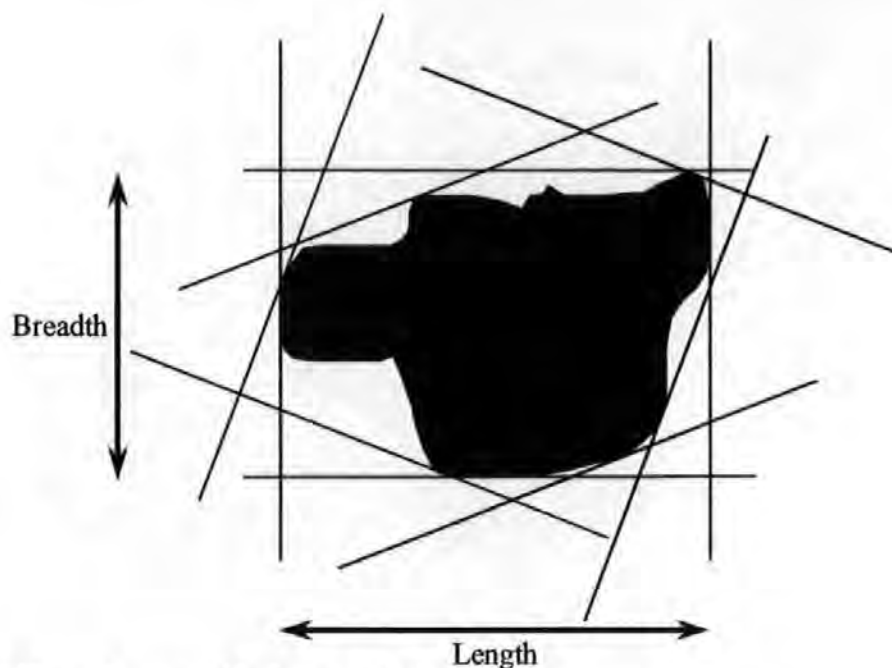
Figure 7.1 A 'feature' measured by image analysis.

Apart from simple measurements of features image analysis can also be used to manipulate images to obtain more detailed information. A process known as *erosion* removes a pixel width line from around each feature. As an image is eroded, each complicated void shape may split into a series of smaller, simpler shapes, which are individually identified. *Dilation* is the reverse of erosion, and is capable of re-growing each feature back to its original shape. However, the identification of each individual feature is retained, and a 1-pixel boundary is marked between each. The result of the overall erosion, identification and dilation process, collectively known as *segmentation*, is an image of the original void space in which complicated shapes are split into individual features, (Glasbey, C. A. and Horgan, G. W., 1995). Ehrlich and co-workers (1991) have characterised the shapes of pores by eroding them, re-dilating with no memory of the original shape, and plotting the rounding process as a histogram.

Thompson et al. (1992) state that any measurements of the two-dimensional image will only be representative of the three-dimensional sample if the sample is homogeneous in the z direction perpendicular to the xy plane of the cut. This statement is normally true - it is unlikely, for example, that one could generate an accurate three-dimensional reconstruction of a laminated sample merely on the basis of a randomly oriented two-

123

dimensional section. However, there are some rarer circumstances, exemplified by a three-dimensional regular chequer-board structure, where a two-dimensional image is representative of a non-homogeneous but isotropic sample, provided that the two-dimensional image is large enough to assure statistical homogeneity. Thompson et al. (1992) also discuss the other main problem of image analysis, which is that the resolution limit, in this case 512 x 512 pixels, cannot easily be overcome by integrating over different scales.

7.1.2 Remaining Problems In Image Analysis

Although there are well developed fundamental, experimental and image analysis methods for measuring void space correlation effects and their effect on fluid intrusion, three major problems remain. The first is the well-known problem of stereology. Suppose a sample comprised spherical pores embedded in a solid. A serial section through the solid would cut the spheres at different distances from their centre points, and in many instances only small chords would be cut by the section plane. Thus the image analyser detects a seemingly random mixture of large and small voids. This stereological effect is illustrated in Figure 7.2, in which the black circles show the full size of the spherical pores, and the grey inner portions show the areas revealed by slicing the pores at random vertical (z) distances from their centres. Correction methods are available for this simple case (Williams, M. A., 1977). However, if the sample comprised packed solid spheres with void space in between, the opposite would be true - serial sections would suggest unrealistically small regions of solid phase. For a natural sample, it is difficult to say which of these cases holds in practice, even if the sample nominally comprises lightly cemented spherical grains. What is clear, however, is that the image analysis of serial sections will incorporate a randomisation, akin to a signal noise, in the measurement of void size or particle size distributions.
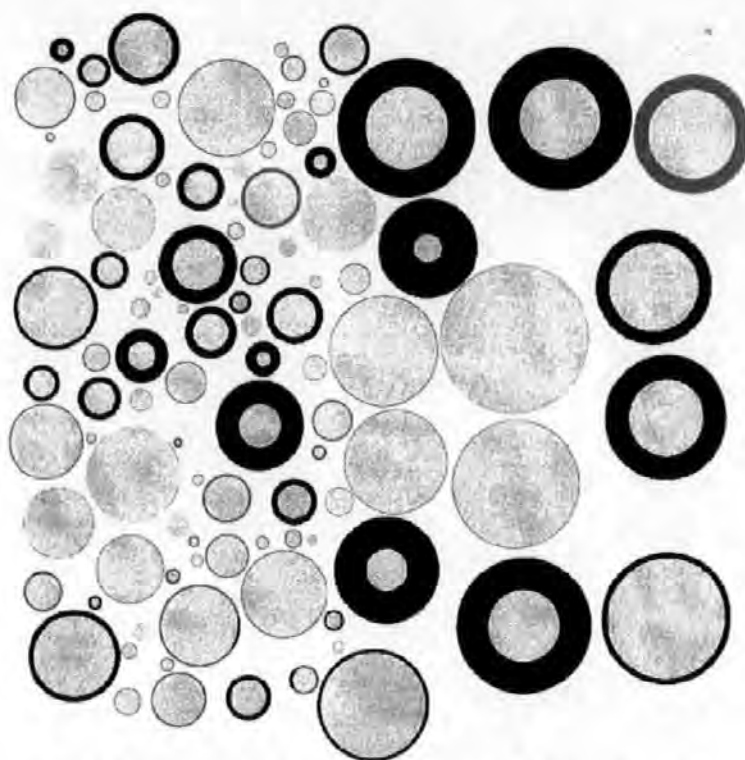
Figure 7.2 Representation of the computer generated 'laminated spheres' sample.

The second problem is that it is virtually impossible to make accurate measurements of connectivity by image analysis, because of the subjectivity of the algorithms, which must be used to interpolate between the serial sections, which are typically more than 5 μm apart. The accurate mapping of clean sandstone samples without the need for interpolation would require accurately located serial sections about 0.1 μm apart, and for reservoir sandstones with clay inclusions, the spacing would need to be 0.01 μm or less. If a sample is isotropic, the connectivity, which is observed within the plane of inspection, can be assumed to be equal to the overall connectivity of the sample, and measurement becomes theoretically possible. In practice, however, what is seen is an irregular array of voids of varying shapes and sizes, and there is no objective way of identifying which are throats, or of generating a three-dimensional throat network of the correct connectivity from the observed two-dimensional one. Slight changes in connectivity can have a huge effect on permeability (Matthews, G. P. et al., 1993), and one response to this problem has been to estimate connectivity (and pore and throat size distribution) from a fit to a carefully selected portion of the mercury intrusion curve (Matthews, G. P. et al., 1995).

The third problem is in measuring distance-related correlation effects such as lamination. Ringrose et al. (1992) address this problem for the case of permeability correlations on a larger scale than considered here, and generate variogram functions for mixed sine periodicities. Pore-Cor already obeys the adjacent pore : throat size correlation for sandstone measured by Wardlaw et al. (1987) when appropriate, and can mimic arbitrarily clustered and laminated samples (Matthews, G. P. et al., 1995). The purpose of this study is to add distance-related correlation effects to provide another source of data for the void-space model. The approach employed has been to measure, rather than generate, variogram functions. The procedure presented here uses an extension of standard sample preparation, electron microscopy, image analysis and variogram techniques, together with a newly developed spline smoothing technique.

7.2 Method

7.2.1 Samples

Three types of sample were analysed using this new combination of methods; computer generated artificial samples, an artificial 'real' sample of two sintered glass discs of markedly different pore size ranges and two types sandstone.

Two artificial samples were generated by computer of the same form as the image analyser output, that is, comprising the x and y co-ordinates and feature size of the 'voids'. The first of these was a straightforward random distribution of spherical pores, the second was a laminated sample comprising two regions of randomly distributed pores with greatly different mean radii. A diagrammatic representation of the second of the computer-generated samples is given in Figure 7.2.

The sintered glass disc samples were prepared by resin filling and joining two filter discs with two different pore size ranges, one containing pores in the range 16-40 μm the other in the range 100-160 μm. These samples were cut and polished perpendicular to the

join plane. The backscattered electron micrograph of a sintered glass disc sample is shown below.
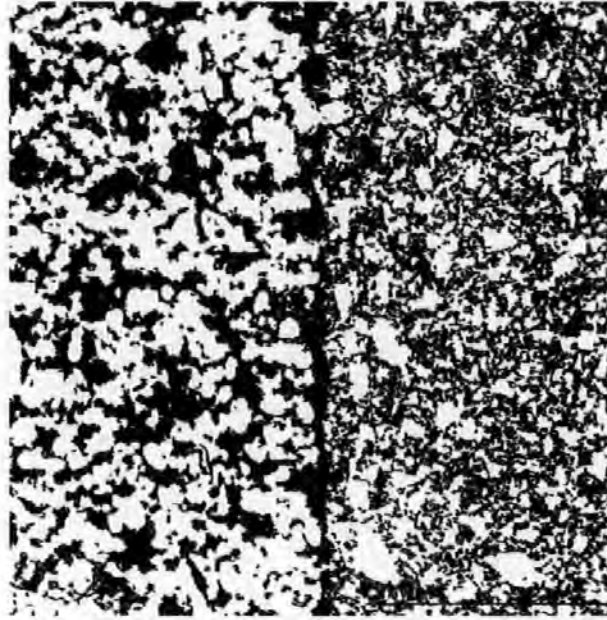
Figure 7.3 A backscattered electron micrograph of a sintered glass disc sample.

Two types of sandstone sample were prepared. Fontainebleau sandstone, chosen for its apparent mineralogical simplicity and structural homogeneity was prepared using the resin impregnation method, while another sandstone (a feldspathic litharenite from the Upper Vosgian Unit, France) was analysed using the simpler method due to its impermeability to resin. Sample micrographs of the two types are shown in Figure 7.4 and Figure 7.5.
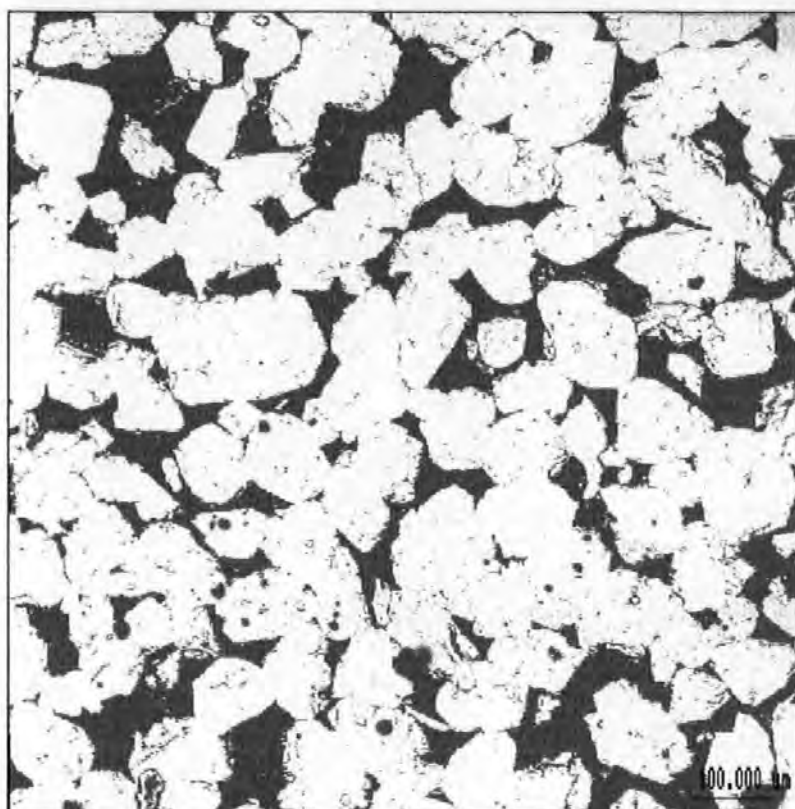
Figure 7.4 Electron micrograph of a resin-impregnated Fontainebleau sandstone sample.
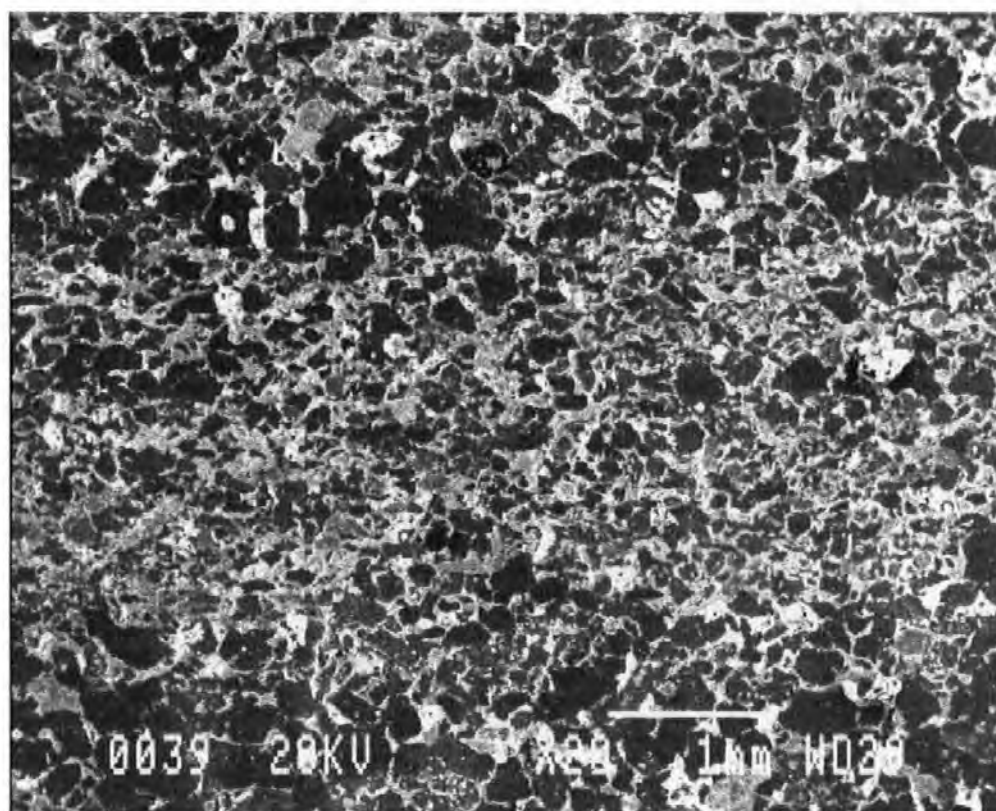
Figure 7.5 An electron micrograph of a feldspar sample.

Two methods of impregnation were attempted on this second sandstone, the epoxy resin method mentioned above and a more sophisticated crystic resin impregnation

(Belbin, S. P., 1994). Despite the latter method being carried out under vacuum and with various viscosities of resin neither method produced penetration of anything bar the very surface pores of the samples. This feldspar sample was chosen for its apparently highly correlated structure, visible to the naked eye as prominent lamina. Although clearly laminated it was not known at the outset whether this would translate into correlations in the void size distribution, or whether the visible layers were entirely mineralogical in nature.

7.2.2 Void Space Identification by Electron Microscopy/Image Analysis

During this study the unambiguous identification of void and solid phases was of paramount importance. Two techniques were developed to achieve this. The simpler, less efficient method merely involved taking electron micrographs of the cut and polished faces of the porous samples. By careful optimisation of the electron microscope (a Jeol 6100) settings micrographs of reasonably high contrast could be produced, but with a small degree of ambiguity in separating void from solid. The more sophisticated method involved forcing epoxy resin under pressure into the samples prior to image analysis. A cut and polished (using silicon carbide paste) face was then observed by backscattered electron microscopy, which unambiguously revealed the low molecular mass resin, and hence the original void space, as dark areas.

The correct identification of these dark areas by an image analyser (Quantimet 570) relied upon the correct adjustment of the analyser *threshold grey level* as described by Gong and Newton (1992). For the non-resin-saturated samples this involved a subjective analysis of which grey levels represented void and which represented solid phase. In the resin-saturated samples however, where solid-void/resin contrast was much greater than in the samples with no resin, the grey level peak was situated in the black void zone, and the threshold, which was now on the edge of the peak, could be chosen with only a small degree of likely error.

Both of the procedures described above produced two-dimensional images from a three-dimensional sample. Any measurements of a two-dimensional image will only be

representative of the three-dimensional sample if the sample is homogeneous in the 'z' direction perpendicular to the 'xy' plane of the cut (Thompson, M. L. et al., 1992). To avoid erroneous edge effects, an inner *guard frame* is defined within the image and only voids with a particular pixel inside the guard frame (e.g. bottom right-hand) are included in the analysis. Samples with wide void size distributions are difficult to analyse completely within one image because of the limit of digitised image resolution, in the present case 512 x 512 pixels. Unfortunately there is no easy way of integrating image analysis results from different scales (Thompson, M. L. et al., 1992).

The position of each feature in the present study was assumed to be the *centroid*. Initially many of the voids observed on an electron micrograph formed large, inter-connected regions rather than a larger number of distinct voids. Segmentation was used to identify individual features. Three erosions of each image were carried out.

(a)   (b)

(c)   (d)
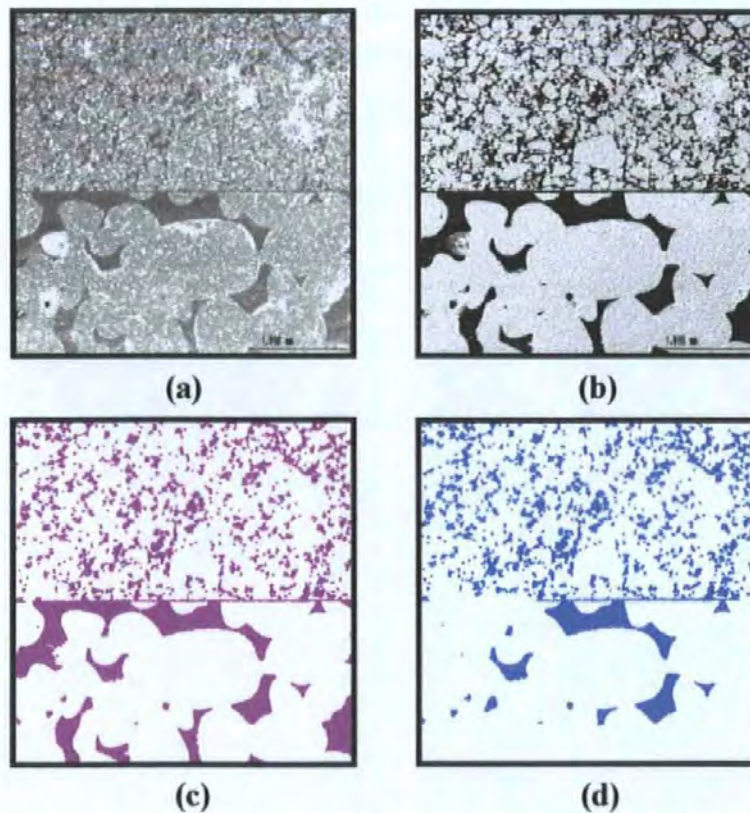
Figure 7.6 (a) Electron micrograph of sintered glass discs, (b) back-scattered electron-micrograph, (c) segmented image and (d) segmented image minus edge features.

Figure 7.6 shows the electron microscopy and image analysis of one of the sintered glass disc samples. The difference between Figure 7.6 a) and b) clearly demonstrates how resin impregnation in conjunction with the backscattered electron detector provides a more definitive representation of the sample porosity. Comparing Figure 7.6 b) and c) demonstrates the effect of segmentation of the image, while Figure 7.6 d) illustrates the removal of features overlapping the guard frame.

7.2.3 Measurement of Void Size Correlation Using Variograms

The most direct method of quantifying such correlation is to measure the breadth of each feature, and plot the difference between log (breadth) of a particular feature and log (breadth) of every other feature as a function of distance between the features. (Using a log scale identifies relative rather than absolute differences in breadth). In practice, this does not produce meaningful results. Even visually obvious correlations, such as can be seen in the micrographs of the glass discs, may be masked in straightforward correlation plots and this method has been shown to be of little use (Mathews, T. J. et al., 1997).

Four methods that can be used to produce meaningful results involve the use of semi-variograms, auto-correlation functions, Fourier transforms or wavelets. The first three methods all give mathematically analogous results. Wavelets provide a powerful means of investigating the structure, but suffer from the major disadvantage that a positional origin needs to be defined, thus introducing a major source of subjectivity when studying natural samples.

Semi-variograms, or variograms as they are generally described, were used to study pore size correlations in all the samples studied. Variograms are based upon regionalized variable theory (Knighton, R. E. and Wagenet, R. J., 1988). A regionalized variable is a continuously distributed variable with geographic variation too complex to represent with a mathematical function. Regionalized variable theory assumes that although samples located near one another may possess similar values, individual values cannot be predicted based on those close by. A regionalized variable is a function, $Z(x)$, that takes a value at every point in the space under consideration but cannot be directly described.

131

Semi-variance is a measure of the increment change in $Z(x)$ over a distance l. Semi-variance, $\gamma(l)$, is defined as (Journel, A. G. and Huijbregts, C. J, 1978),

$$\gamma(l) = \tfrac{1}{2} Var[Z(x_i) - Z(x_{i+l})] \qquad [1]$$

As the semi-variance is dependent on the value of Z at the positions x_i and x_{i+l} it is important that the value of Z is independent of the manner in which those positions are chosen.

A method was used here to calculate directional semi-variograms of the image analysed samples (Knighton, R. E. and Wagenet, R. J., 1988; Ringrose, P. S. et al., 1992). Variograms were used to examine how at different scales of observation pore sizes differ, that is whether at any scale the sizes of different pores were any more or less likely to be similar in size. Initially the study was carried out calculating variograms in one direction only (Mathews, T. J. et al., 1997). However, this was then extended to multiple directions to remove the subjective step of choosing a single search direction.

The variograms of the output from the image analysis was calculated using the public domain computer program GESS (Knighton, R. E. and Wagenet, R. J., 1988). As well as the sample data files the program also required various other parameters for the calculation of the variograms. The first of these were the number of *lags* and the *lag distance*. The number of lags determines the number of distance intervals over which semi-variance was calculated, and therefore the number of points on the semi-variogram. In most of the studies carried out here it was set to between 10-30. The lag distance, l, is the size of the distance intervals and was determined by dividing the maximum distance between two voids in a sample by the number of lags. Thus for the 'sample' shown in Figure 7.7 the maximum distance **d** could be divided into 15 lags, d_1, d_2, $d_3 \ldots d_{15}$, to give a lag distance of **d**/15.
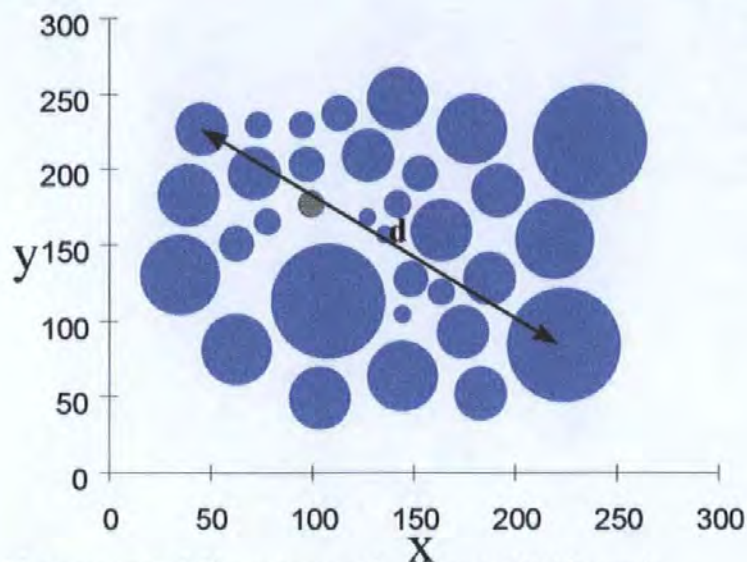
Figure 7.7 Measurement of d in a cross-section of an artificial sample.

The next parameter required by the program is the *search window*. This angle (in degrees) together with the lag distance defines an arc used to determine which pairs of features are compared when calculating semi-variance. The final parameter, *search direction*, is another angle, this one determining the orientation (measured from 'East', or parallel to the *x* axis, away from the *y* axis) of the arc.

An example is shown in Figure 7.8. Here the lag is d_1, search window is 90° and search direction is 0°. At each lag distance interval, l^j, the program places arcs on each feature in the sample and calculates the semi-variance between all pairs made up of the feature and any other centred within the arc. The semi-variance associated with each lag is the mean of all the semi-variances calculated in that lag, Equation 2.

$$\gamma(l) = \frac{1}{2n(l)} \sum_{i=1}^{n(l)} [Z(x_i) - Z(x_{i+1})]^2 \qquad [2]$$

$n(l)$ is the number of paired observations located at a lag distance, l, apart.

The variogram is a plot of each calculated value of semi-variance against weighted average of lag distance range, $< l^j >$. It should be noted that the semi-variances calculated were all based on different numbers of pairs of features, hence each point on the line was

133

of different statistical significance. This was taken into account when fitting the curves, Section 7.2.4.
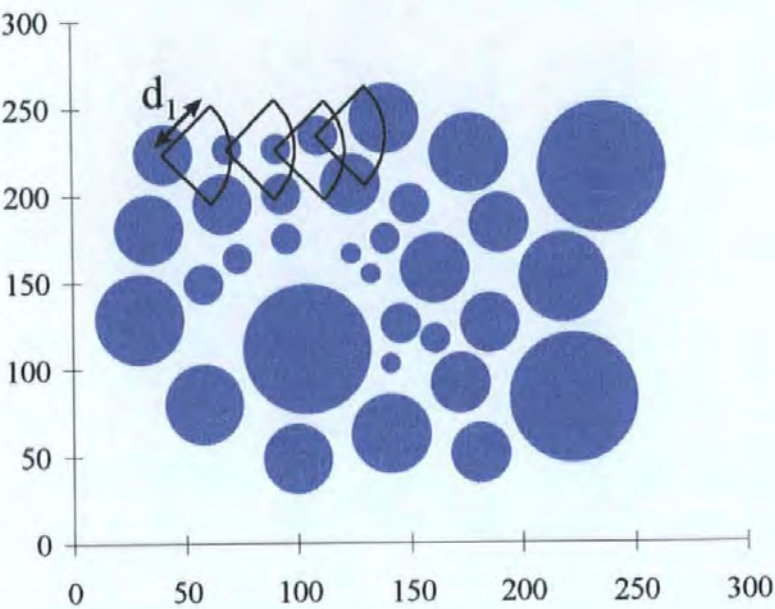
Figure 7.8 Calculation of semi-variance over the first lag, d_1.

A typical variogram is shown in Figure 7.9. It can be seen that initially as distance increases so does semi-variance, almost linearly, until it reaches some maximum where it then remains constant. Thus it can be seen that at small distances of observation the features are fairly similar, however as distance increases the features become increasingly independent until semi-variance is no longer a function of distance or direction. This plateau on the curve is described as a *sill*, the smallest distance separating statistically independent pairs is the *range* and the distance equal to this is known as the *zone of influence*.
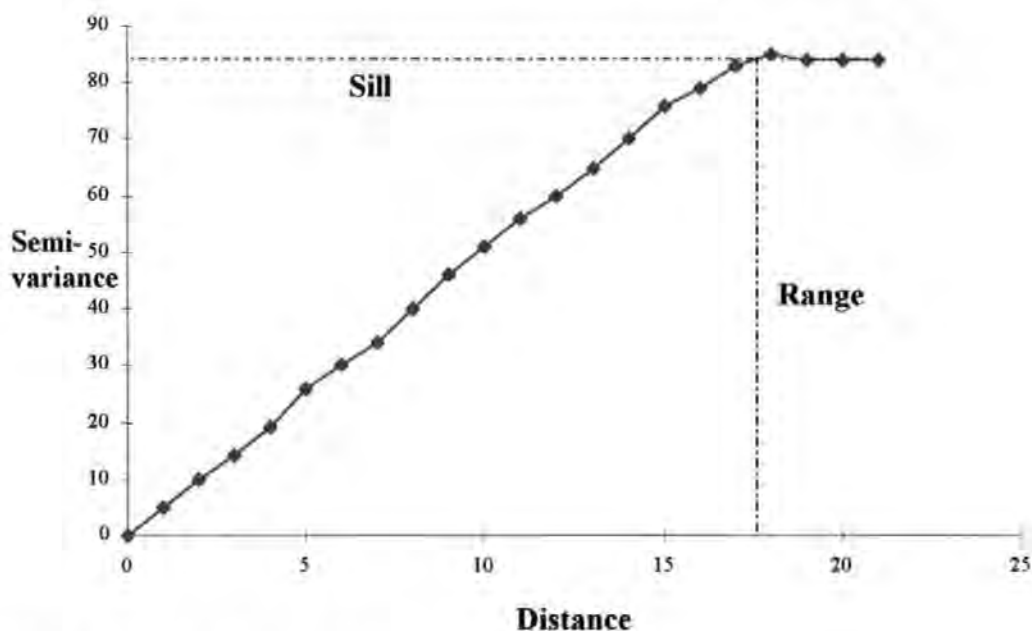
Figure 7.9 A typical semi variogram.

Initial studies focussed on taking a single variogram across a sample, typically with a search direction equivalent to 'North' on the micrograph, or alternatively with a search direction based upon the orientation of apparent correlations in the structure. Obviously the subjectivity of choosing a single search direction is not particularly desirable, hence, after preliminary studies (Mathews, T. J. et al., 1997), an alternative method was developed. This involved taking multiple variograms at $15°$ intervals over $180°$ and plotting the resultant variograms as a surface. This removed the subjectivity of choosing a search direction and also gave more detailed information about the presence of correlations in the distribution of differently sized voids.

Normally the variogram points are simply joined up to indicate the overall variogram shape as shown in Figure 7.9. However, many samples exhibit scatter in the values of semi-variance. The scatter may be caused by real correlation features, or random statistical variations, or stereological effects, or any combination of these effects. Reducing the size of each lag distance range increases the closeness and number of points in the variogram, but reduces the averaging within the range thus increasing the scatter. Therefore the variogram must be smoothed to reveal the features which are not due to random statistical effects. When carrying out this smoothing, additional information can be gleaned from the variogram by noting two points. Firstly, the variogram points are based on different

135

numbers of observations, and their corresponding statistical weights W typically range over between one and two orders of magnitude. Moreover, the statistical weighting tends to be greatest in the middle of the lag distance axis, with lower weighting as $<l^j> \to 0$ and/or $<l^j> \to l_{max}$. This precludes standard fitting procedures, such as polynomial fits, since these become unstable in the high and low $<l^j>$ regions, which are nevertheless important in determining correlation within the sample. Secondly, in a typical natural sample, high lag distance ranges involve a larger inspection area, which is therefore likely to be a more highly averaged observation. Both of these features can be taken into account by fitting a suitably designed cubic spline regression curve.

7.2.4 Curve Fitting

The cubic spline smoothing curve was designed on the basis of the following assumptions:

(i) The minimum investigation distance was limited by the fact that the digitised image was in the form of pixels. Because of this resolution cut-off, it is reasonable to assume that the variogram and its first derivative should both tend to zero as $<l^j> \to 0$.

(ii) It was assumed that the magnification level had been chosen such that the larger l values were greater than the correlation distances of interest, i.e. greater than those distances corresponding to features affecting fluid migration characteristics on a plug scale. It then follows that the variogram of the properties of interest can be assumed to tend to a constant value, and its first derivative to zero, as l becomes large.

(iii) As l increases, the radius of investigation increases, and so do the chances of features being masked by other property values Z. Hence the flexibility of the variogram curve decreases with l.

These three conditions are independent of the fractal nature of the sample, which is masked by the resolution lower limit and the investigation area upper limit. Obviously the

resolution could easily be improved by increasing the magnification, but this might then invalidate assumption (ii) above.

Two best fit spline algorithms, a cubic spline for fitting lines (NAG library E02BAF) and a bicubic spline for fitting surfaces (NAG library E02DAF) were used, accounting for both the statistical weights and the three characteristics listed above. A fuller explanation of best fit splines is given elsewhere (Mathews, T. J. et al., 1997).

7.3 Results

7.3.1 Computer Generated Samples

Any variogram smoothing procedure is only worthwhile if it is stable to stereological interference. The stability of the method described here was tested using the samples described previously.

■ Unfragmented random circles	—— Spline of unfragmented random circles
● Fragmented random circles	—— Spline of fragmented random circles
▲ Unfragmented banded circles	—— Spline of unfragmented banded circles
◆ Fragmented banded circles	- - - Spline of fragmented banded circles
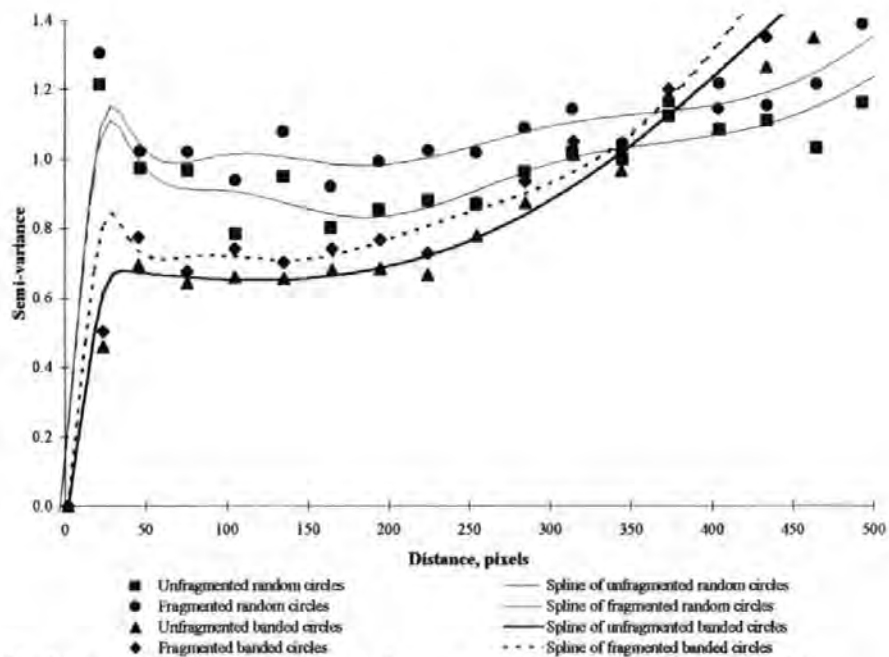
Figure 7.10 Variogram of computer generated structures showing statistical weights.

Figure 7.10 shows the variograms of two of the computer-generated samples, namely the random spherical pores, and the laminated spherical pores of Figure 7.2. Also shown in Figure 7.2 are the sizes of the circular sections through the spheres, assuming that the sectioning has occurred a random distance from the centre of each sphere. The corresponding variograms of the unfragmented and fragmented pores are also shown in

137

Figure 7.10. Also shown in the figure are the cubic spline curves through the structures. It should be remembered that the statistical weights of the points vary widely, and affect the fitting of the spline curves shown in this and other figures. It can be seen that the pairs of spline curves have similar shapes. The lamination of second computer generated sample is still evident in the spline of the fragmented sample, but it is rather more difficult to identify, and the apparent inter-lamina distance decreases.

7.3.2 Sintered Glass Discs

As explained in Section 7.1.2 stereological interference in a natural sample will be more random than applied in Figure 7.10. Random positive and negative signals were therefore applied to the void size measurements before formation into variograms. The ranges were $\leq \pm 10\%$ of the measurement, $\leq \pm 20\%$ and $\leq \pm 50\%$. This stereological noise had the effect of increasing the semi-variance values. The effects on sample 3, the glass disc sample shown in Figure 7.3, is shown in Figure 7.11. It can be seen that the lamination is clearly indicated by all the spline curves regardless of stereological noise level.
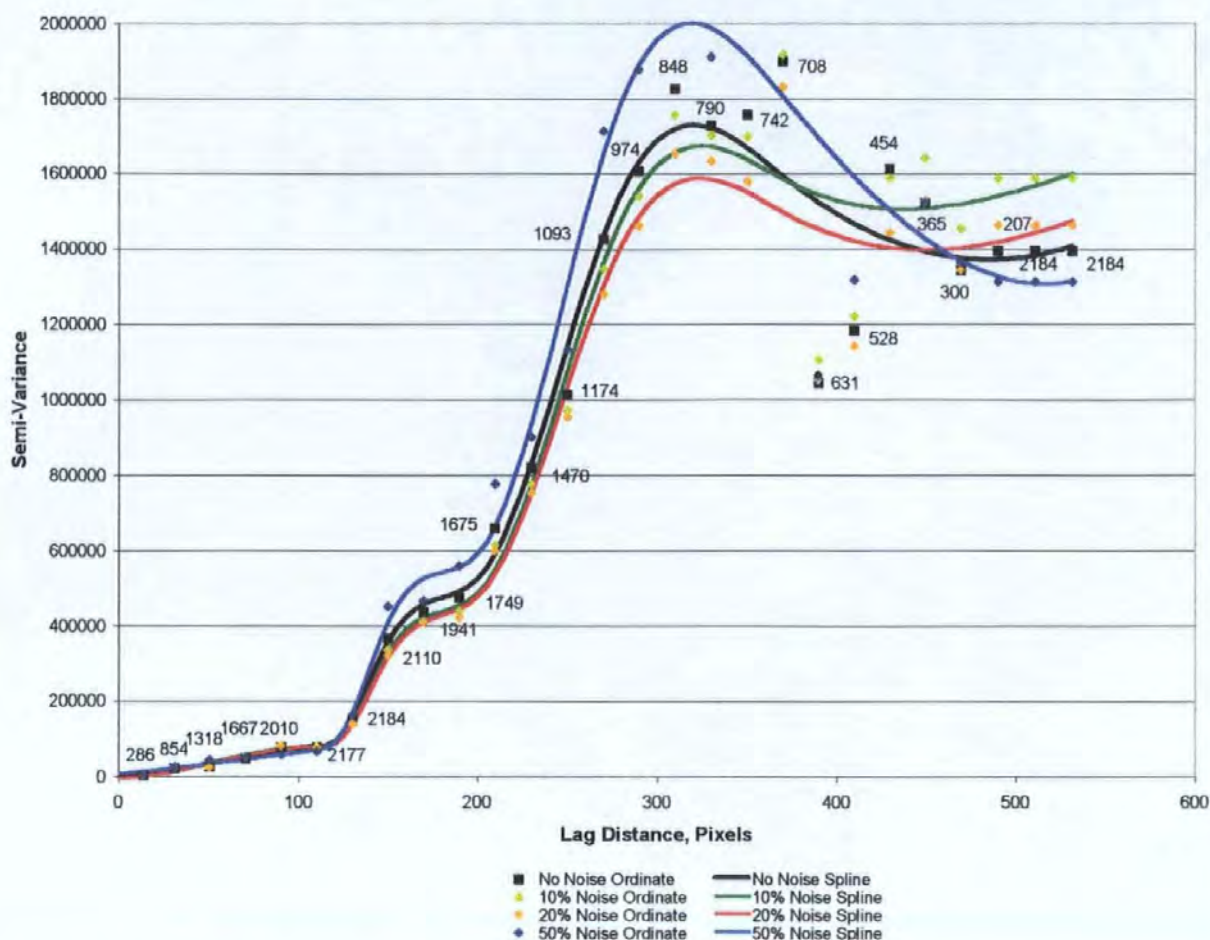
Figure 7.11 Variograms of the sintered glass disc sample showing statistical weights.

Following the original work constructing the two-dimensional variograms, exemplified by Figure 7.10 and Figure 7.11, the glass disc samples were later re-analysed using the new technique for looking at variogram surfaces. The variograms produced for the sample tested previously by the simpler method are given below.

a)

139
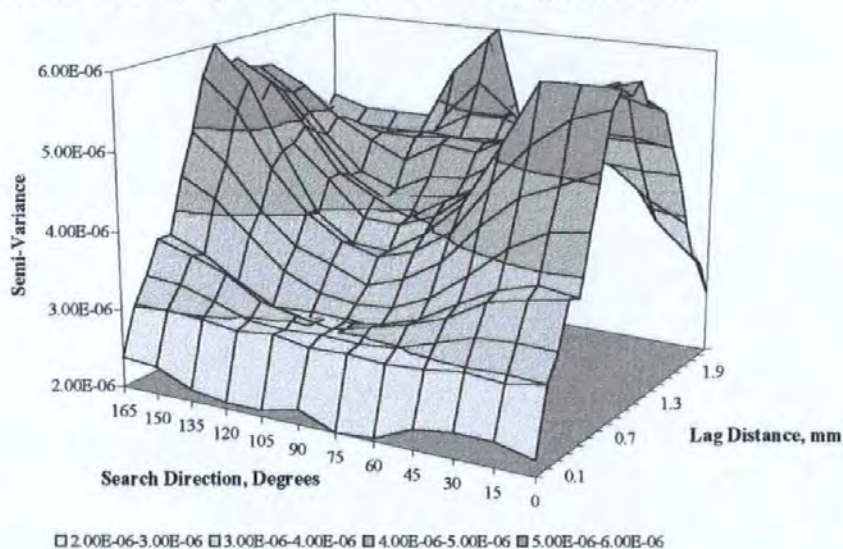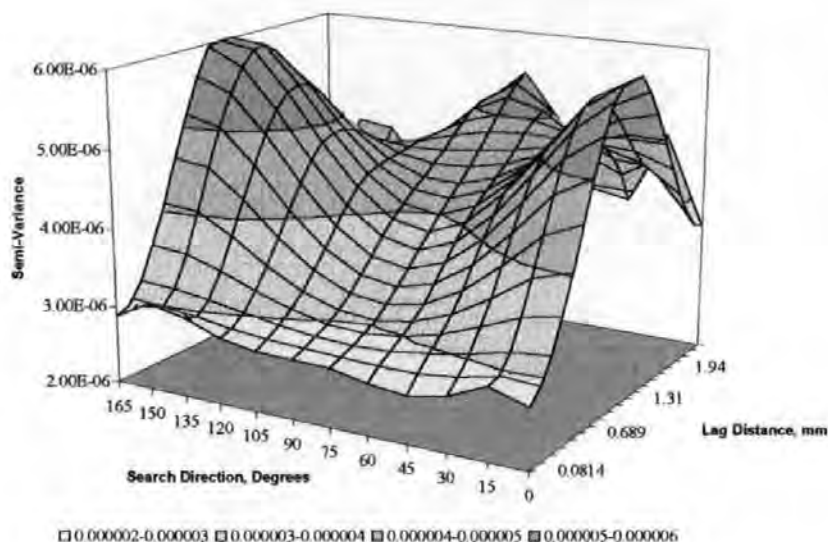
Figure 7.12 a) Variogram surface and b) bicubic spline fitted variogram surface for sintered glass disc sample.

Clearly the more sophisticated technique yields more information regarding correlations in the distribution of void sizes. From Figure 7.12 it can be seen that at search directions of around 0-15° and 150-165° there is a sudden increase in the semi-variance that starts at a distance of around 0.5 mm with a maximum at around 1 mm. Between search directions of 15-75° and 150-90° the steep gradient between 0.5 - 1 mm gradually becomes much shallower until, for search directions between 75-90° the increase in semi-variance is much more gradual, with little change in rate.

Comparing this information with the original micrograph it can be seen that the variogram gives a clear representation of the two vertical lamina. These lamina lie perpendicular to the search direction of roughly 0/180° and are approximately half the image width thick (about 1 mm each).

7.3.3 Sandstone Samples

The void space within sandstones is of greater complexity than that of the sintered glass model, and any correlation present is harder to measure.

A backscattered electron micrograph of the Fontainebleau sandstone was shown in Figure 7.4. The same stereological interference levels were applied to the Fontainebleau

sample as were applied to the sintered glass disc sample, Figure 7.13. Here it can be seen that the interference increased the undulation in the curves, and might have tended to mistakenly imply the presence of correlation features. However, the sharp rise with lag distance (minimal range of influence) remains a clear indication of a random structure. In practice, there would also be positional as well as size interference, which would tend to decrease the undulations. It could be suggested that the spline curve should be made less flexible by the inclusion of fewer knots, but this would increase the risk of missing features. As explained in Section 7.2.4, the inclusion of more knots would amount to statistical over-fitting.
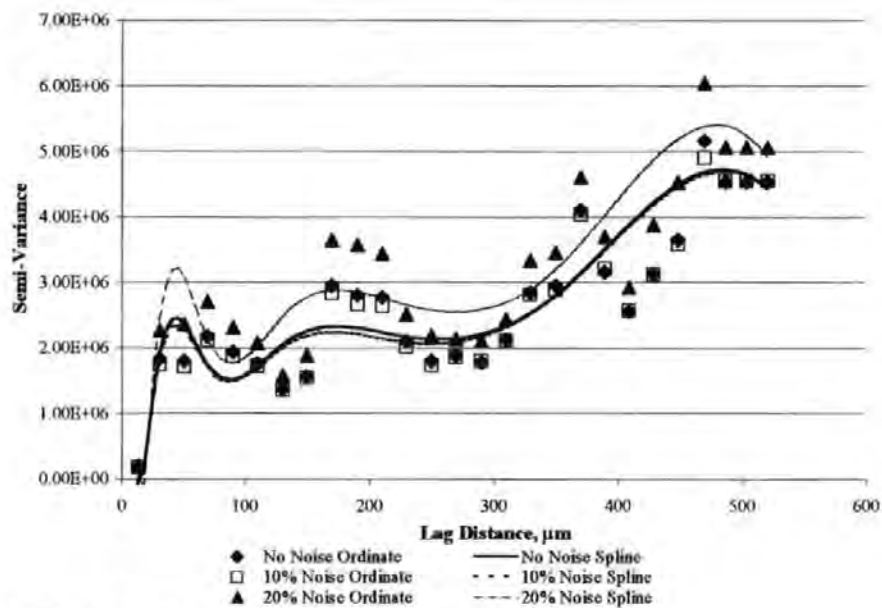
Figure 7.13 Variograms of Fontainebleau sandstone.

The more sophisticated procedure for constructing variogram surfaces was applied to the feldspar sandstone samples. The variograms for Figure 7.4 are shown below.
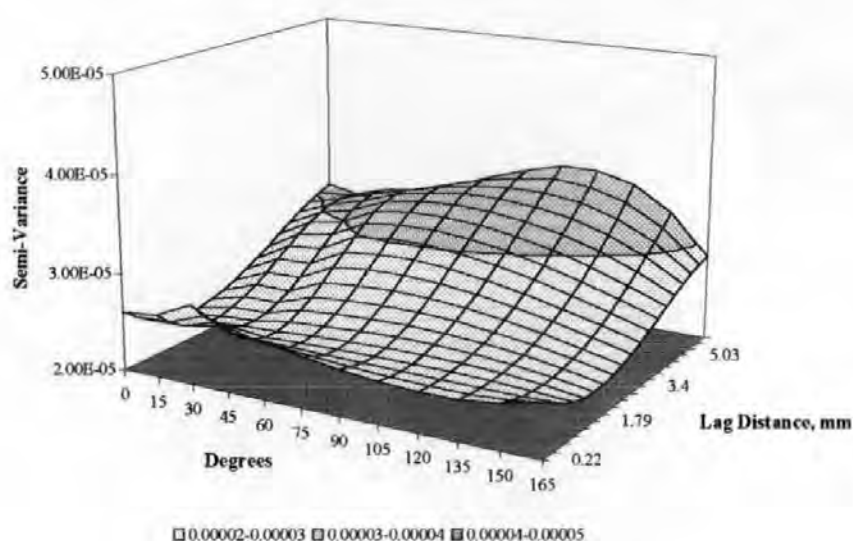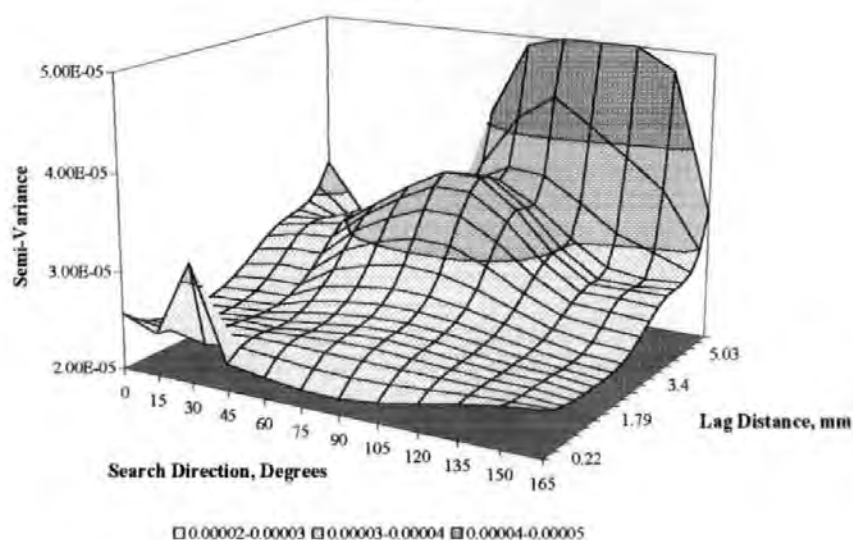
Figure 7.14 a) Surface variogram of feldspar sample and b) surface variogram after bicubic spline fitting.

From Figure 7.14 it is evident that the sample possesses laminations. At search directions corresponding approximately to 'East' (0-30° and 135-165°) only a gradual increase in semi-variance occurs. However, at search directions approximately perpendicular to this (90°), parallel to the y axis of the micrograph, it is clear that at a lag distance of around 2 mm there is a sharp increase in semi-variance to a maximum at approximately 3 mm. It would also appear that at distances beyond roughly 4 mm the semi-variance briefly starts to decline again. (Less significance should be placed on the last 3-4 points of each individual curve as these were calculated from much smaller numbers of pairs than the rest of the curves).

There would appear to be a clear indication of the presence of at least two, if not three, horizontal laminations in the sample at distances of approximately 0-2 mm, 2-3 mm and perhaps 4+ mm. Referring back to the original micrograph it can be seen that there would appear to be a band of small pores running along the bottom 1 mm of the image. Above this there is a larger region, approximately 3 mm in height, of larger pores and the last 2 mm appears to be a region of mixed pore sizes. (It should be borne in mind that the area of the variograms described by the x and y axes does not correspond to the x and y co-ordinates of the original micrograph). The maximum at 3 mm in the smoothed variogram corresponds to the spacing between the mid-points of neighbouring unlike laminae, the minimum at 0-2 mm reflects the presence of at least two layers at least 2 mm thick.

7.4 Discussion

A method has been developed for quantitatively measuring the degree of void size correlation within resin-filled, sectioned porous solids, using spline-smoothed variograms. The procedure has been successfully tested against an artificially correlated void network, consisting of two sintered glass discs of different void size ranges. Spline-smoothed variograms of these samples correctly revealed the obvious lamination features. The smoothing procedure has been shown to be insensitive to stereological interference, although such effects have been shown to dampen and shorten the variogram features. For sandstone samples, those with lamina visible by inspection both of the sample itself and its electron micrograph also reveal their structure in variograms. Any lesser degree of lamination is more difficult to detect in the variograms, at least in part because of stereological effects. Such effects in natural samples are difficult to correct, because it is difficult to judge whether a small void space region is genuinely a small void, or a chord near the edge of a large void.

In response to previously discussed shortcomings inherent in conducting the variogram studies using user-specified search directions (Mathews, T. J. et al., 1997) the technique has been modified to be carried out over a range of directions. The resultant variogram surfaces have been smoothed using a bicubic spline-fitting algorithm.

Additional work would be required to extend this work to the modelling of correlated structures using a network model. The first problem to be overcome would be the superimposition of measured correlations onto a simulated network of voids. As discussed in Chapter 1, other workers have constructed similar network models to that described here, which feature some degree of correlation. Unfortunately these have been, at best, very loosely related to experimental measures of correlation. Many studies by other workers have tended to examine the, often entirely theoretical, effects of various levels of correlation between neighbouring void features on simulated materials. Adler et al (1997; 1992) simulated porous media with the same correlation in phase distribution as their experimental samples. However, modelling correlations in the spatial distribution of differently sized voids via a network model does not appear to have been addressed elsewhere.

There is no direct method of back calculating from the surface variograms described here to a porous network model with the same level of correlation as an experimental sample. To produce simulations with the same properties as observed experimentally, it would be necessary to use correlation as a further constraint on the modelling procedure.

At present the network model described here features a basic simulated microtoming algorithm. This routine effectively takes sections through simulated porous media and calculates the areas of void features cut by the plane of the section. Bitmap images, analogous to electron micrographs and suitable for image analysis, may be produced in addition to files containing numerical details. At present, however, this routine is somewhat limited in that it can only take sections parallel to the x, y and z axes of the unit cell, which would be of limited usefulness in extending the investigation of correlation discussed here. To use this algorithm in the simulation of correlated networks it would require reformulation to take random sections, in all possible planes, through the simulated networks. The complex geometries exposed by such sections would make this process far more complicated than the simple algorithm described above. Additionally it would be necessary to incorporate code for the calculation of semi-variograms. However, the addition of these routines would allow the calculation of multidirectional variograms,

equivalent to those obtained experimentally in this work, from simulations of porous media. Once these were in place it would then be possible to use experimentally obtained measures of correlation as a fitting parameter within the network model, accepting only void space generations with spatial correlations similar to those observed experimentally.

Were this work to be incorporated into the network model as described above, a limitation that would be encountered in its present form stems from the relatively small size of the unit cell. Currently the unit cell is based around a 10 x 10 x 10 cubic lattice, upon which the simulated void structure is constructed. Thus the dimensions of this base unit are limited to a cube of side length somewhat greater than ten times the diameter of the largest pore. Exact dimensions depend on the pore row spacing required to model the experimental porosity. Consequently it would be extremely difficult to model correlations measured over scales greater than this. The diameters of the largest features of the samples tested here were around 300-μm and 1000-μm for the sintered glass and the Fontainebleau sandstone respectively (both measured by mercury porosimetry), and around 350-μm for the feldspar sample (from image analysis results). If the unit cell side length for each of these hypothetical simulations was at least ten times these measurements it can be seen that for the first two samples the unit cell would be considerably larger than the length scale over which correlation was measured. The minimum side length of the feldspar simulation would be around 3.5-mm, slightly less than the measured correlation length scale. However, it is highly likely that the actual pore row spacing would be somewhat larger than this minimum dimension. Extension of the unit cell size, however, would enable the simulation of correlations measured over scales greater than those considered here.

Were void size correlations measured over scales greater than the dimensions of a Pore-Cor simulated unit cell, an alternative modelling approach would need to be adopted. It has been suggested elsewhere (Chapter 6) that composite simulations could be constructed, based on different stochastic generations of the same modelled porous material. In much the same way described above, correlation could be used as a constraint on the construction of these stochastic composites. Although complex, software currently exists for performing such calculations, and could be incorporated into Pore-Cor.

8 Particle Size Distribution Estimation

8.1 Introduction

The work in this chapter was carried out to investigate whether information regarding the particle size distributions of simulated porous media could be extracted from the network model Pore-Cor. It is useful to consider the approximations, successes and deficiencies of the method developed here within the context of the exact solutions mentioned earlier (Chapter 1). Haines (1927) described in detail the intrusion and extrusion of a wetting fluid around the points of contact of regularly packed spheres. His considerations were expressed mainly as the development of a capillary 'pressure deficiency' plotted against T/a, T being the surface tension of the wetting fluid and a the radius of the spheres. The results were compared qualitatively to real randomly packed, approximately mono-disperse samples such as glass beads, lead shot, starch, sand and the confection 'Hundreds and Thousands'.

A more easily usable approach arose from the work of Mayer and Stowe (1965) for fluid penetration in packed arrays of uniform spheres. These packings were defined in terms of a single packing angle, σ (see Figure 8.1), calculated from the porosity of the sample. The packings have largest access openings ('pore-throat entries') varying in shape from 'square' for the most porous (highest values of σ) packings to 'triangular' for the closer packed (smallest values of σ) structures. A relationship is given which relates the porosity, surface free energy of the mercury and experimental breakthrough pressure to a single particle diameter, d_c, characteristic of all particles in the packing. A single example is given by Mayer and Stowe (1965), in which the calculated diameter for a packing of glass beads is shown to be within the measured size range of the beads.
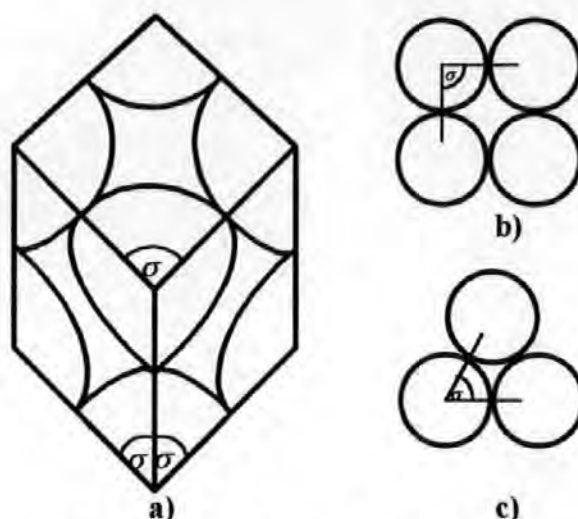
Figure 8.1 a) Illustration of the packing angle, σ, in an array of uniform spheres and examples of b) the square and c) triangular openings formed by packing angles of 90° and 60° respectively.

Current mercury porosimeter software (Micromeritics, 1996) extends this procedure, applying it to every point on a mercury intrusion curve rather then a single breakthrough pressure. Effectively this represents the porous material as being composed of spherical shells of regularly packed uniform spheres, with the smallest on the outside and largest in the middle. A simplified cross-section of such a structure is shown in Figure 8.2. The packing angle σ is assumed to be the same throughout the sample. At successively higher pressures mercury breakthrough occurs through the progressively smaller voids between packings of progressively larger spheres until the material becomes saturated. In fact the geometry inferred by this particular use of Mayer and Stowe's relationship is impossible to represent in two or three dimensions. It is not possible to construct such a simulation with a constant packing angle, which is some indication of the extent to which this is a mis-application of the original work.
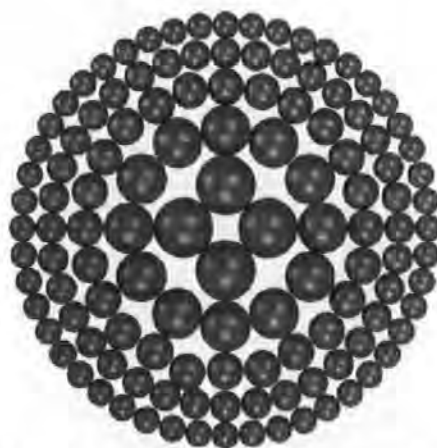
Figure 8.2 A cross-section through a solid as represented by the modified Mayer and Stowe (MMS) method of estimating particle size distributions.

The aim of this study was to improve upon the conceptual shortcomings of this approach, termed here the Modified Mayer and Stowe (MMS) method. This was done by first generating a void space structure using the network model Pore-Cor. The geometrical inverse of this void structure is an irregularly shaped solid phase structure. In the present study the sizes of a regularly spaced array of spherical particles that lie within this solid phase were determined. There are a series of approximations implicit in this calculation, including the simplified geometry of the void space structure, and the fact that the spheres do not fully represent the solid phase structure. This study sought to determine whether, despite these approximations, the new method could provide a useful guide to particle size distributions, and one that was better than the current MMS method. The judgement was made by comparing the modelling predictions with measurements made by the suppliers using sieves, and measurements carried out during this study using a Malvern Instruments Mastersizer X laser diffractometer.

8.2 Theory

For calculation purposes a *primary position, p*, is defined. This is the position of a pore centre displaced by half the pore-row spacing in the x, y and z directions. Each primary position is at the centre of a cube defined by the centres of eight adjacent pores. In addition to more sophisticated calculations described below, two bounding calculations were made for the sizes of solid spheres associated with each primary position. If each sphere were infinitely compressible, it could be deformed into a shape that fully occupied the solid phase space associated with each primary position. If this deformed sphere were then allowed to return to a spherical shape with the same volume, then the diameter of this sphere would be given by:

$$D_c = 2\sqrt[3]{\frac{3 \times \left[S^3 - \left(\frac{1}{8} \sum_{k=1}^{8} C_k^{\,3} + \frac{1}{4} \sum_{k=1}^{12} \pi \, r_k^{\,2} L \right) \right]}{4\pi}} \qquad [1]$$

Here D_c is the diameter of the compressible sphere, S is the Pore-Cor pore row spacing, C is side length of the cubic pores and r is the radius of cylindrical throats. D_c

then provides the upper bound to the sphere diameter at the chosen primary position. The corresponding lower bound, termed the *hard sphere diameter D_h*, is equal to the minimum diagonal distance between opposite pores surrounding the primary position. An example is shown in Figure 8.3, in which the central sphere is touching the opposite pores 1 and 8. D_h is given by the equation:

$$D_h = \sqrt{3}(S - C_I - C_{II})$$ [2]

C_I and C_{II} are the side lengths of the two diagonally opposed pores giving the smallest value of D_h.

Figure 8.3 Calculation of the hard sphere diameter, D_h.

Within the range defined by these two bounding calculations lies the actual sphere diameter associated with each primary position, i.e. the diameter of the largest sphere that can be fitted between the eight pores and up to twelve throats without distortion. In practice the mathematics required to find this value is analytically impossible, and would require a laborious, Monte Carlo -like calculation for its determination. An approximation to the solution can be found by ignoring the throats, which are usually smaller than, and never larger than, the pores, and then calculating the diameters of spheres that touch varying numbers of adjacent pores. The hard sphere calculation represents a two-contact calculation, three- and four-contact calculations carried out by vector mathematics will now be described. To a good approximation, the actual sphere diameter is equal to the largest of the two-, three- and four-contact diameters.

The method of calculating the three- and four-contact diameters, D_3 and D_4, was as follows. The starting point was a spherical 'seed' particle centred on the mid-point between the eight nodes of the pores, with diameter $D_3 \ll S$. The diameter of the seed particle was then increased to a size at which it made contact with the inner-corner of the largest of the eight pores surrounding it. If $\mathbf{p}$ is a vector defining the position, in three-dimensions, of the centre of the seed particle, and $\mathbf{c}_1$ is the vector defining the position of the first contact point (with the corner of the largest pore), then the position vector $\mathbf{u}$ of a point lying on the line through $\mathbf{p}$ and $\mathbf{c}$ can be defined,

$$\mathbf{u} = (1 + \lambda)\mathbf{p} - \lambda\mathbf{c}_1. \qquad [3]$$

It is then possible to move $\mathbf{u}$, by incrementing λ from zero, until the distance from $\mathbf{u}$ to $\mathbf{c}_1$ is equal to the distance to one of the remaining seven inner-corners of the pores. Thus a second contact point, $\mathbf{c}_2$, is found, giving three non-collinear points, $\mathbf{p}$, $\mathbf{c}_1$ and $\mathbf{c}_2$, and a sphere diameter D_2 equal to the distance from $\mathbf{u}$ to $\mathbf{c}_1$ or $\mathbf{c}_2$. It is now possible to move the centre of the sphere away from the final position of $\mathbf{u}$ in a plane determined by $\mathbf{p}$, $\mathbf{c}_1$ and $\mathbf{c}_2$, perpendicular to the line between $\mathbf{c}_1$ and $\mathbf{c}_2$. Its new position vector, $\mathbf{v}$, is given by,

$$\mathbf{v} = (1 + \mu)\mathbf{u} - \frac{\mu}{2}(\mathbf{c}_1 + \mathbf{c}_2). \qquad [4]$$

μ is incremented until another contact point, $\mathbf{c}_3$, is found, equidistant from the sphere centre to $\mathbf{c}_1$ and $\mathbf{c}_2$. Meanwhile the diameter has incremented to the value of D_3.

To find the fourth contact point, $\mathbf{c}_4$, the sphere is moved along the line,

$$\mathbf{w} = \mathbf{v} + \nu\mathbf{n} \qquad [5]$$

$\mathbf{n}$ in the above equation is normal to the plane through $\mathbf{c}_1$, $\mathbf{c}_2$ and $\mathbf{c}_3$, and is given as,

$$n = \frac{(c_3 - c_2) \times (c_2 - c_1)}{|c_3 - c_2||c_2 - c_1|} \tag{6}$$

As before the sphere's position is altered by minutely incrementing v until a fourth equidistant contact point, c_4, is found. Figure 8.4 a-e) gives a graphical representation of five successive stages in the four contact point method, or D_4 calculation. ('D_4' is used to denote the procedure, although in certain cases, described below, less than four points of contact may be made).
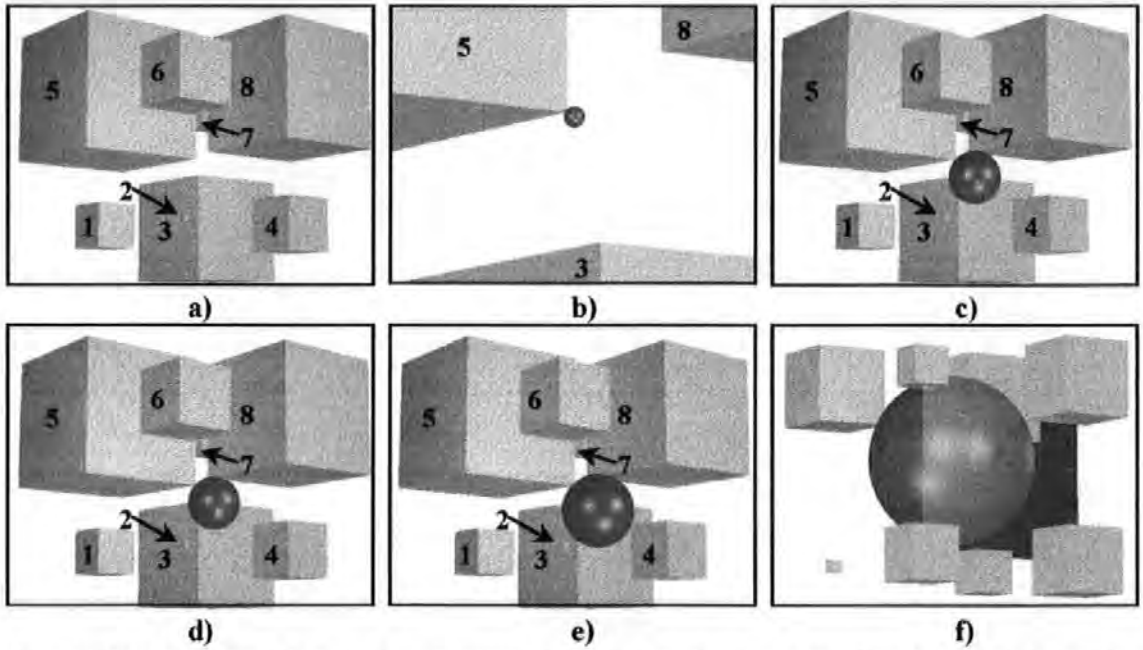
Figure 8.4 Illustration of the iterative process for calculating the diameter, D_4, of a sphere that makes contact with four pores. a) shows the initial array of pores and b-e) show the calculation of the individual points of contact. f) shows the sphere making contact with the edge of the imaginary cube bounding the volume available for the spherical particle.

In certain instances the configuration of pores around the primary position is such that the sphere can make contact with the edge of the cubic volume defined by the centres of the eight pores surrounding it. If the particle were allowed to continue growing it would therefore 'bulge' into an adjacent volume, Figure 8.4f. Due to the extra level of complexity this would add to the calculation the D_4 calculation is aborted whenever a sphere makes contact with this imaginary boundary and the particle size, D_4, taken to be the diameter at this point.

In most cases, $D_4 > D_3 > D_2 \approx D_h$. In some unusual cases, for example when all the largest pores are to one side of the primary position, Figure 8.5, $D_4 < D_h$. Overall, the final sphere diameter D was taken to be the maximum of D_4 and D_h.
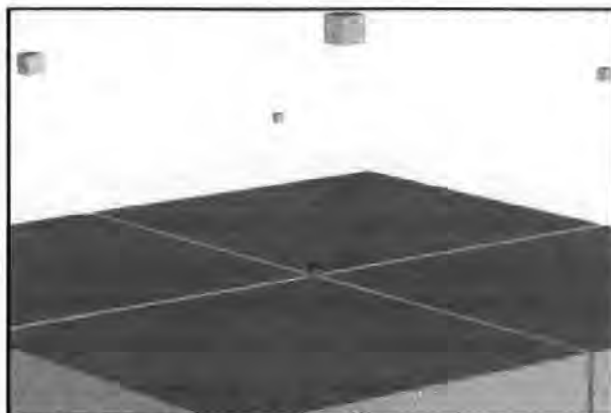
Figure 8.5 A pore configuration that would result in $D_4 << D_h$.

8.3 Method

Four different Redhill sands (Hepworth Minerals and Chemicals, Sandbach, Cheshire, U.K.) were modelled using this new technique. They were Redhill 30, Chelford 60, Redhill 65 and Redhill HH. They contained between 96.7 and 99.3% SiO_2, with other main constituents Fe_2O_3, Al_2O_3 and K_2O. A binary mixture of Redhill 30 and Redhill HH sands, the coarsest and finest grades respectively, and a sample of soda glass Ballotini beads of narrow size range were also studied. Experimentally derived particle size ranges are summarised in Table 8.1.

Particle Size, μm	Redhill 30		Chelford 60		Redhill 65		Redhill HH		Redhill HH-Redhill 30		Ballotini Beads	
	As Supplied, %	Mastersizer, %	As Supplied, %	Mastersizer, %	As Supplied, %	Mastersizer, %	As Supplied, %	Mastersizer, %	As Supplied, %	Mastersizer, %	As Supplied, %	Mastersizer, %
'Pan'	0.00	0.01	0.1	0.00	0.10	0.00	51.30	43.17	25.65	22.16	n/a	76.28
63	0.00	0.02	0.3	0.00	0.40	0.00	29.10	28.21	14.55	33.30	n/a	33.72
90	0.10	0.10	2.7	0.34	3.00	0.50	13.40	18.34	6.75	12.55	n/a	0.00
125	0.40	0.54	23.7	7.76	17.10	9.10	5.00	8.60	2.70	15.93	n/a	0.00
180	2.10	2.31	38.5	25.62	37.70	25.76	0.70	1.35	1.40	15.84	n/a	0.00
250	19.30	10.75	24.2	42.20	33.80	36.74	0.30	0.04	9.80	0.22	n/a	0.00
355	48.50	30.38	8.3	20.77	7.50	22.14	0.20	0.21	23.85	0.00	n/a	0.00
500	27.50	34.95	1.9	3.31	0.30	5.69	0.00	0.03	13.75	0.00	n/a	0.00
710	3.00	15.12	0.2	0.01	0.10	0.07	0.00	0.00	1.50	0.00	n/a	0.00
1000	0.10	4.39	0.1	0.00	0.00	0.00	0.00	0.00	0.05	0.00	n/a	0.00
1410	0.00	1.43	0.0	0.00	0.00	0.00	0.00	0.00	0.00	0.00	n/a	0.00
2000	0.00	0.00	0.0	0.00	0.00	0.00	0.00	0.00	0.00	0.00	n/a	0.00

Table 8.1 PSD's as supplied (sieved) and as measured by laser diffraction using a Malvern Instruments Mastersizer X. 'Pan' refers to particles smaller than 63-μm, which drop through to the final pan during sieving.

It should be noted that the two experimental methods of determining the particle size distribution do not produce identical results. This is to be expected, and arises from differences in the methods themselves. Determining particle size distribution by sieving is relatively simple. The unconsolidated sample is passed through a series of successively finer mesh sieves. The sample fraction retained on each sieve is weighed and attributed to the mesh size of that sieve.

Measuring particle size distribution by laser diffraction is a more complex procedure. The particles of a sample are passed through a monochromatic, collimated beam of laser light, the scattering of which is used to calculate the size of the each particle in the sample. The most important difference between the two methods is that, in laser diffraction, sizing is achieved by calculating the radii of spheres of volume equal to those of the measured sample particles.

The effects of this difference will be most pronounced for samples dominated by particles of a certain shape. For example, samples dominated by long thin particles may appear to be composed of smaller particles when measured by sieving than by laser diffraction. A particle of such dimensions may pass through a mesh size similar to the two smallest of the three orthogonal dimensions of the particle, i.e. the particle is characterised by its 'thin-ness' rather than its 'long-ness'. However, the radius of a sphere with equivalent volume to that of the particle, as measured by laser diffraction, may be considerably greater than this apparent size. It is most likely that it was this difference between the two techniques that gave rise to the difference in measured values.

Mercury porosimetry curves were obtained for the samples, using a Micromeritics Autopore III (Micromeritics Ltd., Dunstable, Bedfordshire, U.K.) instrument. The intrusion curves, shown with the simulated curves in Figure 8.6, were then input into the network model. The simulated intrusion curves were fitted to the experimental curves either by

(i) minimising the sum of the squared differences between the logarithms of the effective pore-entry diameters corresponding to each point on the intrusion curve and the equivalent points on the simulation, (log fit), or

(ii) by minimising the linear difference between the values, (linear fit), as explained in a previous publication (Matthews, G. P. et al., 1995).
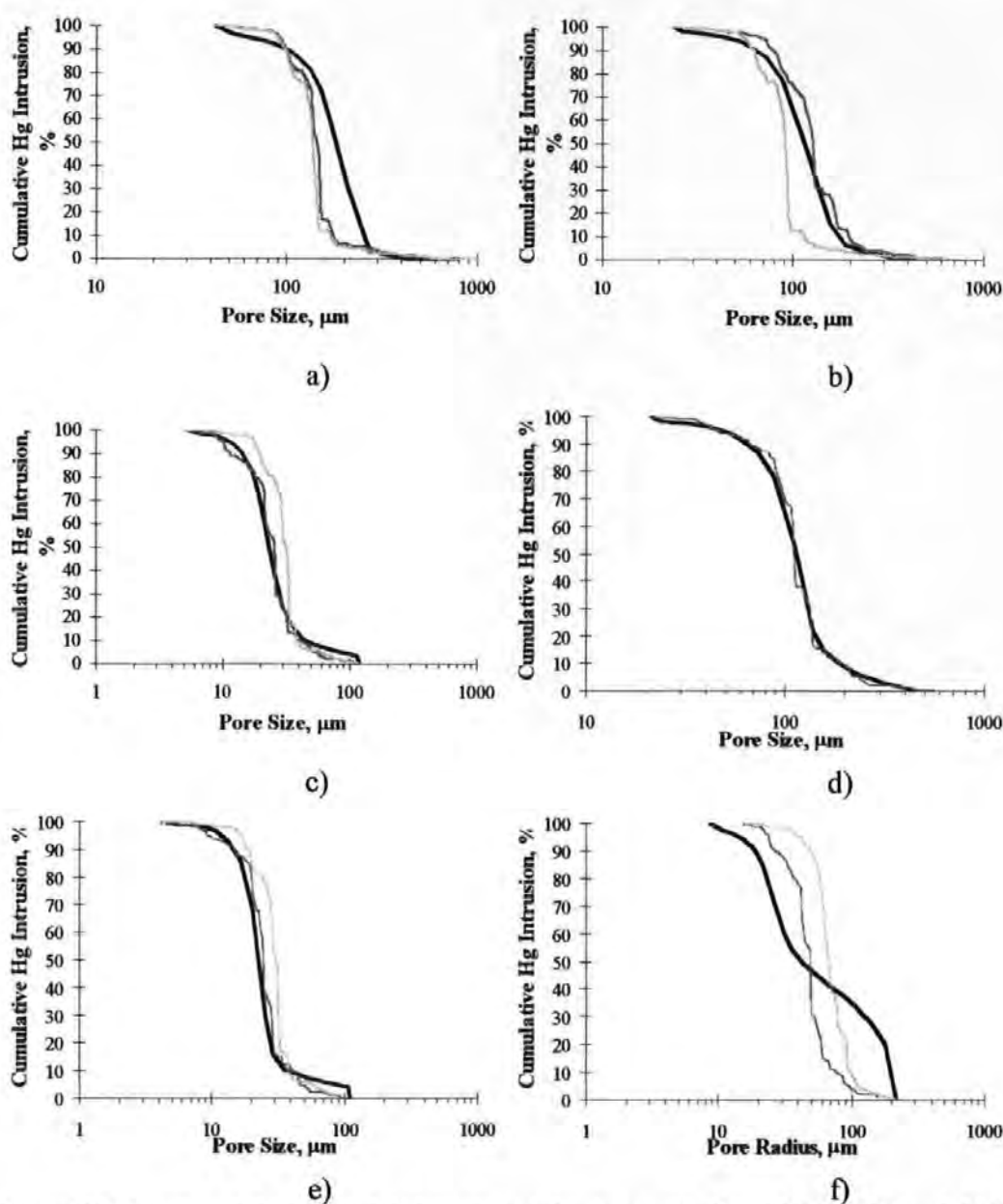
Figure 8.6 Experimental and simulated mercury intrusion curves for a) Redhill 30 sand, b) Redhill 65 sand, c) Redhill HH sand, d) Chelford 60 sand, e) Ballotini beads and f) the 50-50 mixture of Redhill HH and Redhill 30 sands. The dark grey line shows the log fit, the pale grey line the linear fit.

It can be seen that on the logarithmic abscissa usually used to plot mercury intrusion curves, the logarithmic fits look the more satisfactory. The linear fits can be used as a visual measure of the sensitivity of the final calculated PSD to both the type and closeness of the fit. The parameters corresponding to the fitted curves are given in Table 8.2.

Sample	Type of Fit	Throat Skew	Pore Skew	Connectivity
Redhill 30	Log	1.67	1.25	2.9
	Linear	1.97	2.20	3.7
Redhill 65	Log	1.17	1.52	2.9
	Linear	1.87	2.40	3.7
Redhill HH	Log	0.92	1.39	2.8
	Linear	1.12	1.29	3.8
Redhill HH -Redhill 30	Log	0.85	1.10	2.8
	Linear	0.85	-	4.0
Chelford 60	Log	0.87	1.25	2.9
	Linear	0.87	1.25	2.9
Ballotini Beads	Log	0.77	1.20	2.9
	Linear	0.97	1.20	3.8

Table 8.2 Pore-Cor parameters and results for simulated sand samples.

Two of the Pore-Cor unit cells corresponding to these parameters are shown in Figure 8.7, the remaining samples are given in Appendix ??. The unit cells were then used for the calculation of pore and throat size distributions, Figure 8.8, and absolute liquid permeabilities.

a)   b)
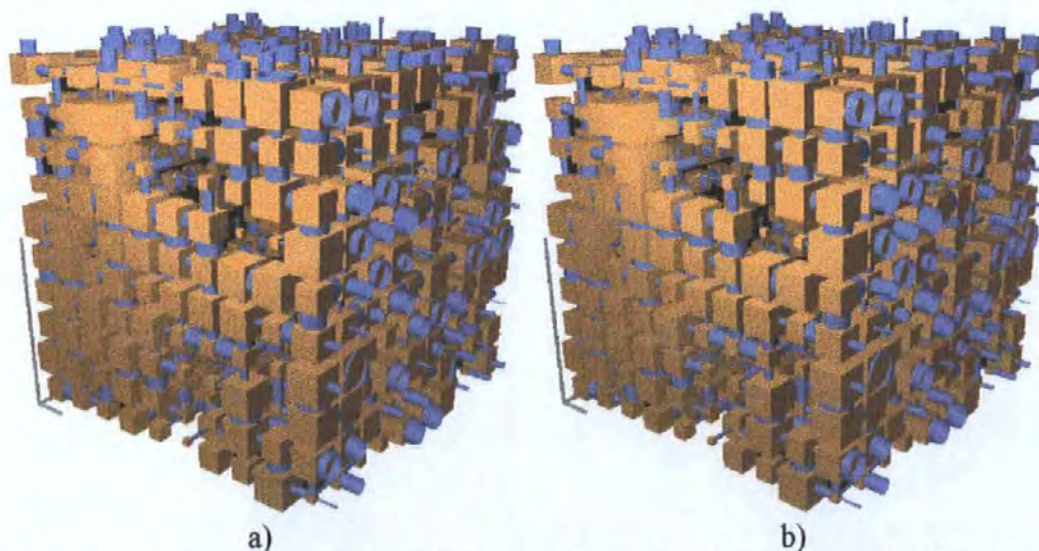
Figure 8.7 The Pore-Cor simulated unit cells for a) Redhill 30, where the large vertical scale bar is equivalent to 2191-μm, the small horizontal bars show 438-μm, and b) Redhill HH sand where the large scale bar is equivalent to 601-μm, and the small scale bar to 120-μm.
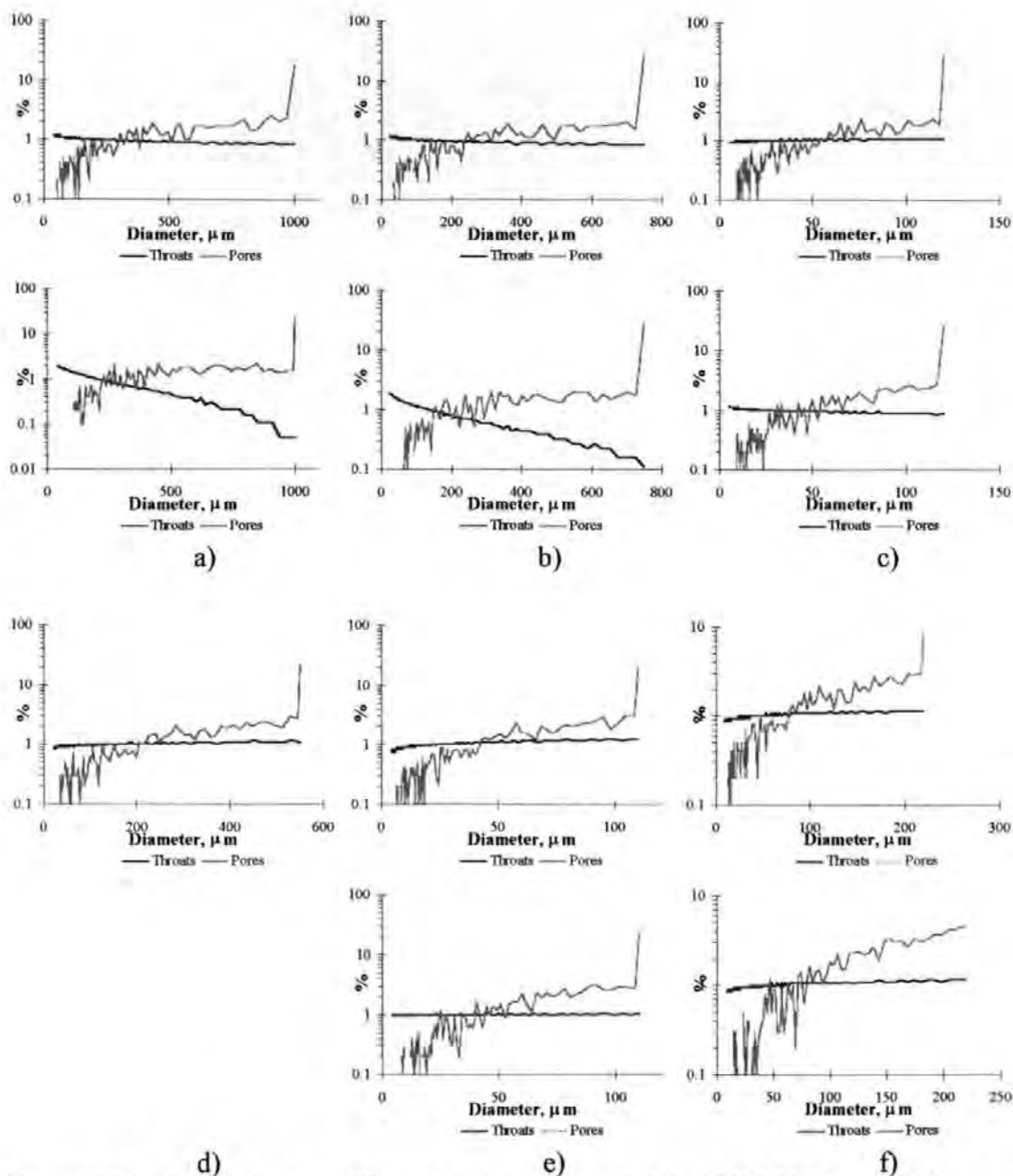
Figure 8.8 The simulated pore and throat size distributions of a) Redhill 30, b) 65 and c) HH sand, d) Chelford 60 sand, e) Ballotini beads and f) the 50-50 mixture of Redhill HH and Redhill 30 sands. The top graphs represents the log fit, the bottom show the linear fit, except for Chelford 60 where both fits gave the same result.

An artefact is that modelling is affected by the maximum and minimum experimental pressures on the intrusion curves, even if these pressures vary outside the range over which intrusion takes place. This arises from inefficient packing of the pores and throats coupled with the smallness of the unit cell, To control this effect, the experimental curves were each truncated at equivalent diameters of $<d_c/5$ and $> 5\ d_c$, where d_c is the pore size at the point of inflection of the intrusion curve.

8.4 Results

The results of the particle size calculations take the form of a list of 1000 sphere diameters, best viewed as frequency histograms. The results and experimental measures of PSD's for the samples are given in Figure 8.9. For clarity, three histograms are shown for each sample, covering the same size intervals. The middle histogram shows the experimental measurements of particle size distributions, measured by laser diffraction for all samples, and by sieving for all the sand samples. The top histogram for each sample shows the bounding calculations for the two types of fit to the mercury intrusion curve. The bottom histograms show the D_4 and MMS calculations.
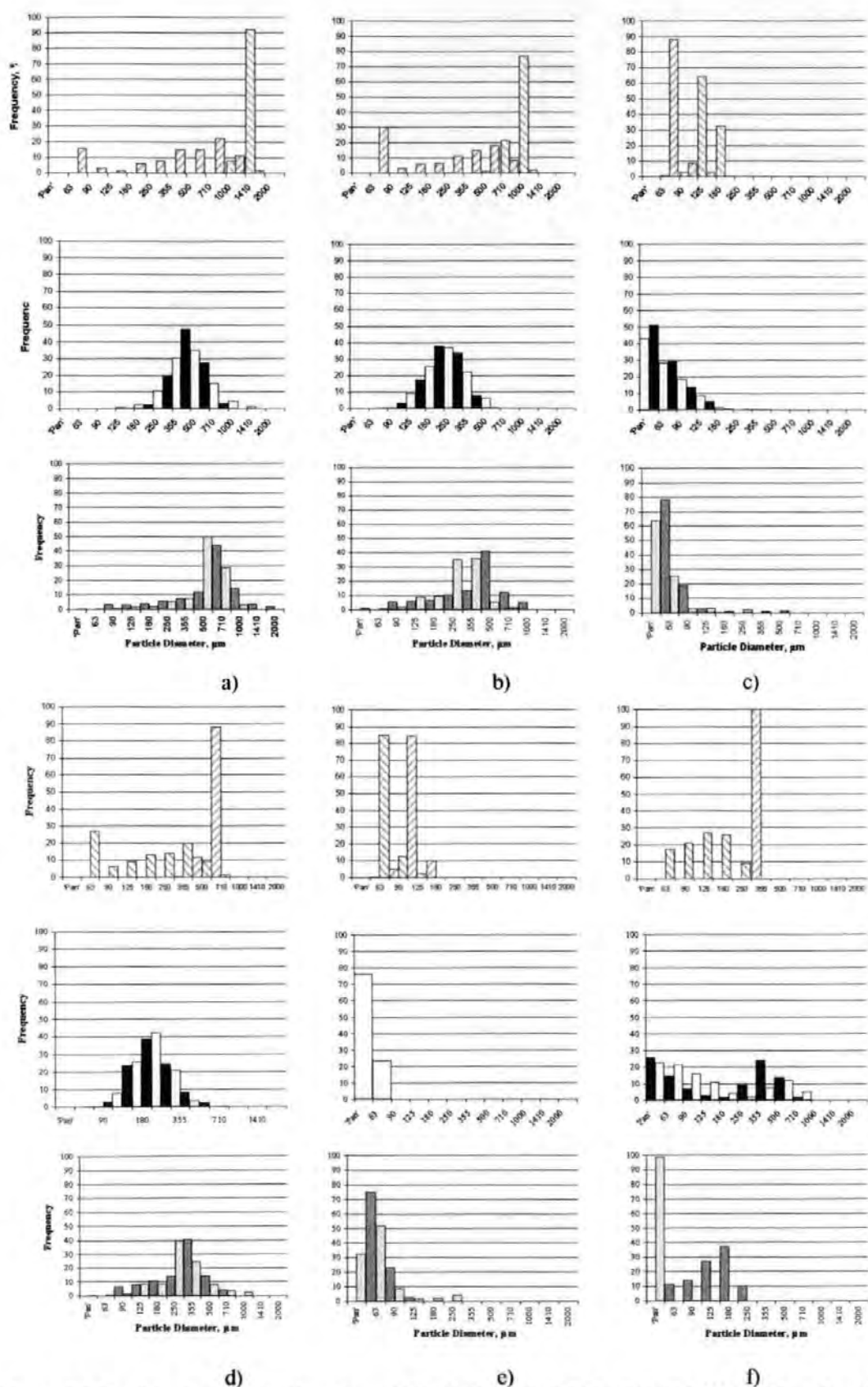
Figure 8.9 Particle size distributions for a-d) Redhill 30, Redhill 65, Redhill HH and Chelford 60 sands respectively, e) Ballotini beads and f) a 50-50 mixture of Redhill HH and 30 sands. For each sample:

Top -   Compressible Spheres, Log Fit   Incompressible Spheres, Log Fit
Middle -   As Supplied (Sieved)   Laser Diffraction
Bottom - D_4 Calculation   MMS Calculation

160

Ideally, the quality of the results should be judged in the light of statistical analysis. However, in this case, such an analysis is difficult. The major problem is that the frequency of the 'Pan' fraction (i.e. the fraction of particles smaller than 63-μm) is often too large to be ignored or combined with another size category. Since it refers to a size range with only an upper limit, and is part of a distribution on a logarithmic scale, it precludes calculation of the distribution mean, and hence also the standard deviation. Two other statistical analyses, namely χ^2- and F-tests, avoid this problem. However, χ^2 analyses in this case are overly sensitive to the spreads of the distribution on the size axis. F-tests can only be carried out on the variance of the percentage readings, with no size information included, and therefore shed little light on these results. Also F-tests require samples to be drawn from Normal distributions, which is clearly not the case for some of the particle size distributions shown in the previous figure. One is therefore left with a visual, qualitative judgement as the criterion for success in this case.

It can be seen from Figure 8.9 that, as expected, the compressible and hard sphere methods provide the upper and lower bounds for the D_4 method. In the cases of the four unmixed sand samples and the glass beads, visual inspection of the D_4 PSD's show that it reproduces the shapes of the experimental distributions well, though skewed slightly towards larger particle sizes. For most of the sands the MMS method also overestimated the number of larger particles, although slightly less than the D_4 calculation.

The glass beads comprise uniform spheres over a narrow size distribution, Figure 8.1e. It might be expected that the MMS method would accurately predict this system. In fact it drastically overestimates the size if the largest particles. From this it may be inferred that the MMS method is over-sensitive to the intrusion at low pressures. In this case an unmodified Mayer and Stowe method, based solely on d_c, produces a result of just under 28 μm. This figure falls comfortably within the tallest peak on the experimentally derived distribution and illustrates the limitations of extending the method over a range of intrusion pressures. In

contrast to the problems experienced using the MMS method, the D_4 calculation modelled the PSD of the glass beads with considerably greater accuracy.

The mixed sand sample has, as expected, a bi-modal size distribution which is clearly indicated by both experimental methods in the centre histogram of Figure 8.9f. This bi-modality is also manifest in the two-step mercury intrusion curve, Figure 8.6f. Unfortunately, the Pore-Cor unit cell network is not extensive enough to model bi-modal distributions, and the possible simulated PSD's are therefore restricted to uni-modal distributions. The consequence of this can be seen in Figure 8.6f - the simulated curves have a single point of inflection and are a poor fit to the shape of the two-step experimental intrusion curve. The fit at low intrusion is also affected by the essential 5 d_c cut-off mentioned above. Nevertheless, the fitted curves do straddle the range of the experimental curve, and the D_4 calculation gives a very much better approximation to the range of particle sizes than does the MMS method, Figure 8.9f.

8.5 Conclusions

It is evident from the results that the distributions produced by the new four contact point method, or D_4 calculation, fall between the bounds of the compressible and hard sphere methods, and compare well with those produced by the MMS method. Both the D_4 and MMS calculations produced acceptable approximations of the PSD's of the unmixed sand samples, although both methods tend to overestimate the fractions of larger particles. For the glass beads and mixture of sands the D_4 method provided a significant improvement over the MMS method.

The D_4 method presented here is based on a wide range of approximations, some of which may be addressed in future work. Thus it would not be sensible to use the method to study unconsolidated material, since the direct experimental methods described here are much more reliable. Nevertheless, the theoretical approximations are less gross than those within the

MMS method. It has been demonstrated, by the trials with unconsolidated material, that the new method could be a useful tool in the study of consolidated material where no direct experimental methods are available for particle size measurement.

8.6 List of Symbols

a	Radius of sphere
A	Cross-sectional area of cell
C	Pore side length
d_c	Characteristic throat diameter
d_{min}, d_{max}	Minimum and maximum throat diameters
D_4	Sphere diameter produced by new 'D_4' method
D_c	Compressible sphere diameter
D_h	Hard sphere diameter
F	Formation factor
k	Absolute permeability
l	Length
N_d	Number percent of throats of diameter d
P	Primary position
s	Throat skew
S	Pore row spacing
t	Time
T	Surface tension of wetting fluid
V	Volume of fluid

8.6.1 Greek Letters

B	Number of tubes in the z direction
λ	Incremental parameter
η	Viscosity of fluid

σ	Packing angle
μ	Incremental parameter
υ	Incremental parameter
Ω	Averaging operator
ψ	Pore skew

8.6.2 Subscripts

cell	Cell
tube	Tube
x, y, z	Pertaining to the x, y or z axis direction, may be positive or negative.

8.6.3 Vector Notation

c	Three-dimensional position vector of a cubic pore corner
n	Vector normal to a plane
p	Three-dimensional position vector of the centre of a spherical 'seed' particle
u, v, w	Three-dimensional position vectors

9 Particle Induced Permeability Damage Study

9.1 Introduction

As discussed in Chapter 1 models of deep-bed filtration developed over the last 20-30 years can generally be attributed to one of four types: empirical, trajectory-analysis based, stochastic and network based. Model complexity varies from extremely simple statistically based simulations, featuring no mechanistic components at all, to highly sophisticated molecular dynamics type simulations, requiring the processing power of supercomputers. A description of model types and some notable examples are given below.

Empirical models, originally developed by Ives (1960), Heertjes and Lerk (1967) and Ison and Ives (1969), based on macroscopic continuum conservation equations depend largely on a system-dependant empirical 'filter coefficient'. Simple empirical models are not concerned with morphological considerations regarding the pore space, and cannot predict permeability decline or effluent concentration. Such models have been criticised for their simplified representations of porous media. For example, such models tend to use the empirical Kozeny-Carman equation for calculating pressure drop across the porous material, which, although appropriate in systems of parallel independent pores, may not be suitable for systems of interconnected pores.

An example of a more sophisticated empirical model is that devised by Gruesbeck and Collins (1982) for predicting productivity declines in producing wells. This model considered two types of pore. The first included those that were smaller than, and therefore became plugged by, the suspended particles. The second were larger pores in which non-plugging deposition could take place. Deposited particles could also be re-entrained, possibly leading to later plugging of the smaller pores. The model allowed the estimation of permeability decline, albeit using unquantified phenomenological constants. Soo and Radke (1986) devised another sophisticated empirical model based on this model combined with the trajectory analysis simulation of Payatakes et al. (1973). Their model simulated the(Tien, C. et al., 1979)

filtration of dilute stable emulsions. Although the model did allow the prediction of effects of filtration on permeability results were rather inaccurate, possibly arising from the Kozeny-Carman capillary assumption implicit in the trajectory analysis calculations.

Trajectory analysis models, used either in isolation (Tien, C. et al., 1979; Nabzar, L. et al., 1996) or coupled with some other technique as described above, tend to consider the porous material to be a number of *unit bed elements* connected in series. As first described by Payatakes et al. (1973) each of these is said to consist of a number of unit cells, which may be a variety of geometric shapes. Particle trajectories are calculated using streamline analysis and consideration of other forces, such as gravity, inertia and van der Waal's forces. Such models tend to give accurate predictions of the filter coefficients and filter efficiency, but do not tend to predict resultant changes in the pressure drop across samples.

Stochastic models are less commonly employed and tend to rely on probabilistic approaches. Fan et al. (1985) devised a simple model based on a probabilistic birth-death approach to predicting the blockage of pores. Here a birth event was equated with clogging of a feature by deposited particles and a death event was equated with a feature becoming unblocked by the removal ('scouring') of deposited particle from its surfaces. The model was calibrated to experimental data, but was over simplistic in that it could only model uniformly sized pores.

More recently network models have been employed to model particle transport behaviour with varying degrees of success. Although many authors favour the use of two-dimensional networks, it has been pointed out that three-dimensional models are likely to be more accurate in their ability to allow flow to bypass regions of low permeability (Constantinides, G. N. and Payatakes, A. C., 1989). Similarly, many models rely on one void type only, typically composing networks purely of cylindrical throats connected at nodes representing pores of zero volume (Rege, S. D. and Fogler, H. S., 1988; Imdakm, A. O. and Sahimi, M., 1991).

Particle transport has been simulated in these network models in a number of ways. Todd et al. (1984) devised a model coupling an unbiased random walk method with two different capture mechanisms, random capture and one based on the geometric relationship between particles and voids. Predicted results were rather inaccurate, and the authors attributed this to failings in the capture mechanisms.

Sharma and Yourtsos (1987) developed an effective medium approximation of the flow field in their network model of deep bed filtration, using this to calculate changes in permeability due to particle capture. Particle capture was governed by population balance type equations, solutions of which were provided for three specific scenarios. Certain dimensionless parameters were used to fit the modelled data, although these could be determined from experimental results. Again modelled predictions, here of the data of Baghdikian et al. (1989), were not very accurate.

Rege and Fogler (1987; 1988) developed a two-dimensional network model in which a probabilistic method was used in addition to size exclusion to model particle capture. Although the model featured some empirical parameters and included no facility for the scouring of deposited particles, it proved reasonably successful in modelling various experimental results (Baghdikian, S. Y. et al., 1989; Soo, H. and Radke, C. J., 1986) and has been adapted for use elsewhere (Wenrong, M. et al., 1996).

Imdakm and Sahimi (1987; 1991) developed a model based on a cubic network of cylindrical pores. The flow field over the network was calculated using Hagen-Pouseuille to calculate pressure drops, and finite numbers of particles were moved through the network using the trajectory analysis model of Payatakes and Tien (1973; 1979). Although computationally complex, the model was in good agreement with the experimental data against which it was tested.

Sallès et al. (1993) developed a theoretical technique for calculating particle deposition and clogging in a variety of different simulated porous media. A numerical scheme was devised, partly based on a random walk model, which tracked the progress of a finite number of particles through the fluid filled material. Particles were deposited when they collided with feature walls, and features were removed from the void matrix when the level of deposition within them exceeded a prescribed level. Although reasonably sophisticated, the model was not compared with any experimental results.

Pore-Cor, as previously described, is a three-dimensional network model, featuring two void types and variable connectivity. Although a small amount of work has already been carried out with regard permeability damage due to deposition of solid material, this has been fairly unsophisticated. A 'colloidal damage' routine has been developed that effectively blocks, or removes, all voids smaller than a certain size (the radius of the uniformly sized particles in a 'colloidal suspension'). Effectively this models an idealised form of size exclusion, where all voids smaller than the mobile particles are accessible to them and become blocked. Due to the small size of the unit cell and the nature of the permeability algorithm, which looks for paths of maximal flow, this tends to have the effect of producing decreases in simulated permeability disproportionately large compared to those observed experimentally (Mathews, T. J. et al., 1994).

In a similar vein a more sophisticated 'polymer plugging'/'air intrusion' routine has also been formulated. A polymer/air front is simulated moving through the unit cell, blocking all features it passes through but unable to pass through features smaller than a certain size. The modelling of this process uses the same percolation algorithm employed by the mercury intrusion routine. Thus, as the front penetrates the randomly arranged voids of the sample it becomes uneven as different areas of the front become stationary. Eventually the entire front ceases to move. This has been used elsewhere (Chapter 6) in this thesis to simulate the partial water saturation of sands.

A major limitation of both of the methods described above is that neither can model the cumulative effects of continuous flow through samples. Nor can either of the simulations model deposition of a range of particle sizes. Finally, the partial blocking of features by comparatively small particles cannot be modelled. Thus, although the mechanisms for modelling simplified particle capture behaviour were in place further development was required to develop a more realistic simulation. The current work aimed to investigate the possibility of incorporating a more sophisticated simulation of the flow and deposition of dilute suspensions into the existing network model.

9.2 Model Formulation

All modelling of actual samples was carried out as described elsewhere (Chapters 2 and 6) with modelling of particle-induced permeability damage taking place subsequently.

One potential method of modelling permeability damage due to fines migration would be to adapt the routines already employed in the calculation of tortuosity within the unit cell. These could be adapted to model the movement of individual particles within the voids. Other workers have utilised both random walk (Todd, A. C. et al., 1984) and flow-biased random walk (Rege, S. D. and Fogler, H. S., 1988) methods with varying degrees of success. Alternatively, it would be possible to adopt a trajectory analysis-based approach, as developed by Payatakes and Tien (1973; 1979) and used by Imdakm and Sahimi (1987; 1991). However, both of these approaches would increase computing times dramatically, especially on the platforms for which the network model has been designed (medium specification IBM PC's and compatibles), without necessarily producing a proportional increase in accuracy.

Rather than looking at individual particles and their progress through the unit cell consideration was given instead to individual features (pores and throats) and the likelihood of differently sized particles being deposited within those volumes. Particle capture was

169

governed by two processes. The first of these was straining or size exclusion, where particle diameter was greater than that of the feature being considered. The second was a probabilistic method of determining whether particles were likely to be deposited within feature as a result of various physicochemical forces.

The first step in the modelling procedure was to calculate a transport volume, that is the volume passing an imaginary observation point, in each individual throat in the unit cell. The Poiseuille equation, re-arranged in terms of transport volume passing through a void, V_t, yields,

$$V_t = t \frac{\Delta P \pi R_t^4}{8 \mu L_t}$$

[1]

where t is the time step, R_t is the throat radius, L_t is the throat length, μ is the viscosity of the suspension and ΔP is the pressure drop across the throat. ΔP, calculated prior to V_t, is also given by re-arranging Equation 1, calculating in terms of flow across the entire sample rather than a single feature.

$$\Delta P = \frac{Q \mu L}{KA}$$

[2]

where Q is the volumetric flow rate across the sample, K is sample permeability, A is sample cross-sectional area and L is sample length.

Although flow in the y-axial throats was assumed to be from top to bottom, neither these calculations nor any others made any assumptions about the direction of flow in the x- and z-axial throats.

The equivalent transport volumes were then calculated for the cubic pores in the network. Because the Poiseuille equation is applicable only to capillaries and no simple equivalent is readily available for cubic voids an estimate of the transport volumes was required. This was achieved by simply halving the sum of the transport volumes of all the throats surrounding each pore. This simplification is at least justifiable in that it is equivalent to assigning half the flow through each pore to input and the other half to output.

Having determined these transport volumes it was then possible to calculate how many of the differently sized particles would pass in that time. Given the concentration, density and particle size distribution of a suspension, and assuming the particles to be uniformly distributed theroughout, it was relatively simple to calculate the number of differently sized particles within a given volume. The total volume of fines, V_f, present in the pore volume of the unit cell, V_p, is given by,

$$V_f = \frac{V_p C}{d}$$ [3]

where C was the initial concentration of fines in suspension and d the fines density. It was then possible to calculate the number of fines of each size present in the unit cell, N_1, N_2, N_3.... N_i, where i is the number of size categories in the particle size distribution. For the purposes of modelling it was necessary to make some assumption about the shape of the suspended particles. For the sake of simplicity particles were assumed to be spherical. Given this assumption the number of fines in a given size category, N_i, present in one pore volume is,

$$N_i = \frac{3 f_i V_f}{4 \pi R_i^3}$$ [4]

171

Here f_i is the frequency of fines in size category i and R_i is the fine radius, obtained experimentally. In this way the initial 'reservoir' of solid material available for deposition was calculated.

Having calculated transport volumes and total number of available fines, deposition was then considered. The features of the unit cell were considered sequentially, moving through the pores in ascending numerical order by pore index. Although this sequence is arbitrary it is realistic in that it simulates the suspension becoming more and more depleted as it flows from plane to plane, perpendicular to the direction of flow. After considering deposition in a pore each of the throats connected to it in the positive x, y and z directions were considered, before moving onto the next pore in the matrix. Initially this involved calculating the number of particles, n_i, of a certain size present in a given feature, given by,

$$n_i = \left(N_i - D_i \right) \frac{V_i}{V_p}$$

[5]

V_p was the pore volume of the unit cell and D_i the number of fines in size category i that have already been deposited.

Having determined whether any particles of a given size were present in a feature the next step was to establish whether deposition would take place due to straining/size exclusion. This was achieved simply by comparing particle radius, R_i to feature radius, R_t in the case of the cylindrical throats, or $L_p/2$, where L_p is side length, in the case of the cubic pores. If fine radius was greater than feature radius then the feature was assumed to have become blocked and D_i was incremented by 1.

A second mechanism by which straining might take place was also used, where no fines of a certain size were expected within a feature (Equation 5) but fines of this size were still

172

present within the unit cell (i.e. $n_i < 1$, $N_i - D_i > 0$). In such cases a biased Monte Carlo type method was used to determine whether a particle would be present in a pore or throat. A pseudo-random number generator was used to return a value, x_{ran}, between zero and one. Then, if the condition,

$$\frac{n_i V_t}{V_p} \geq x_{ran} \qquad [6]$$

was met a particle was deposited and D_i incremented by one. By using the ratio V_t / V_p the likelihood of deposition taking place by this method was skewed towards the larger sized features, where particles were statistically more likely to be present, without ruling out the possibility of deposition taking place in even the smallest pores and throats.

If no straining took place then a probabilistic method was used to determine whether deposition took place due to other forces. The probability of deposition of fines smaller than the voids they are travelling through, P, has been defined for cylindrical throats as (Rege, S. D. and Fogler, H. S., 1988),

$$P = 4[(\theta R_i / R_t)^2 - (\theta R_i / R_t)^3] + (\theta R_i / R_t)^4 \qquad [7]$$

where θ is a lumped parameter that accounts for factors such as fluid velocity, ionic conditions, pH and fluid properties. When the relationship between θR_i and R_t is such that P is equal to, or greater than, 1 then deposition will take place. Equation 7 was also used to determine the probability of deposition taking place in the cubic pores by substituting $L_p/2$ for R_t, although this obviously represents a fairly crude approximation of the depositional probability within a pore. Equation 7 is based on the determination of an annular region of size θR_t within a cylindrical feature experiencing laminar flow, and as such cannot be directly applied to cubic volumes. However, in the absence of a more sophisticated model this adaptation of Equation 7 was employed.

173

θ is defined in this work as (Rege, S. D. and Fogler, H. S., 1988),

$$\theta = \theta_0 \exp(- v / v^*) \qquad [8]$$

θ_0 being a constant dependant on ionic conditions, v representing fluid velocity in the feature and v^* being a critical velocity. A value for v^* can be found either theoretically (Rege, S. D. and Fogler, H. S., 1988) or by calibrating to experimental results, as was done here. Similarly a value for θ_0, another lumped parameter accounting for ionic strength and pH, can be found by adjusting it such that predictions fit experimental data for one run, then using this value for all further predictions. Having already calculated the volume flowing through a throat in a given time v can be calculated as,

$$v = \frac{V_t}{t.\pi.R_t^2} \qquad [9]$$

or by substituting L_p^2 for $\pi.R_t^2$ in the case of pores.

Deposition of a particle within a feature naturally alters the flow characteristics of that void, causing a reduction in flow equivalent to decreasing the effective radius of the feature. Subsequent depositional probability calculations using Equation 7 should reflect this. It was therefore necessary to have some means of determining the new effective radii of features in which fines have been deposited. It has been shown that, considering Poiseuille flow and employing the relevant boundary conditions, the increase in pressure drop due to the presence of a spherical particle in a feature, ΔP_p, may be defined (Happel, J. and Brenner, H., 1980),

$$\Delta P_p = \frac{12\mu R_i U_0}{R_t^2}\left[1 - (1 - R_t)^2\right]^2 . K_1 \qquad [10]$$

where U_0 is the centreline velocity through the feature (here taken to be v) and K_1 is given by,

$$K_1 = \frac{1 - \left(\frac{2}{3}\right)(R_i / R_t)^2 - 0.202(R_i / R_t)^5}{1 - 2.1(R_i / R_t) + 2.09(R_i / R_t)^3 - 1.71(R_i / R_t)^5 + 0.73(R_i / R_t)^6} \qquad [11]$$

174

The total pressure drop, ΔP_{total}, through the feature can be described by,

$$\Delta P_{total} = \Delta P + \Delta P_p \qquad\qquad [12]$$

where ΔP is the pressure drop across the feature prior to deposition. ΔP_{total} may therefore be calculated and substituted back into the Poiseuille equation (Equation 1) which, upon re-arranging, yields the new effective radius of the feature.

When deposition took place in a modelled void there were often large numbers of particles of the same size present in the feature. A process was derived for governing the precise number of particles deposited in this situation. The deposition of particles causes the conditions that govern further deposition within a feature to change. One approach would be to re-calculated these conditions after the capture of every individual particle. The other extreme would be that all particles originally present in the feature were deposited, ignoring the dynamic nature of particle capture.

In preliminary studies both methods were tested for suitability and although the latter process resulted in excessive permeability damage (in terms of pore volumes of the suspension required) the former added to computing times to such a degree as to make the program unusable. The solution took the form of a compromise between the two extremes. Initially the effective size of the feature was calculated assuming that all of the particles under consideration were deposited. Then an intermediate feature size, R_{int}, was calculated as follows. Assuming permeability to be proportional to R^4 then an estimate of this intermediate throat diameter, R_{int} can be made. If the permeabilities of the throat initially and after deposition of all particles are K_i and K_{new} respectively then,

175

$$K_t \propto R_t^{4} \qquad \qquad [13]$$

$$K_{new} \propto R_{new}^{4} \qquad \qquad [14]$$

Taking logs this can be expressed,

$$Log_{10}K_t = 4Log_{10}R_t \qquad \qquad [15]$$

$$Log_{10}K_{new} = 4Log_{10}R_{new} \qquad \qquad [16]$$

To estimate a throat diameter, R_{int}, producing an intermediate permeability the average of the right hand sides of Equations 15 and 16 is taken.

$$Log_{10}R_{int} = \frac{1}{2}\left(Log_{10}R_t + Log_{10}R_{new}\right) \qquad \qquad [17]$$

From Equation 17 it can be seen that R_{int} can be calculated directly as the geometric mean of the two other radii, i.e.,

$$R_{int} = \sqrt{R_t R_{new}} \qquad \qquad [18]$$

This value of R_{int} was then put back into Equation 7, and if the probability of deposition was still greater than 1 then particle capture occurred depositing all available particles. This new method, with probability of deposition now skewed to favour the larger pores and throats, went some way towards dealing with the problem of rapid permeability decline while not adding significantly to computation times.

Having defined all the processes by which fines deposition may take place in the model, the program was structured such that permeability could be re-calculated each time one pore volume of the modelled suspension exited the unit cell. Finally the model was programmed to

run repeatedly until the volume of fines deposited from one pore volume became zero, that is until all possible deposition, given the new effective volume of the unit cell and concentration of the suspension, had taken place.

9.3 Modelling Permeability Decline

Having formulated the model it was tested and its predictions compared to some experimental data. The model requires results from core flooding experiments run at at least two different flow rates before it can be used to predict the results of successive runs. It was necessary to start by using the results from an experimental run carried out at a low flow rate such that it could be assumed that the exponential in Equation 8 would equate to 1. Thus θ_0 could then be set to provide the best fit of modelled to experimental results. Having done this it was then possible, using the results from a second run carried out at a faster flow rate, to determine a value for v^* in the same manner. Having established values for these two parameters it was then possible to predict the results of successive runs. The fit of modelled to experimental curves was quantified by a simple sum of the squared differences between experimental data points and modelled predictions, the aim being to minimise these values in each case.

9.3.1 Sandstone Sample

Initially limited testing of the model was conducted using results from a single core flooding experiment (supplied by Ambellia Consulting, Wiltshire, U.K.) carried out on a plug of sandstone (origin unknown) using unfiltered North Sea water. Experimental details are shown below.

Plug Details		Solution Details	
Initial Permeability, K	3.296 Darcies	Concentration of Solids	36.843 g l^{-1}
Porosity	39.1 %	Viscosity, μ	1.35 cps
Length, L	40mm	Flow Rate, Q	10 ml min^{-1}
Cross-sectional area, A	114mm^2		

Table 9.1 Summary of experimental details.

9.3.1.1 Pore-Cor Modelling

The details of the Pore-Cor simulation of the sample are shown in Table 9.1 and the experimental and modelled mercury intrusion curves are shown in Figure 9.1
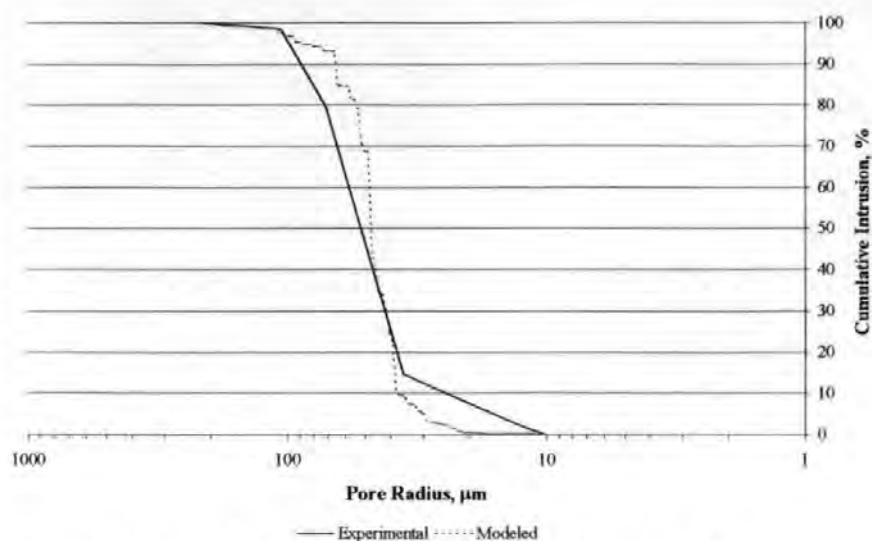
Figure 9.1 Experimental and modelled mercury intrusion for sandstone sample.

Parameter	Value
Modelled Porosity	39.09 %
Modelled Permeability	0.832 Darcies
Type of Fit	Log
Throat Skew	1.33
Pore Skew	1.17
Minimum Throat Diameter	10.14 µm
Maximum Throat Diameter	212.00 µm
Connectivity	3.8

Table 9.2 Pore-Cor modelled parameters.

It can be seen that the fit of modelled mercury intrusion curve to experimental was somewhat inaccurate. This was probably due largely to the shape of the experimental curve. The network model is most suited to modelling intrusion curves of a more sigmoidal shape than that available here. In fact, the original experimental curve ended at the penultimate point of the line shown in Figure 9.1, the final point at 100% (obscured by the modelled curve) had to be added here to enable Pore-Cor to model the sample at all.

The difficulties of curve fitting are indicative of a commonly encountered problem when modelling porous media using this network model. Pore-Cor requires accurate, detailed and complete mercury intrusion curves to produce accurate simulations. Often mercury intrusion is carried out using a small number of pressure points over a narrow pressure range. While this may be adequate for some purposes Pore-Cor is most successful when modelling samples with a greater number of points over the complete range of pressures under which intrusion takes place. Intrusion carried out under such conditions tends to produce the sigmoidal curves most suitable for the model.

9.3.1.2 Results

Due to the lack of data covering core flooding carried out at different volumetric flow rates, only one stage of the procedure developed here could be tested. Nonetheless, this was carried out to ascertain whether the model was likely to be of any use in modelling further experimental data.

Using the supplied data the model was fitted to the experimental results. This was achieved by setting the exponential in Equation 8 equal to one (equivalent to assuming that the experiment was conducted at such a rate that v was extremely small compared to $v*$) and by then adjusting θ_0. Figure 9.2 shows the effect on the model of changing θ_0, including the best fit line, which was accomplished by setting the value of θ_0 equal to 15.9. It can be seen that, although the model somewhat overestimated the rapidity of the permeability decline, it was possible to achieve a satisfactory fit of model to the experiment. Considering the ratio K_{end}/K_0, where K_{end} is the final permeability, we have 0.717 for the experimental and 0.721 for the modelled.
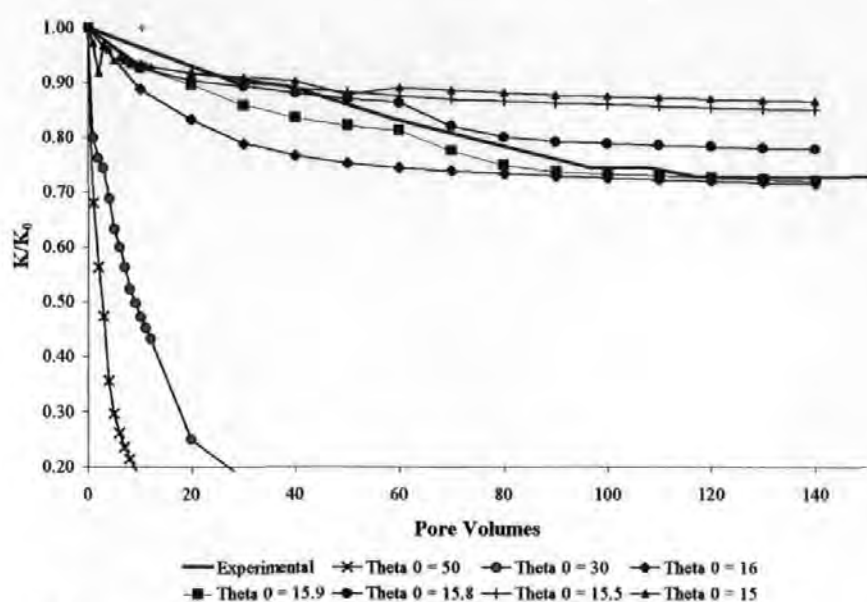
Figure 9.2 Results of varying θ_0 for sandstone sample.

The differences in rates of permeability damage as θ_0 was varied can be interpreted as simulating the effects of varying ionic conditions in experimental work. Increasing ionic strength experimentally would be expected to have the effect of increasing the likelihood of particle deposition taking place, due to the greater attractive forces that would be expected to be present within the system. Hence, increasing θ_0 causes θ to become larger, increasing the probability of fines being captured in features too large for size exclusion to take place and causing accelerated permeability decline. When size exclusion is the chief mechanism of deposition (low values of θ) rates of permeability decline will be slow if, as is the case here, the suspension contains few large (cf. pore size) particles.

9.3.2 Baghdikian Data

The new model was also tested more fully using the experimental data of Baghdikian et al. (1989) who examined particle plugging behaviour by flushing a Bentonite suspension through Ottawa sandpacks. Part of this study involved carrying out several core-flooding experiments keeping all conditions constant apart from flow rate, and these runs (12-14) were used to assess the reliability of the model developed here. A summary of the experimental details is given in Table 9.3.

Sample Details		Solution Details	
Sample	Ottawa sand	**Bentonite Conc.**	400 ppm
Particle Size Range	40/170 mesh	**Density of Solid Phase**	2.35
Initial Permeability, K	1.36 Darcies	**Viscosity, μ**	1.35 cps
Porosity	37.5%	**Flow Rates, Q_1**	5.4 ml min^{-1}
Length, L	322 mm	**Q_2**	11.4 ml min^{-1}
Cross-sectional area, A	3117.2 mm^2	**Q_3**	21.4 ml min^{-1}

Table 9.3 Summary of experimental details.

9.3.2.1 Pore-Cor Modelling

The sample was modelled using Pore-Cor. Table 9.4 shows the modelled conditions and Figure 9.3 shows the modelled and experimental mercury intrusion curves.
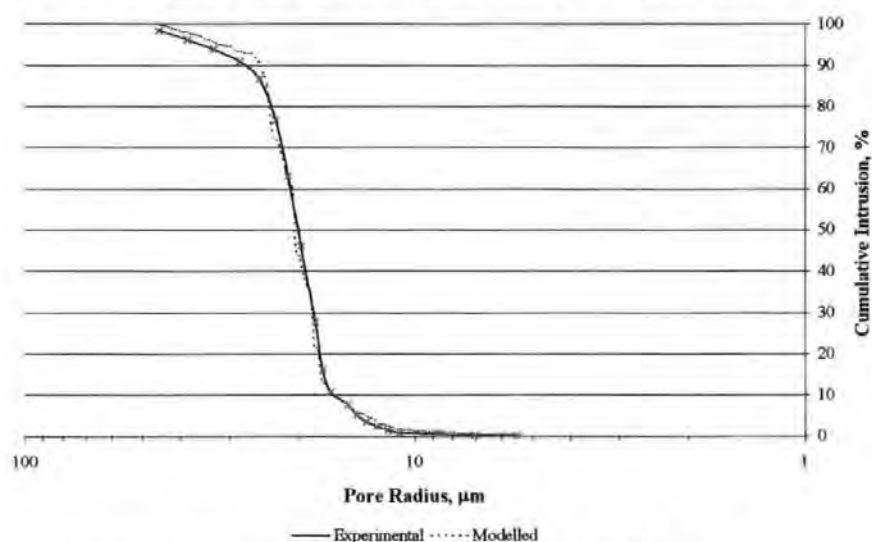
Figure 9.3 Experimental and modelled mercury intrusion for Baghdikian data.

Parameter	Value
Modelled Porosity	37.47 %
Modelled Permeability	0.453 Darcies
Type of Fit	Log
Throat Skew	0.47
Pore Skew	None
Minimum Throat Diameter	5.4780
Maximum Throat Diameter	45.3913
Connectivity	3.2

Table 9.4 Pore-Cor modelled parameters.

As can be seen from Figure 9.3 an extremely close fit of modelled to experimental mercury intrusion curve was achieved. Although the modelled permeability was somewhat low, it was deemed close enough to be acceptable for the purposes of this exercise. The

absolute value of the modelled permeability was not of great importance in this specific case as the study focussed on the ratio K_d/K_0, where K_d was the permeability after deposition and K_0 was initial permeability.

9.3.2.2 Results

Using the new particle capture program permeability damage due to fines deposition was simulated using the experimental conditions employed by Baghdikian et al. (1989). θ_0 was determined by assuming that the run carried out at the lowest volume flow rate, 5.4 ml minute^{-1}, was slow enough that the exponential term in Equation 8 could be ignored. Then θ_0 was varied until the best fit of model to experiment was achieved. Having done this the newly acquired value of θ_0 was used to determine a value for v^* by fitting modelled results to experimental for the experimental run carried out at the intermediate flow rate, 11.4 ml minute^{-1}. Once both of these values had been found they were re-input into the model and used to predict the results of the run carried out at the highest flow rate, 21.4 ml minute^{-1}. By this process the values of θ_0 and v^* were found to be 35.2 and 9 mm s^{-1} respectively. Details of experimental and modelled permeability decline for each run are shown in Figure 9.4 while Table 9.5 summarises experimental and modelled values of K_{end}/K_0.
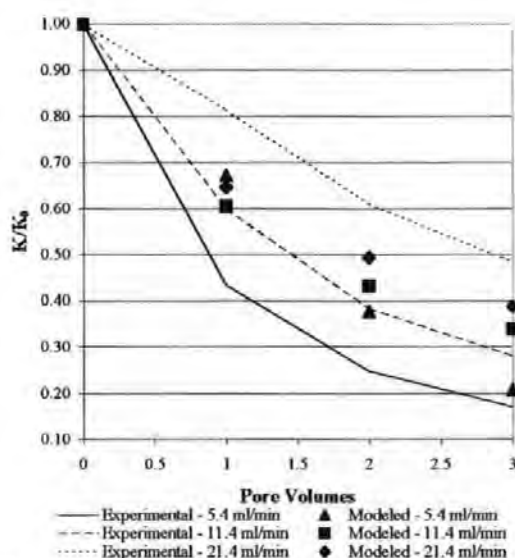
Figure 9.4 Results of modelling Baghdikian experimental data.

Flow Rate, ml minute^{-1}	Experimental K_{end}/K_0	Modelled K_{end}/K_0
5.4	0.17	0.207
11.4	0.28	0.338
21.4	0.55	0.388

Table 9.5 Ratios of K_{end}/K_0 for permeability decline modelling.

Although the model predicted a changing rate of decline between experimental runs it was rather insensitive to changes in flow rate. Final values of relative permeability (Table 9.5) deviate from the experimental results by just 3.7% and 5.8% for the 5.4 and 11.4 ml minute^{-1} flow rates respectively. However, the new model somewhat overestimates the permeability damage for the run carried out 21.4 ml minute^{-1}, predicting a final relative permeability of approximately two-thirds the experimental value. An unusual feature of the simulation is the fact that curves produced for the two highest flow rates cross over between 1 and 2 pore volumes. This is discussed in the next section.

9.4 Conclusions

From the results presented it can be seen that the model described here, although possessing shortcomings in its present form, could be developed into a useful model within the framework already provided by Pore-Cor. The new model produced cumulative permeability damage similar to that observed experimentally. The probabilistic determination of particle capture extended the method to a three-dimensional network model where previously it had only been applied to two-dimensional triangular (Rege, S. D. and Fogler, H. S., 1988) or square networks (Wenrong, M. et al., 1996).

An artefact of the modelling process was the crossing over of the modelled 11.4-ml min^{-1} and 21.4-ml min^{-1} curves between 1 and 2 pore volumes (Figure 9.4). This effect arose as a result of the complex combination of changing conditions (i.e. flow rate), the fact that deposition is modelled by considering the features of the unit cell sequentially and the sensitivity of the modelled permeability to the specific geometry of the unit cell. During the modelling process changes in the modelled flow rate affect the depth in the unit cell to which suspended particles may be transported prior to deposition. Due to the relatively small size of

the unit cell, certain regions of void features may contribute significantly to the overall modelled permeability. Hence, if the effect of a certain modelled flow rate is that a larger number of particles are deposited, coincidentally, in such a region, a large permeability drop will be observed.

Clearly the situation described above represents a limitation in the modelling procedure presented here. The unit cell modelled by Pore-Cor is relatively small and, as a consequence, even individual features may have a considerable effect on simulated permeability as demonstrated here. However, expansion of the unit cell was beyond the scope of this study.

With regards the model formulated in this study there are several areas that would need to be addressed to produce more accurate simulations. Perhaps most obvious of the theoretical problems is the use of the Navier-Stokes equations (Equations 10 and 11) to non-cylindrical volumes. Rectification of this would require the use of equivalent expressions developed for cubic volumes. Although many workers have examined laminar flow in cylindrical voids, which is therefore fairly well characterised, relatively little equivalent work has been conducted on laminar flow in cubes.

At present the model takes no account of particle-particle interactions, post-deposition particle 'scouring' from the sample surface or the effect of particle deposition on the parabolic velocity profiles assumed to be present within the features. Although it is theoretically possible to model these processes, inclusion would add further levels of complexity to the calculations and would add greatly to computation times. Also it was necessary to approximate the suspended particles to spheres. Clearly this is a rather gross approximation, for example the Bentonite modelled in Section 9.3.2 is made up of platelet shaped particles. It is possible that future work could incorporate equivalent solutions of the relevant hydrodynamic equations that would allow the modelling of alternate particle shapes. Another limitation concerning particle deposition is that deposition morphology was not considered.

Particles were assumed to deposit uniformly on the void surfaces. Were the model to be developed further it would be worth considering modelling some form of dendritic deposition.

With reference to the processes included in the model so far, further improvements could also be achieved by enhancing the method of determining how much material would be deposited in a feature containing a large number of fines (Equation 18). Ideally particles would be removed from suspension singly, re-calculating effective feature dimensions after each. However, as mentioned in Section 9.2, this had the effect of increasing computing times on a 166 MHz Pentium PC to over 12 hours per pore volume. The compromise used here served the purpose of allowing this feasibility study to be completed, however were the work to be continued it would be desirable to find a more sophisticated estimate of the number of particles that would be deposited in such circumstances.

The lack of sensitivity experienced here, expressed as the narrow range of possible permeability declines, could be addressed by enlargement of the Pore-Cor unit cell and a corresponding increase in the number of pore sizes within each simulation. The current 10 x 10 x 10 array of pores coupled with the limit of only 100 pore or throat sizes has the effect of limiting the range of permeability declines available through the varying of θ_0 and v^*.

Were this topic to be pursued further, a more fundamental model of particulate behaviour might be more appropriate than the empirical approach employed in this study. The network model as it stands would lend itself well to a trajectory analysis method. The existing procedure for determining the flow field across simulated media could be retained and enhanced, and the relevant calculations, for example those developed by Payatakes and Tien (1973; 1979) for determining particle motion superimposed onto this. For the purposes of this preliminary study, however, the extra computation time required by such a process rendered such an approach unsuitable.

10 Conclusions and Future Work

10.1 Conclusions

The aim of this research was to advance the modelling of porous materials via network modelling, with specific reference to the model Pore-Cor. This has been attempted through a combination of experimental study coupled with advanced modelling techniques.

In the present study it has been demonstrated that flow through apparently homogeneous sand samples was not homogeneous or reproducible. For the samples tested here, the development of flow was not Normally distributed and did not appear to be caused by gross heterogeneities within the sample structure. Nor did it appear to be affected by sample grain size, average permeability, depth or the layering of different sample types. Subsequently it was shown that different random packings alone could give rise to great localised variation in sample porosity and permeability. It was also shown that a network model could accurately reproduce both average values and ranges of these experimentally measured properties. This was achieved by generating different stochastic representations, analogous to different random packings of the real materials, of the simulated porous media. Although the network model cannot at present reproduce the flow paths observed experimentally, the potential to do so has been clearly identified.

A simple analytical solution of the convection-dispersion was tested. The transport of a conservative solute tracer, applied both uniformly to the sample surface and to a point source, through laboratory sand columns was modelled. The model predictions of the uniformly applied solute transport were only partially satisfactory. The accuracy of the predictions of lateral solute transport were similarly accurate, although generally less so for the deeper samples.

The localised variability in sample properties presumed to be responsible for the unpredictable development of flow paths was also thought to be responsible for inaccuracies

186

in the predictions of the convection-dispersion equation. The convection-dispersion equation conceptualises the theoretical transport volume as being a homogeneous continuum, characterised by single values of a diffusion coefficient, a retardation coefficient and the pore water velocity. Using single values of each of these parameters was shown to impose a great degree of inflexibility on the model, limiting its ability to even achieve a completely satisfactory calibration.

However, it was found that conservative tracer transport could be modelled more accurately using a range of pore water velocities, although no information about the nature of variability of this parameter could be inferred from the present study. The network model was used to simulate the samples upon which transport experiments were conducted. A range of unsaturated permeabilities was modelled, based on different stochastic generations of the same simulated materials. A small distribution of pore water velocities was then generated, with a similar variability to the modelled unsaturated permeabilities, and used to re-model the experimental solute transport more successfully than previously possible. Although this modelling was based on a simplified model it clearly demonstrated the potential of the network model to enhance the simulation of transport in porous materials.

Although it was not possible to directly improve the convection-dispersion equation modelling of lateral tracer transport, a possible method by which the network model might be able to assist in this was outlined.

Continuing the theme of examining the influence of microscopic variations in packing, standard image analysis, variogram and curve-fitting techniques were combined and refined to produce an objective method of quantifying levels of correlation in the spatial distribution of differently sized voids within porous materials. The new method, when applied to real and artificial porous samples, gave a clear indication of different levels of correlation in void size distributions. Such information could in future be used as a constraint on network modelling,

187

enabling the generation of simulations that were more realistic with greatly improved simulations of permeability.

An initial study was also carried out concerning the solid phase of network simulations, to the author's knowledge the first of its kind. It was shown that a theoretical particle size distribution could be extracted from the inverse of the void structure generated by the model. The new method was tested against experimental measures of particle size distribution for a variety of samples. Although the new model gave only a partial representation of the available solid phase, the results compared well with those of the only other available method and gave grounds for future development.

The transport and deposition of colloidal suspensions was also considered. A method of calculating the deposition of particles from a flowing suspension was incorporated into the network model. The new model featured deposition by both size exclusion and a probabilistic method, the latter having previously only been applied to two-dimensional networks. Although the work was chiefly a feasibility study, it demonstrated that the new method could model permeability declines similar to those observed experimentally.

10.2 Future Work

In Chapters 4-6 it was demonstrated that the network model Pore-Cor can be used to model the flow and transport characteristics of the samples studied here. It was shown that, through the use of stochastic network modelling, properties of the experimental samples could be accurately reproduced. However, in this study it was not possible to fully realise the potential of some of these findings.

Clearly a limitation of the network model in its present form is the size of its base unit, the unit cell, although it is not unusually small compared to other models in the literature. Currently this is constructed around a 10 x 10 x 10 cubic lattice, and as such represents only a

small volume of most simulated porous media. Much of the work carried out during this research has identified the unit cell size as a constraint on further improvements in modelling accuracy, and as such addressing this limitation might be seen as the natural next step were the current study to be continued. Various approaches to addressing this limitation exist.

Perhaps most obviously, the size of the unit cell could be increased. To date the size of the unit cell has been limited by the computing power offered by the platforms for which it has been developed, medium specification IBM-compatible PC's. Increases in the side length of the lattice result in something approaching a cubing of the computing time required for most calculations involving the unit cell. However, current technology is now such that the size of the unit cell could be probably be increased significantly, without increasing computing times to such a degree as to render the model unusable. The complex re-programming this would involve, however, was beyond the scope of the current study.

As mentioned previously, an alternative to increasing the unit cell size, though more computationally complex, would be to enable the model to construct composite simulations based on a number of different stochastic generations of a given material. As discussed in Chapter 6, this could allow more accurate simulations of the development of liquid flow paths within porous materials. In conjunction with enhancement of the simulated microtoming routines described in Chapter 7, it could also facilitate the simulation of materials with void size correlations over larger scales than those considered here. Such an ambitious development would certainly yield interesting results, and software already exists, such as that used by oil and gas reservoir engineers in the simulation of fossil fuel reservoirs, for constructing complex simulations based on discrete, well characterised elements.

With particular reference to the flow and transport work, both the modelling and characterisation aspects would benefit from further exhaustive experimental testing. As a consequence of this study the experimental apparatus has been re-designed, and is currently

being automated to allow sampling from all of the outputs of the grid lysimeter. This should allow further intensive study of samples similar to those described here.

The results of the new method for predicting the particle size distributions of simulated porous materials only accounted for a portion of the available solid volume. Although algorithms to employ more of this available volume would be considerably more complex than those developed here, they would be likely to improve the quality of model predictions.

The feasibility study of modelling suspended particulate transport and deposition demonstrated that the network model provides a suitable foundation for simulating such processes. Permeability response to deposition was somewhat insensitive, and either of the developments described above for addressing the limitations arising from unit cell size, would probably improve this. In particular the model requires exhaustive testing against experimental data to determine whether significant improvements to the current calculations can be made.

10.2.1 The Upscaling Problem

Beyond direct extension of the research carried out here, future work would also aim to address certain other perceived limitations of current network modelling theory. In particular, work would focus on the problems inherent in using microscopic representations of porous media to predict behaviour at the macroscopic scale, described in the literature as the problem of *upscaling*. The upscaling problem is well known in network modelling, particularly with reference to the prediction of permeability (Wen, X. H. and Gomez-Hernandez, J. J., 1996; Zhang, Q. and Sudicky, E., 1997). It has been demonstrated here and elsewhere (Tidwell, V. C. and Wilson, J. L., 1997; Tidwell, V. C. and Wilson, J. L., 1997) that permeability can exhibit great variability within apparently homogeneous samples. In sandstone and limestone samples it has been demonstrated that permeability may exhibit only weak, point to point spatial correlations (Henriette, A. et al., 1989). Although current upscaling methods attempt to cope with this variability they do not attempt to explain it at a fundamental level. The stochastic method presented here could enable study of the degree to which packing variability

190

causes this variation, and lead to an improved understanding of the upscaling problem in general. An outline of how this might be achieved follows a brief summary of upscaling below.

The upscaling problem may be defined by reference to Figure 10.1 (Wen, X. H. and Gomez-Hernandez, J. J., 1996).

a)   b)
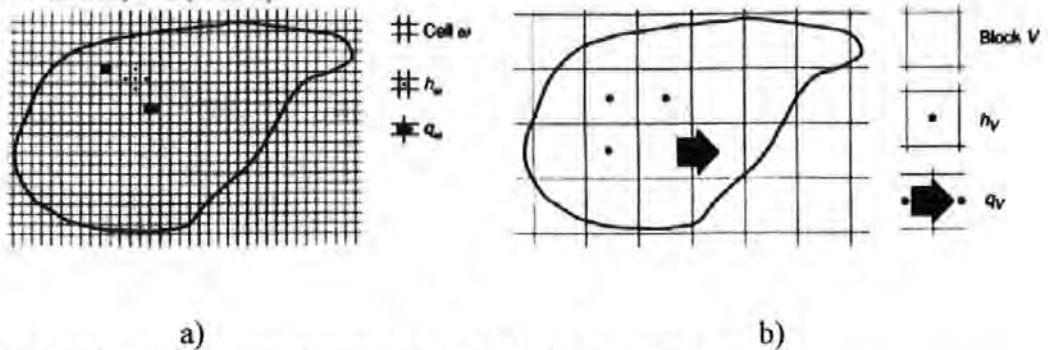
Figure 10.1 Examples of a) the measurement scale, and b) the numerical scale.

Figure 10.1 (a) illustrates a grid at the measurement scale, with possibly millions of cells. Figure 10.1 (b) shows a grid at the numerical scale on which the flow problem is to be solved. The objective of upscaling is to compute the conductivity block values in (b) from the corresponding values in (a). Following Rubin and Gomez-Hernandez (1990), the block conductivity K_v is defined from an extension of Darcy's law as:

$$\frac{1}{V}\int_V q_\omega(\mathbf{u})\,d\mathbf{u} \;=\; -K_V\left(\frac{1}{V}\int_V \nabla h_\omega(\mathbf{u})\,du\right) \qquad ,$$

[1]

where V represents the block support, q_ω is the specific discharge vector at cell ω within the block, $\mathbf{u}$ the position vector which sweeps the inside of the block, and ∇h_ω is the gradient of the piezometric head at cell ω. Vector integration can be performed by integration of its components in the Cartesian co-ordinates x, y, and z.

This equation cannot be solved without additional information about $q_\omega(\mathbf{u})$ and $\nabla h_\omega(\mathbf{u})$. Most approaches detailed in the current literature on the problem involve its circumvention by making approximations not about $q_\omega(\mathbf{u})$ and $\nabla h_\omega(\mathbf{u})$, but by formulating the problem as the much simpler relationship:

$$\mathbf{K_V} \approx \frac{1}{V}\int_V \mathbf{K}_\omega(\mathbf{u})\,d\mathbf{u} \approx \Gamma(\mathbf{K}_\omega) \qquad ,$$

<div align="right">[2]</div>

where $\mathbf{K}_\omega$ is the permeability of the cell ω, and Γ is an averaging operator. These approximations are reviewed by Wen et al. (1996). The simplest approximations involve averaging operators that range between the geometric and arithmetic mean. For shales, a tortuous stream tube approximation has been employed, analogous to the model shown in Figure 10.2, although with a higher tortuosity than that shown. Laplacian techniques involve solution of the Laplace equation, with various areas and boundary conditions.
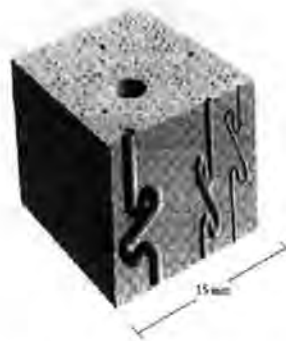
Figure 10.2 Schematic representation of tortuosity

Other approaches include that of 'energy dissipation' (Renard, P. and Demarsily, G., 1997), the use of elastic grids and wavelets (Chu, L. F. et al., 1998; Nilsen, S. and Espedal, M. S., 1996; Nilsen, S. and Espedal, M. S., 1996), and the calculation of pseudo-relative permeabilities (Barker, J. W. and Thibeau, S., 1997). The common theme which runs through all these approaches to upscaling is that the problem is being solved by manipulating the property itself, or by solving the Laplacian parameters directly underlying permeability (Indelman, P., 1993; Sánchez-Vila, X. et al., 1995; Sánchez-Vila, X. et al., 1995).

$q_\omega(\mathbf{u})$ and $\nabla h_\omega(\mathbf{u})$ could be investigated by incorporating additional information related to variations with $\mathbf{u}$, i.e. explicit structural relationships below the continuum level. However, these relationships would have to contribute directly to the property in question, namely permeability. One source of information derives from the property adjacent to permeability on the 'displacement phase diagram' of Lenormand (1988), namely percolation, which can be measured by mercury porosimetry. Another derives from image analysis. The problem here is

that thin sections cannot reveal connectivity, even though workers try to approximate this (Vogel, H. J. and Kretzschmar, A., 1996). Permeability is very dependant on connectivity, an increase in connectivity from 2.8 to 4 causing a permeability increase of four orders of magnitude (Matthews, G. P. et al., 1995). Literature values from thin sections could be used to specify the void size range, and, for example, the three-dimensional image analysis of Wardlaw et al. (1987) to give the void:throat size auto-correlation for sandstone (Matthews, G. P. and Spearing, M. C., 1992).

As mentioned above, methods of upscaling have tended to involve either manipulation of the permeability property itself, or the solving of equations involving the pressure gradients and flow capacities from which permeability is derived. Although variations in permeability are recognised as arising from local variations in void geometries, these variations are not usually explicitly related to void geometries. Where such relationships have been derived (Mourzenko, V. V. et al., 1995; Ma, S. X. et al., 1996), they have not been upscaled. Additional insights could be obtained by incorporating such information, derived from percolation characteristics and image analysis.

The network model, Pore-Cor, used in this study allows such information to be incorporated via a simulated network geometry. A brief outline of how it might be used to provide further insight into the question of upscaling follows.

The first step in such a study would be to characterise as fully as possible a simple porous material, such as the Clashac sandstones upon which initial model development was based. In terms of permeability this could be achieved by measurement over both the core scale, using a through-flow permeameter, and at a more localised scale by taking many spot permeameter measurements throughout the sample. Porosity could also be measured at both levels in an analogous way.

The network model could then be used to model the percolation characteristics gained from the porosimetry. Permeability simulations could be compared to experimental results at the plug scale, attributing variability between stochastic generations to geometric arrangements at the single-grain level. The range of modelled permeabilities could then be compared with samples with identical, and varying, mercury percolation characteristics.

Permeabilities could then be upscaled using finite difference software and the Pore-Cor Dinic network analysis algorithm. The underlying variability of the permeability could be used to generate successive upscaled permeabilities, which could be compared with the actual upscaled values. The interpretation would be based on the nature of the difference between the simulated and actual upscaled distributions. If, for example, the simulated distribution at the upscaled distance had a wider standard deviation than the experimental distribution, then this unwanted discrepancy could arise either from incorrect upscaling or from lack of constraints used in the generation of the simulated values at the unit-cell scale. The constraints at unit-cell level could be modified using additional data from the experimental samples (e.g. a more precise pore:throat correlation), and by altering the nature of the constraints. Currently, for example, connectivity is unconstrained – it attains an average value over the whole unit cell, and has the same expectation value for voids of any size. Fractal arguments would suggest that the connectivity should change with void size, and this additional constraint could be imposed. If, however, the range of simulated values was less than the measured values the additional variability in the experimental samples might be attributed to un-modelled geometric and surface interaction factors. In any case, the subsequent study of further porous materials would be expected to cast further light on the processes involved.

The generic method described here could be used over any range of scales incorporating the same heterogeneity characteristics. Samples such as fissured rock, which exhibit increased heterogeneity at larger scales, could also be better understood in terms of superimposition of the fissure heterogeneity on the modelled variability of the fundamental matrix permeability. These developments are the subject of a proposed future project.

194

Appendix A Sample Details

A.1 Chemical Composition

Chemical Analysis, %	Redhill 30	Redhill 65	Redhill HH	Chelford 60
SiO_2	99.30	99.20	98.30	96.70
Fe_2O_3	0.05	0.06	0.29	0.18
Al_2O_3	0.07	0.11	0.32	1.65
K_2O	0.01	0.01	0.06	1.00
Lost on ignition	0.10	0.09	0.22	0.28

Table A.1 Chemical composition of sands.

The Ballotini Beads (Phase Separations Ltd, Deeside, U.K.) were made of soda glass. No information was available on the compositions of either the sample used by Baghdikian et al. (1989) or the sandstone sample used in Chapter 9.

A.2 Particle Size Distribution

Particle	Beads	Redhill 30		Redhill 65		Redhill HH		Chelford 60	
Size, μm	MX	Supplied	MX	Supplied	MX	Supplied	MX	Supplied	MX
'Pan'	76.28	0.00	0.01	0.10	0.00	51.30	43.17	0.1	0.00
63	33.72	0.00	0.02	0.40	0.00	29.10	28.21	0.3	0.00
90	0.00	0.10	0.10	3.00	0.50	13.40	18.34	2.7	0.34
125	0.00	0.40	0.54	17.10	9.10	5.00	8.60	23.7	7.76
180	0.00	2.10	2.31	37.70	25.76	0.70	1.35	38.5	25.62
250	0.00	19.30	10.75	33.80	36.74	0.30	0.04	24.2	42.20
355	0.00	48.50	30.38	7.50	22.14	0.20	0.21	8.3	20.77
500	0.00	27.50	34.95	0.30	5.69	0.00	0.03	1.9	3.31
710	0.00	3.00	15.12	0.10	0.07	0.00	0.00	0.2	0.01
1000	0.00	0.10	4.36	0.00	0.00	0.00	0.00	0.1	0.00
1410	0.00	0.00	1.436	0.00	0.00	0.00	0.00	0.0	0.00
2000	0.00	0.00	0.00	0.00	0.00	0.00	0.00	0.0	0.00

Table A.2 Particle size distributions as supplied (sieved) and as measured by laser diffraction with a Malvern Instruments Mastersizer X (MX).

No information was available on the compositions of either the sample used by Baghdikian et al (1989) or the sandstone sample used in Chapter 9.

A.3 Porosity and Permeability

Sample	Porosity, %	Permeability, Darcies
Redhill 30	40.68	8.447
Redhill 65	44.46	2.842
Redhill HH	48.62	1.070
Chelford 60	43.05	2.070
Redhill HH on Redhill 30	-	2.300
Redhill 65 on Redhill 30	-	2.200
Ballotini Beads		1.460
Sandstone (Chapter 9)	39.10	3.296
Baghdakian Data	37.50	1.360

Table A.3 Experimental porosities, measured by mercury porosimetry and permeabilities. The methods of measurement for the last two samples are unknown. Permeabilities for all others were measured by constant head permeametry, except for Redhill HH and the Ballotini beads, which were measured by falling head permeametry.

Appendix B Flow Study Variograms

These are the directional variograms from phases 1-3 of the flow study in Chapter 4.
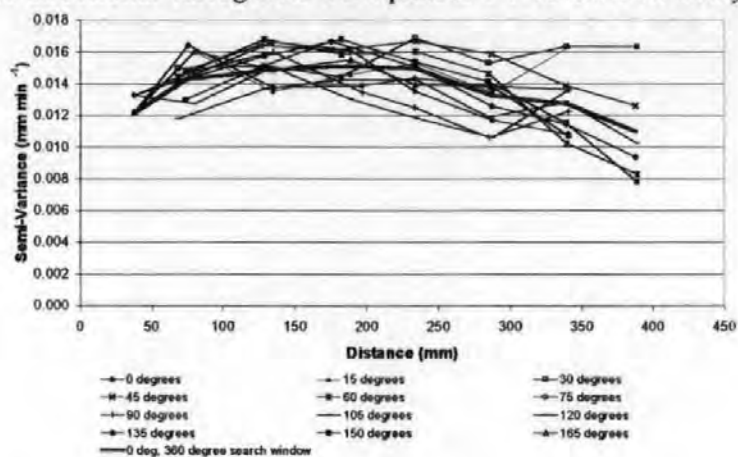
a)
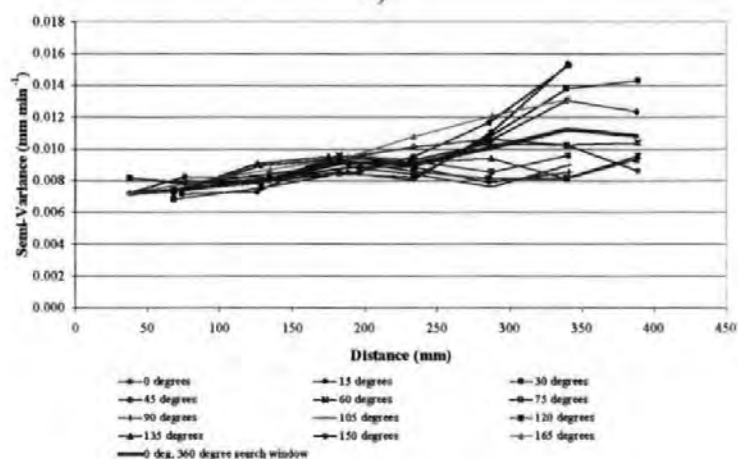
b)
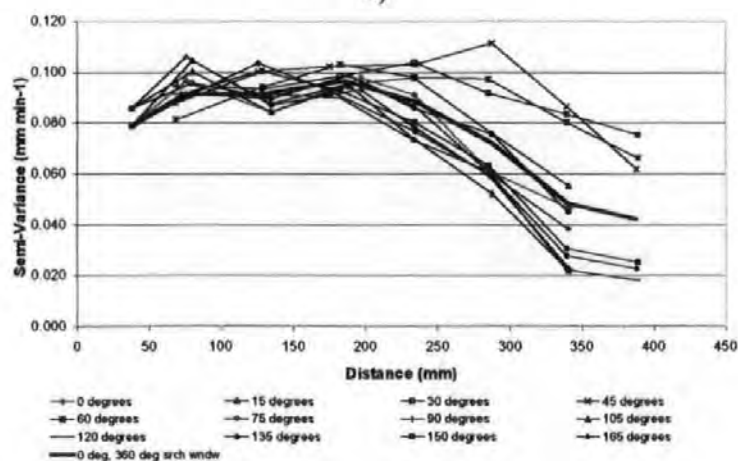
c)

Figure B.1 Directional variograms for phases a) 1, b) 2 and c) 3 of the flow study in Chapter 4.

Reference List

Addiscott, T. M. and Wagenet, R. J. (1985), Concepts of Solute Leaching in Soils: a Review of Modelling Approaches, *Journal of Soil Science*, **36**, pp 411-424

Adler, P. M. (1992), Reconstructed Porous Media, Porous Media: Geometry and Transports, Butterworth-Heinemann, Stoneham, MA, pp 503-538

Adler, P. M. and Brenner, H. (1984), Transport Processes in Spatially Periodic Capillary Networks . 1. Geometrical Description and Linear Flow Hydrodynamics, *Physicochemical Hydrodynamics*, **5**, pp 245-268

Adler, P. M., Jacquin, C. G., and Quiblier, J. A. (1990), Flow in Simulated Porous Media, *International Journal of Multiphase Flow*, **16**, pp 691-712

Ahuja, R. K., Kodialam, M., Mishra, A. K., and Orlin, J. B. (1997), Computational Investigations of Maximum Flow Algorithms, *European Journal Of Operational Research*, **97**, pp 509-542

Aigeltinger, E. H. and DeHoff, R. T. (1975), Quantitative Determination of Topological and Metric Properties During Sintering of Copper, *Metallurgical Transactions A*, **6A**, pp 1853-1862

Amoozegar-Fard, A., Nielsen, D. R., and Warrick, A. W. (1982), Soil Solute Concentration Distributions for Spatially-Varying Pore-Water Velocities and Apparent Diffusion Coefficients, *Soil Science Society Of America Journal*, **46**, pp 3-9

Anderson, P., Davis, G. R., and Elliot, J. C. (1994), Microtomography, *Microscopy and Analysis*, **3**, pp 31-33

Andreini, M. S. and Steenhuis, T. S. (1990), Preferential Paths of Flow Under Conventional and Conservation Tillage, *Geoderma*, **46**, pp 85-102

Baghdikian, S.Y., Sharma, M.M., and Handy, L.L. (1989), Flow of clay suspensions through porous media, SPE, Report 16257, pp 213-220

Bai, M., Bouhroum, A., Civan, F., and Roegiers, J. C. (1995), Improved Model for Solute Transport in Heterogeneous Porous-Media, *Journal of Petroleum Science and Engineering*, **14**, pp 65-78

Baker, J. M. and Lascano, R. J. (1989), The Spatial Sensitivity of Time-Domain Reflectometry, *Soil Science*, **147**, pp 378-384

Baker, R. S. and Hillel, D. (1990), Laboratory Tests of Fingering During Infiltration into Layered Soils, *Soil Science Society Of America Journal*, **54**, pp 20-30

Barker, J. W. and Thibeau, S. (1997), A Critical Review of the Use of Pseudo-relative Permeabilities for Upscaling, *SPE Reservoir Engineering*, **12**, pp 138-143

Belbin, S. P. (1994), A New Standard Method of Impregnation Using Crystic Resin, *Journal Of Sedimentary Research Section A-Sedimentary Petrology And Processes*, **64**, pp 673-673

Bell, W. K., van Brakel, J., and Heertjes, P. M. (1981), Mercury Penetration and Retraction Hysteresis in Closely Packed Spheres, *Powder Technology*, **29**, pp 75-88

Bernadiner, M. G. (1998), A Capillary Microstructure of the Wetting Front, *Transport in Porous Media*, **30**, pp 251-265

Best, J. V., Stephen, W. J., and Wickham, A. J. (1985), Radiolytic Graphite Oxidation, *Progress in Nuclear Energy*, **16**, pp 127-178

Beven, K. and Germann, P. (1982), Macropores and Water Flow in Soil, *Water Resources Research*, **18**, pp 1311-1325

Biggar, J. W. and Nielsen, D. R. (1976), Spatial Variability of the Leaching Characteristics of a Field Soil, *Water Resources Research*, **12**, pp 78-84

Blunt, M. and King, P. (1990), Macroscopic Parameters From Simulations of Pore Scale Flow, *The American Physical Society Physical Review A*, **42**, pp 4780-4787

Blunt, M. and King, P. (1991), Relative Permeabilities From Two and Three Dimensional Pore Scale Network Modelling, *Transport in Porous Media*, **6**, pp 407-433

Bouabid, R., Nater, E. A., and Barak, P. (1992), Measurement of Pore Size Distribution in a Lamellar Bt Horizon Using Epifluorescence Microscopy and Image Analysis, *Geoderma*, **53**, pp 309-328

Bowman, B. T., Brunke, R. R., Reynolds, W. D., and Wall, G. J. (1994), Rainfall Simulator Grid Lysimeter System for Solute Transport Studies Using Large, Intact Soil Blocks, *Journal Of Environmental Quality*, **23**, pp 815-822

Bresler, E. and Dagan, G. (1981), Convective and Pore Scale Dispersive Transport in Unsaturated Heterogeneous Fields, *Water Resources Research*, **17**, pp 1683-1693

Bronswijk, J. J. B., Hamminga, W., and Oostindie, K. (1995), Field-Scale Solute Transport in a Heavy Clay Soil, *Water Resources Research*, **31**, pp 517-526

Brooks, R. H. and Corey, A. T. (1964), Hydraulic Properties of Porous Media, Civil Engineering Department, Colorado State University, Fort Collins, pp 1-

Brusseau, M. L., Gerstl, Z., Augustijn, D., and Rao, P. S. C. (1994), Simulating Solute Transport in an Aggregated Soil With the Dual- Porosity Model - Measured and Optimized Parameter Values, *Journal Of Hydrology*, **163**, pp 187-193

Bryant, S. L., Mellor, D. W., and Cade, C. A. (1993), Physically Representative Network Models of Transport in Porous Media, *AIChE Journal*, **39**, pp 387-396

Buchter, B., Hinz, C., Flury, M., and Flühler, H. (1995), Heterogeneous Flow and Solute Transport in an Unsaturated Stony Soil Monolith, *Soil Science Society Of America Journal*, **59** , pp 14-21

Butters, G. L., Jury, W. A., and Ernst, F. F. (1989), Field Scale Transport of Bromide in an Unsaturated Soil 1.Experimental Methodology and Results, *Water Resources Research*, **25**, pp 1575-1581

Chatzis, I. and Dullien, F. A. L. (1981), Mercury Porosimetry Curves of Sandstones. Mechanisms of Mercury Penetration and Withdrawal, *Powder Technology*, **29**, pp 117-125

Chatzis, I. and Dullien, F. A. L. (1985), The Modelling of Mercury Porosimetry and the Relative Permeability of Mercury in Sandstones Using Percolation Theory, *International Chemical Engineering*, **25**, pp 47-66

Chow, V. T. and Harbaugh, T. E. (1965), Raindrop Production for Laboratory Watershed Experiments, *Journal of Geophysical Research*, **70**, pp 6111-6119

Christiansen, J.E. (1942), Irrigation by sprinkling, University of California, Coll. Agric., Report 670, pp 124-

Chu, L. F., Schatzinger, R. A., and Tham, M. K. (1998), Application of Wavelet Analysis to Upscaling of Rock Properties, *SPE Reservoir Evaluation & Engineering*, **1**, pp 75-81

Clothier, B. E. and Sauer, T. J. (1988), Nitrogen Transport During Fertilisation With Urea, *Soil Science Society Of America Journal*, **52**, pp 345-349

Conner, W.C., Blanco, C., Coyne, K., Neil, J., Mendioroz, S., and Pajares, J. (1988), Measurement of the Morphology of High Surface Area Solids: Inferring Pore Shape Characteristics, Characterisation of Porous Solids, pp 273-281

Conner, W. C., Horowitz, J., and Lane, A. M. (1988b), Correcting Porosimetry Data to Obtain the Actual Pore and Throat Size Distributions, *AIChE Symposium Series*, **84**, pp 29-34

Constantinides, G. N. and Payatakes, A. C. (1989), A Three-dimensional Network Model for Consolidated Porous Media. Basic Studies., *Chemical Engineering Comm.*, **81**, pp 55-81

Costa, J. L., Knighton, R. E., and Prunty, L. (1994), Model Comparison of Unsaturated Steady-State Solute Transport in a Field Plot, *Soil Science Society Of America Journal*, **58**, pp 1277-1287

Dawe, R. A. and Egbogah, E. O. (1978), Oil Recovery From Petroleum Reservoirs, *Contemporary Physics*, **19**, pp 355-376

Day, M., Parker, I.B., Bell, J., Fletcher, R., Duffie, J., Sing, K.S.W., and Nicholson, D. (1994), Modelling of Mercury Intrusion and Extrusion, Studies in Surface Science and Catalysis - Characterization of Porous Solids III, pp 225-234

Deepak, P. D. and Bhatia, S. K. (1994), Transport in Capillary Network Models of Porous-Media - Theory and Simulation, *Chemical Engineering Science*, **49**, pp 245-257

Dekker, L. W. and Ritsema, C. J. (1994), How Water Moves in a Water Repellant Sandy Soil 1. Potential and Actual Water Repellency, *Water Resources Research*, **30**, pp 2507-2517

Dexter, A. R. (1995), Heterogeneity of Unsaturated, Gravitational Flow of Water Through Beds of Large Particles, *Water Resources Research*, **29**, pp 1859-1862

Dullien, F. A. L. and Dhawan, G. K. (1975), Bivariate Pore-Size Distributions of Some Sandstones, *Journal of Colloid and Interface Science*, **52**, pp 129-135

Edwards, W. M., Shipitalo, M. J., and Owens, L. B. (1993), Gas, Water and Solute Transport in Soils Containing Macropores - a Review of Methodology, *Geoderma*, **57**, pp 31-49

Ehrlich, R., Crabtree, S. J., Horkowitz, O., and Horkowitz, J. P. (1991), Petrography and Reservoir Physics I: Objective Classification of Reservoir Porosity, *The American Association of Petroleum Geologists Bulletin*, **75**, pp 1547-1562

Ellsworth, T. R. and Jury, W. A. (1991), A 3-Dimensional Field-Study of Solute Transport Through Unsaturated, Layered, Porous-Media .2. Characterisation of Vertical Dispersion, *Water Resources Research*, **27**, pp 967-981

Ellsworth, T. R., Shouse, P. J., Skaggs, T. H., Jobes, J. A., and Fargerlund, J. (1996), Solute Transport in Unsaturated Soil - Experimental-Design, Parameter-Estimation, and Model Discrimination, *Soil Science Society Of America Journal*, **60**, pp 397-407

Fan, L. T., Nassar, R., Hwang, S. H., and Chou, S. T. (1985), Analysis of Deep-Bed Filtration Literature: Modelling As a Birth-Death Process, *AIChE Journal*, **31**, pp 1781-

Flury, M., Flühler, H., Jury, W. A., and Leuenberger, J. (1994), Susceptibility of Soils to Preferential Flow of Water: A Field Study, *Water Resources Research*, **30**, pp 1945-1954

Freeman, P. R., Hart, B. T., and Mckelvie, I. D. (1993), Dual Flow-Injection Analysis System for Determining Bromide and Reactive Phosphorus in Natural-Waters, *Analytica Chimica Acta*, **282**, pp 379-388

Gane, P. A. C., Kettle, J. P., Matthews, G. P., and Ridgway, C. J. (1996), Void Space Structure of Compressible Polymer Spheres and Consolidated Calcium Carbonate Paper-Coating Formulations, *Industrial and Engineering Chemistry Research*, **35**, pp 1753-1764

Garboczi, E. J. (1991), Mercury Porosimetry and Effective Networks for Permeability Calculations in Porous Materials, *Powder Technology*, **67**, pp 121-125

Ge, S. M. and Lu, N. (1996), A Semianalytical Solution of One-Dimensional Advective-Dispersive Solute Transport Under an Arbitrary Concentration Boundary-Condition, *Ground Water*, **34**, pp 501-503

Ghodrati, M. and Jury, W. A. (1990), A Field Study Using Dyes to Characterize Preferential Flow of Water, *Soil Science Society Of America Journal*, **54**, pp 1558-1563

Glasbey, C. A. and Horgan, G. W. (1995), Image Analysis for the Biological Sciences, John Wiley & Sons, Chichester

Goldman, E. and Byles, D. (1959), Suggested Revision of the Phenol Red Method for Bromide, *Journal of the American Waterworks Association*, **57**, pp 1051-1053

Gong, R. H. and Newton, A. (1992), Image Analysis Techniques Part 1: The Measurement of Pore Size Distribution, *J. Text. Inst.*, **83**, pp 253-268

Good, R. J. and Mikhail, R. Sh. (1981), The Contact Angle in Mercury Intrusion Porosimetry, *Powder Technology*, **29**, pp 53-62

Gruesbeck, C. and Collins, R. E. (1982), Entrainment and Deposition of Fine Particles in Porous-Media, *Society of Petroleum Engineers Journal*, **22**, pp 847-856

Haines, W. B. (1927), Studies in the Physical Properties of Soils. IV. A Further Contribution to the Theory of Capillary Phenomena in Soil, *Journal of Agricultural Science*, **17**, pp 264-290

Happel, J. and Brenner, H. (1980), Wall Effects on the Motion of a Single Particle, Low Reynolds Number Hydrodynamics, Nordhoff International Publishing, Leyden, pp 286-357

Heerjtes, P. M. and Lerk, F. F. (1967), The Function of Deep-Bed Filters, *Transactions of the Institute of Chemical Engineers*, **45**, pp

Hendrickx, J. M. H., Dekker, L. W., and Boersma, O. H. (1993), Unstable Wetting Fronts in Water Repellent Field Soils, *Journal Of Environmental Quality*, **22**, pp 109-118

Henriette, A., Jacquin, C. G., and Adler, P. M. (1989), The Effective Permeability of Heterogeneous Porous-Media, *Physicochemical Hydrodynamics*, **11**, pp 63-80

Hignett, C. T., Gusli, S., Cass, A., and Besz, W. (1995), An Automated Laboratory Rainfall Simulation System With Controlled Rainfall Intensity, Raindrop Energy and Soil Drainage, *Soil Technology*, **8**, pp 31-42

Hu, Q. H. and Brusseau, M. L. (1995), Effect of Solute Size on Transport in Structured Porous-Media, *Water Resources Research*, **31**, pp 1637-1646

Huang, K. L., van Genuchten, M. Th., and Zhang, R. D. (1996), Exact-Solutions for One-Dimensional Transport With Asymptotic Scale- Dependent Dispersion, *Applied Mathematical Modelling*, **20**, pp 298-308

Imdakm, A. O. and Sahimi, M. (1987), Transport of Large Particles in Flow Through Porous-Media, *Physical Review A-General Physics*, **36**, pp 5304-5309

Imdakm, A. O. and Sahimi, M. (1991), Computer-Simulation of Particle-Transport Processes in Flow Through Porous-Media, *Chemical Engineering Science*, **46**, pp 1977-1993

Indelman, P. (1993), Upscaling of Permeability of Anisotropic Heterogeneous Formations .3. Applications, *Water Resources Research*, **29**, pp 935-943

Ioannidis, M. A. and Chatzis, I. (1993a), A Mixed-Percolation Model of Capillary Hysteresis and Entrapment in Mercury Porosimetry, *Journal of Colloid and Interface Science*, **161**, pp 278-291

Ioannidis, M. A., Chatzis, I., and Sudicky, E. A. (1993b), The Effect of Spatial Correlations on the Accessibility Characteristics of Three-Dimensional Cubic Networks As Related to

Drainage Displacements in Porous Media, *Water Resources Research*, **29**, pp 1777-1785

Ison, C. R. and Ives, K. J. (1969), Removal Mechanisms in Deep-Bed Filtration, *Chemical Engineering Science*, **24**, pp 717-

Ives, K. J. (1960), Rational Design of Filters, *Proceedings of the Institute of Civil Engineers*, **20**, pp 189-

Journel, A. G. and Huijbregts, C. J (1978), Mining Geostatistics, Academic Press, London

Jury, W. A. (1982), Simulation of Solute Transport Using a Transfer Function Model., *Water Resources Research*, **18**, pp 363-368

Jury, W. A. and Flühler, H. (1992), Transport of Chemicals Through Soil: Mechanisms, Models and Field Applications, *Advances in Agronomy*, **47**, pp 141-201

Jury, W. A., Gardner, W. R., and Gardner, W. H. (1991), Soil Physics, John Wiley and Sons, New York

Jury, W. A. and Sposito, G. (1985), Field Calibration and Validation of Solute Transport Models for the Unsaturated Zone, *Soil Science Society Of America Journal*, **49**, pp 1331-1341

Keng, J. C. W., Scott, T. W., and Lugo-Lopez, M. A. (1998), Fertiliser Management With Drip Irrigation in an Oxixol, *Agronomy Journal*, **71**, pp 971-980

Kettle, J.P. and Matthews, G.P. (1993), Computer Modelling of the Pore Structure and Permeability of Pigmented Coatings, Advanced Coating Fundamentals Symposium, pp 121-126

Khan, A. A., Yitayew, M., and Warrick, A. W. (1996), Field-Evaluation of Water and Solute Distribution From a Point- Source, *Journal Of Irrigation And Drainage Engineering-ASCE*, **122**, pp 221-227

Khan, A. U. and Jury, W. A. (1990), A Laboratory Study of the Dispersion Scale Effect in Column Outflow Experiments, *Journal Of Contaminant Hydrology*, **5**, pp 119-131

Kirkham, D. and Powers, W. L. (1972), Fundamental Concepts of Unsaturated Flow, Advanced Soil Physics, Wiley-Interscience, 235-285

Kirkham, D. and Powers, W. L. (1995), Miscible Displacement, Advanced Soil Physics, Wiley-Interscience, 379-427

Kloubek, J. (1981), Hysteresis in Porosimetry, *Powder Technology*, **29**, pp 63-73

Knighton, R. E. and Wagenet, R. J. (1987), Simulation of Solute Transport Using a Continuous Time Markov Process 1. Theory and Steady State Application, *Water Resources Research*, **23**, pp 1911-1916

Knighton, R. E. and Wagenet, R. J. (1988), A Computer Program to Calculate Autocorrelograms, Semivariograms and Cross-Semivariograms, *Agronomy Mimeo*, 1-23

Koplik, J. (1982), Creeping Flow in Two-Dimensional Networks, *Journal of Fluid Mechanics*, **119**, pp 219-247

Kosugi, K. (1994), Three-Parameter Lognormal Distribution Model for Soil-Water Retention, *Water Resources Research*, **30**, pp 891-901

Kung, K.-J. S. (1990a), Preferential Flow in a Sandy Vadose Zone: 2. Mechanism and Implications, *Geoderma*, **46**, pp 59-71

Kung, K.-J. S. (1990b), Preferential Flow in a Sandy Vadose; 1. Field Observation, *Geoderma*, **46**, pp 51-58

Ledieu, J., de Ridder, P., de Clerk, P., and Dautrebande, S. (1986), A Method of Measuring Soil Moisture by TDR, *Journal Of Hydrology*, **88**, pp 319-328

Leij, F. J., Toride, N., and van Genuchten, M. Th. (1993), Analytical Solutions for Nonequilibrium Solute Transport in 3- Dimensional Porous-Media, *Journal Of Hydrology*, **151**, pp 193-228

Lenormand, R., Touboul, E., and Zarcone, C. (1988), Numerical Models and Experiments on Immiscible Displacements in Porous Media, *Journal of Fluid Mechanics*, **189**, pp 165-187

Li, Y., Laidlaw, W. G., and Wardlaw, N. C. (1986), Sensitvity of Drainage and Imbibition to Pore Structures As Revealed by Computer Simulation of Displacement Process, *Advances in Colloid and Interface Science*, **26**, pp 1-68

Li, Y. and Wardlaw, N. C. (1990), Quantitative Determination of Pore Structure From Mercury Capillary Pressure Curves, Interfacial Phenomena in Petroleum Recovery, Marcel Dekker, Inc., New York, Basel, pp 101-156

Liu, H. H. and Dane, J. H. (1996), An Extended Transfer-Function Model of Field-Scale Solute Transport - Model Development, *Soil Science Society Of America Journal*, **60**, pp 986-991

Losic, N., Thovert, J. F., and Adler, P. M. (1997), Reconstruction of Porous Media With Multiple Solid Phases, *Journal of Colloid and Interface Science*, **186**, pp 420-433

Lowry, M. I. and Miller, C. T. (1995), Pore-Scale Modelling of Non-wetting-Phase Residual in Porous-Media, *Water Resources Research*, **31**, pp 455-473

Lymberopoulos, D. P. and Payatakes, A. C. (1992), Derivation of Topological, Geometrical, and Correlational Properties of Porous Media From Pore Chart Analysis of Serial Section Data, *Journal of Colloid and Interface Science*, **150**, pp 61-80

Ma, S. X., Mason, G., and Morrow, N. R. (1996), Effect of Contact Angle on Drainage and Imbibition in Regular Polygonal Tubes, *Colloids And Surfaces A-Physicochemical And Engineering Aspects*, **117**, pp 273-291

Mason, G. and Mellor, D.W. (1991), Analysis of the Percolation Properties of a Real Porous Material, Characterization of Porous Solids II, pp 41-50

Mathews, T. J., Matthews, G. P., Moss, A. K., and Powell, G. (1994), Measurement and Simulation of Colloidal Flow Formation Damage in Sandstone, *Journal of the Society of Petroleum Engineers: Formation Evaluation pre-prints,*

Mathews, T. J., Matthews, G. P., Ridgway, C. J., and Moss, A. K. (1997), Measurement of Void Size Correlation in Inhomogeneous Porous Media, *Transport in Porous Media,* **28**, pp 135-158

Matthews, G. P., Moss, A. K., and Ridgway, C. J. (1995), The Effects of Correlated Networks on Mercury Intrusion Simulations and Permeabilities of Sandstone and Other Porous Media, *Powder Technology,* **83**, pp 61-77

Matthews, G. P., Moss, A. K., Spearing, M. C., and Voland, F. (1993), Network Calculation of Mercury Intrusion and Absolute Permeability in Sandstone and Other Porous Media, *Powder Technology,* **76**, pp 95-107

Matthews, G.P. and Ridgway, C.J. (1997), Simulation of the Effects of Diagenesis, Cementation and Compaction on the Absolute Permeability of Rock, 644-644

Matthews, G. P., Ridgway, C. J., and Small, J. S. (1996), Modelling of Simulated Clay Precipitation Within Reservoir Sandstones, *Marine and Petroleum Geology,* **13**, pp 581-589

Matthews, G. P., Ridgway, C. J., and Spearing, M. C. (1995), Void Space Modelling of Mercury Intrusion Hysteresis in Sandstone, Paper Coating and Other Porous Media, *Journal of Colloid and Interface Science,* **171**, pp 8-27

Matthews, G. P. and Spearing, M. C. (1992), Measurement and Modelling of Diffusion, Porosity and Other Pore Level Characteristics of Sandstones, *Marine and Petroleum Geology,* **9**, pp 146-154

Mayer, R. P. and Stowe, R. A. (1965), Mercury Porosimetry - Breakthrough Pressure for Penetration Between Packed Spheres, *J.Coll.Sci.,* **20**, pp 893-911

Micromeritics. Mercury Porosimetry Particle Size Distribution Template. Application Note (79). 1996. Micromeritics.
Ref Type: Generic

Miller, J C. and Miller, J N. (1993), Statistics for Analytical Chemistry, Ellis Horwood, NY

Miyazaki, T. (1993a), Preferential Flow, Water Flow in Soils, Marcel Dekker, New York, pp 93-121

Miyazaki, T. (1993), Water Flow In Soils, Marcel Dekker, New York

Mourzenko, V. V., Thovert, J. F., and Adler, P. M. (1995), Permeability of a Single Fracture - Validity of the Reynolds- Equation, *Journal De Physique Ii,* **5**, pp 465-482

Mualem, Y. (1976), A New Model for the Predicting the Hydraulic Conductivity of Unsaturated Porous Media., *Water Resources Research*, **12**, pp 513-522

Nabzar, L., Chauveteau, G., and Rocque, C. (1996), A new model for formation damage by particle retention, 31119, pp 1-16

Nachabe, M. H., Islas, A. L., and Illangasekare, T. H. (1995), Analytical Solutions for Water-Flow and Solute Transport in the Unsaturated Zone, *Ground Water*, **33**, pp 304-310

Nielsen, D. R. and Biggar, J. W. (1962), Miscible Displacement: 3. Theoretical Considerations, *Soil Science Society of America Proceedings*, **26**, pp 216-221

Nilsen, S. and Espedal, M. S. (1996), Wavelet Upscaling Based on Piecewise Bilinear Approximation of the Permeability Field, *Transport in Porous Media*, **23**, pp 125-134

Payatakes, A. C., Tien, C., and Turian, R. M. (1973), A New Model for Granular Porous Media. I: Model Formulation, *AIChE Journal*, **19**, pp 58-

Peat, D. M. W., Matthews, G. P., Worsfold, P. J., and Jarvis, S. (1998), Three-Dimensional Void Space Modelling of Soil Water Retention and Prediction of Saturated Hydraulic Conductivity, *European Journal of Soil Science*,

Petersen, L. W., Thomsen, A., Moldrup, P., Jacobsen, O. H., and Rolston, D. E. (1995), High-Resolution Time-Domain Reflectometry - Sensitivity Dependency on Probe-Design, *Soil Science*, **159**, pp 149-154

Phillips, R. E., Quisenberry, V. L., and Zeleznik, J. M. (1995), Water and Solute Movement in an Undisturbed, Macroporous Column - Extraction Pressure Effects, *Soil Science Society Of America Journal*, **59**, pp 707-712

Porter, K. E. (1968), Liquid Flow in Packed Columns 1. The Rivulet Model, *Transactions of Institution of Chemical Engineers*, **46**, pp 69-73

Porter, K. E. (1989), An Overview of Formation Damage, *Journal of Petroleum Technology*, 780-786

Porter, K. E., Barnet, V. D., and Templeman, J. J. (1968), Liquid Flow in Packed Columns 2. The Spread of Liquid Over Random Packings, *Transactions of Institution of Chemical Engineers*, **46**, pp 74-85

Quisenberry, V. L., Phillips, R. E., and Zeleznik, J. M. (1994), Spatial-Distribution of Water and Chloride Macropore Flow in a Well-Structured Soil, *Soil Science Society Of America Journal*, **58**, pp 1294-1300

Raats, P. A. C. (1973), Unstable Wetting Fronts in Uniform and Nonuniform Soils, *Soil Science Society Of America Journal*, **37**, pp 681-685

Rege, S. D. and Fogler, H. S. (1987), Network Model for Straining Dominated Particle Entrapment in Porous- Media, *Chemical Engineering Science*, **42**, pp 1553-1564

Rege, S. D. and Fogler, H. S. (1988), A Network Model for Deep Bed Filtration of Solid Particles and Emulsion Drops, *AIChE Journal*, **34**, pp 1761-1772

Renard, P. and Demarsily, G. (1997), Calculating Equivalent Permeability: A Review, *Advances In Water Resources*, **20**, pp 253-278

Ridgway, C. J., Ridgway, K., and Matthews, G. P. (1997), Modelling of the Void Space of Tablets Compacted Over a Range of Pressures, *Journal of Pharmacy and Pharmacology*, **49**, pp 377-383

Ringrose, P.S., Pickup, G.E., Jensen, J.L., and Sorbie, K.S. (1992), The Use of Correlation Statistics for Modelling Immiscible Displacements in Petroleum Reservoirs, 3rd European Conference on the Mathematics of Oil Recovery, DELFT, pp 15-29

Ritsema, C. J. and Dekker, L. W. (1994), How Water Moves in a Water Repellent Sandy Soil 2. Dynamics of Fingered Flow, *Water Resources Research*, **30**, pp 2519-2531

Romkens, M. J. M., Glenn, L. F., Nelson, D. W., and Roth, C. B. (1975), A Laboratory Rainfall Simulator for Infiltration and Soil Detachment Studies., *Soil Science Society of America Proceedings*, **39**, pp 158-160

Rubin, Y. and Gomez-Hernandez, J. J. (1990), A Stochastic Approach to the Problem of Upscaling of Conductivity in Disordered Media - Theory and Unconditional Numerical Simulations, *Water Resources Research*, **26**, pp 691-701

Ruzyla, K. (1986), Characterization of Pore Space by Quantitative Image Analysis, *Society of Petroleum Engineers Formation Evaluation*, 389-398

Sallès, J., Thovert, J. F., and Adler, P. M. (1993), Deposition in Porous-Media and Clogging, *Chemical Engineering Science*, **48**, pp 2839-2858

Sánchez-Vila, X., Girardi, J. P., and Carrera, J. (1995), A Synthesis of Approaches to Upscaling of Hydraulic Conductivities, *Water Resources Research*, **31**, pp 867-882

Schlicting, H. (1979), Boundary Layer Theory, McGraw-Hill, New York

Sharma, M. M. and Yortsos, Y. C. (1987), A Network Model for Deep Bed Filtration Processes, *Aiche Journal-American Institute Of Chemical Engineers*, **33**, pp 1644-1653

Shaw, D. J. (1986), Introduction to Colloid and Surface Chemistry, Butterworth, London

Soo, H. and Radke, C. J. (1986), A Filtration Model Form the Flow of Dilute, Stable Emulsions in Porous Media - 1 Theory, *Chemical Engineering Science*, **41**, pp 263-272

Sorbie, K. S. and Clifford, P. J. (1991), The Inclusion of Molecular-Diffusion Effects in the Network Modelling of Hydrodynamic Dispersion in Porous-Media, *Chemical Engineering Science*, **46**, pp 2525-2542

Spanne, P., Thovert, J. F., Jacquin, C. J., Lindquist, W. B., Jones, K. W., and Adler, P. M. (1994), Synchrotron Computed Microtomography of Porous-Media - Topology and Transports, *Physical Review Letters*, **73**, pp 2001-2004

Spearing, M. C. and Matthews, G. P. (1991), Modelling Characteristic Properties of Sandstones, *Transport in Porous Media*, **6**, pp 71-90
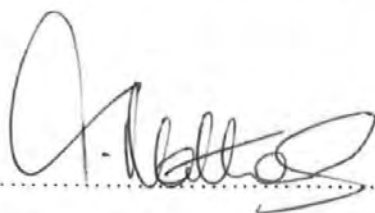
Taylor, J. M. (1950), Pore-Space Reduction in Sandstones, *Bulletin of the American Association of Petroleum Geologists*, **34**, pp 701-716

Templeton, C. (1954), *Petroleum Transactions AIME*, **201**, pp 161-

Thompson, A.H., Katz, A.J., and Raschke, R.A. (1987), Estimation of Absolute Permeability From Capillary Pressure Measurements, 62nd Annual Technical Conference and Exhibition of the Society of Petroleum Engineers, pp 475-481

Thompson, M. L., Singh, P., Corak, S., and Straszheim, W. E. (1992), Cautionary Notes for the Automated Analysis of Soil Pore-Space Images, *Geoderma*, **53**, pp 399-415

Thompson, P. A. and Troian, S. M. (1997), A General Boundary Condition for Liquid Flow at Solid Surfaces, *Nature*, **389**, pp 360-362

Tidwell, V. C. and Wilson, J. L. (1997), Laboratory Method for Investigating Permeability Upscaling, *Water Resources Research*, **33**, pp 1607-1616

Tien, C., Turian, R. M., and Pendse, H. (1979), Simulation of the Dynamic Behaviour of Deep-Bed Filters, *AIChE Journal*, **25**, pp 385-

Todd, A.C., Somerville, J.E., and Scott, G. (1984), The application of depth of formation damage measurements in predicting water injectivity decline, SPE, Report 12498, pp

Topp, G. C. and Davis, J. L. (1985), Measurement of Soil-Water Content Using Time-Domain Reflectrometry (Tdr) - a Field-Evaluation, *Soil Science Society Of America Journal*, **49**, pp 19-24

Topp, G. C., Davis, J. L., and Annan, A. P. (1980), Electromagnetic Determination of Soil Water Content: Measurements in Coaxial Transmission Lines, *Water Resources Research*, **16**, pp 574-582

Tsakiroglou, C. D. and Payatakes, A. C. (1991), Effects of Pore-Size Correlations on Mercury Porosimetry Curves, *Journal of Colloid and Interface Science*, **146**, pp 479-494

van Brakel, J. (1975), Pore Space Models for Transport Phenomena in Porous Media Review and Evaluation With Special Emphasis on Capillary Liquid Transport, *Powder Technology*, **11**, pp 205-236

van Brakel, J., Modry, S., and Svata, M. (1981a), Mercury Porosimetry: State of the Art, *Powder Technology*, **29**, pp 1-12

van Brakel, J., Modry, S., and Svata, M. (1981b), Mercury Porosimetry: State of the Art, *Powder Technology*, **29**, pp 1-12

van Genuchten, M.Th. and Alves, W.J. (1982), Analytical solutions of the one-dimensional convective-dispersive solute transport equation, United States Department of Agriculture, Report 1661, pp

van Genuchten, M. Th. and Jury, W. A. (1987), Progress in Unsaturated Flow and Transport Modeling, *Reviews of Geophysics*, **25**, pp 135-140

van Genuchten, M. Th. and Wierenga, P. J. (1976), Mass Transfer Studies in Porous Sorbing Media 1. Analytical Solutions, *Soil Science Society Of America Journal*, **40**, pp 473-480

Vogel, H. J. and Kretzschmar, A. (1996), Topological Characterization of Pore-Space in Soil - Sample Preparation and Digital Image-Processing, *Geoderma*, **73**, pp 23-38

Ward, A. L., Kachanoski, R. G., and Elrick, D. E. (1994), Laboratory Measurements of Solute Transport Using Time-Domain Reflectometry, *Soil Science Society Of America Journal*, **58**, pp 1031-1039

Ward, A. L., Kachanoski, R. G., Vonbertoldi, A. P., and Elrick, D. E. (1995), Field and Undisturbed-Column Measurements for Predicting Transport in Unsaturated Layered Soil, *Soil Science Society Of America Journal*, **59**, pp 52-59

Wardlaw, N. C. (1990), Quantitative Determination of Pore Structure and Application to Fluid Displacement in Reservoir Rocks, North Sea Oil and Gas Reservoirs - II, Graham and Trotman, Tronheim, Norway, pp 229-243

Wardlaw, N. C. and Cassan, J. P. (1979), Oil Recovery Efficiency and the Rock-Pore Properties of Some Sandstone Reservoirs, *Bulletin of Canadian Petroleum Geology*, **27**, pp 117-138

Wardlaw, N. C., Li, Y., and Forbes, D. (1987), Pore-Throat Size Correlation From Capillary Pressure Curves, *Transport in Porous Media*, **2**, pp 597-614

Wardlaw, N. C. and McKellar, M. (1981), Mercury Porosimetry and the Interpretation of Pore Geometry in Sedimentary Rocks and Artificial Models, *Powder Technology*, **29**, pp 127-143

Wardlaw, N. C. and Taylor, R. P. (1976), Mercury Capillary Pressure Curves and the Interpretation of Pore Structures and Capillary Behaviour in Reservoir Rocks, *Bulletin of Canadian Petroleum Geology*, **24**, pp 225-262

Wen, X. H. and Gomez-Hernandez, J. J. (1996), Upscaling Hydraulic Conductivities in Heterogeneous Media: An Overview, *Journal Of Hydrology*, **183**, pp R9-R32

Wenrong, M., Shihong, S., Tianhua, L., Wenzhong, L., and Guoheng, H. (1996), Pore and throat network model and its application to the optimal selection of temporary plugging particles, SPE, Report 31099, pp 293-300

Whittaker (1984), Network Analysis, Operational Research on the Micro, 43-65

Williams, A. G., Scholefield, D., Dowd, J. F., Holden, N. M., and Deeks, L. (1999), Investigating Preferential Flow in a Large Intact Soil Block Under Pasture, *Soil Use And Management*,

Williams, M. A. (1977), Quantitative Methods in Biology, North Holland, Amsterdam

Yanuka, M., Dullien, F. A. L., and Elrick, D. E. (1984), Serial Sectioning and Digitisation of Porous Media for Two- and Three-Dimensional Analysis and Reconstruction, *Journal of Microscopy*, **135**, pp 159-168

Yanuka, M., Dullien, F. A. L., and Elrick, D. E. (1986), Percolation Processes and Porous Media I. Geometrical and Topological Model of Porous Media Using a Three-Dimensional Joint Pore Size Distribution, *Journal of Colloid and Interface Science*, 112, pp 24-41

Yao, J., Thovert, J. F., Adler, P. M., Tsakiroglou, C. D., Burganos, V. N., Payatakes, A. C., Moulu, J. C., and Kalaydjian, F. (1997), Characterization, Reconstruction and Transport Properties of Vosges Sandstones, *Revue De L Institut Francais Du Petrole*, 52, pp 3-21

Zhang, Q. and Sudicky, E. (1997), Upscaling in Porous Media: Theories and Computations, *Advances In Water Resources*, 20, pp 251-

Zhang, R. D. (1995), Prediction of Solute Transport Using a Transfer-Function Model and the Convection-Dispersion Equation, *Soil Science*, 160, pp 18-27

Signed...

14th July, 1999

i